Structural insights into ribosomes from pathogenic bacteria and their complexes with antibiotics and antibiotic-resistance ABC-F proteins

David Nicholson

Submitted in accordance with the requirements for the degree of Doctor of Philosophy

The University of Leeds

Faculty of Biological Sciences, School of Molecular and Cellular Biology

June 2021

Intellectual Property and Publication

The candidate confirms that the work submitted is his own, except where work which has formed part of jointly authored publications has been included. The contribution of the candidate and the other authors to this work has been explicitly indicated below. The candidate confirms that appropriate credit has been given within the thesis where reference has been made to the work of others.

Chapter 3 is based on work from a jointly authored publication:

Nicholson, D., Edwards, T.A., O'Neill, A.J. & Ranson, N.A. Structure of the 70S Ribosome from the Human Pathogen *Acinetobacter baumannii* in Complex with Clinically Relevant Antibiotics. *Structure* **28**, 1087-1100 e3 (2020). https://doi.org/10.1016/j.str.2020.08.004

D.N. carried out experiments and analysed the data. D.N., T.A.E., A.J.O., and N.A.R. conceived and directed the project. D.N., T.A.E., A.J.O., and N.A.R. wrote the manuscript.

Acknowledgements

First and foremost, I would like to thank my supervisors, Neil Ranson, Alex O'Neill and Thomas Edwards, for providing me the opportunity to work on this project and for their support and guidance throughout. A special thanks to Neil for his sage life and career advice, I really appreciate it. Thanks also to Merianne Mohamad for her patience whilst teaching me the basics of cloning and bacteriology and her invaluable assistance in isolating the Sal(B)-ribosome complex.

Specifically, research for the Sal project (Chapter 4) was carried out by myself and Merianne Mohamad. Both Merianne and I contributed equally to the molecular cloning, FLAG-tag affinity purification and silver-stain SDS-PAGE visualisation of the Sal(A-E) variants. My own contributions were the negative stain TEM, cryo-EM structure determination, model building and figure making. Merianne's contributions, as made clear in the main text, were the molecular cloning and MIC experiments that involved the mutants of Sal(B) and Sal from *S. saprophyticus*.

I'm also grateful to Justin Clarke for his expert technical help and advice relating to this project. Thanks also to the Wellcome Trust for their generous funding.

Thanks to Becky Thompson, Emma Hesketh, Dan Maskell, Charlie Scarff and Martin Fuller for their invaluable microscopy support and for putting up with my terabytes of data! A special extra thanks to Becky for your career advice and help with my internship application. You really went above and beyond despite being so busy, and I am ever so grateful. I am also indebted to Matt Iadanza, Dan Hurdiss and Shaun Rawson for their patience in teaching me the ins and outs of image processing.

Thank you to all members of the Ranson and O'Neill groups, as well as the wider Leeds cryo-EM community, for all your help and companionship over the years. Special shout-outs to Matt Byrne, Rodrigo Gallardo, Josh White, Joe Snowden, Sam Haysom, Rachel Johnson, David Klebl, Lorelai Vennard, Sammy Hover, Oliver Debski-Antoniak and Ben Chadwick, without whom the ups-and-downs of PhD life would have certainly been more difficult to ~~swim~~ get through. And to all my friends I've made throughout the past 5 years, not least my fellow Flags of the Flagship: thank you for making Leeds Life so special.

Finally, I owe a huge debt of gratitude to my family for their tremendous and unconditional support, without which I would not be where I am today. Thank you.

Abstract

Ribosome-targeting antibiotics are commonly used to treat infections caused by pathogenic bacteria, yet, concerningly, resistance to these drugs often develops following their introduction to the clinic. To effectively combat this threat, our understanding of the mechanisms by which antibiotics work and by which bacteria acquire resistance must be improved. To this end, this thesis presents an analysis of the cryo-electron microscope (cryo-EM) structures of ribosomes from pathogenic bacteria in complex with either an antibiotic or an ATP-binding cassette (ABC)-F antibiotic resistance protein.

Structures of the ribosome from *Acinetobacter baumannii* in complex with clinically relevant antibiotics amikacin or tigecycline reveal species-specific ribosomal features, particularly around the exit of the nascent peptide exit tunnel (NPET) and around the edge of the subunit interface. Amikacin and tigecycline interact with the *A. baumannii* ribosome at known aminoglycoside and tetracycline small subunit binding sites, respectively; however, tigecycline unexpectedly also binds at a secondary site within the central protuberance of the large subunit.

The structure of the ribosome from *Staphylococcus aureus* in complex with the antibiotic resistance ABC-F protein Sal(B) reveals that this protein binds the E site of the ribosome, with its interdomain linker protruding towards the peptidyl transferase centre (PTC), where it likely displaces pleuromutilin, lincosamide and streptogramin A antibiotics by a purely allosteric mechanism. Mutagenesis experiments and sequence comparison with Sal variants that mediate different resistance phenotypes show that tyrosine-264 of Sal(B) plays an important role in resistance, but that other residues must also contribute.

Overall, the work outlined in this thesis contributes to our molecular understanding of antibiotic action and resistance, and makes steps towards the structure-based rational design or modification of drugs that have improved activity against pathogens such as *A. baumannii* or *S. aureus*, or that have the ability to circumvent or inhibit the ABC-F target protection resistance mechanism.

Table of Contents

Table of Figures

Table of Tables

Abbreviations

2-DOS	2-deoxystreptamine
A site	aminoacyl site
aa-tRNA	aminoacyl-transfer RNA
ABC	ATP-binding cassette
ARE	antibiotic resistance
ArfA	alternative rescue factor A
ArfB	alternative rescue factor B
BAP	biofilm-associated protein
BLAST	Basic Local Alignment Search Tool
CC	correlation coefficient
CCD	charged coupled device
cryo-EM	cryo-electron microscopy
CTF	contrast transfer function
DC	decoding centre
DED	direct electron detector
DEPC	diethyl pyrocarbonate
DQE	detective quantum efficiency
E site	exit site
EF	elongation factor
EM	electron microscopy
EMDB	Electron Microscope Data Bank
EMPIAR	Electron Microscopy Public Image Archive
fMet	formylmethionine
FSC	Fourier shell correlation
IF	initiation factor

LB	Luria-Bertani
LS_AP	lincosamides, type A streptogramins and pleuromutilins
MAPS	monolithic active pixel sensors
MIC	minimum inhibitory concentration
MLD	messenger-like domain
MLS_BK	macrolides, lincosamides, type B streptogramins and ketolides
mRNA	messenger RNA
MS_B	macrolides and type B streptogramins
NBD	nucleotide binding domain
NPET	nascent polypeptide exit tunnel
OD_{600}	optical density at 600 nm
P site	peptidyl site
PDB	Protein Data Bank
PTC	peptidyl transferase centre
RF	release factor
RRF	ribosome recycling factor
rRNA	ribosomal RNA
S_A	type A streptogramins
S_B	type B streptogramins
SD	Shine-Dalgarno
SDS-PAGE	sodium dodecyl sulphate-polyacrylamide electrophoresis
smFRET	single molecule fluorescence resonance energy transfer
SmpB	small protein B
SPA	single particle analysis
TEM	transmission electron microscopy
TLD	tRNA-like domain
tmRNA	transfer-messenger RNA

tRNA	transfer RNA
TRPP	tetracycline ribosomal protection protein
WT	wild type

Chapter 1 Introduction

Ribosomes are molecular machines that synthesise proteins in all living cells, and since protein synthesis is essential to life, antibiotics that target the bacterial ribosome slow bacterial growth or cause cell death [1,2]. Such antibiotics are commonly used to treat infections caused by pathogenic bacteria, yet, concerningly, resistance to these drugs often develops following their introduction to the clinic [3].

In this chapter, the structure of the bacterial ribosome and the mechanism of translation is described. This is then followed by an overview of the major antibiotic classes that target the ribosome, and the mechanisms by which bacteria resist their effects.

1.1 Structure of the bacterial 70S ribosome

The bacterial 70S ribosome is a ~2.5 MDa ribonucleoprotein particle composed of ribosomal RNA (rRNA) and ribosomal proteins. It consists of a small, 30S subunit, which contains 16S rRNA and about 20 ribosomal proteins, and a large, 50S subunit, which contains 23S rRNA, 5S rRNA and about 30 ribosomal proteins [4]. The cores of both subunits and the subunit interface is mostly rRNA, with the ribosomal proteins largely being localised to the periphery of the ribosome, often with extensions towards the cores containing little or no secondary structure. The 30S subunit is comprised of a ‘body’, and a ‘head’ that can swivel relative to the body [5]. The 50S is largely rigid, though it contains two flexible stalks at its flanks, namely the L1 and L7/L12 stalks [4]. The L1 stalk facilitates the binding, movement and release of deacylated transfer RNA (tRNA) [6], whilst the L7/L12 stalk promotes recruitment of soluble factors to the ribosome and stimulates their GTP hydrolysis activity [7].

The ribosome uses messenger RNA (mRNA) as the template for protein synthesis, with each amino acid being specified by a triplet of bases (or codon), and an aminoacyl-transfer RNA (aa-tRNA) molecule being used to link an mRNA codon with an amino acid. The mRNA binds in a cleft between the head and body of the 30S subunit, where the anticodon of the tRNA interacts with the codon of the mRNA. At the other end of the tRNA molecule, the acceptor arm carries an amino acid or the nascent peptide, which binds to the 50S subunit. Each ribosome subunit has three tRNA binding sites: the A (aminoacyl) site, which binds incoming aa-tRNA, the P (peptidyl) site, which binds the peptidyl-tRNA carrying the nascent polypeptide chain, and the E (exit) site, which contains deacylated tRNA that is to be ejected from the ribosome [4].

The ribosome contains three key functional centres: the decoding centre (DC) in the 30S subunit, which ensures a correct, base-paired match between the mRNA codon and aa-tRNA anticodon, the peptidyl transferase centre (PTC) in the 50S subunit, where rRNA catalyses the peptide bond forming reaction, and the nascent polypeptide exit tunnel (NPET), which connects the PTC with the solvent-facing back of the 50S subunit, and through which the nascent protein traverses during translation [4,8,9]. The PTC and DC both largely consist of rRNA, which acts as the catalyst for peptide bond formation [10]. Conversely, the main role of the ribosomal proteins is to provide a scaffold that stabilises and orients the catalytic rRNAs [10], though there are some protein-dominated functional hotspots such as the mRNA entry pore, the translation factor binding site and the solvent-facing exit of the NPET [11]. The overall architecture of the ribosome is shown in Figure 1, with the DC, PTC and binding sites of the tRNA and mRNA molecules highlighted.

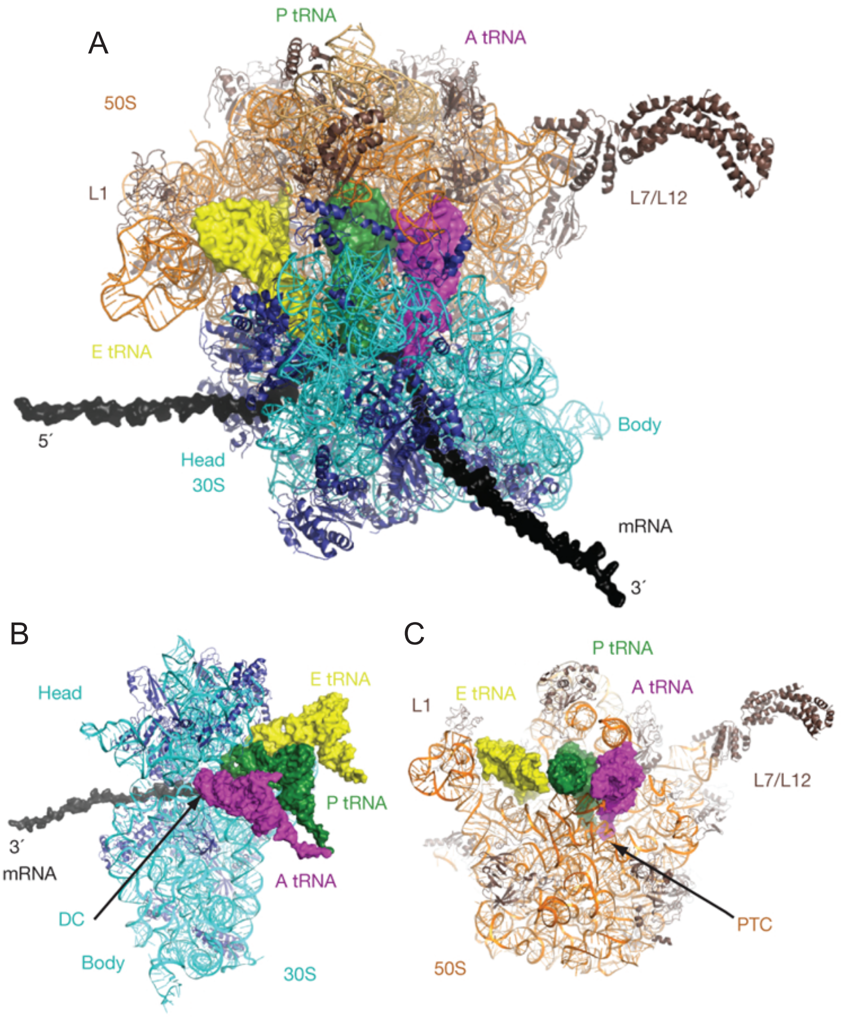

Figure 1 Structure of the 70S bacterial ribosome. A) Structure of the 70S ribosome with mRNA and A-, P- and E-tRNAs. B) The small 30S subunit, viewed from the subunit interface. C) The large 50S subunit, viewed from the subunit interface. Figure made using the model of the *T. thermophilus* ribosome [12], with a model of the L7/L12 stalk superimposed [7], and mRNA elongated by modelling. DC = decoding centre. Figure adapted from Schmeing & Ramakrishnan (2009) [4] with permission from Springer Nature © 2009.

1.2 The mechanism of translation

Bacterial translation can be divided into three main stages: initiation, elongation and termination. In initiation, an initiator formylmethionine (fMet)-tRNA^{fMet} is positioned over the mRNA start codon in the P-site, whilst during elongation, amino acids are sequentially added to the polypeptide chain. Finally in termination, the newly formed polypeptide is released, and the ribosome is recycled [4]. An overview of the translation cycle is shown in Figure 2, and each stage is described in more detail below.

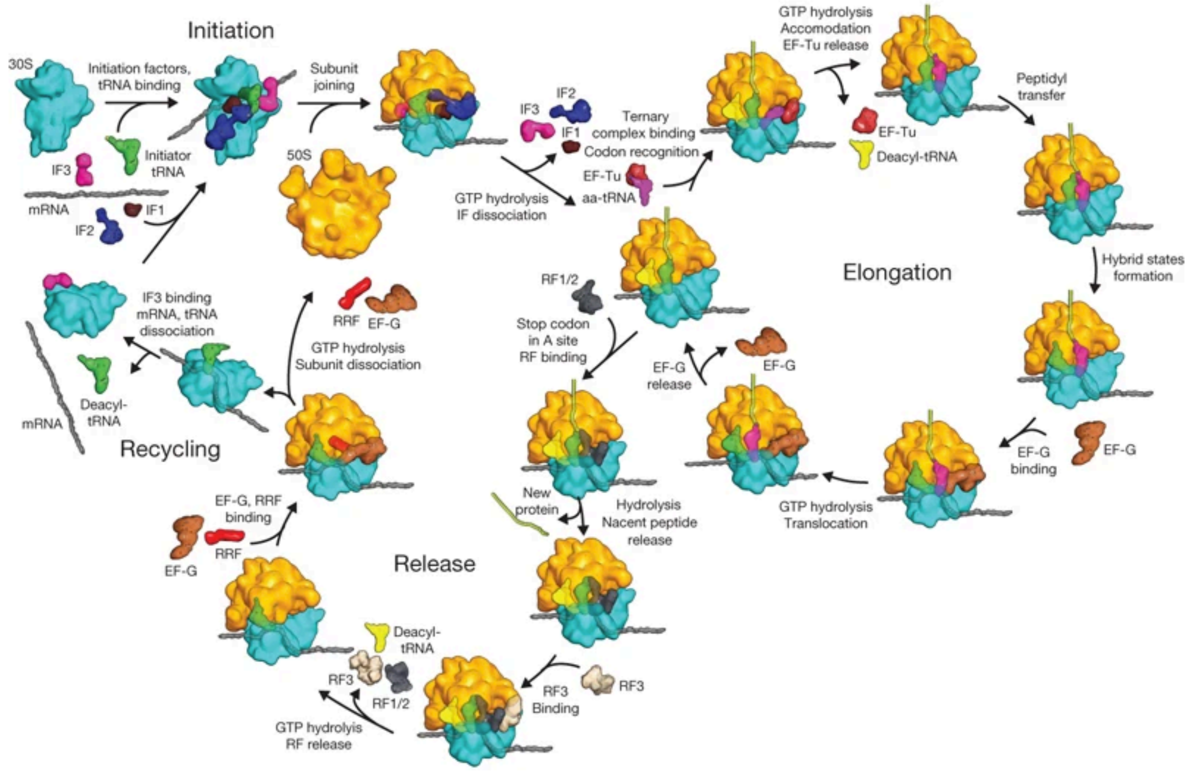

Figure 2 Overview of the translation cycle. Figure from Schmeing & Ramakrishnan (2009) [4] with permission from Springer Nature © 2009.

1.2.1 Initiation

Translation initiation is aided by three initiation factors, IF1-3. In cases where the mRNA contains a Shine-Dalgarno sequence, the initiation factors, mRNA and tRNA bind to the 30S subunit. IF3 likely binds first to stimulate release of leftover mRNA and tRNA from a previous round of translation, and to prevent the 50S subunit from re-associating [13]. Following this, mRNA, IF1, IF2 and initiator tRNA bind to the 30S-IF3 complex, with the combined action of the initiation factors ensuring that fMet-tRNA^{fMet} is selected over other tRNAs [14]. The Shine-Dalgarno (SD) sequence binds to the 3'-end of the 16S rRNA containing the anti-SD sequence [8]. The subunits join to form a 70S initiation complex, IF3 is released [15], and IF2 hydrolyses GTP to undergo a conformational change that allows fMet-tRNA^{fMet} to fully move into the PTC [16].

In contrast, leaderless mRNAs bind to 70S ribosomes directly, with recruitment of fMet-tRNA^{fMet} being facilitated by IF2 and IF3 [17]. Ribosomes can also perform 70S scanning initiation, where the ribosome stays associated to the mRNA after translating a cistron, and scans to the initiation site of a downstream cistron. In this case, IF3 binds to the 70S ribosome to maintain the 70S scanning complex. This process is promoted by IF1, which probably prevents entry of ternary complexes to the A site before the complex reaches the next initiation site. 70S scanning requires the initiation site of the downstream cistron to contain a Shine-Dalgarno sequence [18].

1.2.2 Elongation

At the start of each elongation cycle, the P-site contains either fMet-tRNA^{fMet} (in the first cycle) or peptidyl-tRNA carrying the nascent polypeptide chain (in later cycles). The next amino acid to be added to the nascent chain is brought to the A-site as part of a ternary complex between elongation factor Tu (EF-Tu), GTP and an aa-tRNA. If the correct aa-tRNA is delivered to the A-site (i.e. the tRNA with an anticodon that base pairs with the mRNA codon), EF-Tu will hydrolyse GTP and dissociate from the ribosome. This moves the aminoacyl end of the aa-tRNA into the A-site of the PTC in a process known as accommodation [4].

The selection of the correct aa-tRNA at the A-site is mediated by the DC of the ribosome. Specifically, G530, A1492 and A1493 of the 16S rRNA (*E. coli* numbering throughout) probe the minor groove of the first two base pairs of the anticodon-codon helix to sense Watson-Crick base pairing and discriminate against near-cognate tRNA. The third ‘wobble’ position is free to accommodate noncanonical base pairs [19]. The 16S rRNA residues flip to close in on the anticodon-codon helix, with G530 acting as a latch that induces a domain closure of the 30S subunit [20]. This brings EF-Tu closer to the sarcin-ricin loop of the 50S subunit, which activates EF-Tu for GTP hydrolysis [9]. A more recent model proposes that domain closure occurs for both cognate and non-cognate tRNAs, and rejection of non-cognate tRNA is in fact caused by the high energy cost of adopting unfavourable non-canonical base-pairing [21]. A further proofreading step occurs at the accommodation stage: if the tRNA is cognate it will be held tightly at the DC, which accelerates the relaxation of the tRNA into the PTC [4,22].

A peptide bond is then formed between the nascent chain and the new amino acid in the PTC by the peptidyl-transferase reaction. Specifically, the α-amino group of the aminoacyl-tRNA at the A-site attacks the ester carbon of the peptidyl-tRNA at the P-site to form the bond. The 23S rRNA catalyses this reaction entropically, partly by positioning the substrates and excluding bulk solvent from the active site [23]. The rate-limiting step of the reaction involves the movement of three protons, which includes the abstraction of a proton from the nucleophile, and the ribosome may further catalyse peptidyl transfer through the ordering of water molecules in a hydrogen bonding network to facilitate this [24]. Proton transfer may occur via a ‘proton shuttle’, where the 2’ OH of A76 of peptidyl-tRNA simultaneously abstracts the proton from the nucleophile and donates a proton to the electrophilic carbonyl oxygen through an adjacent water molecule [25]. An alternative ‘proton wire’ model proposes that the proton from the nucleophile is donated to the 2’ OH of A76 of peptidyl-tRNA, which in turn donates a proton to the 2’ OH of 23S rRNA A2451, which donates a proton to a water molecule that holds a partial negative charge [26].

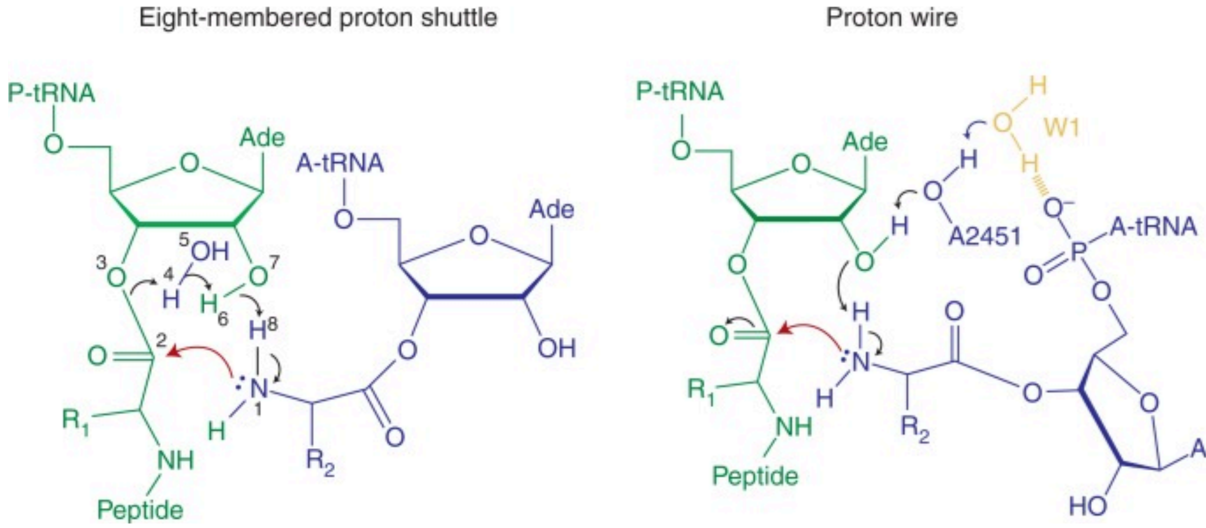

Figure 3 Models for proton transfer during the peptidyl-transferase reaction. Proton transfer may occur via a ‘proton shuttle’ (left), where the 2’ OH of A76 of peptidyl-tRNA simultaneously abstracts the proton from the nucleophile and donates a proton to the electrophilic carbonyl through an adjacent water molecule. An alternative ‘proton wire’ model (right), proposes that the proton from the nucleophile is donated to the 2’ OH of A76 of peptidyl-tRNA, which in turn donates a proton to the 2’ OH of 23S rRNA A2451, which donates a proton to a water molecule that holds a partial negative charge. Nucleophilic attack shown by the red curly arrow. Figure adapted from Polikanov et al. (2014) [26] with permission from Springer Nature © 2014.

After the peptidyl-transferase reaction, the peptide chain is attached to the A-site tRNA, and the P-site tRNA is deacylated. The mRNA then shifts by one codon and the tRNAs move from the A- and P-sites to the P- and E-sites in a process known as translocation. Initially, the ribosome oscillates between its original, non-ratcheted state, and a ratcheted state, where the 30S subunit has rotated about 6° relative to the 50S (anticlockwise, when viewed from below the 30S) and the 30S head swivels with respect to the 30S body (anticlockwise, when viewed from the front of the 30S head) [4,9]. In the ratcheted state, the tRNAs have moved with respect to the 50S subunit to form P/E and A/P hybrid states (30S positioning / 50S positioning), and the L1 stalk moves to a closed position to interact with the P/E-site tRNA [27,28]. Elongation factor G (EF-G) then binds the ribosome, stabilising the ratcheted state. GTP hydrolysis by EF-G moves tRNA and mRNA with respect to the 30S subunit in a multistep process, with domain IV of EF-G inserted into the A-site of the 30S to prevent reverse movement of tRNA and mRNA [9].

A number of intermediate states after this hydrolysis step have been elucidated by structural studies, ensemble kinetics and single molecule fluorescence resonance energy transfer (smFRET) experiments. These states have tRNA positions that correlate with the degree of subunit rotation and small subunit head swivelling. Specifically, after GTP hydrolysis by EF-G, the 30S subunit reverses back slightly from its ratcheted state by rotating in a clockwise manner (when viewed from below the 30S), whilst the 30S head remains swivelled. This movement is thought to unlock the codon-anticodon complexes from the DC of the ribosome. As the 30S subunit continues to rotate clockwise, the 30S head also begins to swivel backwards towards the non-ratcheted state (clockwise, when viewed from the front of the 30S head), the tRNAs adopt canonical E- and P-site positioning, and EF-G releases Pi. The 30S head then swivels further clockwise and both E-site tRNA and EF-G dissociate [29].

This results in a ribosome containing P-site tRNA that carries the nascent polypeptide chain, and an empty A-site. The elongation cycle continues as above: another tRNA is delivered to the A-site, the peptidyl-transferase reaction occurs and the tRNAs and mRNA are translocated through the ribosome. The growing peptide chain traverses through the NPET to emerge at the cytoplasmic surface of the 50S subunit. As the protein extrudes from the tunnel, folding can initiate from the N-terminus and proceeds in a vectoral manner as more of the protein emerges. The ribosome surface around the NPET can modulate folding by inhibiting the formation of kinetically trapped intermediates, as well as act as a hub for Trigger Factor, a molecular chaperone that suppresses misfolding between protein domains [30]. This site is also where the signal recognition particle and Sec translocon bind to traffic nascent proteins into or across the cytoplasmic membrane [31].

1.2.3 Termination

When an mRNA stop codon arrives in the A site, the elongation cycle terminates. The stop codon is recognised by a class I release factor, either RF1 or RF2 depending on the precise stop codon, which cleaves the nascent polypeptide chain from the P-site tRNA.

Specifically, the release factor adopts a conformation that bridges the DC and the PTC at the A site to stabilise the ribosome in a non-ratcheted state [32-34]. It induces conformational changes in the DC residues, causing 16S rRNA A1493 to stack with 23S rRNA A1913, and 16S rRNA G530 to stack with the third stop codon base [4]. Interactions between the stop codon and a combination of residues in both the release factor and the distorted DC are responsible for stop codon recognition [35]. A conserved GGQ motif of the release factor positions into the PTC, shifting 23S rRNA U2585 to expose the ester bond between the P-site tRNA and the nascent chain. The sidechain of the glutamine of GGQ may coordinate a water for nucleophilic attack [34], and its backbone forms a hydrogen bond that may stabilise the 3' OH leaving group of A76 of the deacylated P-site tRNA [36]. Only one proton is transferred throughout the reaction mechanism [25]. One model proposes that the attacking water molecule donates a proton to a hydroxide ion, while another proposes that a hydroxide acts as the nucleophile, and the 2' OH of A76 or a water molecule donates a proton to the oxygen atom of the nascent chain C-terminal carbonyl [25,37].

Binding of the class II release factor RF3 in its GTP-bound form induces conformational changes in the ribosome that break the interactions between the class I release factor and the PTC and DC, leading to dissociation of the factor. Hydrolysis of GTP then causes RF3 itself to release from the ribosome [38]. Next, ribosome recycling factor (RRF) and EF-G recycle the ribosome components for further rounds of protein synthesis. Specifically, RRF binds to the A site to stabilise the ribosome in its ratcheted state with P-site tRNA in a hybrid P/E state, and GTP hydrolysis by EF-G induces rotation of the head domain of RRF in a manner that disrupts intersubunit bridges B2a and B3, which causes subunit dissociation [39]. Finally, IF3 removes mRNA and tRNA from the 30S subunit, and the translation cycle starts anew [4]. An alternative mechanism proposes that RRF and EF-G first catalyse mRNA release, followed by tRNA release, with subunit splitting being the final step [40].

1.2.4 Stalling

Translation does not always progress smoothly from initiation, through elongation to termination. It can stall for a number of different reasons, after which factors are recruited to resume translation or to rescue stalled ribosomes.

Translation of polyproline stretches causes ribosome stalling because the favourable *trans* conformation of the Pro-Pro peptide would clash with residues in the NPET. This can be alleviated by elongation factor P (EF-P), which binds to the E-site of the ribosome to stabilise the binding of P-site tRNA, position the nascent chain to extend into the lumen of the NPET, and allow the CCA ends of the tRNAs to adopt catalytically productive orientations [41].

Translational stalling can be used to regulate gene expression. Such systems employ leader peptides that often contain proline-rich stretches to induce stalling at the elongation or termination stage, hence regulating expression of a downstream gene. Stalling during translation of bacterial leader peptides often leads to up-regulation of expression of downstream genes, either by anti-termination, where the ribosome stalls at a position that blocks the binding sites of the Rho transcription terminator, or by causing conformational rearrangements in the mRNA that allow for ribosome binding at a downstream SD sequence. In some cases, leader peptide stalling requires the presence of cofactors, such as erythromycin in the stalling of ErmCL [42].

Ribosomes also become stalled at the 3’ end of mRNAs that do not contain a stop codon, which arise from premature transcription termination or mRNA damage. Non-programmed frameshifting or stop codon read-through can also induce stalling events on mRNAs even when they do contain stop codons. Three different methods of rescuing these so-called ‘non-stop complexes’ have evolved in bacteria: trans-translation, mediated by transfer-messenger RNA (tmRNA) and small protein B (SmpB), alternative rescue factor A (ArfA)-mediated rescue, and ArfB-mediated rescue [43].

During trans-translation, EF-Tu delivers tmRNA to the A site, and the globular domain of SmpB occupies the DC to probe the mRNA channel, which is vacant in non-stop complexes. tmRNA contains a tRNA-like domain (TLD) which can be charged with an alanine, and a messenger-like domain (MLD) that encodes a short peptide. The TLD accommodates into the PTC, where its alanine forms a peptide bond with the nascent protein chain. The TLD is then translocated to the P-site, and the first codon of the MLD moves into the A site, ready to be decoded. Translation of the full MLD adds a degradation tag to the C-terminus of the nascent peptide, targeting it for proteolysis. Most importantly, the MLD contains a stop codon, allowing for translation to be terminated [43].

Some bacteria utilise ArfA or ArfB as backups when trans-translation is impaired or overwhelmed. ArfA interacts with the small subunit and its C-terminus probes the mRNA channel. If the channel is empty, as is the case in non-stop complexes, or holds a short mRNA, the ArfA C-terminus can bind in the channel, and RF2 is recruited to hydrolyse the nascent peptide [43]. Conversely, ArfB rescues translation independently of a release factor. Initially, the N-terminus of ArfB rapidly binds the 50S subunit of the ribosome, no matter the length of bound mRNA. The protein has a flexible interdomain linker that allows the C-terminal tail to probe the mRNA channel, and when the channel is empty, as in non-stop complexes, or the mRNA is short enough to be displaced, the tail can accommodate into the channel. Such an event rapidly triggers peptidyl-tRNA hydrolysis by the N-terminus, which contains a GGQ motif that positions into the PTC in a similar way to RF1 and RF2 [44].

Finally, a number of antibiotics stall translation by preventing the binding of elongation-competent tRNAs, by inhibiting translocation, or by hindering the transit of nascent peptide through the NPET [45]. The major ribosome-targeting antibiotic classes and methods by which bacteria resist their effects are outlined in the next sections.

1.3 Ribosome-targeting antibiotics

Despite the large size and complexity of the ribosome, most ribosome-targeting antibiotics bind to one of three sites: the 30S DC, the 50S PTC, or the entrance to the NPET, adjacent to the PTC [2,3,45-47]. Many of these antibiotics are used in humans to treat bacterial infections, although others are unsuitable for the clinic due to low solubility, poor specificity, or toxicity, and are instead used as tools in understanding translation and translation inhibition. In this section, the major classes of antibiotics that bind to the ribosome will be briefly described in turn.

1.3.1 Antibiotics that target the 30S subunit

A number of antibiotic classes bind to the 30S subunit (Figure 4), either to inhibit translation initiation by preventing initiator tRNA binding (e.g. edeine, kasugamycin, thermorubin), or to inhibit translation elongation by preventing delivery of A-site tRNA (e.g. tetracyclines) or by preventing translocation (e.g. 2-deoxystreptamine (2-DOS) aminoglycosides, tuberactinomycins, spectinomycin). Most aminoglycosides also induce misreading of the genetic code, which imparts their bactericidal effect, probably caused by oxidative stress arising from mistranslation and misfolding of proteins into the cell membrane [48]. The binding site and mode of action of 30S-targeting antibiotics are briefly described below.

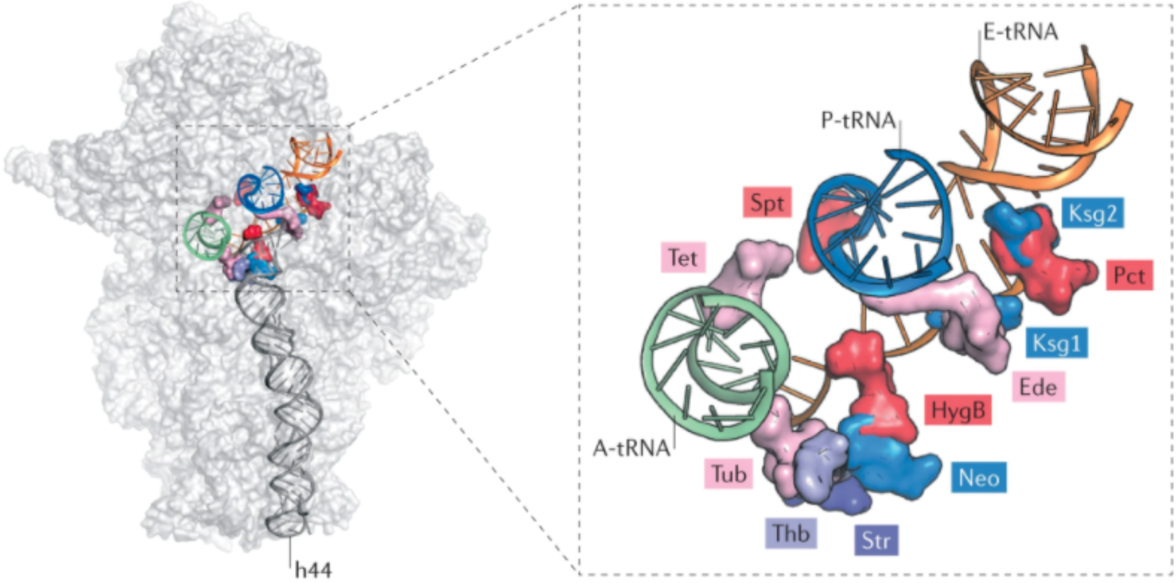

Figure 4 Antibiotics that target the 30S subunit. Binding sites of antibiotics along the mRNA channel of the 30S subunit, showing tetracycline (Tet, PDB 4V9A), spectinomycin (Spt, PDB 4V56), kasugamycin (Ksg, PDB 2HHH), pactamycin (Pct, PDB 1HNX), edeine (Ede, PDB 1I95), hygromycin B (HygB, PDB 4V64), neomycin (Neo, PDB 4V9C), streptomycin (Str, PDB 1FJG), thermorubin (Thb, PDB 4V8A), and tuberactinomycins (Tub, 4V7L). A-site, P-site and E-site tRNAs are shown in green, blue and orange respectively. Figure adapted from Wilson (2014) [45] with permission from Springer Nature © 2013.

Edeine is a pentapeptide amide that inhibits translation initiation in all phylogenetic kingdoms. In bacteria, it binds at a site that spans h24, h44 and h45 of 16S rRNA and induces base pair formation between G693 of h23 and C795 of h24 [49]. This prevents a codon-anticodon interaction at the P-site, thereby inhibiting binding of initiator fMet-tRNA^{fMet} to the small subunit [50]. However, it is not used in the clinic due to its activity against both bacteria and eukaryotes [45]. Kasugamycin also inhibits initiation by preventing fMet-tRNA^{fMet} binding. It binds at the top of 16S rRNA h44 and interacts with residues of h23 and h28. This site overlaps the mRNA path in the P and E sites; therefore on kasugamycin binding, mRNA is distorted, thereby preventing initiator tRNA from binding [51,52]. Since kasugamycin inhibits fungal ribosomes, it is commercially used to treat rice blast infestation [2].

Pactamycin is an inhibitor of both translation initiation and elongation. It binds to the E site to interact with h23 and h24 of 16S rRNA and mimics an RNA dinucleotide, taking the place of the last two E-site mRNA codons. Therefore, pactamycin binding disrupts the path of mRNA through the ribosome, and may also prevent the interaction between the Shine-Dalgarno and anti-Shine-Dalgarno sequence upstream of the E-site, thereby inhibiting initiation, and translocation of mRNA and tRNA into the E site, thereby inhibiting elongation [50,53]. Similar to edeine, this drug has poor specificity, and so is not used in the clinic [2].

Members of the tetracycline class are commonly used to treat bacterial infections in the clinic [54]. They inhibit elongation by sterically blocking the recognition of the A-site codon by the anticodon of the aa-tRNA [53]. In addition, tetracycline derivatives such as the glycylcycline tigecycline have been developed that bind the ribosome more tightly than the parent molecule and that are not affected by the most common tetracycline resistance mechanisms. Both tetracycline and tigecycline interact with 16S rRNA h31 and h34 through coordination of magnesium ions, with the increased binding affinity of tigecycline stemming from its additional 9-t-butylglycylamido moiety, which stacks with C1054 of the 16S rRNA [55,56].

Thermorubin is an antibiotic chemically related to tetracycline that inhibits both initiation and elongation. It binds at a different site to tetracycline, at the subunit interface between 16S rRNA h44 and 23S rRNA H69 (bridge B2a). It rearranges A1913 and C1914 of H69, which may perturb IF1 and IF2 activity, thus preventing the binding of fMet-tRNA^{fMet}. C1914 is also positioned to overlap with the A-site tRNA binding site, thus thermorubin also prevents A site accommodation, even in the event that an initiation complex forms. Despite its strong antibacterial activity, its low solubility in aqueous solution precludes its clinical use [57].

Aminoglycosides can be categorized into non-DOS aminoglycosides, such as streptomycin, and 2-DOS aminoglycosides, such as neomycin, paromomycin, gentamicin and amikacin. Streptomycin binds to the 30S, interacting with h1, h18, h27 and h44 of 16S rRNA, as well as the ribosomal protein uS12, leading to domain closure of the 30S subunit. This has been proposed to reduce the rate of GTPase activation for incoming cognate tRNAs and enhancing the rate for near-cognate tRNAs, thus inducing translational misreading [58,59]. 2-DOS aminoglycosides bind nearby at the top of h44, and most induce a flipped out conformation of 16S rRNA A1492 and A1493 so that they interact with the minor groove of the codon-anticodon helix [58]. One model suggests that forcing this flipped-out conformation facilitates the binding of near-cognate tRNAs, thereby inducing misreading [19]. Another model proposes that misreading is caused by local changes in h44 and H69 on aminoglycoside binding, which relax the constraints of the decoding pocket and compensate for energetically unfavourable near-cognate tRNA-mRNA interactions [21].

2-DOS aminoglycosides also inhibit translocation, but the molecular mechanism of inhibition differs between different molecules. Hygromycin B is an atypical aminoglycoside that binds in h44 in a slightly displaced position, and does not induce the same conformational change in the DC as other aminoglycosides, likely explaining its relatively limited effect on misreading. However, it strongly inhibits translocation, either by contacting the mRNA, trapping it in the A and P sites, or by blocking the tRNA path between the A and P sites [60]. Some aminoglycosides, such as gentamicin and neomycin, have a secondary binding site at H69 of the 50S subunit. Binding of these aminoglycosides has been suggested to lock H69 to the subunit interface and stabilise the ribosome in a ratcheted state, thereby inhibiting translocation and RRF-mediated ribosome recycling [61,62]. Other aminoglycosides, such as kanamycin, lack this secondary binding site, but inhibit translocation by stabilising the pre-translocation state [63].

Other classes of 30S-binding antibiotics that inhibit translocation of the mRNA-tRNA complex through the ribosome include the tuberactinomycins and spectinomycin. The tuberactinomycin antibiotics viomycin and capreomycin are circular peptides that bind to the ribosome at a site that spans 16S rRNA h44 and 23S rRNA H69. They inhibit translocation by stabilising an intermediate ratcheted state of the ribosome [64,65]. In addition, like aminoglycosides, they stabilise flipped out conformations of 16S rRNA 1492 and 1493, and have the potential to cause misreading. However, translocation inhibition is the major cause of cell growth inhibition [66,67]. Spectinomycin is closely related to the aminoglycosides, but interacts with 16S rRNA h34, likely limiting 30S head swivelling, thereby inhibiting translocation [58,68]. It is mainly used to treat *Neisseria gonorrhoea* infections, but has been largely withdrawn from human use due to rising resistance [69].

1.3.2 Antibiotics that target the 50S subunit

Most antibiotics that target the 50S subunit (Figure 5) bind to the A site (e.g. puromycin, lincosamides, chloramphenicol, sparsomycin, oxazolidinones), the P site (e.g. blasticidin S), or both the A and P sites (e.g. pleuromutilins, type A streptogramins) of the PTC, or at the entrance to the NPET (e.g. macrolides, type B streptogramins). However, some 50S-targeting antibiotics instead bind at sites that interfere with translation factor binding (e.g. orthosomycins, thiopeptides). The binding site and mode of action of 50S-targeting antibiotics are briefly described below.

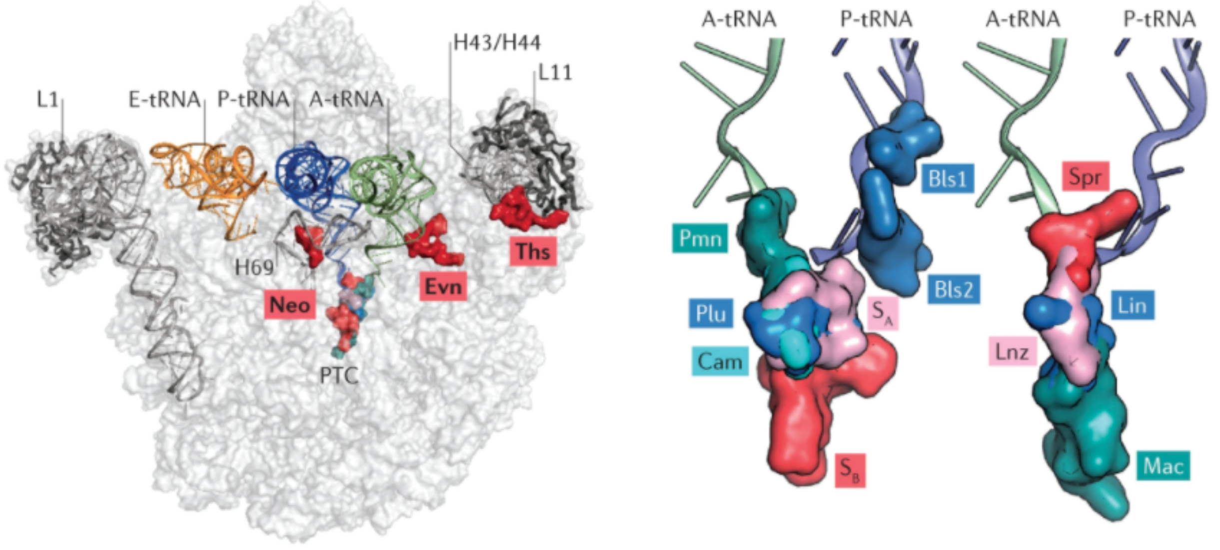

Figure 5 Antibiotics that target the 50S subunit. Binding sites of antibiotics that target the 50S at sites other than the PTC or NPET (left) and those that target the PTC or NPET (right), showing neomycin (Neo, PDB 4V9C), evernimicin (Evn), thiostrepton (Ths, PDB 3CF5), blasticidin S (Bls, PDB 1KC8), sparsomycin (Spr, PDB 1M90), lincomycin (Lnc, PDB 4V7V), linezolid (Lnz, PDB 3DLL), macrolides (Mac, PDB 1K9M), puromycin (Pmn, PDB 1M90), pleuromutilins (Plu, PDB 1XBP), chloramphenicol (Cam, PDB 4V7T), and stretogramins A and B (S_A, S_B, PDB 1SM1). A-site, P-site and E-site tRNAs are shown in green, blue and orange respectively. Figure adapted from Wilson (2014) [45] with permission from Springer Nature © 2013.

Puromycin is composed of an amino acid-like moiety linked by an amide bond to a ribose, and mimics the 3’-CCA end of A-site tyrosyl-tRNA. It undergoes peptide transfer with P-site tRNA, covalently linking the peptide chain to the drug. The peptide-puromycin conjugate then dissociates from the ribosome. Puromycin is a universal inhibitor of translation, therefore is not used in the clinic, but rather as a tool to understand peptide bond transfer [70,71].

Lincosamides, such as lincomycin and clindamycin, bind in the A site pocket to inhibit peptide bond formation. They have a galactose ring that extents towards the NPET to overlap with the macrolide binding site, and a pyrrolidinyl propyl group that overlaps the site of the aminoacyl moiety of A-site tRNA, preventing its accurate placement [72,73]. Chloramphenicol is a translation elongation inhibitor that also binds in the A site pocket, with a nitrobenzyl ring that forms a π-stacking interaction with the base of 23S rRNA C2452. This aromatic ring of chloramphenicol overlaps with the site of the aminoacyl moiety of A-site tRNA in a similar manner to lincosamides [73,74]. Chloramphenicol acts in a context-specific manner, with its activity dependent on the identity of residues in the nascent chain and the residue entering the A site [75]. The sulphur-containing tail of sparsomycin also overlaps with the A-site tRNA to inhibit peptidyl transfer, and its uracil moiety is sandwiched between the CCA end of P-site tRNA and 23S rRNA A2602, which stabilises P-site tRNA binding and induces translocation of peptidyl-tRNA to the P/P-state [76,77].

Oxazolidinones such as linezolid also bind the A site. The oxazolidinone ring of linezolid forms a π-stacking interaction with the base of 23S rRNA U2504, and the fluorophenyl moiety stacks with the base of 23S rRNA C2452 [78]. Oxazolidinones are thought to perturb the positioning of initiator tRNA in the P site by stabilising 23S rRNA U2585 in a non-productive conformation, and prevent A-site tRNA accomodation [79].

Blasticidin S is a nucleoside analogue that binds the P site of the PTC. It forms a Watson-Crick like interaction with 23S rRNA G2251 in the P loop, and intercalates between C74 and A76 of P-site tRNA, causing C75 to flip towards the A site. This distortion in the P-site tRNA may prevent access of release factors into the A site, and make the tRNA less well positioned for nucleophilic attack. Therefore, the peptidyl-tRNA is less able to be hydrolysed by release factors, and translation termination is inhibited. Peptide bond formation is also inhibited, though to a lesser extent [80]. Blasticidin S is active against both eukaryotic and prokaryotic ribosomes, therefore it is not used in the clinic [2].

Pleuromutilins are diterpenoids that bridge both the A and P sites, thereby interfering with binding of both A-site and P-site tRNAs. The tricyclic mutilin core of the pleuromutilin lefamulin stacks against 23S rRNA U2504 and C2452, blocking the A site, and the C14 extension points into the P site [81]. Pleuromutilins appear to inhibit initiation, by destabilising fMet-tRNA^{fMet} binding to the P site, or the early stages of elongation, by preventing binding of aa-tRNAs to the A site [82-84].

Macrolide antibiotics include a number of different molecules containing 12-, 14-, 15- or 16-membered lactone rings. The most well studied being the 14-membered erythromycin, which binds adjacent to the PTC, at the entrance to the NPET. Macrolides inhibit the ribosome in a context specific manner, i.e. they arrest translation at specific amino acid sequences. They do this by restricting the freedom of movement of these growing nascent peptides, enforcing them to adopt a specific trajectory, which relays a stalling signal to the PTC to prevent further peptide bond formation [85]. In effect, macrolides reshape the proteome rather than block protein synthesis globally [86,87]. Larger 16-membered macrolides have an extended tail that reaches further into the PTC. In the case of carbomycin A, this tail overlaps with the aminoacyl moiety of A-site tRNA, thereby inhibiting peptide bond formation directly [88]. Ketolides are semisynthetic derivatives of macrolides. Examples include telithromycin and solithromycin, which have an alkyl-aryl arm that interacts with the base pair A752-U2609 of 23S rRNA, which increases their ribosome binding affinity compared to erythromycin [89,90].

Streptogramin antibiotics comprise a mixture of type A and type B streptogramins which synergistically target the PTC and NPET respectively. Type A streptogramins (S_A), such as dalfopristin, are cyclic unsaturated macrolactones, whereas type B streptogramins (S_B), such as quinupristin, are depsipeptides. S_A antibiotics bridge the A and P sites of the PTC, thereby preventing proper positioning of both A- and P-site tRNAs. S_B antibiotics bind the NPET in the same site as macrolide antibiotics, and are thought to interfere with the progression of the nascent chain through the NPET. In addition, S_A antibiotics induce a stable conformational change in 23S rRNA U2585, which is likely responsible for the continued activity of S_A even after removal of drug [91]. Originally, it was proposed that synergy arose from a conformational change in A2062 induced by S_A binding promoting the binding of S_B antibiotics [91]. More recent data suggests that there is no general synergistic effect in transcription-translation systems, and therefore synergy likely arises independently of protein synthesis [92].

Not all 50S-targeting antibiotics bind to the PTC or NPET. The orthosomycins, evernimicin and avilamycin, interact with 23S rRNA H89 and H91 and protein uL16, where they are thought to sterically interfere with IF2 binding to inhibit translation initiation [93,94]. Unfortunately, evernimicin and avilamycin are not used clinically due to toxicity and use in animal feed as a growth promoter respectively [2]. Thiopeptide antibiotics such as thiostrepton and micrococcin interact with 23S rRNA H43 and H44 and protein uL11, where they prevent accommodation of EF-G onto the ribosome, and so inhibit translocation [93,95]. These are not used clinically due to poor solubility [45].

1.4 Mechanisms of resistance to ribosome-targeting antibiotics

Antibiotic resistance is a natural phenomenon that predates clinical antibiotic use [96]. Microorganisms such as soil-dwelling actinomycetes have long utilised drug resistance mechanisms to protect themselves from the antibiotics that they create [97]. In modern times, resistance genes on mobile genetic elements can be acquired by pathogens by horizontal gene transfer under selection pressures caused by the use of antibiotics in humans and agriculture [98,99], or through point mutations in their DNA [99]. There are four main mechanisms by which bacteria resist the action of antibiotics: prevention of net drug uptake into the cell, modification or degradation of drug, mutation or modification to the drug target, and target protection (Figure 6). These four mechanisms are described in more detail below, focussing on ribosome-targeting antibiotics.

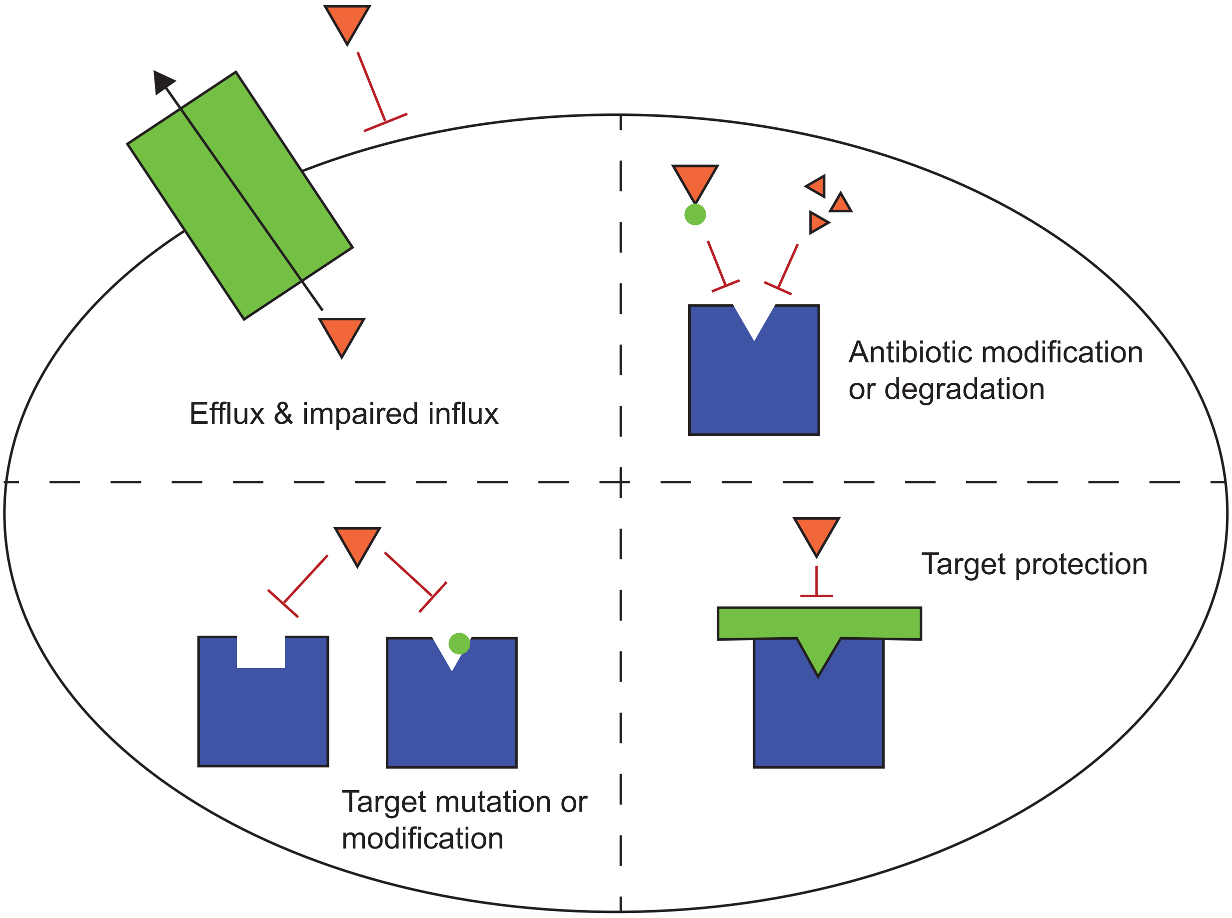

Figure 6 Mechanisms of resistance to antibiotics. Mechanisms of antibiotic resistance include prevention of net uptake of drug into the cell by impaired influx or active efflux, modification of degradation of drug, mutation or modification of the target, and target protection.

1.4.1 Prevention of antibiotic access into the cell

Gram-negative bacteria are intrinsically resistant to hydrophobic antibiotics, such as macrolides, due to the permeability barrier presented by the outer membrane [100]. Hydrophilic antibiotics can pass through non-specific outer membrane porins, such as OmpF of *E. coli* [101]. As such, downregulation of porins or replacement of porins with more selective channels are mechanisms by which bacteria limit antibiotic uptake [102]. In addition, porins such as TolC use adaptor proteins to recruit inner membrane efflux pumps, such as AcrB, which exports multiple antibiotics including chloramphenicol and tetracycline, and MacB, which exports macrolides [103,104].

1.4.2 Antibiotic modification and degradation

Antibiotics can be modified in ways that prevent their binding to the ribosome due to steric hindrance. Aminoglycosides are particularly susceptible to modification due to their many exposed hydroxyl and amide groups, and can be modified by enzymes such as acetyltransferases, phosphotransferases and nucleotidyltransferases, which have been discovered in a wide range of bacterial species, including pathogens [105]. These enzymes are diverse, varying in the specific aminoglycosides and functional groups that they modify [106]. Antibiotics can also be enzymatically degraded. For example, tetracycline can be modified by the monooxygenase TetX to generate a hydroxyl-tetracycline which spontaneously breaks down [107]. Two plasmid-encoded variants of TetX have been found in Enterobacteriaceae and *Acinetobacter* strains isolated from humans and animals, conferring resistance to even tigecycline [108]. In addition, a family of TetX-related genes, known as destructases, have been discovered from soil metagenomes, with some found in potential mobile genetic elements, posing a risk of dissemination into human pathogens [109]. Macrolides can also be degraded; for example, the *E. coli* enzymes ereA and ereB degrade erythromycin by cleaving its macrocycle ester bond [110].

1.4.3 Changes to the ribosome

Since most antibiotic binding sites are composed of rRNA, mutations in the genes encoding rRNAs can confer resistance. Most bacteria have multiple copies of rRNA-encoding genes and resistance is a recessive trait in this context, meaning such resistance occurs more often in bacteria containing only one or two operons [3]. Examples include resistance to linezolid in *Streptococcus pneumoniae*, which is conferred in proportion to the number of 23S rRNA gene copies with the G2576T mutation [111], and mutations in A2058 or A2059, which confer resistance to macrolides, lincosamides, type B streptogramins and ketolides (MLS$_B$K antibiotics) in *Mycobacterium, Brachyspira, Helicobacter, Treponema* and *Streptococci* [112]. Mutations in ribosomal proteins can also confer resistance, generally by causing conformational changes in the rRNA that comprises antibiotic binding sites. For example, mutations in uL3 and uL22 in *E. coli* confer resistance to tiamulin and macrolides respectively, despite no direct overlap of these proteins with the drug [72,113,114].

Resistance can also arise from modification of the drug site in ways that reduce binding affinity. For example, methylation of 16S rRNA G1405 or A1408 by KgmB or KamA respectively confers resistance to some aminoglycosides [115,116], and the most frequent mechanism of macrolide resistance in bacterial pathogens is mono- or dimethylation of 23S rRNA A2058 by erythromycin resistance methyltransferase (Erm) enzymes, which confer resistance to MLS_BK antibiotics by preventing drug binding [117,118]. Similarly, the chloramphenicol-florfenicol resistance (Cfr) methyltransferase, observed in staphylococci and *E. coli*, targets 23S rRNA A2503 to confer resistance to phenicols, lincosamides, oxazolidinones, pleuromutilins and type A streptogramins [119].

1.4.4 Ribosome protection

Target protection involves the binding of a resistance protein with the target (in this case, the ribosome) to rescue it from antibiotic-mediated inhibition. There are three types of target protection: Type I, where the resistance protein sterically removes the drug from the target; Type II, where the protein induces conformational changes within the target that allosterically displace the drug; and Type III, where the protein induces conformational changes in the target that restore function without displacement of drug [120] (Figure 7).

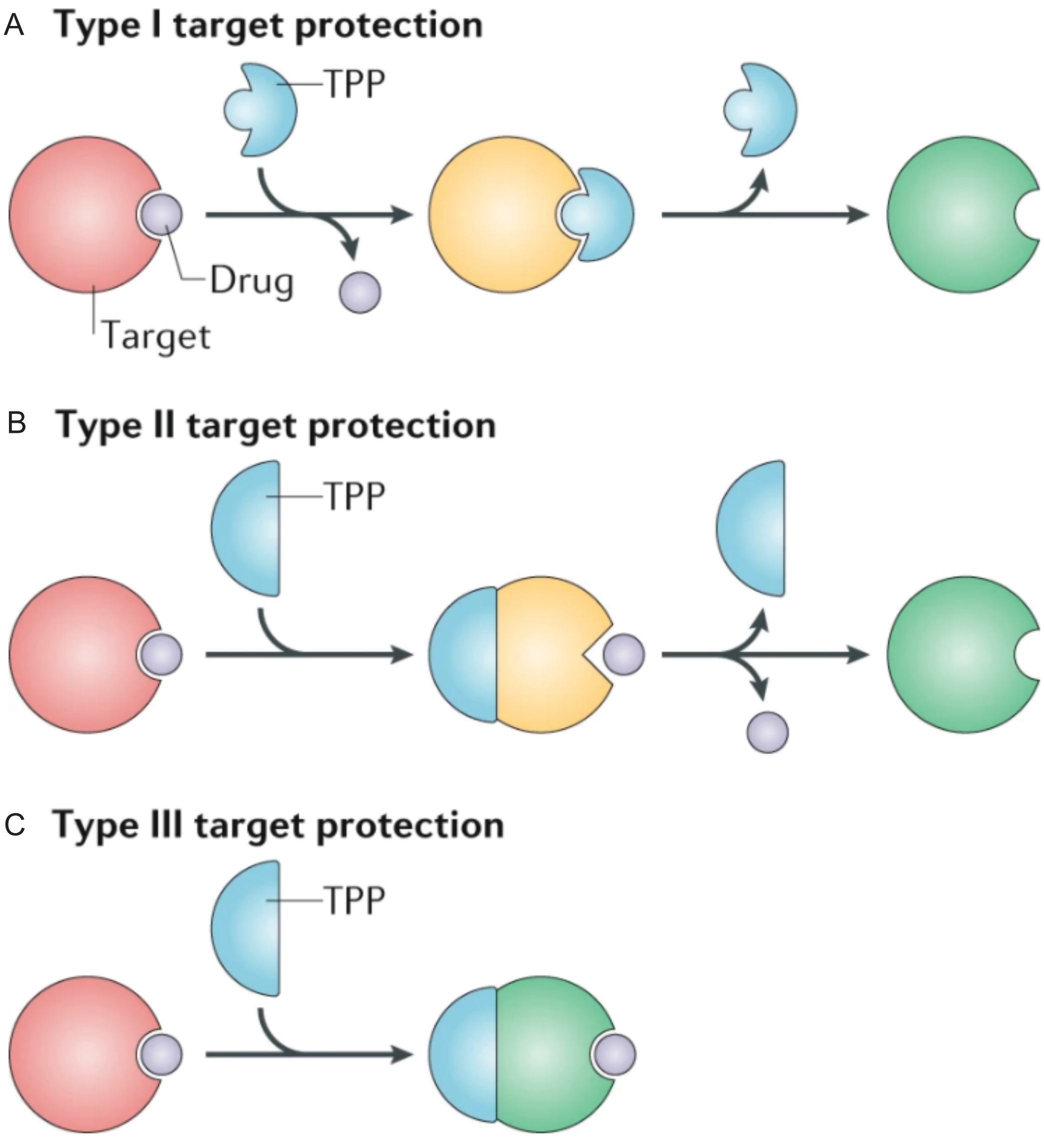

Figure 7 Schematic of the mechanisms of target protection. A) Type I target protection, where the resistance protein sterically removes the drug from the target. B) Type II target protection, where the protein induces conformational changes within the target that allosterically displace the drug. C) Type III target protection, where the protein induces conformational changes in the target that restore function without displacement of drug. Figure taken from Wilson, D.N., Hauryliuk, V., Atkinson, G.C. & O'Neill, A.J. (2020) [120] with permission from Springer Nature © 2020.

The first proteins recognised to mediate target protection were Tet(M) and Tet(O) [121,122], which confer resistance to tetracycline by the type I mechanism. Tetracycline ribosomal protection proteins (TRPPs), which include Tet(M) and Tet(O), represent the major cause of tetracycline resistance in Gram-positive pathogens [120]. They are GTPases that bind the post-translocation ribosome that contains P- and E-site tRNA, but no A-site tRNA due to the presence of tetracycline. They bind at the same site as EF-G, with residues of domain IV interacting with 16S rRNA C1054 to directly overlap with the tetracycline site, thereby displacing the drug [123]. On GTP hydrolysis, the protein dissociates from the ribosome in a manner that alters the conformation of the binding site so that immediate rebinding of drug is disfavoured and delivery of A-site tRNA by EF-Tu is favoured [124]. Tigecycline, a tetracycline derivative, is not affected by TRPPs. This is likely due to its additional 9-t-butylglycylamido moiety, which may sterically hinder the access of TRPP domain IV to C1054, preventing drug displacement [55].

Antibiotic resistance (ARE) ATP-binding cassette (ABC)-F proteins mediate resistance to PTC- or NPET-targeting antibiotics by either type I or type II target protection [125-127]. These proteins are discussed in detail in Chapter 4.

FusB-type proteins mediate resistance to fusidic acid in *S. aureus* and other staphylococci by a type III target protection mechanism. Fusidic acid is an antibiotic that binds between domains II and III of ribosome-bound EF-G, tethering the N-terminal and C-terminal super-domains together. This prevents the rearrangements necessary for EF-G release from the ribosome following GTP hydrolysis, and locks the ribosome in a post-translocation state [128]. FusB binds to the C-terminal super-domain of EF-G, well away from the fusidic acid binding site. By doing so, it induces conformational changes in domains IV and V and alters the dynamics of domain III, which presumably drives EF-G dissociation from the ribosome, countering the action of fusidic acid [129].

1.5 Aims of PhD project

Antimicrobials are crucial to modern medicine, allowing treatment of life-threatening infections and enabling surgical procedures, cancer chemotherapy and organ transplantation. However, pathogens are rapidly evolving to resist their effects, with antimicrobial resistant infections predicted to cause approximately 10 million deaths globally each year by 2050 [130]. This growing prevalence of resistance casts doubt on their future efficacy, and the development of novel antibiotics is not happening at sufficient speed to match this accumulation of resistance [131]. To effectively combat the threat of antibiotic resistance, our structural and molecular understanding of both the mechanisms by which antibiotics work and the mechanisms by which bacteria acquire resistance must be improved.

Accordingly, this work presents structures of ribosomes from pathogenic bacteria in complex with antibiotics or protection proteins by cryo-electron microscopy (cryo-EM). Chapter 2 summarises the single particle cryo-EM workflow and outlines the methods used to produce the experimental data for this thesis. Chapter 3 describes structures of the ribosome from pathogen *A. baumannii* in complex with amikacin and tigecycline, antibiotics used in the clinic to treat infections caused by this bacteria. Unique structural features of the *A. baumannii* ribosome are elucidated, as are the interactions of amikacin and tigecycline with the ribosome. Chapter 4 describes the structure of the ribosome from *S. aureus* in complex with the ARE ABC-F protein Sal(B), provides analysis of the Sal variants that mediate different resistance profiles, and outlines mutagenesis experiments that probe the precise mechanism by which Sal(B) displaces PTC-bound antibiotics. Finally, Chapter 5 discusses how the findings presented in this thesis might contribute to the structure-based rational design or modification of drugs that have improved activity against pathogenic bacteria or the ability to circumvent or inhibit resistance mechanisms.

Chapter 2 Materials and Methods

Cryo-electron microscopy (cryo-EM) structures of ribosomes from pathogenic bacteria in complex with either an antibiotic or ribosome protection protein form the basis of this thesis. In this section, the single particle cryo-EM workflow will be outlined, followed by a detailed description of the specific methodology used.

2.1 Single particle cryo-electron microscopy (cryo-EM)

Single particle analysis (SPA), helical reconstruction and tomography are the three main methodologies that use cryo-EM to determine structures of biological complexes. SPA involves the computational averaging of thousands of projection images of identical particles to generate a 3D reconstruction [132]. Helical reconstruction uses similar principles to SPA, but takes advantage of the many different views of identical subunits provided by the projection of a helix [133]. Tomography is used to obtain a 3D volume, or tomogram, of a specimen by taking images at multiple tilt angles. Regions of tomograms containing the same object can be averaged together to obtain higher-resolution reconstructions, in a process known as sub-tomogram averaging [134]. The structures described in this thesis were generated by SPA cryo-EM, therefore the SPA workflow from biological sample to 3D atomic model is outlined below.

2.1.1 Sample preparation

Sample preparation is the process of applying a thin (10-80 nm) layer of an aqueous solution of biological macromolecule (or ‘particle’) to a support grid, and then rapidly freezing this to avoid formation of ice crystals [135]. The layer of vitreous ice is necessary to visualise the specimen in the high vacuum of an electron microscope, and allows visualisation at liquid nitrogen temperatures to provide partial protection from radiation damage [136]. This layer needs to be as thin as possible to achieve high contrast and minimize defocus spread arising from varying heights of particles in the ice, whilst still being thick enough to encompass the particles [132].

The first step is to apply a purified sample onto a grid. EM grids are usually 3 mm in diameter, and made of a metal mesh (usually gold or copper) overlaid with a thin support film of amorphous carbon or sometimes gold [132]. The support film of a cryo-EM grid contains holes that can be either regularly shaped and spaced or irregular, in which particles are suspended in vitreous ice. Before sample application, the grid is usually glow-discharged, which involves the deposition of ionised gas molecules onto the grid surface to render it hydrophilic. This step facilitates the spreading of the aqueous sample solution over the grid surface [135]. Following this, grids are commonly prepared using automatic plunge-freezing tools such as the Thermo Fisher Scientific Vitrobot and Leica EM GP. These machines have a temperature- and humidity-controlled chamber, in which the glow-discharged grid is held by tweezers. Around 3 μL of sample is pipetted onto the grid, which is subsequently blotted with filter paper to remove excess liquid, leaving a thin film of particles in buffer in the holes, before being plunged rapidly into a cryogen, typically liquid ethane cooled by liquid nitrogen [137].

In ideal circumstances, such an approach would yield a cryo-EM grid with an even, thin layer of vitreous ice in which the particles are evenly distributed across the support film holes in a variety of orientations without interactions with the air-water interface. In practice, particles often interact with the air-water interface [138], promoting adoption of preferred orientations or even denaturation, they can interact with the carbon support rather than locate to the holes, and they can clump around the edges of holes where the ice is often thicker [139] (Figure 8). Some of these issues can be solved by optimising the grid type, for example using grids with a very thin (about 2 nm) continuous support made from amorphous carbon, graphene or graphene oxide that overlays the thicker holey carbon support. Since particles interact with such continuous supports, they can be helpful in both bringing particles away from the denaturing air-water interface and increasing particle distribution across the holes. The downside of this approach is that such a support contributes additional background electron scattering and so decreases the signal-to-noise ratio, which makes small particles difficult to align in the downstream image processing steps [139]. Other potential solutions include adding surfactants to protect particles from the air-water interface [140], or using completely different devices that decrease the time between sample application and freezing, with the aim to outrun particle adsorption to the air-water interface [141-143].

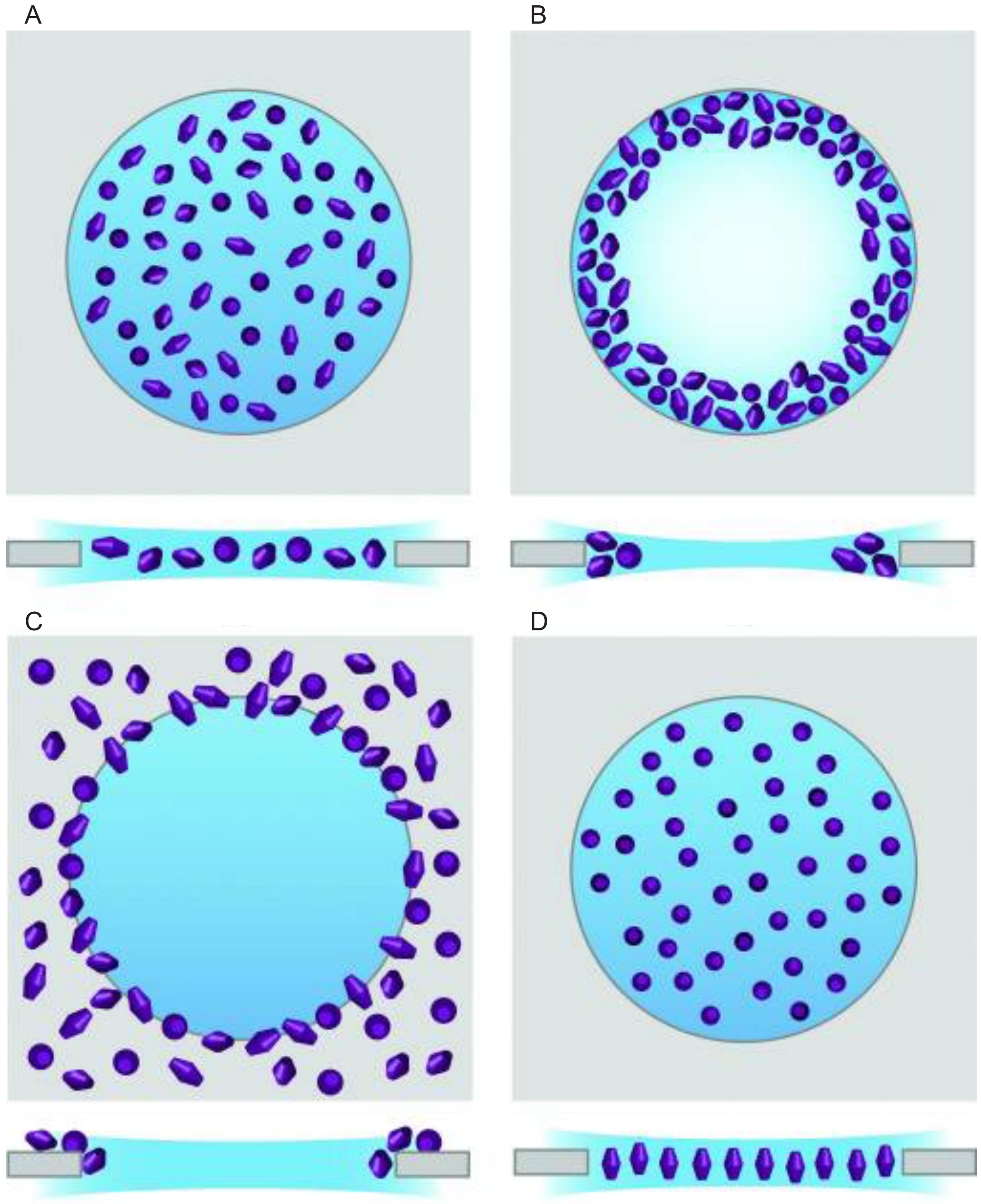

Figure 8 Schematic of possible particle distributions in vitreous ice. A) Ideal vitrified sample with particles dispersed across the hole in a wide variety of orientations. B) Particles clumped around the edge of the hole where the ice is often thicker. C) Particles adhered to the support film rather than the holes. D) Particles that have adopted a single orientation. Top panels = views from top. Bottom panels = views from side. Figure adapted from Drulyte et al. (2018) [139].

2.1.2 The Transmission Electron Microscope (TEM)

After sample application and plunge-freezing, cryo-EM grids are inserted into a transmission electron microscope (TEM) for visualisation of the biological macromolecule of interest. A TEM contains an electron source that emits electrons that are focused by a series of electromagnetic lenses to interact with the sample and then arrive at a detector. The whole column is held at high vacuum to avoid unwanted scattering of electrons by gas molecules [134]. A schematic of a TEM is shown in Figure 9, and each component will be briefly described below.

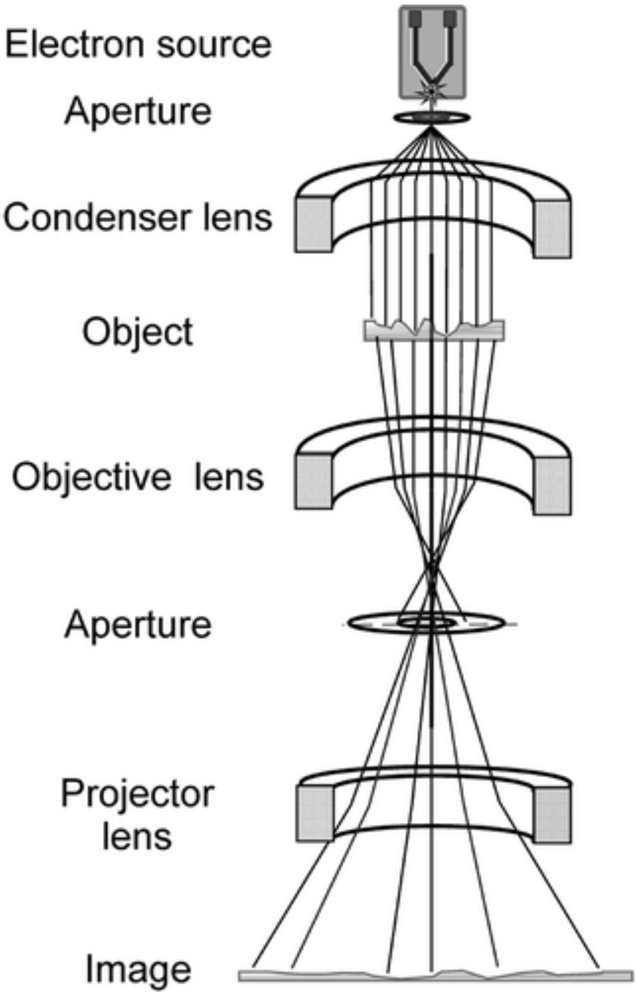

Figure 9 Schematic of a transmission electron microscope. Electron beam described by solid lines. Each component is briefly described below. Figure taken from Orlova & Saibil (2011) [134] with permission from American Chemical Society © 2011. https://pubs.acs.org/doi/10.1021/cr100353t

Electrons are emitted by either a traditional thermionic electron source, such as tungsten or lanthanum hexaboride, or a field emission gun (FEG). FEGs utilise an electric field to extract electrons with higher coherence than traditional sources [144]. For this reason, high-resolution cryo-EM employs FEGs to emit electrons, which are then typically accelerated through a voltage of 300 kV. This results in electrons with a wavelength of about 2 pm, meaning that the electron beam does not impose a limit on resolution [136].

Condenser lenses then convert the diverging electron beam into a parallel one that illuminates the specimen. The specimen sits within the objective lens, which contains an aperture in the back focal plane to improve image contrast by filtering out electrons strongly scattered by the sample. The image is magnified by the objective and projector lenses before reaching the detector [134].

Although some electrons are elastically scattered by the sample, others are inelastically scattered, meaning that energy is transferred to the specimen. This can directly cause chemical bonds to break or create free radicals that cause secondary damage [136]. Such radiation damage is the limiting factor in solving high resolution structures of biological molecules. Low total electron doses (~20-80 $e^-/Å^2$) are used to minimise radiation damage, resulting in low contrast, a problem exacerbated by the nature of biological specimens, which contain light atoms that only weakly scatter incident electrons. To rectify this, small amounts of defocus are introduced to induce a phase shift between scattered and unscattered electrons, known as phase contrast [134].

Applied defocus and aberrations in the microscope together produce an image that can be modelled by an ideal phase-contrast image that is modulated by a defocus-dependent contrast transfer function (CTF) of the microscope [145]. The CTF is an oscillating function of decreasing amplitude and increasing frequency which measures contrast as a function of spatial frequency. Therefore, the Fourier transform of a defocused micrograph contains alternating light and dark Thon rings according to the CTF (Figure 10). The amplitudes at higher spatial frequencies, or higher resolutions, are attenuated by an envelope function that mostly arises from partial incoherence in the electron beam [132]. Higher defocus values give a higher CTF frequency and a stronger attenuating envelope function, i.e. higher defocus boosts the lower resolution image contrast at the expense of higher resolution contrast [146]. Therefore, values of defocus are applied that allow visualisation of the particles whilst maintaining as much high resolution information as possible. Furthermore, since the CTF crosses the x-axis (where contrast is zero) multiple times, images are collected at a variety of defocus values to ensure information at all spatial frequencies is sampled [132].

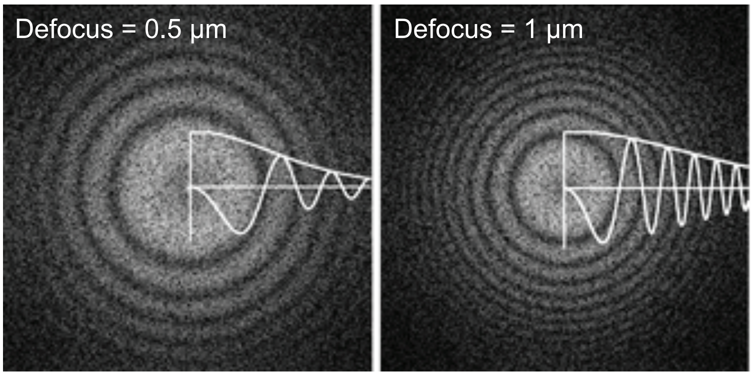

Figure 10 Fourier transforms of micrographs of carbon film imaged at different defocus values. Left = Fourier transform of image taken with defocus of 0.5 μm. Right = Fourier transform of image taken with defocus of 1 μm. Overlaid in white are the corresponding one-dimensional CTF curves with the envelope function shown. At higher defocus values, the Thon rings of the 2D Fourier transforms are closer to the origin, oscillate more rapidly and decay more strongly at higher spatial frequencies. Figure adapted from Orlova & Saibil (2011) [134] with permission from American Chemical Society © 2011. https://pubs.acs.org/doi/10.1021/cr100353t

After passing through the column, the electrons are recorded by a detector. Photographic film and charged coupled device (CCD) cameras have been used historically, though direct electron detectors (DEDs) [144] are now routinely used for high resolution cryo-EM. DEDs use monolithic active pixel sensors (MAPS) which detect incident electrons via a voltage drop across a capacitor that arises from electron-hole pair excitations in a semiconductor membrane. MAPS can record in integrating mode, where this voltage drop is measured after a fixed time and contains contributions from multiple incident electrons, or counting mode, where the voltage drop is measured for each individual electron event [147]. Examples of DEDs include the Falcon 3 from Thermo Fisher Scientific and K2 from Gatan [148].

DEDs have a high detective quantum efficiency (DQE), a measure of the resolution-dependent efficiency of a detector in converting an incident electron to signal, and can record dose-fractionated movies that allow for computational correction of particle movements [132]. Furthermore, the high-frequency components of the first few frames can be down-weighted to account for initial beam-induced movement, and the high-frequency components can be progressively down-weighted throughout the movie to account for increasing radiation damage, which aids structure determination [149].

2.1.3 Image processing

To solve a high resolution structure, hundreds to thousands of dose-fractionated micrograph movies are recorded by a DED, each containing many particle projections. Such data can be collected automatically, so that the user only needs to select areas of the cryo-EM grid to image and set the electron dose rate and defocus parameters, before allowing the microscope to record micrograph movies unattended. SPA is the generation of a 3D reconstruction by averaging many projection images of identical particles lying in varying orientations in the ice layer [132]. Since biological macromolecules are imaged using low electron doses to avoid radiation damage, resulting in noisy images, this averaging is done over many tens or hundreds of thousands of particles to improve signal [150]. The SPA image processing pipeline from 2D micrograph movies to a high resolution 3D reconstruction of the particle of interest is outlined below. Before this, the Fourier Slice Theorem and associated ‘projection matching’ approach will be described, as these are core SPA principles on which many steps in the pipeline rely.

2.1.3.1 Principles of SPA

3D reconstruction from particle projection images makes use of the Fourier Slice Theorem. This states that if a 3D object is projected along a particular direction, or projection vector, d, the Fourier transform of that 2D projection image is identical to a slice-through of the 3D Fourier transform of the original object. This slice passes through the Fourier origin (i.e. it is a ‘central slice’) and is normal to d (Figure 11).

Therefore, if d is known for each 2D projection image in a large dataset, the Fourier transforms of each projection can be assembled in 3D to give the Fourier transform of the object. An inverse Fourier transform will then give a 3D reconstruction of the object [145].

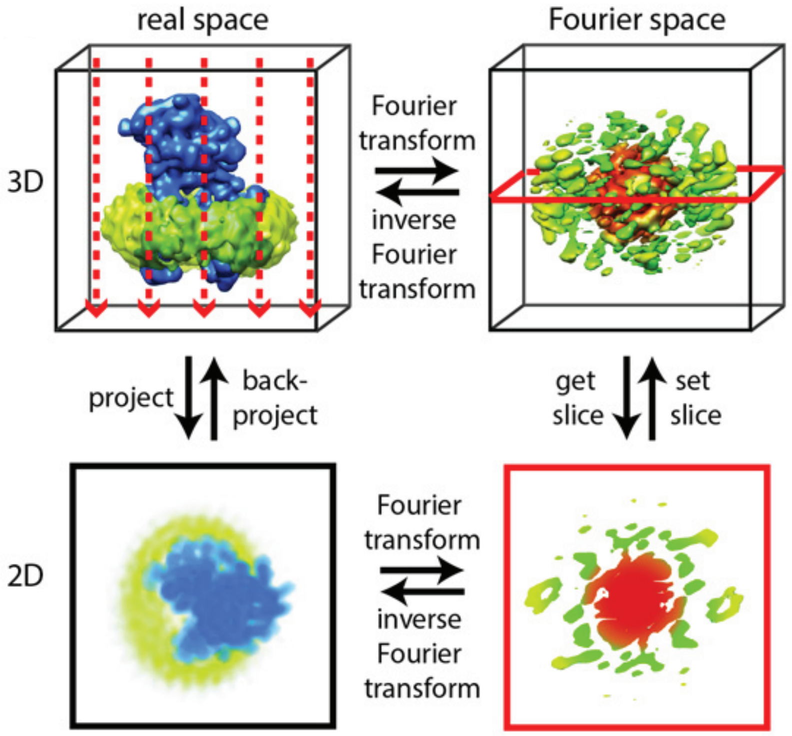

Figure 11 The Fourier Slice Theorem. When a 3D object (top left) is projected along a projection vector (red dashed arrows), the resulting projection image (bottom left) has a Fourier transform (bottom right) that is identical to a slice through of the Fourier transform of the initial 3D object (top right). The slice (red frame) is normal to the projection vector. Figure adapted from Nogales & Scheres (2015) [150] with permission from Elsevier © 2015.

The main issue with SPA is that the projection vectors, *d*, are completely unknown. These vectors have to be determined using a technique known as ‘projection matching’. Here, an initial 3D model is provided that is approximately the expected shape and size of the actual particle, and 2D projections representing a wide range of projection vectors are calculated from this model. Next, each particle image is aligned and compared with each 2D projection reference to estimate a projection vector for each particle image. These projection vectors are then used to assemble the 2D Fourier transforms of the projection images into a 3D Fourier transform according to the Fourier Slice Theorem, with many images of similar *d* averaged to improve the signal-to-noise ratio. An inverse Fourier transform results in a 3D reconstruction, which is then used as the initial model for a next iteration [145,150] (Figure 12). Assuming there is good experimental coverage of all projection vectors, this reconstruction will be a more accurate representation of the object than the initial model. The process is repeated a number of times, sampling finer angular and translational space as iterations progress, until it converges on the ‘true’ structure of the particle. The final resolution will depend on a number of factors, including the amount of projection images used, and the compositional and conformational homogeneity of the sample [150].

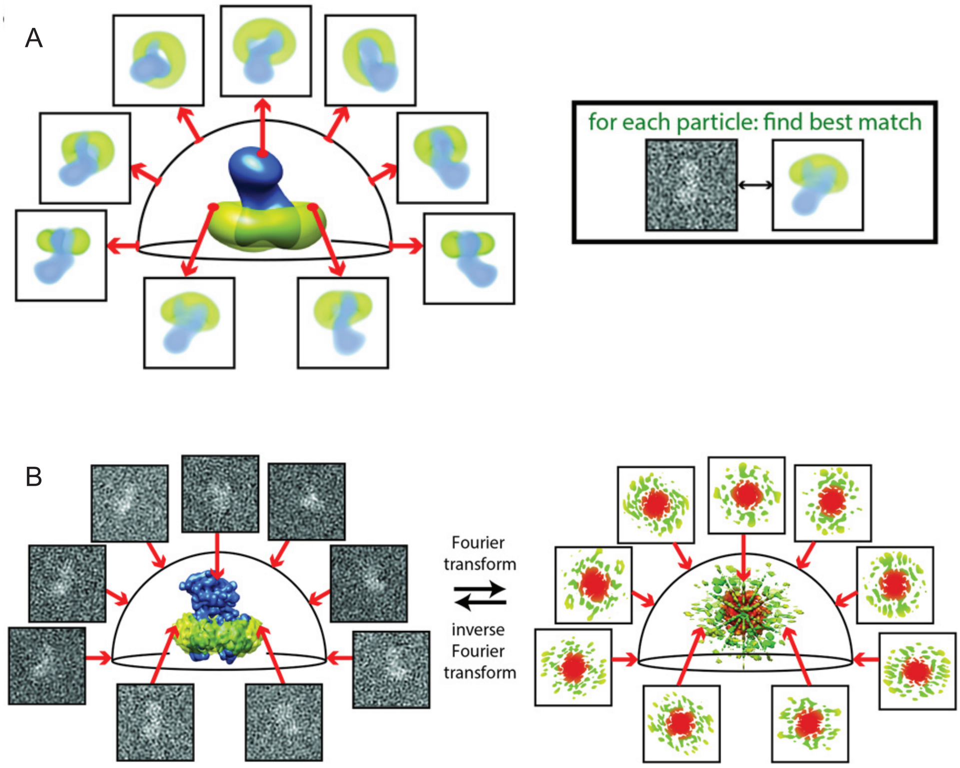

Figure 12 3D particle reconstruction by projection matching. A) Each single particle image is compared against 2D projections of a low resolution initial model to estimate a projection vector for each particle. B) These projection vectors are used to assemble the 2D Fourier transforms of the projection images into a 3D Fourier transform according to the Fourier Slice Theorem. An inverse Fourier transform results in a 3D reconstruction to be used as an initial model in the next iteration. Figure adapted from Nogales & Scheres (2015) [150] with permission from Elsevier © 2015.

To prevent bias in assignment of particle orientations, a low-resolution initial model should be used. Generation of a 3D reconstruction of higher resolution than the initial model provides confidence that model bias has been avoided, especially if such a reconstruction includes expected protein features such as α-helices. Alternatively, an *ab initio* starting model can be derived from the particle images themselves, relying on the fact that pairs of 2D Fourier transforms of projection images will have a common line that intersects in the 3D Fourier transform of the object [145].

Most modern SPA approaches do not assign a single projection vector to each 2D projection image. Rather, statistical methods such as the maximum-likelihood approach are employed that integrate over the probability distribution of all possible orientations [145]. The RELION program uses a special maximum-likelihood approach called the Bayesian approach, which includes a 'smoothness' regularization term that expresses prior knowledge about the 3D reconstruction throughout the refinement to inhibit accumulation of noise [151]. The maximum-likelihood approach is also used in the computational separation of mixtures into structurally homogenous subsets in both two- and three-dimensions. These classifications can be performed without knowing the amount or type of structural variability in the data beforehand [150].

2.1.3.2 The image processing pipeline

The SPA image processing pipeline from micrograph movies to sharpened 3D reconstruction is summarised in Figure 13. Each step is explained in detail below.

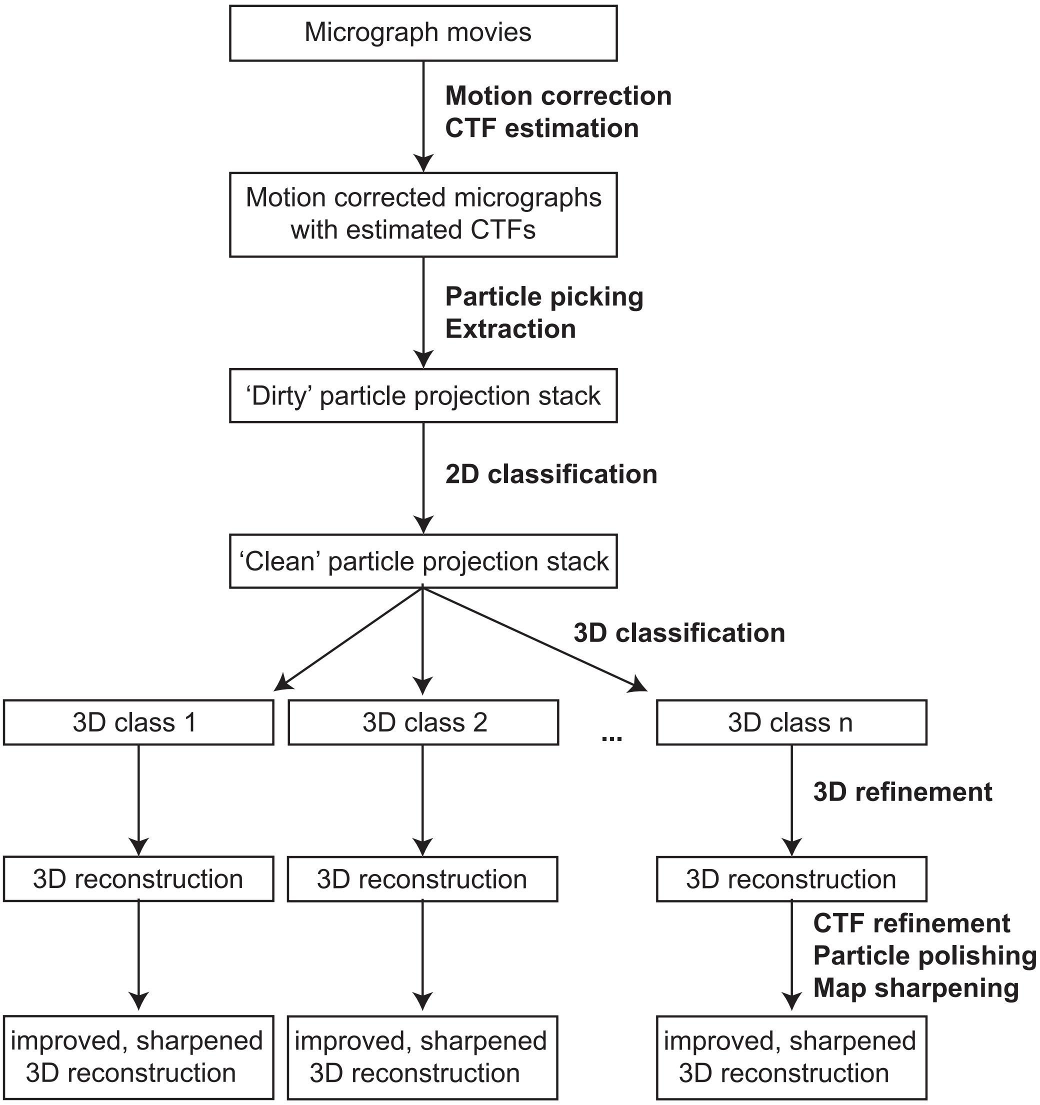

Figure 13 Overview of the SPA image processing pipeline.

After collecting hundreds to thousands of dose-fractionated micrograph movies, the frames are aligned and averaged to correct for micrograph-wide beam-induced motions using software such as MotionCor2 [152]. Down-weighting of the high resolution components of the first and last few frames to mitigate the effects of sample movement and radiation damage respectively, is also performed at this stage [153]. Following this, the CTF parameters of each averaged micrograph are estimated by programs such as CTFFIND4 [154] and GCTF [155]. The effects of CTF are later corrected for during particle reconstruction.

Next, the coordinates of the particles within each micrograph are specified. Particles can be picked by hand or by a number of different automated methods. For example, RELION allows for the application of a Laplacian-of-Gaussian filter to pick all ‘blobs’ of a specified size [156]. A semi-automated approach can also be used, where a few thousand particles are picked manually, from which 2D templates are generated which are used as references to automatically find particles from the rest of the dataset. These templates should be low-pass filtered to around 20-30 Å resolution to avoid the picking of background noise [153]. More recently, deep learning programs such as crYOLO have been developed that use neural networks trained to recognise particles in micrographs, or networks that can be user-trained to recognise particles in a specific dataset [157]. After specifying the particle coordinates by any method, the particles are then extracted from the micrographs into small square regions (boxes), which are collected into a stack of particle images.

Since no method of particle picking is perfect, all particle stacks will include ‘junk’ boxes containing noise, ice contamination, grid hole edges, impurities and/or partially unfolded protein. 2D classification is an effective way of removing these boxes, or ‘cleaning’ the dataset. This approach groups together and averages particles with the same projection vector using a regularized maximum likelihood algorithm marginalised over in-plain orientations [153]. True particles are grouped together into classes with strong signal that contain high resolution features, whereas lowly populated, noisy classes can be attributed to ‘junk’ particles, which are removed from the dataset.

Even after removal of junk particles, most datasets will still contain heterogeneity due to conformational or compositional differences in the particles. The particles can be separated into distinct groups by unsupervised 3D classification, which uses a maximum likelihood projection matching approach to marginalise over both the orientation and class assignments of the particle images. The user provides a single low-resolution initial model and specifies the desired number of classes. The user can also provide a mask around an area of interest to classify the dataset based on a specific region of the biomolecule of interest [153].

High resolution structures of the particle in its various conformational or compositional states can then be solved by refinement of the particles contributing to each 3D class. During 3D refinement, the dataset is split into two independent subsets which are refined separately. This involves projection matching using a maximum likelihood approach to marginalise over the particle orientation assignments, with iterative improvement in angular and translational sampling until convergence of both the estimated resolution and particle orientation assignments. Upon convergence, a final iteration is performed by combining the two half sets in a single reconstruction [151]. Splitting the data into two half sets allows the use of the Fourier shell correlation (FSC) gold-standard approach to estimate resolution throughout refinement. Specifically, the FSC between the two maps derived from the half sets (half maps) is measured, which specifies the similarity between the maps across different spatial frequencies. The spatial frequency at an FSC cut-off of 0.143 is used to estimate resolution. This approach reduces the risk of overfitting, since background noise is unlikely to correlate across the two half sets [158]. Even so, it is important to visually assess the final map for secondary structure elements or sidechain density to check that the reconstruction and resolution estimate are consistent.

Following initial structure determination, per-particle refinement of CTF parameters (CTF refinement) and per-particle beam-induced motion correction (particle polishing) can be carried out, and the refinement repeated in an iterative manner to improve the reconstruction resolution further [156]. Finally, the high frequency components in the reconstruction, which are disproportionately dampened during image formation, detection and processing, are modelled by a Gaussian decay using a B-factor, and then appropriately corrected for, thereby ‘sharpening’ the map [153].

The FSC gold standard approach gives a single resolution refinement of the entire reconstruction. In reality, the resolution will vary throughout the map due to sample heterogeneity: flexible regions of the particle will be more poorly resolved than static regions. When a single sharpening B-factor is applied, then it is likely that either the high resolution regions of the map will be under-sharpened or the low resolution regions over-sharpened. Local resolution can be estimated by dividing the map into smaller sub-volumes and calculating FSC resolutions for each. Maps can then be locally low-passed filtered according to estimated resolution, to allow for easier visualisation of all regions when using a single sharpening B-factor [159]. Other approaches include local sharpening based on an atomic model reference (LocScale [160]), or deep learning algorithms that use neural networks trained to carry out masking-like and sharpening-like operations automatically (DeepEMhancer [161]).

So far, the workflow to determine a single, ‘consensus’, high-resolution reconstruction from a dataset of cryo-EM micrographs has been described. However, samples that exhibit considerable flexibility cannot be fully described by such consensus maps. In such cases, multibody refinement can be performed. Here, masks are used to define regions of the consensus reconstruction as rigid bodies that move independently from each other, and two procedures are iteratively carried out for each body: particle subtraction and focussed refinement. Particle subtraction goes back to the particle projection stack (now with known projection vectors) and removes signal that corresponds to regions outside the mask. Focussed refinement then performs the projection matching algorithm using the masked region of the consensus map as the initial reference. The relative orientations of all bodies for each particle image are analysed at every iteration to continuously improve the particle subtraction procedure. The end result of a successful multibody refinement is a reconstruction for each body with improved resolution compared to the respective regions in the consensus reconstruction. Furthermore, principal component analysis of the refined relative orientations of the bodies after convergence of the multibody refinement can be used to visualise the major motions that exist within the dataset [162].

2.1.4 Model building and refinement

To enable biological interpretation of a structure at a molecular level, a model must be fitted to the cryo-EM reconstruction.

Atomic models can be built into cryo-EM reconstructions with resolutions higher than about 3.5 Å with resolved sidechain density. Models might be built *de novo* or based on a starting model that is rigid-body fitted into the density. This starting model might be a Protein Data Bank (PDB) coordinate file of an existing structure solved by cryo-EM or X-ray crystallography, or it may be a homology model predicted using software such as SWISS-MODEL [163]. To improve the fit to map and geometry, the model is then edited manually in programs like Coot, and automatically refined in programs like Phenix [164] or Refmac [165]. Manual and automatic model refinement is performed iteratively until the model geometry and map fit is optimised, as assessed by validation tools such as MolProbity [166].

Models cannot be built *de novo* into lower resolution maps, however existing models can be fitted. If the map is resolved only to the protein domain level, then models should only be rigid-body fitted, but if secondary structure features are resolved, then the model can be flexibly fitted into the map. For example, FlexEM is a flexible fitting tool that splits the structure into progressively smaller rigid bodies, and optimises fit based on structure-map cross correlation, stereochemistry and non-bonding interactions [167].

The resolution of the map must be kept in mind when interpreting the structure. For example, if side chain density is not resolved in the map, then any biological interpretation that relies on side chain positioning in the model is speculative.

2.2 *Acinetobacter baummannii* 70S ribosome project

2.2.1 Materials

All buffer components were purchased from Sigma-Aldrich except KOH (VWR) and KCl (Thermo Fisher Scientific). Buffers were made using deionised water treated with diethyl pyrocarbonate (DEPC): DEPC was added 0.1% v/v to deionised water and incubated for 12 hours at 37ºC, and then autoclaved (121ºC, 20 minutes). Buffers were then filter sterilised (0.22 µm filters, Merck Millipore). All plasticware and glassware were heat-treated (121ºC, 20 minutes) or thoroughly rinsed with DEPC-treated water before adding ribosome sample.

2.2.2 *A. baumannii* growth curves

A. baumannii type strain ATCC 19606 was grown overnight at 37ºC on Luria-Bertani (LB) agar plates. A colony was picked and used to inoculate 9 mL of LB media which was then grown overnight at 37ºC. An aliquot (0.1 mL) of the saturated culture was then used to inoculate 250 mL of LB media, which was grown at 37ºC with vigorous aeration. Samples were taken at regular time intervals for optical density at 600 nm (OD_{600}) measurements.

2.2.3 Purification of tightly-coupled *A. baumannii* 70S ribosomes

Ribosomes were purified from *A. baumannii* according to a protocol adapted from parts of the protocols used in Khusainov et al. (2016) [168] and Mehta et al. (2012) [169]. A two-litre culture of *A. baumannii* type strain ATCC 19606 was grown at 37ºC in LB media and harvested at early-mid log phase (OD_{600} of ~0.5). The cell pellet was washed with 10 mM Tris-HCl (pH 7.5) and stored at -80°C. After thawing, each 1 g of cell pellet was resuspended in 2 mL lysis buffer (20 mM HEPES-KOH pH 7.5, 100 mM NH_4Cl, 20 mM $Mg(OAc)_2$, 0.5 mM EDTA, 1 mM DTT) supplemented with cOmplete protease inhibitor cocktail (Roche, one tablet per 10 mL) and RNase-free DNase (300 U). The resuspension was lysed by two passes at 25K psi through a cell disruptor (Avestin EmulsiFlex C3) and cleared by centrifugation at 30,000 x *g* for 30 minutes. The top 80% of the supernatant was collected and recentrifuged at 30,000 x *g* for 30 minutes, and the resulting supernatant, also known as the ‘S30 fraction’, was layered onto a sucrose cushion buffer (10 mM HEPES-KOH pH 7.5, 500 mM KCl, 25 mM $Mg(OAc)_2$, 1.1 M sucrose (40% w/v), 0.5 mM EDTA, 1 mM DTT) and spun by ultracentifugation at 150,000 x *g* for 16 hours. The resulting crude ribosome pellet was gently resuspended in 200 µL of sucrose gradient buffer (10 mM HEPES-KOH pH 7.5, 100 mM KCl, 10 mM $Mg(OAc)_2$, 0.5 mM EDTA, 1 mM DTT) and layered on top of a 10-40% w/v sucrose density gradient (made by dissolving different amounts of sucrose in sucrose gradient buffer). Ultracentrifugation was subsequently carried out at 50,000 x *g* for 16 hours. The gradient was fractionated and the sedimentation profile assessed by measuring absorbance at 260 nm (A_{260}) of samples taken from all the fractions using an Implen NanoPhotometer NP80. The fractions that contributed to the largest A_{260} peak were collected and dialysed into storage buffer (10 mM HEPES-KOH pH 7.5, 50 mM KCl, 10 mM NH_4Cl, 10 mM $Mg(OAc)_2$, 1 mM DTT) using a 20K molecular weight cut-off Slide-A-Lyzer MINI Dialysis Device (Thermo Fisher Scientific), flash frozen in liquid nitrogen, and stored at −80°C.

2.2.4 RNA agarose gel electrophoresis

RNA loading buffer (Thermo Fisher Scientific) was added to 500 ng of purified ribosome sample. This dye contains ethidium bromide, a fluorescent tag that intercalates the nucleic acid bases, and formamide, a denaturing agent that stabilises RNA and ensures RNA fragments separate according to size during electrophoresis. The sample was then heated for 3 minutes at 95°C and loaded onto a 1% agarose gel made with TAE buffer (40 mM Tris-acetate, 1 mM EDTA, pH 8.3). The gel was run at 90 V for 30 minutes in TAE buffer before visualisation under UV light.

2.2.5 Negative stain TEM

Continuous carbon-coated 100 mesh copper grids were glow discharged at 10 mA for 30 s (PELCO easiGlow). An aliquot (3 µL) of diluted ribosome sample (0.6 A_{260} units, 14.4 nM, 0.03 mg ml^{-1}) was applied to a glow discharged grid and left for 30 seconds. Excess sample was blotted off, and the grid washed twice with storage buffer. Uranyl acetate (1% w/v) was added, blotted away, and added again and the grid left for 30 seconds. The excess uranyl acetate was then blotted off and the grid dried under a lamp. The grid was then visualised using an FEI Tecnai F20 transmission electron microscope at a nominal magnification of 50,000x (2 Å / pixel).

2.2.6 Cryo-EM of amikacin-ribosome complex

Purified 70S ribosomes (120 nM) were incubated with amikacin (100 µM, Cayman chemical) at room temperature for 30 minutes. A Quantifoil grid (R1.2/1.3, 400 Cu mesh, with a 2 nm carbon overlay) was glow discharged (10 mA, 30 s, Quorum GloQube) and then transferred to the humidity- and temperature-controlled chamber of an FEI Vitrobot Mark IV (Thermo Fisher Scientific, 100% humidity, 4°C). An aliquot (3 µL) of the amikacin-ribosome reaction mixture was applied to the grid, excess sample immediately removed by blotting, and vitrification performed by plunging the grid into liquid nitrogen-cooled liquid ethane.

Data was collected on a Thermo Fisher Scientific Titan Krios electron microscope (Astbury Biostructure Laboratory, University of Leeds) at 300 kV. Data collection was set up as described previously [170]. In brief, the sample was exposed to an electron dose of 58 $e^-/Å^2$ across 10 s, and 2717 micrograph movies were recorded by a Gatan K2 summit detector in counting mode, split into frames in which each received a dose of 1.16 $e^-/Å^2$. A nominal magnification of 130,000x was applied, resulting in a final object sampling of 1.07 Å/pixel. A defocus range of -0.8 to -2.7 µm was used. Micrograph movies with poor ice quality were removed, leaving 554 for single particle image analysis.

Drift-corrected and dose-corrected averages of each movie were created using MOTIONCOR2 [152], and the contrast transfer functions estimated using Gctf [155]. All subsequent image processing steps were carried out using RELION 3.0 [156]. Laplacian-of-Gaussian autopicking was used to select 85,863 particles, which were then extracted with 4x binning. Reference-free 2D classification and 3D classification were performed on these particles to remove junk images by removing particles contributing to 50S classes or lowly populated classes containing no high resolution features. The remaining 51,958 particles were re-extracted without binning and aligned and refined in 3D using a 60 Å low-passed filtered *ab initio* starting model made by a stochastic gradient descent procedure. Rounds of Bayesian polishing and CTF refinement were performed until the resolution of the map stopped improving. Solvent masking and map sharpening yielded a reconstruction resolved to 2.8 Å.

Multibody refinement was performed using soft extended masks to define the 50S, 30S body and 30S head as rigid bodies. This procedure uses iteratively-improved partial signal subtraction and focussed refinement to generate higher quality reconstructions for each body [162]. Following this, solvent masking and map sharpening yielded reconstructions for the 50S, 30S body and 30S head at estimated resolutions of 2.7, 2.9, and 3.0 Å, respectively. The 30S head and 30S body multibody maps contained better resolved density than the corresponding regions in the consensus map. The 50S multibody map comprised density of similar resolution to the corresponding region in the consensus map. The sharpened consensus and multibody reconstructions were lowpass filtered by local resolution, using RELION's own implementation of local resolution estimation. These maps were used to make figures comprising maps coloured by local resolution. Maps that had undergone sharpening and solvent masking without local resolution lowpass filtering were used for model building and refinement.

2.2.7 Cryo-EM of tigecycline-ribosome complex

Purified 70S ribosomes (240 nM) were incubated with tigecycline (71.7 µM, LKT Labs) at room temperature for 30 minutes. A Quantifoil grid (R1.2/1.3, 400 Cu mesh, with a 2 nm carbon overlay) was glow discharged (10 mA, 30 s, Quorum GloQube) and then transferred to the humidity- and temperature-controlled chamber of an FEI Vitrobot Mark IV (Thermo Fisher Scientific, 100% humidity, 4°C). An aliquot (3 µL) of the tigecycline-ribosome reaction mixture was applied to the grid, excess sample was immediately removed by blotting and vitrification performed by plunging the grid into liquid nitrogen-cooled liquid ethane.

Data was collected on a Thermo Fisher Scientific Titan Krios electron microscope (Astbury Biostructure Laboratory, University of Leeds) at 300 kV. The sample was exposed to an electron dose of 62 $e^-/Å^2$ across 1.1 s, and 6228 micrograph movies were recorded by a Thermo Fisher Scientific Falcon 3EC detector in integrating mode, split into frames which each received a dose of 1.44 $e^-/Å^2$. A nominal magnification of 75,000x was applied, resulting in a final object sampling of 1.065 Å/pixel. A defocus range of -0.8 to -2.6 µm was used.

Image processing was carried out in the same way as for the amikacin-ribosome complex, with a few differences listed below. Laplacian-of-Gaussian autopicking was used to select 1.68 million particles, which were extracted with 4x binning. 924,636 particles remained after removal of junk particles by 2D and 3D classification. To save computing time, a random selection comprising only a quarter of this dataset was taken forward for high-resolution 3D reconstruction (231,159 particles) Solvent masking and map sharpening yielded a reconstruction resolved to 2.6 Å. Multibody refinement yielded reconstructions for the 50S, 30S body and 30S head at estimated resolutions of 2.5, 2.7, and 3.0 Å.

In all cases, final resolutions were estimated using the gold-standard Fourier shell correlation (FSC = 0.143) criterion.

2.2.8 Model building of drug-bound ribosomes

The cryo-EM structure of an *E. coli* ribosome (PDB 5MDZ) [171] was used as a starting point for modelling the *A. baumannii* 23S, 16S and 5S rRNAs into the sharpened multibody reconstructions. The *E. coli* ribosome was chosen for its high sequence similarity to the *A. baumannii* ribosome (e.g. the 23S rRNA sequence identity between the two is ~84%). Homology models were generated for the ribosomal proteins using the SWISS model server [172] and rigid-body fitted into the reconstructions in UCSF Chimera [173] using PDB 5MDZ as a reference to guide placement. The models were inspected using COOT [174], and in all three amikacin-ribosome multibody reconstructions and the tigecycline-ribosome 50S and 30S body multibody reconstructions, regions of protein where side chains could not be resolved were modelled with truncated side chains, and regions where the protein or rRNA backbone could not be traced were deleted. The tigecycline-ribosome 30S head reconstruction was of slightly poorer quality than the other maps and so such highly stringent trimming of the model was not carried out. Instead, the full amikacin-ribosome 30S head model was predicted to be a good approximation for the tigecycline-ribosome 30S head and hence was used as a starting model and retained with no further deletion of backbone or side chains throughout model refinement.

Weak tRNA-like density present in the ribosome E-site, likely corresponding to a mixture of different tRNAs that remained associated with a subpopulation of ribosomes throughout the purification procedure, was modelled using fMet-tRNA from *E. coli* (PDB 5AFI) [175] as a starting model. Only the regions near the 50S and 30S subunits with resolved nucleotide density were retained. Density corresponding to a short mRNA at the E-site was also resolved, and this was modelled as a short polyuridine chain.

COOT was used to manually adjust the models to improve map and rotamer fit and reduce the number of Ramachandran outliers, before iterative rounds of model refinement and manual model editing were carried out using PHENIX real space refine [164] and COOT respectively. Models were validated using MolProbity [166] within PHENIX and PDB OneDep [176]. Throughout the process, the models for the 50S, 30S body and 30S head were kept separate and refined independently into their corresponding maps, as this reflects the data from the multibody refinement procedure which generates independent reconstructions [162].

2.2.9 Atomic model analysis and figure making

Figures of the growth curve and sedimentation profile were made using Microsoft Excel, EM micrographs using ImageJ [177], atomic models and cryo-EM maps using UCSF ChimeraX [178] and PyMOL, and structural formulae of amikacin and tigecycline using MolView. Interactions between the tigecycline molecules in the secondary binding site and the surrounding ribosome were calculated using Arpeggio [179], and then represented in 2D using LigPlot+ [180].

2.2.10 Data deposition

Motion corrected cryo-EM micrographs were deposited to the Electron Microscopy Public Image Archive (EMPIAR), accession codes EMPIAR-10406 (amikacin-ribosome dataset) and EMPIAR-10407 (tigecycline-ribosome dataset). Cryo-EM reconstructions were deposited in the Electron Microscopy Data Bank (EMDB), accession codes EMD-10809 (amikacin-ribosome 50S), EMD-10869 (amikacin-ribosome 30S body), EMD-10892 (amikacin-ribosome 30S head), EMD-10898 (tigecycline-ribosome 50S), EMD-10914 (tigecycline-ribosome 30S body) and EMD-10915 (tigecycline-ribosome 30S head). Masks, half maps and consensus reconstructions are deposited as additional files alongside these reconstructions. Atomic model coordinates were deposited to the PDB, accession codes PDB 6YHS (amikacin-ribosome 50S), PDB 6YPU (amikacin-ribosome 30S body), PDB 6YS5 (amikacin-ribosome 30S head), PDB 6YSI (tigecycline-ribosome 50S), PDB 6YT9 (tigecycline-ribosome 30S body) and PDB 6YTF (tigecycline-ribosome 30S head).

2.3 Sal-type ABC-F resistance protein project

Research for the Sal project was carried out by myself and Merianne Mohamad. Both Merianne and I contributed equally to the molecular cloning, FLAG-tag affinity purification and silver-stain SDS-PAGE visualisation of the Sal(A-E) variants. My own contributions were the negative stain TEM, cryo-EM structure determination, model building and figure making. Merianne's contributions were the molecular cloning and MIC experiments that involved the mutants of Sal(B) and Sal from *S. saprophyticus*.

All buffer components were purchased from Sigma-Aldrich except KOH (VWR), KCl (Thermo Fisher Scientific), and ATP (New England Biolabs). Buffers were made using deionised water treated with DEPC: DEPC was added 0.1% v/v to deionised water and incubated for 12 hours at 37ºC, and then autoclaved (121ºC, 20 minutes). Buffers were then filter sterilised (0.22 µm filters, Merck Millipore). All plasticware and glassware were heat-treated (121ºC, 20 minutes) or thoroughly rinsed with DEPC-treated water before adding ribosome sample. Bacterial strains and plasmids used in this study are listed in Table 1.

Bacterial strains			
Organism	**Strain**	**Comments**	**Reference/source**
Escherichia coli	XL10-Gold	Genotype: *endA1 glnV44 recA1 thi-1 gyrA96 relA1 lac Hte* Δ(*mcrA*)183 Δ(*mcrCB-hsdSMR-mrr*)173 *tetR* F'[*proAB lacI*qZΔM15 Tn10(*TetR Amy CmR*)]	Agilent Technologies
Staphylococcus aureus	RN4220	Restriction deficient derivative of *S. aureus* 8325-4	Fairweather et al. (1983) [181]
Staphylococcus aureus	SH1000	Derivative of 8325-4 strain, with functional rsbU gene reinstated	Horsburgh et al. (2002) [182]
Plasmids			
Plasmid		**Comments**	**Reference/source**
pUC57			Genewiz
pRMC2		An *E. coli* / *S. aureus* shuttle vector. A modified variant of the pRMC2 expression vector, allowing the regulated expression of cloned genes under the control of the tetracycline inducible, Pxyl/tet promoter	Corrigan & Foster (2009) [183]

Table 1 Bacterial strains used in this study

2.3.1 Molecular cloning of *sal* variants

Plasmid pUC57 carrying genes that coded for 'EQ$_2$ mutants' of Sal variants A-E were obtained from Genewiz as a lyophilised powder. EQ$_2$ refers to E156Q and E456Q mutations in the coded protein. All constructs contained the mutant gene flanked by two different restriction sites, with 20 nucleotide spacers in between the start/stop codons and the restriction sites. They also contained a C-terminal diglycine linker and FLAG$_3$-tag immediately before the stop codon. The full gene sequences can be found in the Appendix.

2.3.1.1 Making *E. coli* CaCl$_2$ competent cells

The protocol used for making transformation-competent *E. coli* cells was adapted from Sambrook & Russell (2006) [184]. Specifically, a single colony of *E. coli* XL10-Gold was used to inoculate 5 mL of LB media, and then grown overnight at 37 ºC. An aliquot (1 mL) of this overnight culture was used to inoculate 100 mL of LB, which was grown at 37 ºC for 3 hours. The culture was held on ice for 10 minutes before pelleting. The pellet was resuspended in 10 mL ice-cold 0.1 M $CaCl_2$ before being incubated on ice for 20 minutes. The pellet was spun down again and then resuspended in 5 mL ice-cold 0.1 M $CaCl_2$/15% glycerol. The resulting competent cells were stored in 300 µL volumes at -80 ºC.

2.3.1.2 Making *S. aureus* competent cells

The protocol used for making transformation-competent *S. aureus* cells was adapted from Schenk & Laddaga (1992) [185]. Specifically, a single colony of *S. aureus* (strain RN4220 or SH1000) was used to inoculate 5 mL of TSB + 2.5% yeast extract, and then grown overnight at 37 ºC. An aliquot (1 mL) of this overnight culture was used to inoculate 25 mL of TSB + 2.5% yeast extract, which was grown at 37 ºC until OD_{600} of 0.5-0.6. The cells were harvested and the pellet was washed three times in 25 mL deionized water, then once with 5 mL 10% glycerol (in deionized water). A 2.5 mL volume of 10% glycerol was added before incubation on ice for 15 minutes. Cells were recovered and resuspended in 800 µL 10% glycerol. These competent cells were stored in 80 µL volumes at -80 ºC.

2.3.1.3 Transformation of pUC57 plasmid into *E. coli*

An aliquot (100 µL) of *E. coli* competent cells was mixed with 50 ng of pUC57 plasmid containing the *sal* gene variant before incubation for 30 minutes on ice. The mixture was subjected to heat shock for 45 seconds at 42 ºC, and then immediately put back on ice. LB media (900 µL) was then added and the cells incubated at 37 ºC for 60 minutes. Volumes (100 µL) of the cells were plated onto LB agar plates containing 100 µg/mL carbenicillin to select for transformants and grown overnight at 37 ºC.

2.3.1.4 Isolation of gene insert from pUC57 plasmid

Plasmid DNA was purified from transformants generated in 2.3.1.3. Briefly, transformants were picked and used to inoculate 9 mL of LB media, which was grown for ~16 hours at 37 ºC. Plasmid DNA was then isolated using the QIAprep Spin Miniprep Kit (Qiagen) according to manufacturer’s instructions. Plasmids were double-digested with the appropriate two restriction enzymes for the restriction sites flanking the *sal* gene. Specifically, miniprepped plasmid was mixed with 5 µL of 10X rCutSmart buffer (New England Biolabs), 10 U of each restriction enzyme (high fidelity versions, New England Biolabs) for every 1 µg of DNA, and nuclease-free water (New England Biolabs) to make up to 50 µL. The mixture was incubated for 15 minutes at 37 ºC.

An aliquot (10 µL) of 6X gel loading dye (Promega) was added to the 50 µL digestion reaction, which was then run on a 0.8% agarose gel made using TAE buffer (40 mM Tris-acetate, 1 mM EDTA, pH 8.3) containing 3 µL 10,000X SYBR Safe DNA stain (Thermo Fisher Scientific). The gel was run at 90 V for 30 minutes in TAE buffer and visualised under a blue light to aid excision of the band containing the *sal* gene. DNA was extracted from this band using the QIAquick Gel Extraction Kit (Qiagen) according to the manufacturer's instructions. The DNA was further purified by using the QIAquick PCR Purification Kit (Qiagen), according to the manufacturer's instructions.

2.3.1.5 Ligation of insert into pRMC2 plasmid and transformation of *E. coli* and *S. aureus*

The purified digested DNA was ligated into an appropriately double-digested pRMC2 vector (digested according to the same protocol as outlined above) using the Quick Ligation Kit (New England Biolabs). The ligation product was then transformed into *E. coli* $CaCl_2$ competent cells, according to the protocol outlined in section 2.3.1.3, except that 5 µL of ligation product was used, and 100 µg/mL ampicillin used for selection.

Plasmid DNA was isolated from these transformants using the QIAprep Spin Miniprep Kit (Qiagen) as above, and used to transform *S. aureus* RN4220 cells by a protocol adapted from Schenk & Laddaga (1992) [185]. Specifically, 1 µg of plasmid was mixed with 50 µL competent cells at 20 ºC. The mixture was transferred to a 0.1 cm gap electroporation cuvette (Geneflow) and pulsed at 2.3 kV, 100 Ω, 25 µF. 950 µL of room temperature TSB + 2.5% yeast extract was immediately added, before incubation for 1 hour at 37 ºC. The cells were then plated on LB agar plates containing 25 µg/mL chloramphenicol and grown overnight at 37 ºC. A colony was picked and used to inoculate 9 mL of LB media, which was grown overnight at 37 ºC. Plasmid DNA was isolated using the QIAprep Spin Miniprep Kit (Qiagen) according to manufacturer's instructions, but with 100 µg/mL recombinant lysostaphin (affinity purified in our laboratory) used to supplement the cell resuspension buffer, and an additional 10 minute 37 ºC incubation of the lysostaphin : cell resuspension before proceeding to alkaline lysis.

The above procedure was then repeated using *S. aureus* SH1000 competent cells, yielding *S. aureus* SH1000 culture containing the pRMC2 plasmid, which in turn contained the *sal* gene insert. A negative control strain, containing the pRMC2 plasmid without the *sal* gene insert was also generated. Aliquots of this culture were mixed 1:1 with 50% glycerol (so the final stock was 25% glycerol), and stored at -80 ºC.

Transformation of *S. aureus* SH1000 cells was carried out because the Sal-ribosome purification protocol (section 2.3.2) that was developed by Dr Vasili Hauryliuk uses this strain. The SH1000 strain cannot be transformed with DNA directly isolated from *E. coli*, hence the intermediary step of transformation of the RN4220 strain [186].

2.3.2 FLAG-tag affinity purification of *S. aureus* ribosome : Sal variant complexes

Sal-ribosome complexes were purified according to a protocol developed by Dr Vasili Hauryliuk [187]. Volumes (400 mL) of the transformed *S. aureus* SH1000 cells were grown at 37 ºC in LB media supplemented with 20 µg/mL chloramphenicol to an OD_{600} of about 0.5, before inducing expression of *sal* genes with 100 ng/mL anhydrotetracycline hydrochloride (Sigma-Aldrich) for 1 hour. The cells were then harvested, and the pellet resuspended in 2 mL HEPES:polymix buffer (20 mM HEPES-KOH pH 7.5, 5 mM $Mg(OAc)_2$, 95 mM KCl, 5 mM NH_4Cl, 0.5 mM $CaCl_2$, 8 mM putrescine, 1 mM spermidine) supplemented with 0.5 mM ATP, 2 mM DTT and 1 tablet of cOmplete protease inhibitor cocktail (Roche). The resuspension was divided into 1 mL aliquots and transferred to tubes containing silica beads (Lysing Matrix B, MP Biomedicals). The cells were mixed thoroughly with the beads and then lysed by a FastPrep-24 Classic homogenizer (MP Biomedicals) using 4 cycles of 20 seconds at 6 m/s with 1 minute cooling on ice between cycles. The beads and cell debris were spun down at 30,000 x *g* for 30 minutes.

Meanwhile, an anti-FLAG column was prepared. An aliquot (200 µL) of anti-FLAG M2 affinity gel (Sigma-Aldrich) was added to a 600 µL Pierce Spin Cups with a paper filter (Thermo Fisher Scientific). This was centrifuged for 1 minute at 1000 x *g*, and the flow-through discarded. All following centrifugations were also performed for 1 minute at 1000 x *g.* The beads were then washed four times with 500 µL HEPES:polymix buffer.

The clarified lysate was then incubated with the washed beads for 2 hours at 4 ºC, with periodic, gentle mixing. The beads were centrifuged and the flow through collected. The beads were then washed with 500 µL HEPES:polymix buffer four times, with the flow-through from the final wash collected. An aliquot (300 µL) of 0.1 mg/mL 3X FLAG peptide solution (Sigma-Aldrich) prepared in HEPES:polymix buffer was incubated with the beads for 20 minutes at 4 ºC. The column was then centrifuged, and the elution fractions collected. The elution step was repeated twice more, and then the beads were washed once more with 500 µL HEPES:polymix buffer, and then stripped with 0.1 M glycine-HCl pH 3.5. Later attempts to purify Sal(D)- and Sal(E)-ribosome complexes used 100 µL of 0.4 mg/mL 3X FLAG peptide.

2.3.3 Silver-stain sodium dodecyl sulphate-polyacrylamide gel electrophoresis (SDS-PAGE)

SDS Blue Loading Buffer (New England Biolabs) was mixed with samples taken at various stages throughout the purification procedure and heated to 95 ºC for 5 minutes. An aliquot (10 µL) of sample-dye mixture was added to a 4–20% Mini-PROTEAN TGX Precast Protein Gel (Bio-Rad), except for the flowthrough-dye mixture, of which only 2 µL was loaded. The gel was run for 60 minutes at 120 V in TGS buffer (25 mM Tris, 192 mM glycine, 0.1% SDS, pH 8.3). Silver staining was carried out using the PlusOne Silver Staining Kit (GE healthcare), according to manufacturer's instructions.

2.3.4 Negative stain TEM

Continuous carbon-coated 100 mesh copper grids were glow discharged at 10 mA for 30 s (PELCO easiGlow). 3 µL of elution fraction (non-diluted in the case of Sal(A)-, Sal(C)-, Sal(D)- and Sal(E)-ribosome complexes, and diluted 10x in the case of the Sal(B)-ribosome complex) was applied to a glow discharged grid and left for 30 seconds. Excess sample was removed by blotting, and the grid washed twice with storage buffer. Uranyl acetate (1% w/v) was added, blotted away, and added again and the grid left for 30 seconds. The excess uranyl acetate was then blotted off and the grid dried under a lamp. The grid was then visualised using an FEI T12 transmission electron microscope at a nominal magnification of 30,000x (3.7 Å / pixel).

2.3.5 Cryo-EM of Sal-ribosome complexes

2.3.5.1 Sal(B)-ribosome complex

Cryo-EM grid preparation, data collection and image processing of Sal(B) was carried out as above for the amikacin-ribosome sample (section 2.2.6), with some differences highlighted below.

In the microscope, the sample was exposed to an electron dose of 60 $e^-/Å^2$ across 8.0 s, and 847 micrograph movies were recorded by a Gatan K2 summit detector in counting mode, split into frames which each received a dose of 1.20 $e^-/Å^2$. A nominal magnification of 130,000x was applied, resulting in a final object sampling of 1.07 Å/pixel. A defocus range of -0.8 to -2.6 μm was used.

All image processing steps after MOTIONCOR2 [152] and Gctf [155] were carried out using RELION 3.1 [156]. Laplacian-of-Gaussian autopicking was used to select 99,615 particles, which were extracted with 4x binning. 67,139 particles remained after removal of junk particles, which were aligned and refined in 3D using a 60 Å low-passed filtered 3D class as a starting model. 3D classification without particle alignment was performed to remove further poorly-aligned particles, leaving 64,101 particles. These yielded a 2.9 Å 3D reconstruction after alignment and refinement with solvent masking. Focussed 3D classification was performed using a mask around the E- and P-sites of the ribosome to yield classes containing E- and P-site density containing 59,889 particles. These were aligned and refined in 3D, yielding a 2.9 Å 70S ribosome reconstruction after solvent masking.

Multibody refinement was performed to yield reconstructions for the 50S, 30S body and 30S head at estimated resolutions of 2.8, 3.0, and 3.0 Å. The consensus map was used to build models for the 50S subunit rRNA and ribosomal proteins, Sal(B) and the P-site tRNA, and the 30S body and 30S head multibody maps used to build models for the 30S subunit rRNA and ribosomal proteins.

2.3.5.2 Other Sal-ribosome complexes

In general, a similar methodology was used to solve 3D reconstructions of the other Sal-ribosome complexes. Differences are outlined below and in Table 2.

For the Sal(A)-ribosome complex, a ‘double-blotting’ procedure was carried out to increase particle concentration on the grid. Specifically, 3 μL of the Sal(A)-ribosome elution fraction was applied to the grid, excess sample was immediately blotted off, a further 3 μL of sample was added and immediately blotted off, and then vitrification was performed by plunging the grid into liquid nitrogen-cooled liquid ethane. In the microscope, the sample was exposed to an electron dose of 60 $e^-/Å^2$ across 1.5 s, and 7719 micrograph movies were recorded by a Thermo Fisher Scientific Falcon 3EC detector in integrating mode, split into frames which each received a dose of 1.21 $e^-/Å^2$. A nominal magnification of 75,000x was applied, resulting in a final object sampling of 1.065 Å/pixel. Laplacian-of-Gaussian autopicking was used to select 508,937 particles, which were extracted with 4x binning. Removal of junk particles left 149,658 particles, which were re-extracted without binning and 2D classification was repeated. This time, classes representing a number of diverse views were taken forward to mitigate the non-uniform distribution of projection views. The corresponding 106,743 particles were aligned and refined in 3D. Focussed 3D classification was performed as above, leaving 49,621 particles which were aligned and refined in 3D. After CTF refinement and solvent masking, these particles yielded a 3.3 Å reconstruction.

For the Sal(C)-ribosome complex, the sample was exposed to an electron dose of 63 $e^-/Å^2$ across 1.2 s, and 1677 micrograph movies were recorded by a Thermo Fisher Scientific Falcon 3EC detector in integrating mode, split into frames which each received a dose of 1.33 $e^-/Å^2$. A nominal magnification of 75,000x was applied, resulting in a final object sampling of 1.065 Å/pixel. Laplacian-of-Gaussian autopicking was used to select 144,036 particles, which were extracted with 4x binning. Removal of junk particles left 66,665 particles, which were re-extracted without binning, and aligned and refined in 3D. to yield a final 3D reconstruction of 3.0 Å resolution.

For the Sal(D)-ribosome complex, a ‘double-blotting’ procedure was carried out as for the Sal(A)-ribosome complex. In the microscope, the sample was exposed to an electron dose of 61 $e^-/Å^2$ across 1.4 s, and 7086 micrograph movies were recorded by a Thermo Fisher Scientific Falcon 3EC detector in integrating mode, split into frames which each received a dose of 1.15 $e^-/Å^2$. A nominal magnification of 75,000x was applied, resulting in a final object sampling of 1.065 Å/pixel. Laplacian-of-Gaussian autopicking was used to select 479,436 particles, which were extracted with 4x binning. Removal of junk particles left 150,506 particles, which were re-extracted without binning and aligned and refined in 3D. Focussed 3D classification was performed as above, leaving 41,537 particles which were aligned and refined in 3D to yield a 3.6 Å reconstruction after solvent masking.

For the Sal(E)-ribosome complex, a ‘double-blotting’ procedure was carried out as for the Sal(A)-ribosome complex. In the microscope, the sample was exposed to an electron dose of 60 $e^-/Å^2$ across 1.4 s, and 7237 micrograph movies were recorded by a Thermo Fisher Scientific Falcon 3EC detector in integrating mode, split into frames which each received a dose of 1.13 $e^-/Å^2$. A nominal magnification of 75,000x was applied, resulting in a final object sampling of 1.065 Å/pixel. Laplacian-of-Gaussian autopicking was used to select 694,865 particles, which were extracted with 4x binning. Removal of junk particles left 213,820 particles, which were re-extracted without binning and aligned and refined in 3D. Focussed 3D classification was performed as above, leaving 99,958 particles which were aligned and refined in 3D to yield a 3.6 Å reconstruction after solvent masking.

In all cases, final resolutions were estimated using the gold-standard Fourier shell correlation (FSC = 0.143) criterion.

	Sal(A)	Sal(B)	Sal(C)	Sal(D)	Sal(E)
Blotting method	Double blot	Single blot	Single blot	Double blot	Double blot
Total electron dose	60 $e^-/Å^2$	60 $e^-/Å^2$	63 $e^-/Å^2$	61 $e^-/Å^2$	60 $e^-/Å^2$
Exposure (s)	1.5	8	1.2	1.4	1.4
Movies collected	7719	847	1677	7086	7237
Detector	Thermo Fisher Scientific Falcon 3EC	Gatan K2 Summit	Thermo Fisher Scientific Falcon 3EC	Thermo Fisher Scientific Falcon 3EC	Thermo Fisher Scientific Falcon 3EC
Detector mode	Integrating	Counting	Integrating	Integrating	Integrating
Dose / frame	1.21 $e^-/Å^2$	1.20 $e^-/Å^2$	1.33 $e^-/Å^2$	1.15 $e^-/Å^2$	1.13 $e^-/Å^2$
Nominal magnification	75,000x	130,000x	75,000x	75,000x	75,000x
Pixel size	1.065 Å/pixel	1.07 Å/pixel	1.065 Å/pixel	1.065 Å/pixel	1.065 Å/pixel
Autopicked particles	508,937	99,615	144,036	479,436	694,865
Final particle number	49,621	59,889	66,665	41,537	99,958
Consensus resolution	3.3 Å	2.9 Å	3.0 Å	3.6 Å	3.6 Å

Table 2 Differences in grid making, data collection and image processing parameters for the Sal variants.

2.3.6 Model building of the Sal(B)-ribosome complex

The cryo-EM structure of an *S. aureus* ribosome (PDB 6S0X) [188] was used as a starting model for the ribosomal proteins and rRNAs, *E. coli* P-site fMet-tRNA^{fMet} (PDB 5MDZ) [171] as a starting model for the distorted P-site tRNA, and a homology model was generated for EQ$_2$-Sal(B) using the SWISS model server [172]. These were rigid-body fitted into the cryo-EM reconstructions using UCSF Chimera [173], and the P-site tRNA was mutated to *S. aureus* tRNA^{fMet}. A short mRNA was built *de novo* at the P-site codon. COOT [174] was used to manually adjust the models to improve map and rotamer fit and reduce the number of Ramachandran outliers, before iterative rounds of model refinement and manual model editing were carried out using PHENIX real space refine [164] and COOT respectively. Note that the model of the whole ribosome was kept intact, and the 50S, 30S body and 30S head regions were each refined into the appropriate consensus or multibody reconstruction whilst keeping the rest of the model fixed. Regions of protein where side chains could not be resolved were modelled with truncated side chains, and regions where the protein or rRNA backbone could not be traced were deleted. Models were validated using MolProbity [166] within PHENIX and PDB OneDep [176].

2.3.7 Atomic model analysis and figure making

Figures of EM micrographs were made using ImageJ [177], and figures of atomic models and cryo-EM maps using UCSF ChimeraX [178]. Virtual amino acid mutation was carried out using the ‘swapaa’ function in ChimeraX, which picks the best rotamer based on clash score, hydrogen bonding and prevalence according to the Dunbrack library [189].

2.3.8 Mutagenesis experiments

Mutagenesis experiments were carried out by Merianne Mohamad, but the methodology is outlined below for reference.

S. aureus RN4220 cells containing pRMC2 plasmid, in turn containing the *sal* mutant genes, were made following the same protocol as outlined in section 2.3.1. However, after transformation into *S. aureus* RN4220, a colony was used to inoculate cation-adjusted MHB. The cells were grown at 37 ºC with vigorous aeration to an OD_{600} of 0.6, and then expression was induced with anhydrotetracycline hydrochloride (Sigma-Aldrich) at a final concentration of 100 ng/mL for 3 hours.

These strains were then subjected to susceptibility determinations with retapamulin (AdooQ Bioscience), tiamulin (Sigma-Aldrich), lincomycin (Sigma-Aldrich) and clindamycin (Cayman Chemical) by broth microdilution according to CLSI methodology [190].

Chapter 3 Structure of the 70S ribosome from *Acinetobacter baumannii* in complex with clinically-relevant antibiotics

3.1 Introduction

The bacterial ribosome is a major target of antibiotics used in the clinic. Structural studies of bacterial ribosomes have contributed to a greater understanding of bacterial protein synthesis and provided a platform for the design and improvement of antibiotics. In addition, structures of ribosomes from a range of bacteria may elucidate species-specific translation mechanisms and allow for the development of drugs particularly effective against a specific pathogen. In this chapter, high resolution structures of the 70S ribosome from *Acinetobacter baumannii* in complex with the clinically-relevant antibiotics amikacin and tigecycline are presented. Several unique structural features of this ribosome are identified, and the interactions between the antibiotics and the ribosome are described. The biological relevance of an additional tigecycline binding site is also discussed.

To introduce this chapter, the clinical prevalence and symptoms of infections caused by *A. baumannii* are described, and antibiotics used to treat these infections are outlined alongside a discussion about the growing concerns of antibiotic resistant strains of this pathogen. Next, an argument for the need to solve more ribosome structures from pathogenic bacteria is presented, highlighting differences between bacterial ribosomes that might be exploited in antibacterial drug discovery.

3.1.1 Bacterial infections caused by *A. baumannii*: prevalence, symptoms, treatment and drug resistance

A. baumannii is an opportunistic pathogen and an important source of hospital-acquired infection. It may target the respiratory tract, blood, pleural fluid, urinary tract, surgical wounds, central nervous system, skin and eyes to cause diseases such as pneumonia, meningitis, and septicaemia [191-194].

In the early 2000s, the key risk group for *A. baumannii* infection were soldiers in conflict zones, particularly Iraq. It is thought that the bacteria's ability to survive for long times on environmental surfaces may have allowed it to become prevalent in the harsh conditions associated with desert campaigns [195]. The return of soldiers to the UK and US may have contributed to the rise of *A. baumannii* infections subsequently observed in these countries [196], where it mainly affects immunocompromised patients who require prolonged hospital stays. Other high-risk groups include patients who have undergone dialysis and those that acquire medical devices such as catheters and ventilators. In particular, *A. baumannii* can form biofilms, i.e. cells embedded in an extracellular matrix of DNA, polysaccharides and proteins [197], on the surfaces of ventilator endotracheal tubes, increasing the risk of pneumonia [192,198].

Several virulence factors contribute to the disease-causing capability of *A. baumannii*, including OmpA, which is involved in mitochondrial dysfunction and cytochrome c release [199], phospholipase C, which enhances toxicity to epithelial cells [200], and phospholipase D, which is involved in epithelial cell invasion [201]. Pilus assembly and biofilm-associated protein (BAP) are also important for biofilm production, which help promote bacterial survival inside and outside a host [202].

As a Gram-negative bacterium equipped with an outer membrane and an array of efflux transporters, *A. baumannii* is intrinsically well defended against antibacterial drugs. The antibiotics available for treatment of *A. baumannii* infections in the clinic include beta-lactams, polymyxins, and ribosome-targeting antibiotics such as the aminoglycosides (e.g., amikacin) and tigecycline (a third-generation tetracycline derivative) [203]. However, the effectiveness of these agents is diminishing, and there are few recently approved drugs or candidates in late-stage development to replace them [204-208]. For example, a study of *A. baumannii* isolates from the US showed that resistance to carbapenems more than doubled from 21% to 48% from 2003 to 2012 [209], and tigecycline resistance has been reported around the world, with 74% of isolates taken from patients with ventilator-acquired pneumonia at a Greek hospital showing tigecycline resistance [210]. Concerningly, multidrug-resistant strains, including strains resistant to most or all classes of antibiotics have emerged [211-214].

Such resistance develops through a number of different molecular mechanisms. For example, aminoglycoside resistance in *A. baumannii* is largely mediated by aminoglycoside modifying enzymes [215] and rRNA methylases [216], tigecycline resistance via efflux pumps [217] and drug modification [218], and resistance to the polymyxin colistin, a drug of last resort, can occur from mutations that result in loss or modification of lipopolysaccharide, an initial target of the drug [205,219].

Emerging drug resistance is facilitated by the ability of *A. baumannii* to readily acquire novel resistance determinants through horizontal gene transfer. For example, a genomic comparison of a multidrug resistant epidemic strain (AYE) and a strain associated with human body lice that was fully susceptible to antibiotics (SDF) showed that the former contained an extra ‘resistance island’ containing 45 antimicrobial resistance genes. The same location in strain SDF was smaller and contained none of these genes, but was flanked by transposases [212]. This suggests that *A. baumannii* might be able to quickly switch its genomic structure to capture a large number of resistance genes under antimicrobial selection pressure, such as in hospital intensive care units.

Accordingly, *A. baumannii* has been classified as one of the ESKAPE pathogens, a designation reserved for those bacteria most commonly associated with multidrug resistance [220]. Furthermore, the World Health Organization has placed carbapenem-resistant *A. baumannii* in the top tier of their priority pathogens list for research and development of new antibiotics [221]. A more detailed molecular understanding of how current antibiotics bind their targets and exert their inhibitory effects on this pathogen may aid the design and development of such drugs. One strategy to increase such understanding is through the structural determination of drug-bound antibiotic targets.

3.1.2 Bacterial ribosome structures

Structures of ribosomes and antibiotic-ribosome complexes from a range of bacterial species have previously been determined. The first high resolution structures of prokaryotic ribosome subunits, solved by X-ray crystallography in 2000, were the *H. marismortui* large subunit [222] and the *T. thermophilus* small subunit [223,224], which were closely followed by structures of the whole ribosome [225] and antibiotic-bound bacterial ribosome subunits [53,58,226]. More recently, cryo-EM has replaced X-ray crystallography as the method of choice to solve structures of large macromolecules such as ribosomes, as it can achieve comparable resolution without requiring crystallization. Furthermore, comparatively small amounts of sample are needed, and it can cope with some degree of sample heterogeneity [227]. This has facilitated the elucidation of structures of translation intermediates, revealing mechanistic detail of different stages of protein synthesis, as well as ribosome assembly intermediates and ribosome super-complexes [41,228-231].

The rise of cryo-EM has also accelerated the high-resolution structural elucidation of ribosomes from a wider variety of organisms, including pathogenic bacteria. These include *Escherichia coli* [232,233], *Staphylococcus aureus* [168,234]*, Mycobacterium tuberculosis* [235]*, Pseudomonas aeruginosa* [236]*, A. baumannii* [237] and *Enterococcus faecalis* [238]. However, structures of drug-bound ribosomes have been solved from only three species of pathogenic bacteria to date, namely *E. coli* [51,61], *S. aureus* [188,239], and *M. tuberculosis* [235].

Expanding this repertoire of pathogenic bacterial ribosome and antibiotic-ribosome complex structures further could shed light on species-specific translation and translation inhibition mechanisms, and inform the rational redesign of existing antibiotics or the development of new antibiotics with increased activity against specific pathogens [45,168].

3.1.3 Structural differences between ribosomes from different bacteria

Solving structures of bacteria from a wider range of pathogenic bacteria is only necessary if such structures contain differences. The overall structure of the ribosome is similar between bacterial species, which is unsurprising considering the high sequence conservation of the ribosome. For example, the 23S rRNA sequence identity between *A. baumannii* and *E. coli, S. aureus* and *T. thermophilus* is 84%, 75% and 70% respectively. Despite this similarity, a number of important structural differences between ribosomes from different species have been found.

Such variation can be substantial, as seen in the *M. tuberculosis* ribosome, which contains an 100-nt rRNA expansion segment which forms a unique intersubunit bridge, as well as two proteins that appear to be unique to *Mycobacterium* ribosomes [235,240]. Ribosomes may also contain species-specific protein paralogs, for example *S. aureus* which contains only the type B paralog of bL31 [168].

However, variation can also be more subtle, e.g. minor changes in protein and rRNA folds, insertions, deletions and chemical modifications [239,241,242]. For example, helix h26 of the 16S rRNA, which interacts with the Shine-Dalgarno helix, varies slightly in length between ribosomes from *T. thermophilus*, *E. coli*, *B. subtilis*, and *S. aureus*. Such variation could lead to species-specific involvement of h26 in translation initiation [168]. A species-specific protein difference is exhibited by the N-terminus of ribosomal protein bL27, likely involved in peptidyl transfer [243], which takes up different conformations in ribosomes from *S. aureus* and *T. thermophilus* [239]. In detail, the bL27 N-terminus in *S. aureus* is cleaved from position 9 during ribosome assembly [244], whereas in *T. thermophilus* it is long enough to reach the PTC and interact with the 3’ end of A-site and P-site tRNA [12]. Functional differences between ribosomes have even been found to arise from single amino acid differences, as seen in uL22, which lines the NPET and leads to species-specific stalling during the translation of the MifM leader peptide in *Bacillus subtilis* but not *E. coli* [230]. Even variations between ribosomes from different strains of the same species can have a significant functional impact, as seen for a strain of *P. aeruginosa* with a mutation in ribosomal protein uL6 that leads to structural changes resulting in aminoglycoside resistance and ribosome instability [236].

Furthermore, there are some examples of the same antibiotic binding in different ways to ribosomes from different species of bacteria [245]. For instance, chloramphenicol binds to the 50S subunit of *T. thermophilus* and *E. coli* ribosomes at the PTC so that its nitrobenzene moiety interferes with A-site tRNA positioning [73], but in a *D. radiodurans* chloramphenicol-ribosome structure, the chloramphenicol molecule is flipped compared to these other structures; and the nitrobenzene moiety is twisted by 90º, which would render it unable to make the same interactions with the ribosome [226]. However, it should be noted that this different orientation could be attributable to incorrect interpretation of poor density in the *D. radiodurans* structure [73]. Another example is the binding site of a 14-membered ring macrolide troleandomycin, which is located deeper in the NPET of *D. radiodurans* compared with the macrolide binding site in other bacterial species [73,74]. Binding of troleandomycin to this different site has been suggested to flip the tip of the uL22 into the NPET lumen to play a role in translational stalling [246].

If small differences between bacterial species can indeed affect drug binding, then determining the structures of ribosomes from a range of pathogenic bacteria could play an important role in the rational design of new antibiotics.

3.1.4 Project aims

Since ribosomes from different bacterial species vary in structure, and antibiotics might bind to them in different ways, solving more structures of ribosomes and drug-ribosome complexes from pathogenic bacteria may contribute toward a greater understanding of species-specific features of translation, and provide a platform for the rational redesign of existing antibiotics and development of new ones. Furthermore, if drugs that target specific pathogens can be developed, they might avoid the harmful side effects that can arise from disturbance of the gut microbiota by broad spectrum antibiotic therapy [247].

Specifically, the aim of this work is to solve high resolution cryo-EM structures of ribosomes from the ESKAPE pathogen *A. baumannii*, in complex with the antibiotics amikacin and tigecycline, both of which are used in the clinic to treat infections caused by this bacteria. These will be compared with ribosomes from other bacteria to identify unique structural features, which could potentially be exploited in antibiotic design. The interactions of amikacin and tigecycline with the *A. baumannii* ribosome will be analysed in molecular detail to provide a platform for rational drug modification, with a focus on binding modes unique to this ribosome. Collectively, these structures may pave the way towards development of antibiotics effective at tackling increasingly drug-resistant *A. baumannii* infections.

3.2 Results

3.2.1 Purification of tightly coupled 70S ribosomes from *A. baumannii*

Ribosomes were extracted from *A. baumannii* Type strain ATCC 19606. To ensure high yields of undegraded ribosome, the cells were harvested at early-mid log phase, before translation starts to slow [248]. To ascertain the OD_{600} of cell culture corresponding to early-mid log phase, growth curves of this strain cultured in LB at 37ºC were first generated. An OD_{600} of ~0.5 was found to represent this stage in cell growth.

After reaching an OD_{600} of ~0.5, the cells were pelleted, frozen, thawed and lysed by cell disruption. The lysate was clarified by centrifugation before being pelleted through a sucrose cushion to isolate tightly coupled ribosomes. To purify these further, the ribosome pellet was resuspended and spun through a 10-40% w/v sucrose density gradient. The sedimentation profile was assessed by measuring absorbance at 260 nm to reveal peaks in the parts of the gradient containing RNA, and therefore ribosomes. This revealed a dominant peak about two-thirds down the gradient, flanked by smaller peaks (Figure 14A). Since this purification was carried out in buffers with high magnesium concentration throughout to promote ribosome subunit association [249], the dominant peak was assumed to contain 70S ribosomes, with the lower density fractions (left of the dominant peak in Figure 14A) likely corresponding to ribosome subunits and the higher density fractions (right of the dominant peak in Figure 14A) likely polysomes or cellular debris that was not removed in the earlier purification steps. Fractions corresponding to the dominant peak were collected and dialysed into storage buffer to remove sucrose. The sample was then visualised on an RNA agarose gel, which showed intact bands at masses expected for 23S rRNA and 16S rRNA when compared with a total RNA reference (Figure 14B). Negative stain TEM was also used to visualise the purification product, revealing a pure and largely homogenous sample of predominantly 70S ribosomes (Figure 14C).

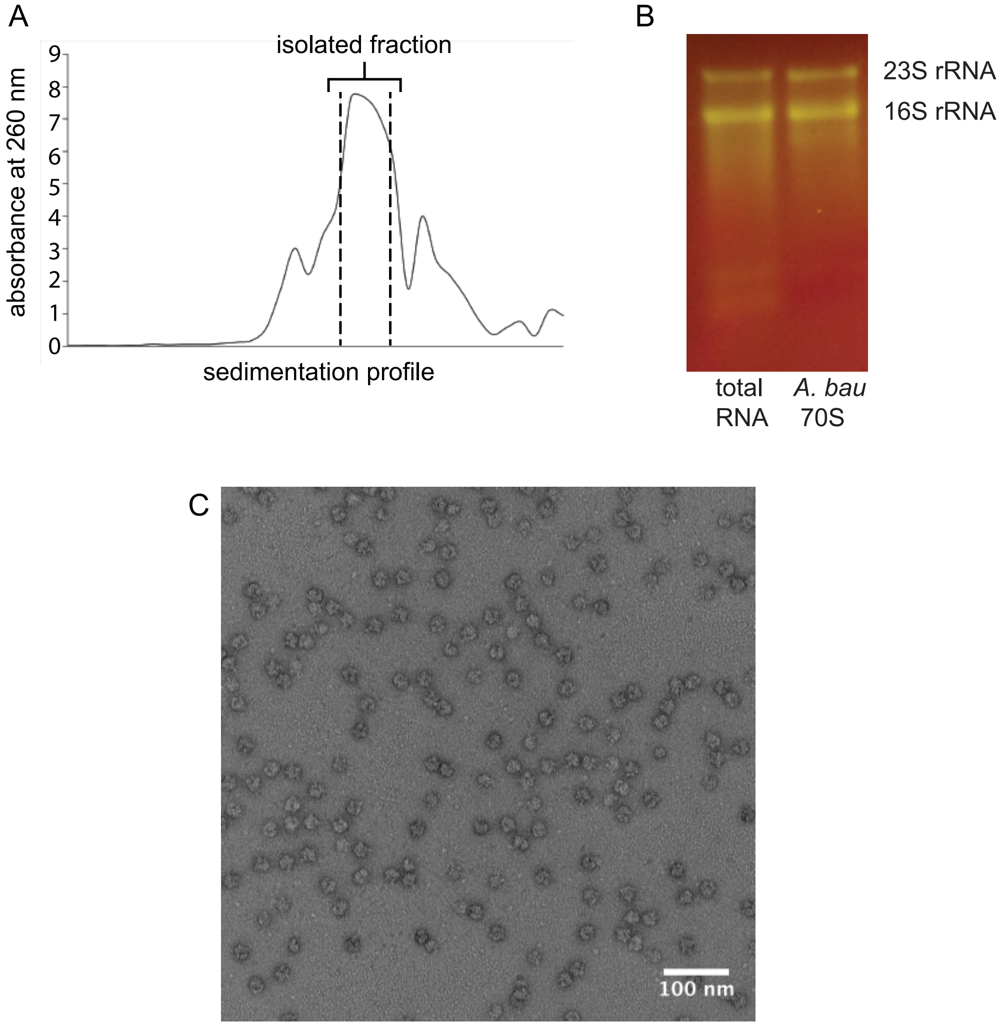

Figure 14 Characterisation of *A. baumannii* 70S ribosome sample. A) Sucrose gradient A_{260} sedimentation profile, showing the peak where fractions were collected. B) RNA agarose gel of the sample compared with total RNA standard, showing clear 23S rRNA and 16S rRNA bands. C) Representative negative stain TEM micrograph of purified sample, showing a pure and homogenous 70S ribosome sample.

3.2.2 Cryo-EM image processing of amikacin- and tigecycline-bound ribosome complexes

Purified *A. baumannii* 70S ribosomes were incubated with either amikacin (100 µM drug with 120 nm ribosome) or tigecycline (71.7 µM drug with 240 nm ribosome), applied to Quantifoil grids with a 2 nm carbon overlay, and plunge-frozen in liquid ethane. Visual inspection of these grids by cryo-EM confirmed the presence of predominantly intact 70S ribosomes which were uniformly dispersed across the grid holes to allow large numbers of particles per micrograph (Figure 15A-B).

554 micrograph movies of the amikacin-ribosome sample were recorded, from which 85,863 particles were extracted. These were aligned and classified in 2D, yielding mostly 70S ribosome classes, along with some 50S subunit classes (Figure 15A). The particles contributing to the most highly populated 70S classes which contained high resolution features were selected, and the rest discarded as junk. A similar approach using 3D classification was used to further cull junk particles, leaving 51,958 particles which were aligned and refined in 3D. Postprocessing steps were performed, including Bayesian polishing, CTF refinement, solvent masking and map sharpening, yielding a final reconstruction resolved to 2.8 Å (Figure 15C-D).

6228 micrograph movies of the tigecycline-ribosome sample were recorded, from which 1.68 million particles were extracted. These were aligned and classified in 2D, again yielding a mainly 70S ribosome classes with some 50S subunit classes (Figure 15B). Similarly to the amikacin-ribosome dataset, rounds of 2D classification and 3D classification were performed to remove 50S and junk particles, leaving 924,636 particles. Since ribosome particles require large box sizes, refinement of 3D angular assignments for the whole dataset was too computationally expensive, therefore only a quarter of the dataset was taken forwards (231,159 particles). These were aligned and refined in 3D, and Bayesian polishing, CTF refinement, solvent masking and map sharpening were performed, yielding a final reconstruction resolved to 2.6 Å (Figure 15E-F).

The local resolution of the reconstructions ranged from ~2.3 Å in the core of the 50S subunit to >6 Å in the flexible peripheral regions of the ribosome (Figure 15C&E). In both reconstructions, image alignment was dominated by the larger 50S subunit, leaving the smaller 30S subunit, particularly its head, poorly resolved due to movements in the ribosome necessary to facilitate the translocation of a tRNA-mRNA complex. These include intersubunit rotation between the 50S and the 30S subunits [250] and 30S head swivelling [5]. Interestingly, the quality of the 30S subunit density, especially the 30S head density, was particularly poor in the amikacin-ribosome complex (Figure 15C). Presumably, this was because intersubunit rotation and 30S head swivelling occurred more freely in this complex compared with the tigecycline-ribosome complex, as discussed below (Figure 15E).

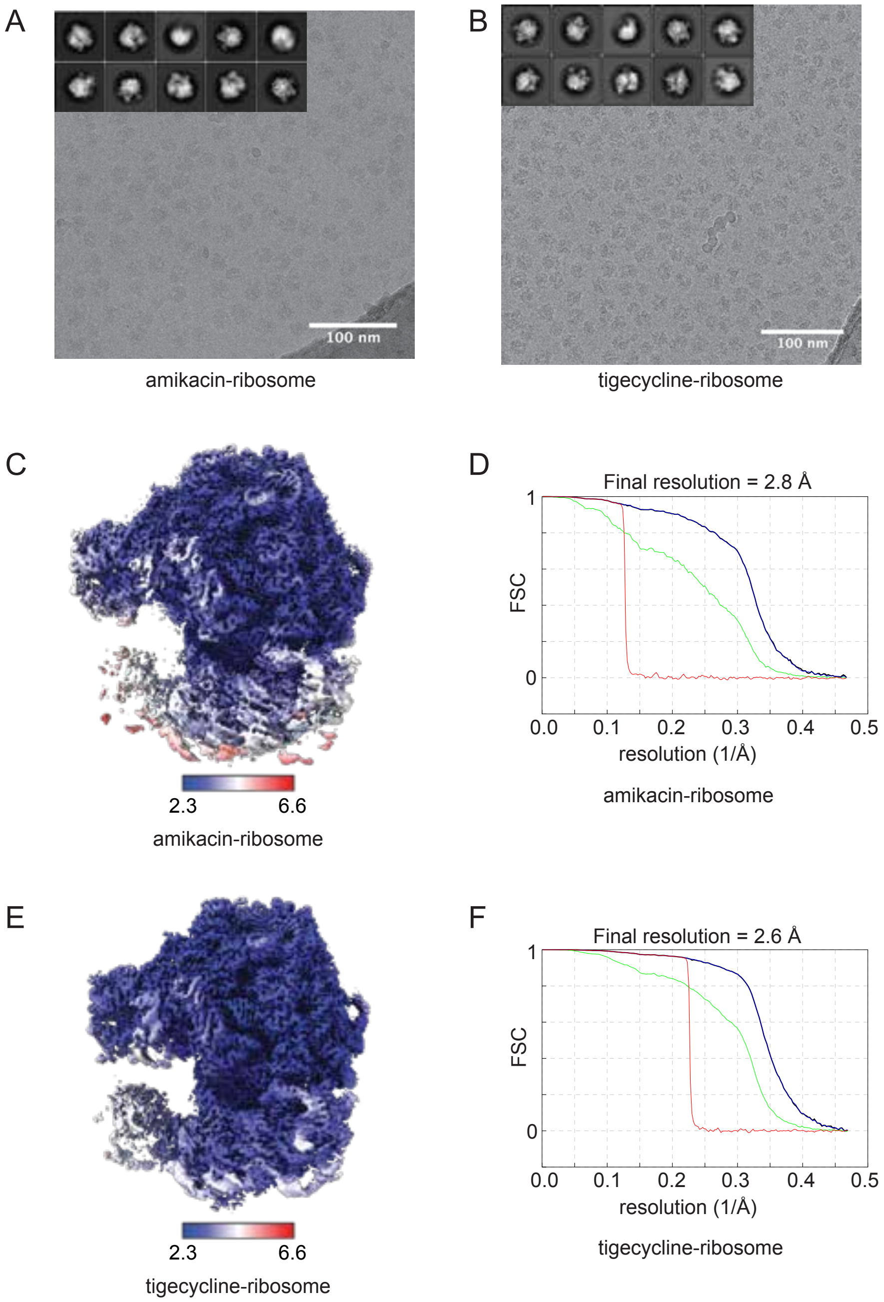

Figure 15 Cryo-EM image processing of drug-ribosome complexes. A) Representative cryo-EM micrograph of the *A. baumannii* ribosome-amikacin sample, scale bar 100nm. Inset: most populated classes after 2D alignment and classification. B) Representative cryo-EM micrograph of the *A. baumannii* ribosome-tigecycline sample, scale bar 100nm. Inset: most populated classes after 2D alignment and classification. C) Sharpened cryo-EM reconstruction of the *A. baumannii* ribosome-amikacin structure, filtered by local resolution. D) FSC curves as a function of resolution for the amikacin-ribosome structure. The resolution that corresponds to an FSC coefficient of 0.143 is 2.8 Å. E) Sharpened cryo-EM reconstruction of the *A. baumannii* ribosome-tigecycline structure, filtered by local resolution. F) FSC curves as a function of resolution for the tigecycline-ribosome structure. The resolution that corresponds to an FSC coefficient of 0.143 is 2.6 Å. Maps coloured by local resolution, from 2.3 Å (blue) to 6.6 Å (red). FSC curves are shown for phase-randomised maps (red), unmasked maps (green), masked maps (blue), and masked maps after correction for mask convolution effects (black).

3.2.3 Multibody refinement to improve 30S subunit resolution and assess conformational heterogeneity

To improve the resolution of the 30S subunit in both maps, multibody refinement was performed using soft extended masks to define the 50S, 30S body and 30S head as independent rigid bodies (Figure 16A). This procedure uses iteratively-improved partial signal subtraction and focussed refinement to generate higher quality reconstructions for each body [162]. The resulting reconstructions were then subjected to solvent masking and map sharpening. This procedure yielded reconstructions for the 50S, 30S body and 30S head with nominal resolutions of 2.7, 2.9, and 3.0 Å for the amikacin-ribosome complex (Figure 16B,D-F) and 2.5, 2.7, and 3.0 Å for the tigecycline-ribosome complex (Figure 16C,G-I), respectively. The multibody refinement procedure vastly improved the density of the 30S head in the amikacin-ribosome structure, making it amenable to model building, but was less successful in improving the 30S head density of the tigecycline-ribosome structure. Note that padding in Fourier space was not performed in order to save computer memory, resulting in artefacts around the edge of the box, which are not masked out in maps filtered by local resolution within RELION. These artefacts were masked out along with solvent noise for model building and refinement.

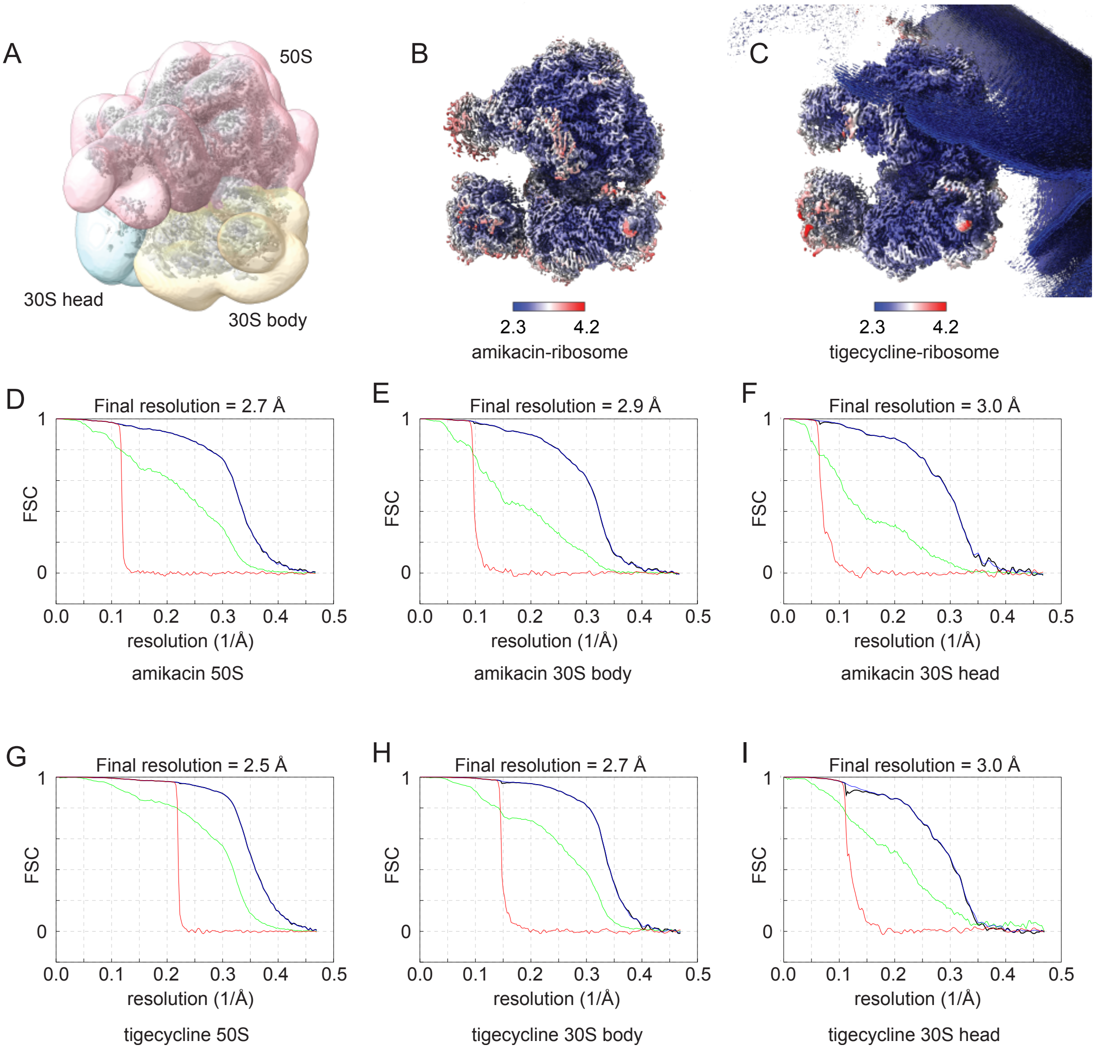

Figure 16 Multibody refinement of drug-ribosome reconstructions. A) Masks used to specify the 50S (pink), 30S body (brown) and 30S head (blue) rigid bodies, shown around the pre-multibody consensus reconstruction of the *A. baumannii* ribosome-amikacin complex (grey). B) Sharpened cryo-EM reconstructions of the three bodies comprising the amikacin-ribosome structure after multibody refinement, filtered by local resolution. C) Sharpened cryo-EM reconstructions of the three bodies comprising the tigecycline-ribosome structure after multibody refinement, filtered by local resolution. Maps coloured by local resolution, from 2.3 Å (blue) to 4.2 Å (red). Note that padding in Fourier space was not performed in order to save memory, resulting in artefacts around the edge of the box. This noise was masked out before undertaking model building and refinement. D-F) FSC curves as a function of resolution for the amikacin-ribosome multibody reconstructions. G-I) FSC curves as a function of resolution for the tigecycline-ribosome multibody reconstructions. FSC curves are shown for phase-randomised maps (red), unmasked maps (green), masked maps (blue), and masked maps after correction for mask convolution effects (black).

The 30S head reconstruction of the tigecycline-ribosome structure contained significantly more density outside the expected region compared with the equivalent reconstruction of the amikacin-ribosome structure (Figure 17A&B), suggesting that the particle subtraction and focused refinement steps within the multibody refinement procedure were less effective. Furthermore, despite similar FSC-derived resolution estimates for the 30S head reconstruction in the two structures, the masked and sharpened 30S head map of the tigecycline-ribosome structure was visually poorer than the corresponding map from the amikacin-ribosome complex, with protein side-chain and RNA base density less consistently resolvable across the map (Figure 17C-D), no matter the sharpening B factor used. The comparatively small improvement in the tigecycline-ribosome reconstruction on multibody refinement could not be rectified, despite trying a number of different masks to define the rigid-body boundaries as well as different standard deviation values to describe rotational and translational priors for each of the bodies.

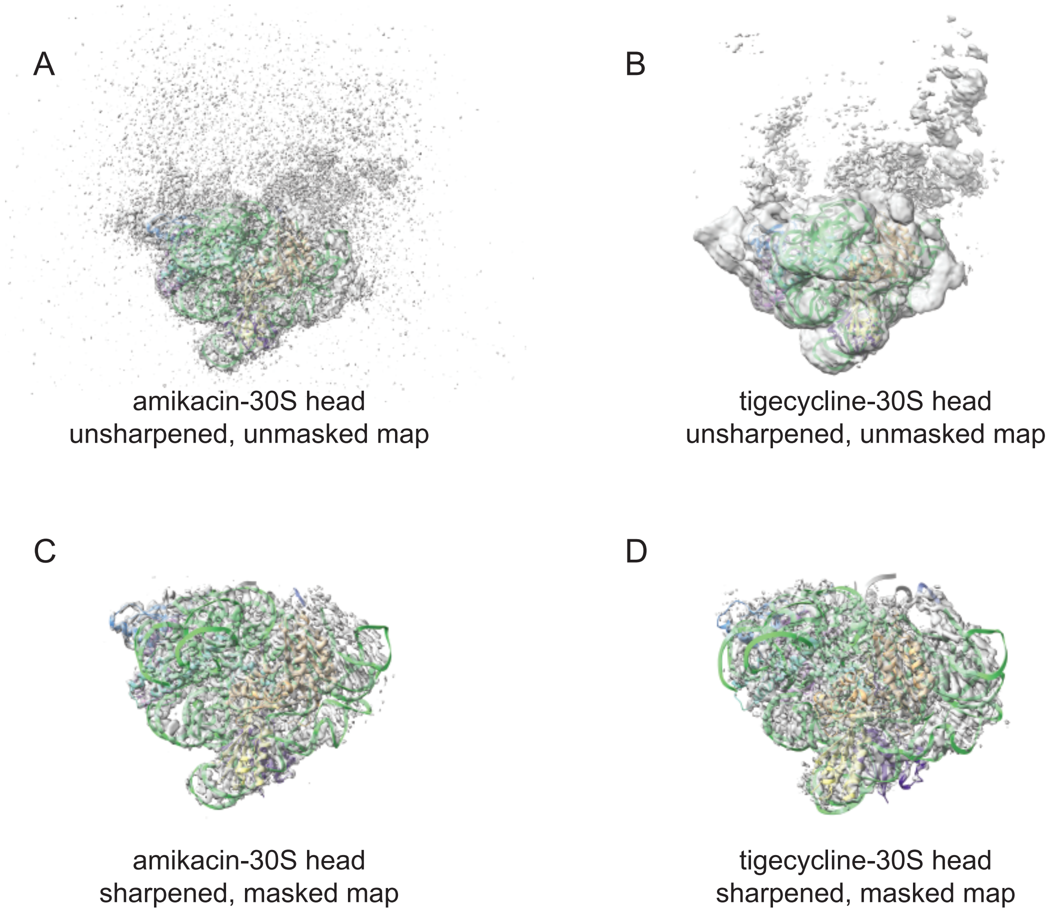

Figure 17 Comparison of the 30S head EM reconstructions of the *A. baumannii* ribosome-amikacin and *A. baumannii* ribosome-tigecycline complexes. A) Atomic model and cryo-EM density of the 30S head of the amikacin-ribosome complex. B) Atomic model and cryo-EM density of the 30S head of the tigecycline-ribosome complex. Semi-transparent grey densities correspond to the unsharpened and unmasked outputs of multibody refinement. C) Atomic model and cryo-EM density of the 30S head of the amikacin-ribosome complex. D) Atomic model and cryo-EM density of the 30S head of the tigecycline-ribosome complex. Semi-transparent grey densities correspond to the sharpened and solvent masked maps after post-processing of the multibody refinement outputs.

The reason for the larger improvement in the 30S head in the amikacin-ribosome reconstruction compared with the 30S head in the tigecycline-ribosome reconstruction is unclear. One possible reason is that tigecycline locks the 30S head to the 30S body in a way similar to that of spectinomycin [68], reducing 30S head rotation, and thus improvement from multibody refinement would be expected to be less significant than if the 30S head were rotating more freely, since the density would be better to start with. Such tigecycline-induced locking of the 30S head is plausible, considering that the primary tigecycline binding site is at the interface of the 30S head and body [55]. Indeed, the 30S head density is more complete in the tigecycline-ribosome pre-multibody refinement reconstruction than in the corresponding amikacin-ribosome reconstruction (Figure 15C&E), a phenomenon that could be explained by reduced 30S head swivelling when tigecycline is bound. Furthermore, principal component analysis of the multibody refinement procedure reveals that the largest contribution to the conformational variety in the data for the tigecycline-bound ribosome (28% of total variation) is 50S-30S intersubunit rotation (Figure 18B), whereas the largest contribution to the conformational variety in the amikacin-bound ribosome dataset (27% of total variation) is a combination of 30S head rotation and intersubunit rotation (Figure 18A). However, it should be noted that if the multibody refinement image analysis procedure simply did not work as well for the tigecycline-ribosome complex (perhaps due to non-optimum processing parameters or poorer quality data), then it might follow that results from principal component analysis are less reliable.

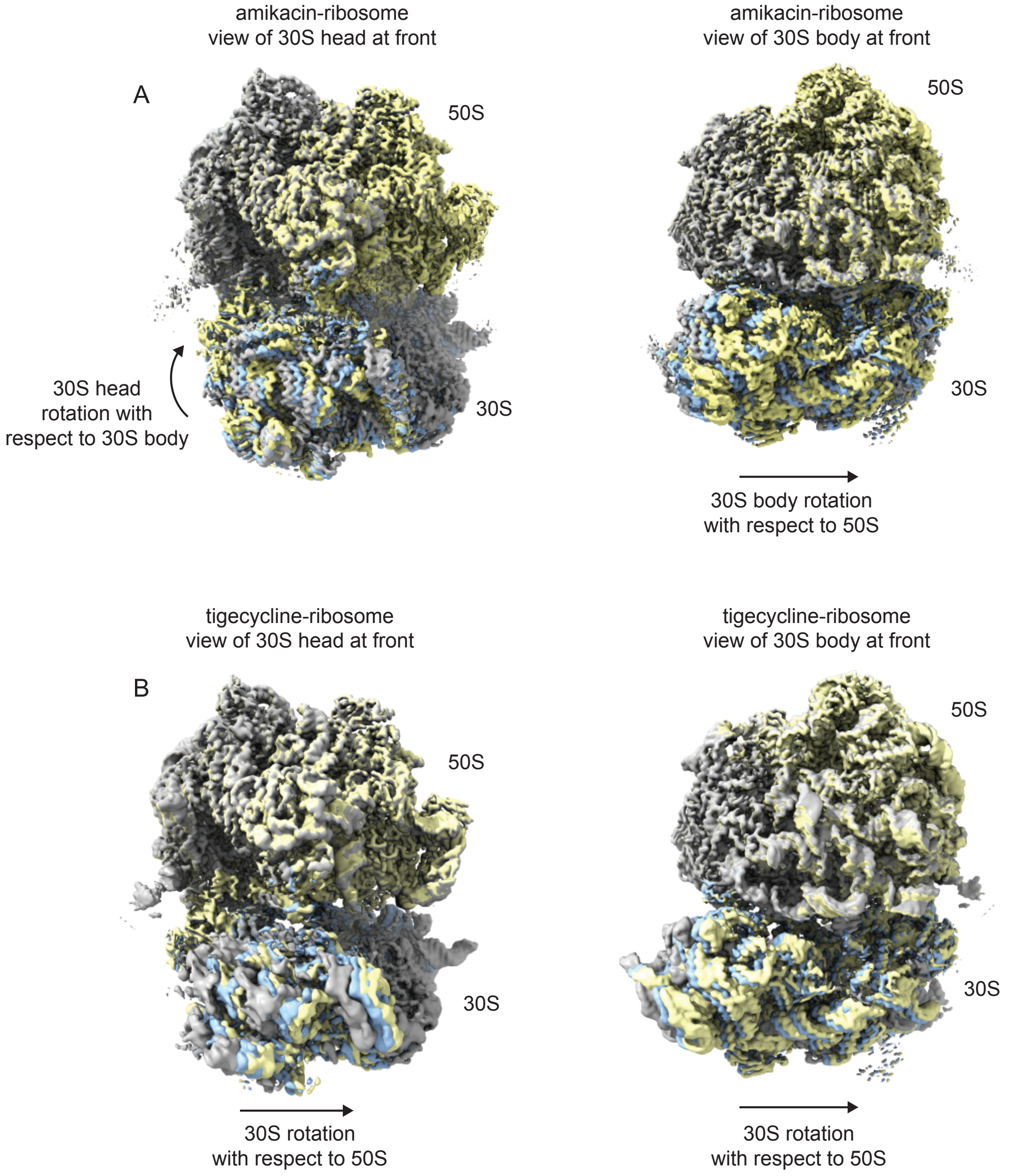

Figure 18 Comparison of the components contributing the largest variations to the data for the *A. baumannii* ribosome-amikacin and ribosome-tigecycline complexes. A) The principle component describing 27% of the variation in the data for the amikacin-ribosome complex. Movement is described along a trajectory from grey to blue to yellow cryo-EM density. This component describes a rotation of the 30S head as well as intersubunit rotation between the 50S and 30S body. B) The principle component describing 28% of the variation in the data for the tigecycline-ribosome complex. Movement is described along a trajectory from grey to blue to yellow EM density. This component describes predominantly intersubunit rotation between the 50S and 30S.

3.2.4 Structure of the *A. baumannii* 70S ribosome

Homology models based on experimental structures of *E. coli* ribosomal proteins and rRNA from PDB 5MDZ [171] were fitted and refined into the sharpened *A. baumannii* antibiotic-ribosome cryo-EM multibody reconstructions. In all three amikacin-ribosome multibody reconstructions and the tigecycline-ribosome 50S and 30S body multibody reconstructions, regions of protein where side chains could not be resolved were modelled with truncated side chains, and regions where the protein or rRNA backbone could not be traced were removed from the model. The tigecycline-ribosome 30S head reconstruction was of slightly poorer quality than the other maps and so such highly stringent trimming of the model was not carried out. Instead, the full amikacin-ribosome 30S head model was predicted to be a good approximation for the tigecycline-ribosome 30S head and hence was used as a starting model with no further deletion of backbone or side chains throughout model refinement.

The overall structure comprises a large 50S subunit, composed of 23S rRNA, 5S rRNA, and 28 resolved ribosomal proteins, and a small 30S subunit composed of 16S rRNA and 20 resolved ribosomal proteins. These constituent parts form the recognizable structural elements of the ribosome, including the central protuberance, L1 stalk, and L12 stalk of the 50S subunit, and the head, body, platform, shoulder, and spur of the 30S subunit (Figure 19). At this resolution (2.8 Å), most rRNA nucleobases (Figure 19A&D) and protein side chains (Figure 19B&C) can be distinguished in both subunits.

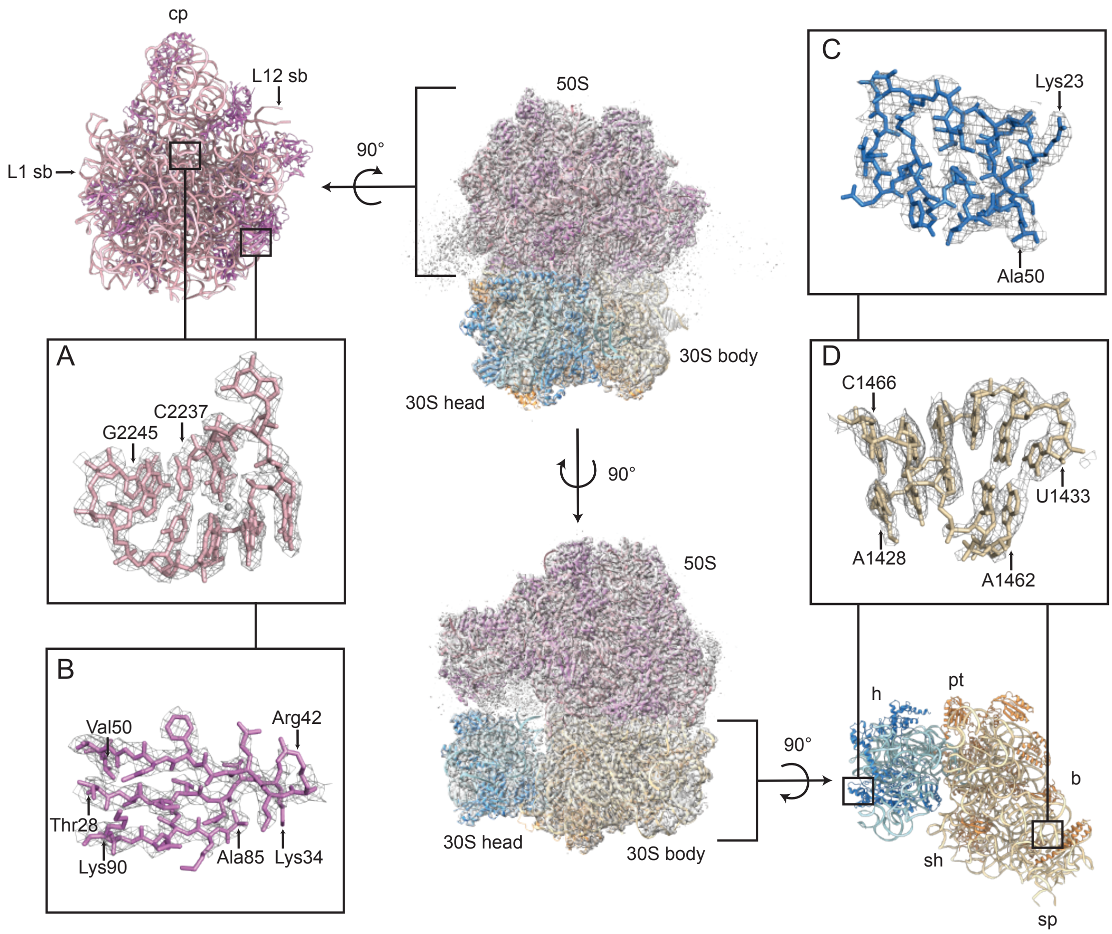

Figure 19 Structure of the 70S ribosome from *A. baumannii*. Centre: two views of the *A. baumannii* ribosome-amikacin complex with atomic models of the 50S (rRNAs light pink, proteins dark pink), 30S body (rRNA light brown, proteins dark brown) and 30S head (rRNA light blue, proteins dark blue), and corresponding cryo-EM densities (grey volume). These three models were refined separately in the three multibody reconstructions (after sharpening and masking), and the models and maps are superimposed. Top left: atomic model of the 50S subunit showing key structural elements (cp, central protuberance; L1 sb, L1 stalk base; L12 sb, L12 stalk base). Bottom right: atomic model of the 30S subunit showing key structural elements (h, head; pt, platform; b, body; sp, spur; sh, shoulder). A) Cryo-EM density (grey mesh) and atomic model of the 23S rRNA P loop C2237–G2245. B) Cryo-EM density (grey mesh) and atomic model of a β sheet in protein bL19: Thr28–Lys34, Arg42–Val50, Ala85–Lys90. C) Cryo-EM density (grey mesh) and atomic model of a helix-turn-helix in protein uS14: Lys23–Ala50. D) Cryo-EM density (grey mesh) and atomic model of part of the 16S rRNA helix h44: A1428–U1433, A1462–C1466.

Most rRNA residues were modelled, with missing regions mostly belonging to the flexible stalks of the 50S subunit, which had poorly resolved density, as has been seen previously in other ribosome cryo-EM reconstructions. Of the 54 known core ribosomal proteins, 41 were modelled with side chains included, 7 had ambiguous or poor side-chain density and were modelled, at least in part, without side chains, and 6 were not modelled (Table 3). These unmodeled proteins are known to be located in flexible parts of the ribosome (uL1, bL9, uL10, uL11, and bL12), or to be loosely associated (bS1), and all had weak or nonexistent density. Density corresponding to protein bL31, which bridges the two subunits, was resolved only in the tigecycline-ribosome reconstruction.

rRNA chains

chain ID	rRNA name	GenBank accession number	locus tag	modelled residues	corresponding EM map
1	23S	KL810966	DJ41_1033	2-868; 891-1034; 1101-1511; 1535-1712; 1726-2086; 2181-2891	50S
2	16S 5’	KL810966	DJ41_1036	3-77; 90-199; 210-837; 843-923	30S body
3	16S central	KL810966	DJ41_1036	924-1022; 1031-1384	30S head
4	16S 3’	KL810966	DJ41_1036	1385-1530	30S body
5	5S	KL810966	DJ41_1032	2-116	50S

protein chains

chain ID	protein name	UniProt accession number	full size (residues)	modelled residues	corresponding EM map	notes
A	uL2	D0CD00	274	2-273	50S	
B	uL3	D0CCZ7	212	2-212	50S	
C	uL4	D0CCZ8	200	2-200 (2-12 no side chains)	50S	
D	uL5	D0CD09	178	(2-177 no side chains)	50S	
E	uL6	D0CD12	177	2-176	50S	
F	uL13	D0CG35	142	1-142	50S	
G	uL14	D0CD07	122	1-122	50S	

H	uL15	D0CD16	146	2-145	50S	
I	uL16	D0CD04	137	1-137	50S	
J	bL17	D0CD23	125	1-119	50S	
K	uL18	D0CD13	116	2-116	50S	
L	bL19	D0CCR8	122	2-118	50S	
M	bL20	D0CA76	119	2-118	50S	
N	bL21	D0CDQ6	103	1-103	50S	
O	uL22	D0CD02	110	2-110	50S	
P	uL23	D0CCZ9	106	1-92	50S	
Q	uL24	D0CD08	105	2-103	50S	
R	bL25	D0C9L7	98	3-98	50S	
S	bL27	D0CDQ7	85	9-84	50S	
T	bL28	D0CAL0	78	2-78	50S	
U	uL29	D0CD05	65	2-62	50S	
V	uL30	D0CD15	58	1-57	50S	
W	bL31	D0CBZ8	74	(1-43 no side chains)	50S	tigecycline model only
X	bL32	D0C9K5	61	2-55	50S	

Y	bL33	D0CAL1	51	1-51	50S	
Z	bL34	D0CG06	44	1-44	50S	
a	bL35	D0CA77	64	2-64	50S	
b	bL36	D0CD18	38	1-38	50S	
c	uS2	D0CC74	250	(8-226 no side chains)	30S body	
d	uS3	D0CD03	250	2-211	30S head	
e	uS4	D0CD21	208	2-208 (23-30; 43-51 no side chains)	30S body	
f	uS5	D0CD14	165	10-164	30S body	
g	bS6	D0C5Z0	127	1-103	30S body	
h	uS7	D0C9P7	156	3-70; 97-145 (126-145 no side chains)	30S head	
i	uS8	D0CD11	131	2-131	30S body	
j	uS9	D0CG36	128	2-128	30S head	
k	uS10	D0CCZ6	103	4-103	30S head	
l	uS11	D0CD20	128	15-128	30S body	
m	uS12	D0C9P6	124	2-123	30S body	
n	uS13	D0CD19	118	2-116	30S head	
o	uS14	D0CD10	101	2-101	30S head	

p	uS15	D0CAU9	89	2-89	30S body	
q	bS16	D0CCR5	83	1-80	30S body	
r	uS17	D0CD06	85	5-83	30S body	
s	bS18	D0C5Y9	75	21-73	30S body	
t	uS19	D0CD01	91	2-84	30S head	
u	bS20	D0C7N1	88	2-87	30S body	
v	bS21	D0C5Q3	71	2-61 (2-36 no side chains)	30S body	

other chains

chain ID	name	corresponding EM map	notes
6	tRNA 5’	50S	residues 2-6 from PDB 5AFI E-site fMet-tRNA, probably actually a mixture of tRNAs
7	tRNA central	30S head	residues 26-45 from PDB 5AFI E-site fMet-tRNA, probably actually a mixture of tRNAs
8	tRNA 3’	50S	residues 69-76 from PDB 5AFI E-site fMet-tRNA, probably actually a mixture of tRNAs
9	mRNA	30S head	4 nucleotide polyU mRNA model, probably actually a mixture of mRNAs

unmodelled proteins	
uL1	uL11
bL9	bL12
uL10	bS1

Table 3 ***A. baumannii*** **70S ribosome atomic model details.**

Weak density was seen in the E-site corresponding to tRNA (modelled as “E-site tRNA,” derived from the E-site fMet-tRNA from PDB 5AFI [175]) (Figure 20). Only the regions near the 50S and 30S subunits which had resolved nucleotide density were retained. The density was not sufficiently well resolved to enable identification of a specific *A. baumannii* tRNA molecule, but the density likely corresponds to a mixture of different tRNAs that remained associated with subpopulations of ribosomes throughout the purification procedure. Density corresponding to a short mRNA at the E-site was also resolved, and this was modelled as a short polyuridine chain (Figure 20C).

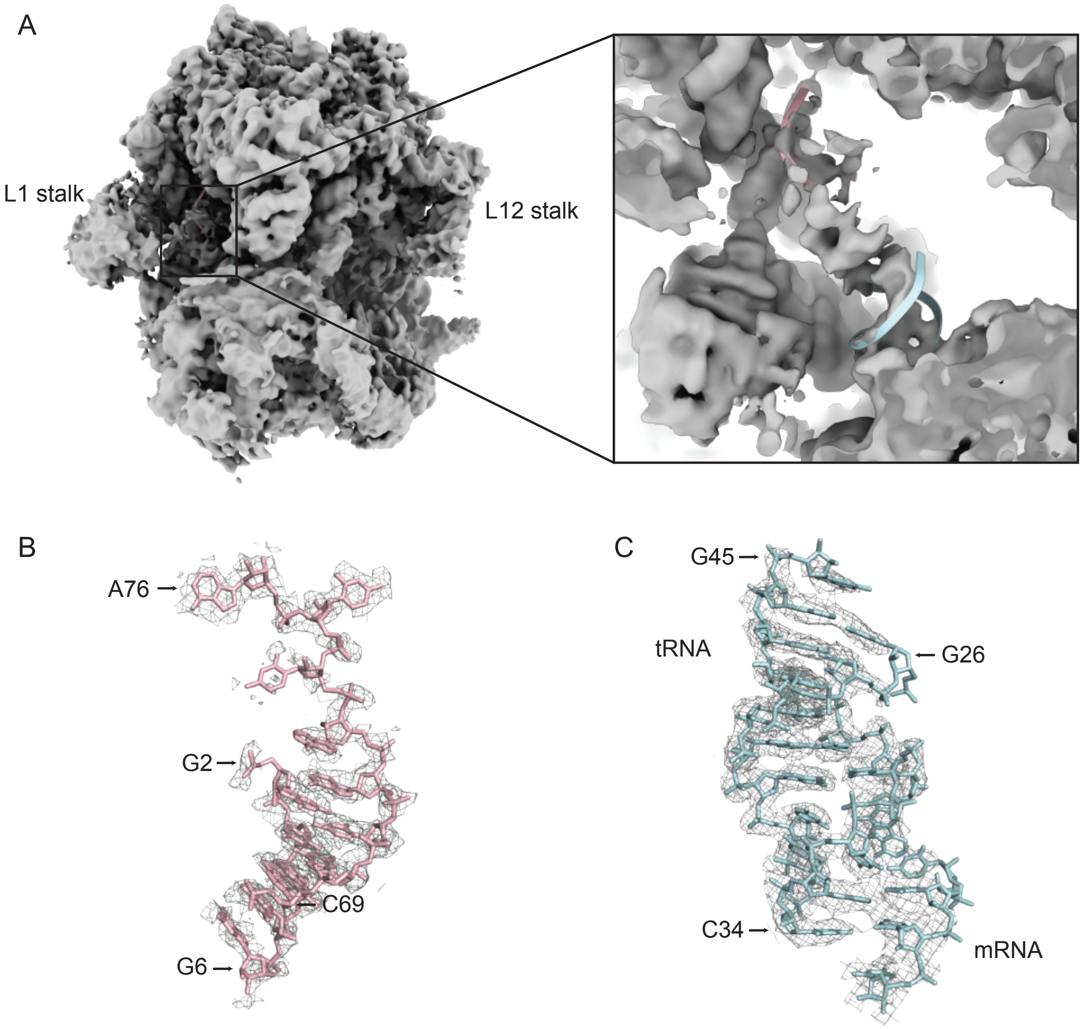

Figure 20 Cryo-EM density and atomic model of E-site tRNA and mRNA. A) Unsharpened consensus reconstruction of the amikacin-ribosome complex lowpass filtered to 5 Å. Weak cryo-EM density is seen in the E-site of the ribosome that can be fitted with tRNA and mRNA (ribbon). B) Atomic model of the 5' and 3' ends of E-site tRNA (light pink), derived from an *E. coli* fMet-tRNA starting model and fitted and refined into the sharpened 50S multibody reconstruction (grey mesh). C) Atomic model of the anticodon stem-loop of the E-site tRNA, derived from an *E. coli* fMet-tRNA starting model, and a short polyuridine mRNA (light blue), fitted and refined into the sharpened 30S head multibody reconstruction (grey mesh).

Throughout the process, the models for the 50S, 30S body and 30S head were kept separate and refined independently into their corresponding maps, as this reflects the data from the multibody refinement procedure which generates independent reconstructions [162]. Model refinement and validation statistics are found in Table 4.

	amikacin-ribosome 50S	**amikacin-ribosome 30S body**	**amikacin-ribosome 30S head**	**tigecycline-ribosome 50S**	**tigecycline-ribosome 30S body**	**tigecycline-ribosome 30S head**
Map resolution (Å) (FSC = 0.143)	2.7	2.9	3.0	2.5	2.7	3.0
Map sharpening B-factor ($Å^2$)	-47.3	-55.7	-51.6	-82.5	-99.3	-131.4
Model composition						
Non-hydrogen atoms	83514	33322	16864	83855	33279	16906
Protein residues	3069	1496	852	3112	1496	852
Nucleic acid residues	2800	1040	477	2800	1040	477
Metal ions	161	59	24	163	56	24
Ligand	none	amikacin	none	tigecycline x3	none	tigecycline
General validation						
CC[a] (model to map fit)	0.86	0.83	0.86	0.86	0.84	0.70
Clashscore	4.84	7.09	5.25	5.86	9.42	15.11
R.m.s. deviations						
Bond lengths (Å)	0.007	0.012	0.007	0.008	0.010	0.007
Bond angles (°)	0.775	0.974	0.702	0.730	0.794	0.853
Protein geometry validation						
Rotamer outliers (%)	7.08	11.02	7.15	5.70	8.22	11.24
Ramachandran outliers (%)	0.03	0.20	0.00	0.07	0.00	0.24
Ramachandran favoured (%)	94.46	90.54	92.58	95.42	91.90	91.03

RNA geometry validation[b]						
Sugar pucker outliers (%)	0.64	0.38	0.21	0.57	0.38	0.42
Backbone conformation outliers (%)	17.14	20.48	17.19	15.89	19.71	22.85

Table 4 Model refinement and validation statistics. Values obtained from Phenix refinement log unless otherwise stated. [a]CC, correlation coefficient. [b]Obtained from MolProbity web server

3.2.5 Unique structural features of the *A. baumannii* ribosome

Structural differences in bacterial ribosomes may be exploited to design drugs that have improved activity against specific pathogenic species. To identify unique structural features in the *A. baumannii* ribosome, the structure was compared with that of ribosomes from other bacteria, namely *E. coli* (PDB 4YBB and PDB 5MDZ) [171,232], *S. aureus* (PDB 5LI0) [168], and *T. thermophilus* (PDB 5E81) [251]. Insertions, deletions, and differences in the fold of all modelled ribosomal proteins and rRNA in the *A. baumannii* ribosome compared with *E. coli* were identified. Specifically, each ribosomal protein and rRNA chain of the *A. baumannii* ribosome-amikacin and ribosome-tigecycline atomic models were visually compared with the equivalent chain from *E. coli* ribosome models PDB 4YBB and PDB 5MDZ. Regions where the *A. baumannii* ribosome was structurally different to both *E. coli* models are defined as ‘unique structural features’ in this initial overview.

The overall architecture of the *A. baumannii* ribosome is broadly similar to that of other bacterial ribosomes; in particular, the regions around the PTC and DC are structurally conserved. Differences were mostly located on the solvent-facing portions of the subunits, as well as around the periphery of the subunit interface (Figure 21A&B). Table 5 lists these structural differences, detailing the type of difference (different fold, deletion, or insertion), and the scale of the difference. The table also describes the quality of the density of the *A. baumannii* amikacin-ribosome reconstruction in the regions where differences are identified to give a measure of confidence in each difference.

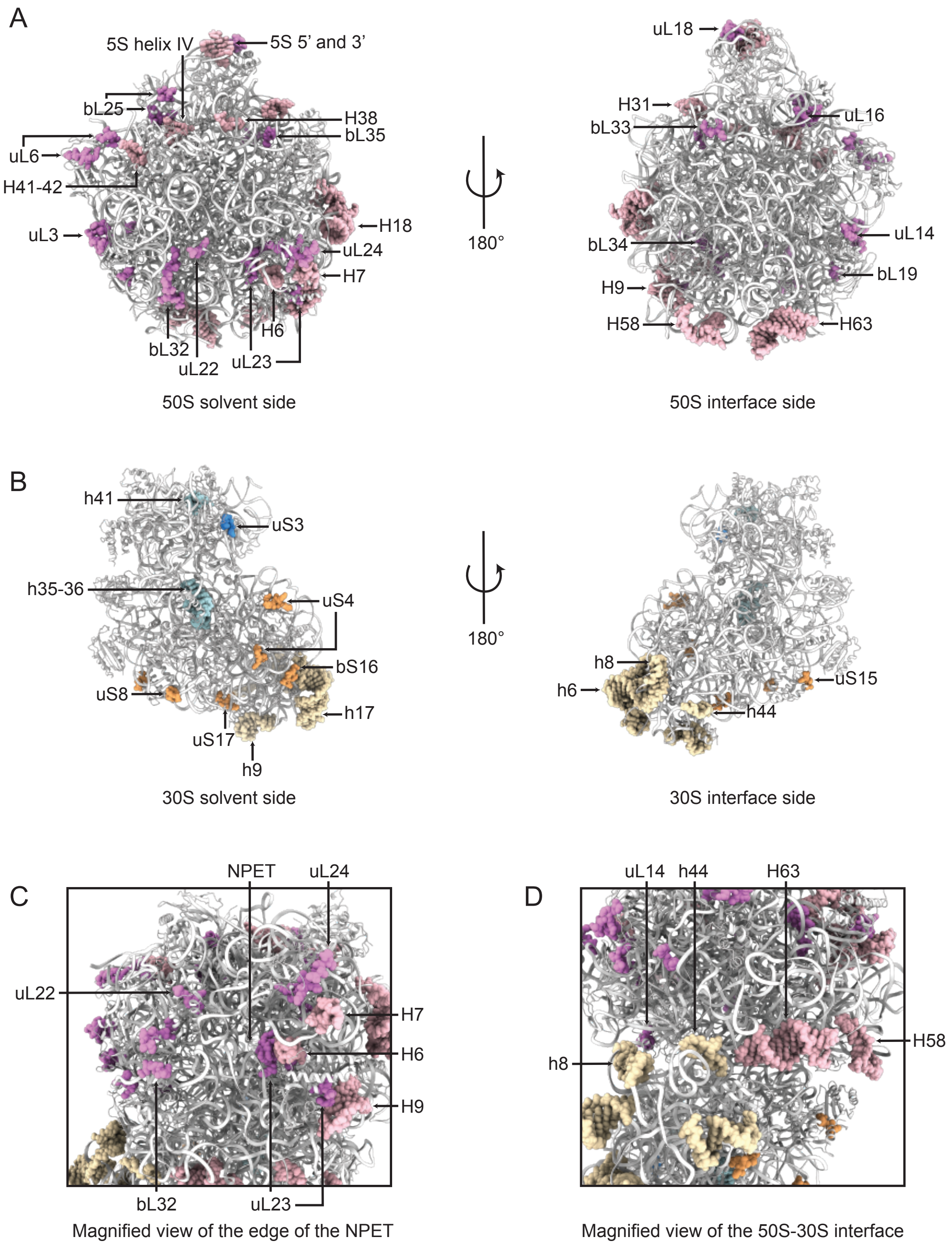

Figure 21 Unique structural features of the *A. baumannii* ribosome. Insertions, deletions, and differences in the fold of loops and secondary structures of the ribosomal proteins and rRNA in the *A. baumannii* ribosome compared with *E. coli* (PDB: 5MDZ and 4YBB). A) Two views of the atomic model of the 50S subunit (white cartoon), with unique features highlighted (rRNA light pink spheres, protein dark pink spheres). B) Two views of the atomic model of the 30S subunit (white cartoon), with unique features highlighted (30S body rRNA light brown spheres, protein dark brown spheres; 30S head rRNA light blue spheres, protein dark blue spheres). C) Magnified view of unique features around the edge of the NPET. D) Magnified view of unique features around the subunit interface. The structure of the *A. baumannii* ribosome-amikacin complex is shown here, but all highlighted differences hold true for the *A. baumannii* ribosome-tigecycline complex.

chain	***A. baumannii* residue number**	***E. coli* residue number**	**rRNA helix**	**details**	**scale of difference**	**quality of density**
			rRNAs			
23S	60-64	60-64	H6	different fold	minor	good
	99-105	99-105	H7	different fold	major	good
	135-147	135-147	H9	different fold	minor	fair
	263-284	263-289	H18	deletion	major	fair
	349-365	354-373	H18	deletion	major	good
	634-639	643-648	H31	different fold	minor	good
	921-925	930-935	H38	deletion	minor	good
	1130-1134	1140-1143	H41-42	insertion	minor	good
	1490-1503	1502-1514	H58	insertion	minor	fair
	1701-1738	1710-1749	H63	deletion	major	positions 1713-1725 not resolved
16S	70-98	68-102	h6	deletion	major	positions 78-89 not resolved
	153-165	157-169	h8	different fold	minor	fair
	175-189	179-193	h9	different fold	major	good
	447-479	451-482	h17	insertion	minor	fair
	1065-1081	1068-1084	h35-36	different fold	minor	good
	1252-1256	1255-1259	h41	different fold	minor	good
	1436-1440	1439-1443	h44	different fold	minor	fair
5S	5'- and 3'-ends	5'- and 3'-ends		shorter	minor	fair
	82-91	83-93	helix IV	deletion	major	good
			proteins			
uL3	85-96	84-93		insertion	major	good
	104-109	101-106		different fold	major	good
uL6	15-23	15-23		different fold	minor	fair

	54-60	54-60		different fold	major	fair
uL14	88-92	88-93		deletion	minor	good
uL16	20-24	20-23		insertion	minor	good
uL18	54-64	53-65		deletion	major	fair
bL19	N-terminus	N-terminus		extension	major	good
uL22	C-terminus	C-terminus		deletion	minor	good
uL23	N-terminus	N-terminus		deletion	minor	fair
	65-74	66-75		different fold	minor	good
uL24	N-terminus	N-terminus		deletion	minor	good
	27-31	28-33		deletion	minor	good
	C-terminus	C-terminus		extension	minor	fair
bL25	11-16	9-12		insertion	minor	good
	83-90	79-86		different fold	minor	good
bL32	23-33	23-34		deletion	major	good
	51-55	52-56		different fold	minor	good
bL33	N-terminus	N-terminus		deletion	major	good
bL34	C-terminus	C-terminus		deletion	major	good
bL35	17-21	17-22		deletion	minor	good
uS3	59-65	59-65		different fold	minor	good
uS4	31-37	31-36		insertion	major	fair
	82-88	80-86		different fold	minor	good
uS8	53-57	53-56		insertion	minor	good
uS15	N-terminus	N-terminus		different fold	minor	good
bS16	44-50	44-50		different fold	minor	good
uS17	N-terminus	N-terminus		different fold	minor	good

Table 5 Unique structural features of the *A. baumannii* ribosome.

Hotspots of structural differences were identified around the exit of the NPET on the solvent-exposed face of the 50S subunit, specifically in proteins uL22, uL23, uL24, and bL32, and in the 23S rRNA helices H6, H7, and H9 (Figure 21C). This site is where ribosome-associated factors dock, such as the molecular chaperone trigger factor [252], the signal recognition particle, and the Sec translocon [31]. For example, the 23S rRNA helix H6, situated near uL23 at the edge of the polypeptide tunnel exit, adopts a different fold in *A. baumannii* compared with *E. coli*, *S. aureus*, and *T. thermophilus* (Figure 22A). The fold of H6 is consistent across multiple *E. coli* structures, no matter the structural technique or ribosome buffer used (Figure 22B), so this difference can be attributed to species specificity with confidence. Note that the conformation of the nearby β-hairpin loop of uL23, although clearly different between the different species (Figure 22A), does not always maintain the same conformation in different *E. coli* structures (Figure 22B). This makes it more difficult to assign as a species-specific difference with as high a confidence as H6, as different buffer conditions or crystal contacts could be affecting the conformation of this β-hairpin loop in the *E. coli* structures.

Clusters of differences were also identified around the periphery of the subunit interface, specifically in the 23S rRNA helices H58 and H63, the 16S rRNA helices h8 and h44, and protein uL14 (Figure 21D). The consensus reconstruction (i.e. the cryo-EM map determined without using multibody refinement) was used to confirm the validity of the multibody models in these regions, because models fitted to multibody maps can be unreliable at the body interfaces [162]. H63 is shorter in *S. aureus* and *T. thermophilus* than in *E. coli* or *A. baumannii*, and takes up a slightly different conformation in *E. coli* compared with *A. baumannii* (Figure 22C). Contacts at the interface keep the ribosome intact and are important for the dynamic processes involved in translocation [253], and some antibiotics, such as neomycin and thermorubin, inhibit translation by perturbing these intersubunit bridges [57,62].

To confirm the validity of the unique structural features in H63 of *A. baumannii*, as well as the other identified features near the subunit interface, we compared these helices and proteins with those in *E. coli* ribosome structures exhibiting a range of 50S-30S rotation states: the two ribosome conformations in PDB 4YBB and the ribosome from PDB 5MDZ (Figure 22D). The conformations of these helices and proteins remained consistent across these three *E. coli* ribosome structures, and hence were all different from the corresponding conformations in the *A. baumannii* ribosome (Figure 22E shows this for H63). This strongly suggests that the unique structural features identified near the subunit interface truly are differences between *E. coli* and *A. baumannii* ribosomes, rather than arising from different functional states.

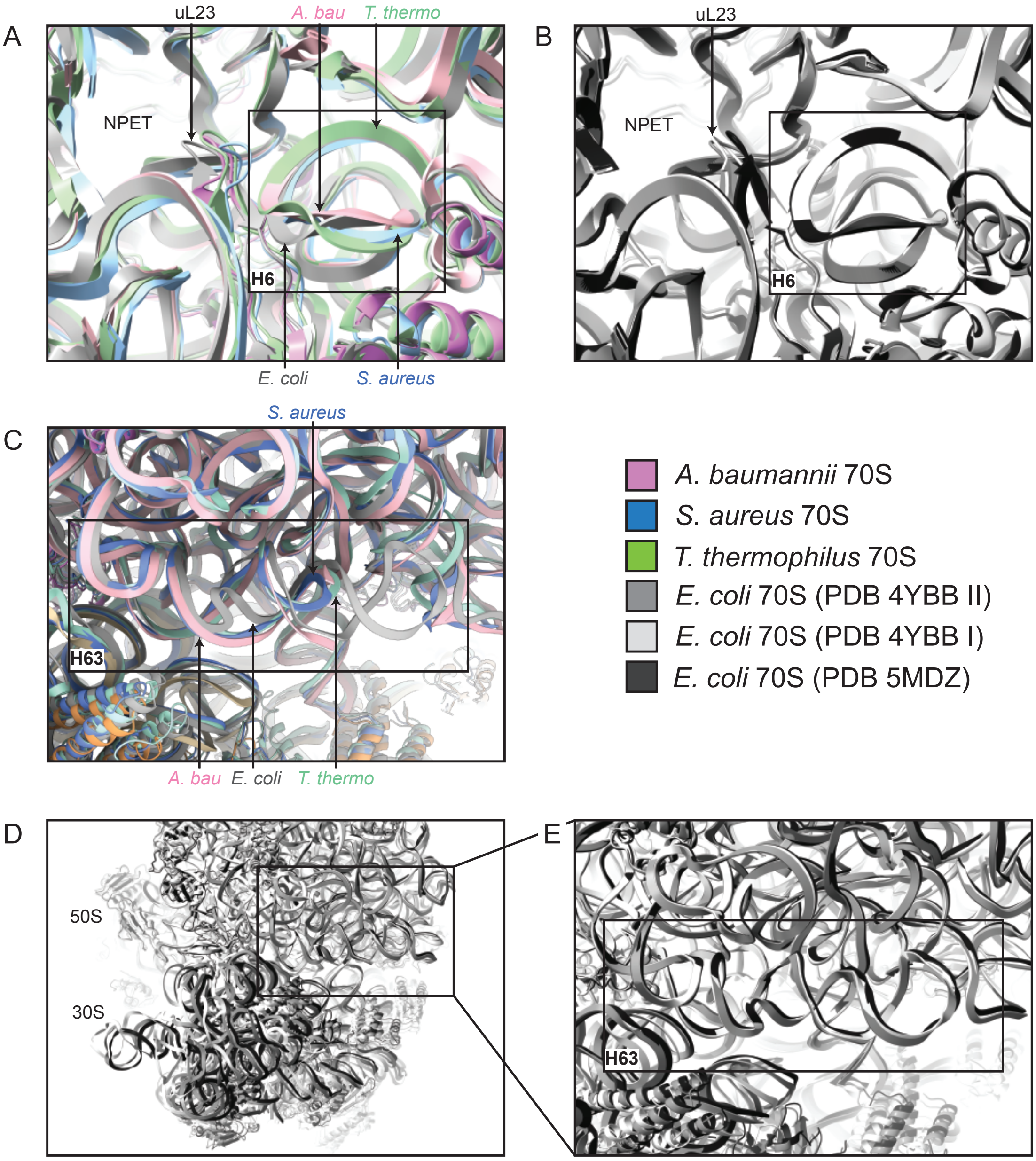

Figure 22 Unique structural features in the 23S rRNA helices H6 and H63. A) H6 of *A. baumannii* (pink) takes a different conformation to that of H6 of *E. coli* (grey, PDB 4YBB), *S. aureus* (blue, PDB 5LI0), and *T. thermophilus* (green, PDB 5E81). B) H6 maintains the same conformation across various *E. coli* ribosome structures, as shown here in a crystal structure (light grey, PDB 4YBB ribosome I; mid-grey, PDB 4YBB ribosome II) and a cryo-EM structure (dark grey, PDB: 5MDZ), unlike the nearby β-hairpin loop of uL23, which shows some variation. C) H63 of *A. baumannii* (pink) takes a different conformation to that of H63 of *E. coli* (grey, PDB 4YBB) and is longer than in *S. aureus* (blue, PDB 5LI0) and *T. thermophilus* (green, PDB 5E81). D) *E. coli* ribosome models aligned on their 23S rRNA chains, representing a range of rotation states of the 30S ribosomal subunit. Empty ribosome in an intermediate rotated state (light grey, PDB 4YBB ribosome I), empty ribosome in non-rotated state (mid-grey, PDB 4YBB ribosome II), and ribosome with A-site and P-site tRNA (dark grey, PDB 5MDZ). E) H63 in these three *E. coli* ribosome models. Despite the difference in intersubunit rotation states, the conformation of H63 remains similar across the three models. The structure of the *A. baumannii* ribosome-amikacin complex is used to represent the *A. baumannii* ribosome in this figure, but the structures of all highlighted regions hold true for the *A. baumannii* ribosome-tigecycline complex.

3.2.6 Structural comparison of ribosomes from two strains of *A. baumannii*

As discussed, ribosomes from different species of bacteria can contain different structural features. Intriguingly, even ribosomes from different strains of the same species can exhibit significant structural and functional variations, as described for *P. aeruginosa* above [236].

The structure of the ribosome from *A. baumannii* strain AB0057 was recently solved in empty and tRNA-bound states, and the authors identified three unique structural features of this ribosome [237]. First, H18 of *A. baumannii* AB0057 was significantly shorter than in other bacterial ribosomes, which was also the case in the model of the ribosome from *A. baumannii* ATCC 19606 presented here (Figure 23A). The authors also identified a conformational difference in H58 of *A. baumannii* AB0057, which forms a straight helix without bending to contact H54/H55 as it does in other ribosomes. However, although H58 of *A. baumannii* ATCC 19606 is longer and has a slightly different conformation compared with H58 of the *E. coli* ribosome, the helix still follows an overall similar path to form contacts with H54/H55 as *E. coli* H58 does (Figure 23B). Finally, the authors found that H69 of *A. baumannii* AB0057 bends toward the 50S subunit instead of forming intersubunit bridge B2a/d with h44 of the 30S subunit, much the same as seen in the structure of an aminoglycoside-resistant *P. aeruginosa* ribosome [236], and they suggested this could contribute toward low aminoglycoside susceptibility. However, strain AB0057 used in their study is reported to be susceptible to aminoglycosides amikacin and tobramycin [254], and in antibiotic-susceptible [255] *A. baumannii* ATCC 19606, H69 forms contacts with h44 as seen in other bacterial ribosomes (Figure 23C), suggesting a more complex relationship between the conformation of H69 and aminoglycoside resistance.

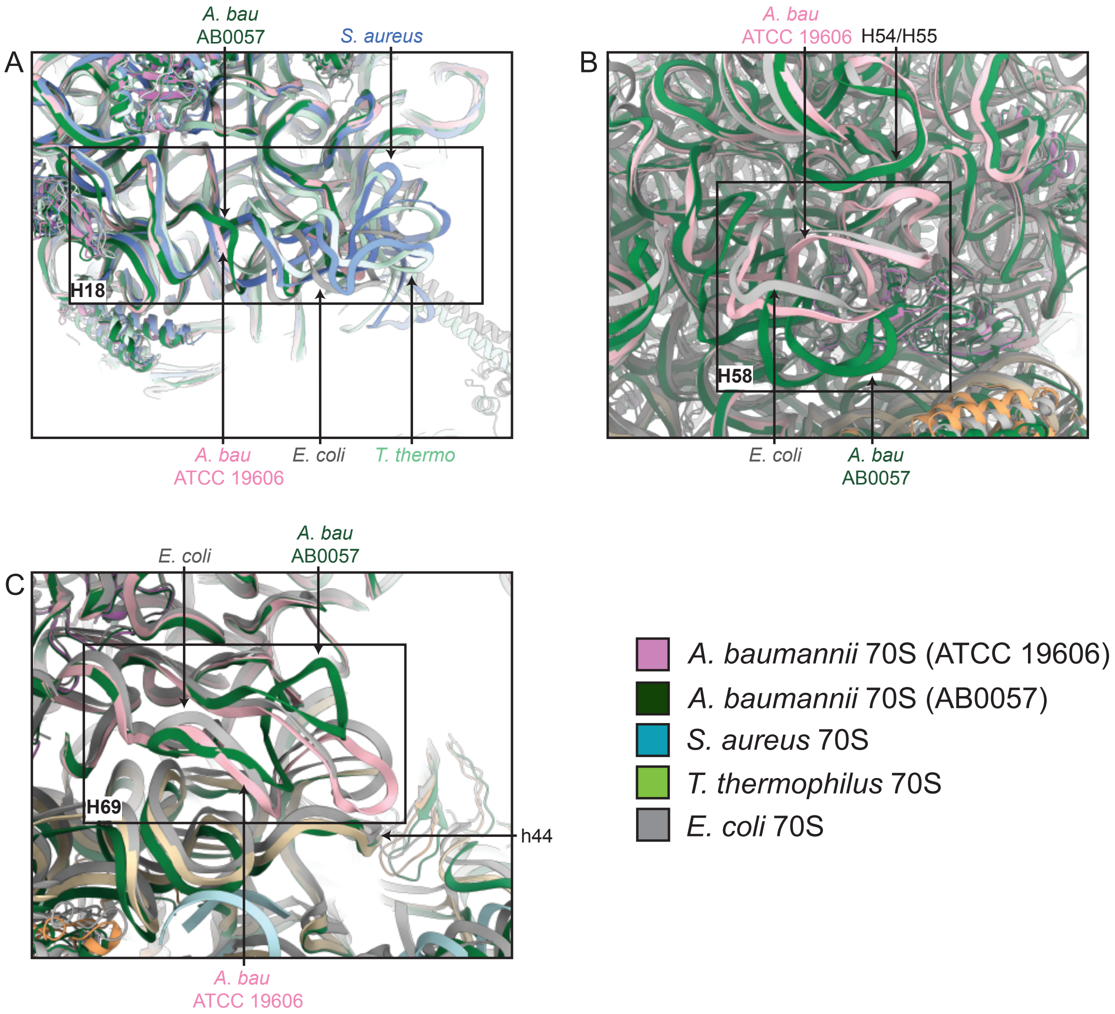

Figure 23 Structural comparison of the ribosome from two different strains of *A. baumannii*. A) H18 takes up different conformations in *A. baumannii* (pink, strain ATCC 19606; dark green, strain AB0057, PDB 6V3B), *E. coli* (grey, PDB 4YBB), *S. aureus* (blue, PDB 5LI0), and *T. thermophilus* (light green, PDB 5E81). B) H58 bends to interact with H54/H55 in the ribosome of *A. baumannii* ATCC 19606 (pink) and the *E. coli* ribosome (grey, PDB 4YBB), but not in the ribosome of *A. baumannii* AB0057 (dark green, PDB 6V3B). C) H69 reaches toward the 30S subunit to interact with h44 in the ribosome of *A. baumannii* ATCC 19606 (pink) and the *E. coli* ribosome (grey, PDB 4YBB), but instead bends back toward the 50S subunit in the ribosome of *A. baumannii* AB0057 (dark green, PDB 6V3B). The structure of the *A. baumannii* ribosome-amikacin complex is used to describe the ribosome of *A. baumannii* strain ATCC 19606, but the structures of all highlighted regions hold true for the *A. baumannii* ribosome-tigecycline complex.

The cause of the differences in H58 and H69 between these two structures is unclear. Indeed, there are no sequence differences in the stem-loops or in the proteins in the immediate vicinity that might explain any change in conformation. However, similar purification procedures and final ribosome buffers were used when preparing the two samples, so it seems unlikely that these differences are artefactual. Note that these differences are not due to modelling errors, as the density is quite clear for both helices in both structures (Figure 24). The discrepancies between these two structures provide another example of ribosomes from different strains of the same bacterial species containing unique structural features, and further study could aid understanding of divergent antibiotic susceptibilities in different strains.

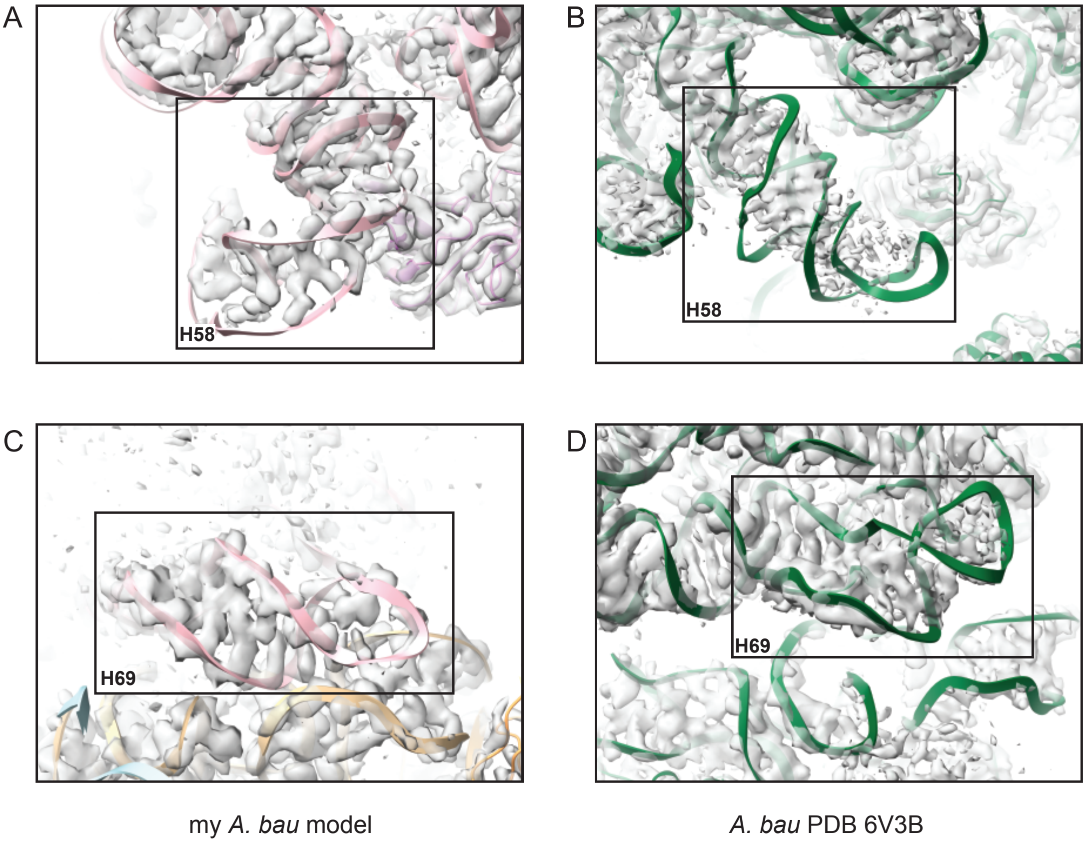

Figure 24 Cryo-EM density of 23S rRNA H58 and H69 of the *A. baumannii* ATCC 19606 and *A. baumannii* AB0057 ribosomes. A) H58 of the *A. baumannii* ATCC 19606 amikacin-ribosome model (pink), shown in the consensus cryo-EM reconstruction filtered by local resolution (grey). B) H58 of the *A. baumannii* AB0057 ribosome model (green, PDB 6V3B) shown in the corresponding cryo-EM map (grey, EMD-21032). C) H69 of the *A. baumannii* ATCC 19606 amikacin-ribosome model (pink), shown in the consensus cryo-EM reconstruction filtered by local resolution (grey). D) H69 of the *A. baumannii* AB0057 ribosome model (green, PDB 6V3B) shown in the corresponding cryo-EM map (grey, EMD-21032). The cryo-EM density shows that the different helix conformations shown in Figure 23 correspond to the cryo-EM data and are not modelling errors.

3.2.7 Interactions of amikacin and tigecycline with the *A. baumannii* ribosome

Additional cryo-EM density into which models of amikacin and tigecycline can be built is present in the amikacin-ribosome and tigecycline-ribosome cryo-EM reconstructions respectively (Figure 25). In this section, *A. baumannii* rRNA nucleotide numbering will be followed by *E. coli* numbering in parentheses to allow for easier comparison with the literature.

Aminoglycosides are known to impede the translocation of the mRNA-tRNA complex through the ribosome [256], inhibit ribosome recycling [61], and promote translational misreading [2,257]. Similarly to aminoglycoside in other aminoglycoside-ribosome structures [19,58], amikacin binds within an internal loop of h44 of the 16S rRNA at the A site and in a position that would sterically overlap with nucleotides A1489 (1492) and A1490 (1493), promoting an alternate conformation where these nucleotides are flipped out into the DC (Figure 25C). These nucleotides usually probe the minor groove of the codon-anticodon duplex in the A-site, and hence are involved in distinguishing cognate from non-cognate tRNAs. The stabilization of this flipped-out conformation even in the presence of non-cognate tRNA is a plausible mechanism for aminoglycoside-induced misreading [258]. Nearby, A1902 (1913) of the 23S rRNA H69 moves toward the tRNA binding site, and the phosphate of 16S rRNA A1490 (1493) moves in toward to centre of h44, away from the DC upon amikacin binding (Figure 25C). These movements support an alternative model proposing that aminoglycoside binding promotes misreading by inducing local changes in h44 and H69, which relax the constraints of the decoding pocket and otherwise compensate for energetically unfavourable non-cognate tRNA-mRNA interactions [21]. It may be the concerted effect of both these mechanisms that ultimately drives misreading.

Tetracyclines inhibit translation elongation by binding to the 30S ribosomal subunit and interfering with the delivery of A-site tRNA [49,53]. Tigecycline, a third-generation tetracycline derivative, targets the head of the 30S subunit to overlap with the A-site in a way similar to that seen for tetracycline. It interacts with the phosphate backbone of h34 of the 16S rRNA through coordination between polar groups of rings B and C and a magnesium ion (Mg-1), and with the 16S rRNA nucleotides C1051 (1054) and A1193 (1196) through a stacking interaction of its 9-t-butylglycylamido moiety (Figure 25E), a group not present in tetracycline. Also, the sugar ring of C1192 (1195) is in a position to form polar interactions with the amide of ring A of tigecycline.

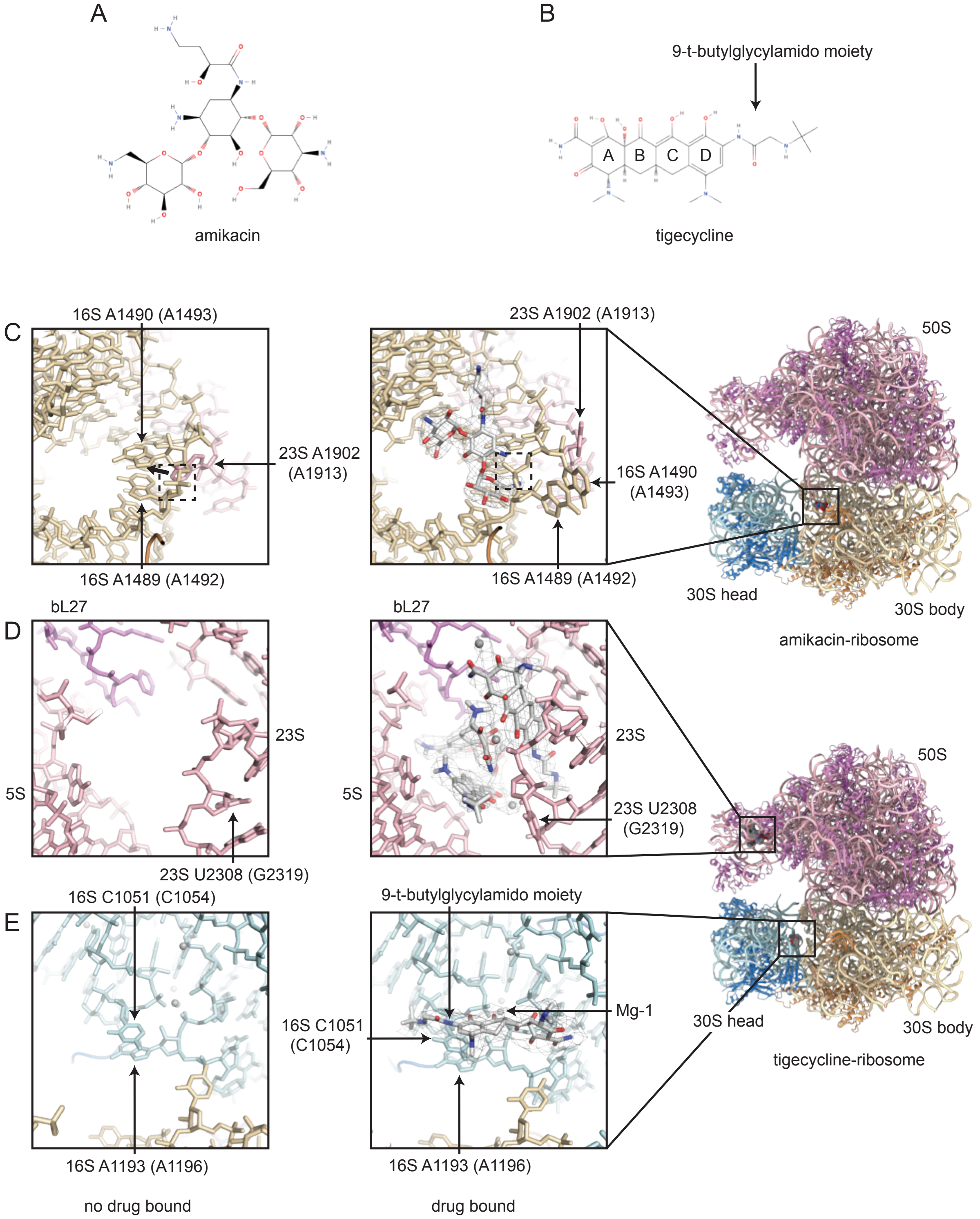

Figure 25 Interactions of amikacin and tigecycline with the *A. baumannii* ribosome. A) Structural formula of amikacin. B) Structural formula of tigecycline. Both drawn in MolView. C) Amikacin bound to the primary aminoglycoside binding site of the *A. baumannii* ribosome (right), drug shown as an atomic model (grey) with carved EM density (grey mesh). The tigecycline-ribosome structure, left, shows this site with no amikacin bound. Nucleotides A1489 (1492) and A1490 (1493) of the 16S rRNA and A1902 (1913) of the 23S rRNA, and the phosphate between A1489 (1492) and A1490 (1493), all of which change conformation upon drug binding, are highlighted. D) A secondary tigecycline binding site showing three tigecycline molecules bound to the *A. baumannii* ribosome (right), drugs shown as an atomic model (grey) with carved cryo-EM density (grey mesh). The amikacin-ribosome structure, left, shows the site with no tigecycline

bound. Nucleotide U2308 (G2319) of the 23S rRNA, which changes conformation upon drug binding, is highlighted. E) The primary tigecycline binding site showing tigecycline bound to the *A. baumannii* ribosome (right), drug shown as an atomic model (grey) with carved EM density (grey mesh). The amikacin-ribosome structure, left, shows the site with no tigecycline bound. Nucleotides C1051 (1054) and A1193 (1196) of the 16S rRNA, along with a magnesium ion, which all interact with the drug, are highlighted. *E. coli* numbering is shown in parentheses.

These interactions are similar to those seen in other structures (Figure 26) [55,56,259]; however, there are a few noteworthy differences. Firstly, the nature of the stacking interaction of tigecycline with C1051 (1054) varies slightly among the different structures. This interaction is thought to account for tigecycline's increased ability to interfere with A-site tRNA binding as well as its increased binding affinity compared with tetracycline [55], and may also hinder access of the ribosomal protection protein TetM, likely explaining why TetM-mediated resistance does not apply to tigecycline [55,56]. In the *A. baumannii* 70S ribosome-tigecycline and the *T. thermophilus* 30S subunit-tigecycline complexes, the base of C1051 (1054) appears to form a π-π stacking interaction with ring D of tigecycline (Figure 26A&C), whereas it appears to stack with the amide of the 9-t-butylglycylamido moiety in the *T. thermophilus* 70S ribosome-tigecycline and *E. coli* 70S ribosome-tigecycline complexes (Figure 26B&D).

Furthermore, although the density of the 9-t-butylglycylamido moiety is not strong in our data, it appears to adopt an extended conformation, similar to that seen when tigecycline is bound to the *T. thermophilus* 30S subunit, rather than a bent conformation as seen when bound to the whole *T. thermophilus* 70S ribosome. This bent conformation has previously been suggested to help accommodate a “closed” conformation of h18, which occurs when the 30S head and shoulder rotate inwards toward the DC [56]. This is supported by a comparison of the structures of tigecycline bound to the *T. thermophilus* 70S ribosome and the *T. thermophilus* 30S ribosomal subunit, where the movement of h18 away from the tigecycline site in the latter correlates with an extended conformation of tigecycline's 9-t-butylglycylamido moiety (Figure 26B&C). In the *A. baumannii* ribosome-tigecycline structure presented here, h18 is even further away from the tigecycline site, and the 9-t-butylglycylamido moiety adopts an extended conformation, following the expected trend (Figure 26A). The cryo-EM consensus reconstruction was used to confirm the relative proximity of these features, because the tigecycline site forms part of the 30S head, whereas h18 is part of the 30S body. It should be noted that the model of the 9-t-butylglycylamido moiety has been built to adopt a bent conformation in the *E. coli* 70S ribosome structure, despite h18 being far from the tigecycline binding site, which appears to contradict this trend (Figure 26D). However, the density corresponding to this moiety is not well defined, so it is not clear whether it does indeed adopt a bent, rather than an extended, conformation [259].

In addition, all previous tigecycline-ribosome structures place a magnesium ion (Mg-2) that coordinates ring A of tigecycline to the phosphate of G963 (2N-methyl-G966). From an examination of the exact location of this ion, in the *T. thermophilus* 70S-tigecycline structure this coordination appears to occur primarily through ring A's hydroxyl oxygen, in the *T. thermophilus* 30S-tigecycline structure primarily through the ring's amide oxygen, and in the *E. coli* 70S-tigecycline structure though an even mixture of the two (Figure 26). However, there is no density for a second magnesium ion in the *A. baumannii* ribosome-tigecycline reconstruction when visualised at high contour levels (Figure 26E). At lower contour levels there is some density present in this region, though at these levels, signal is impossible to discern from noise (Figure 26F). This is in contrast to the magnesium ion in site 1 (Mg-1), which fits into strong and clearly defined cryo-EM density.

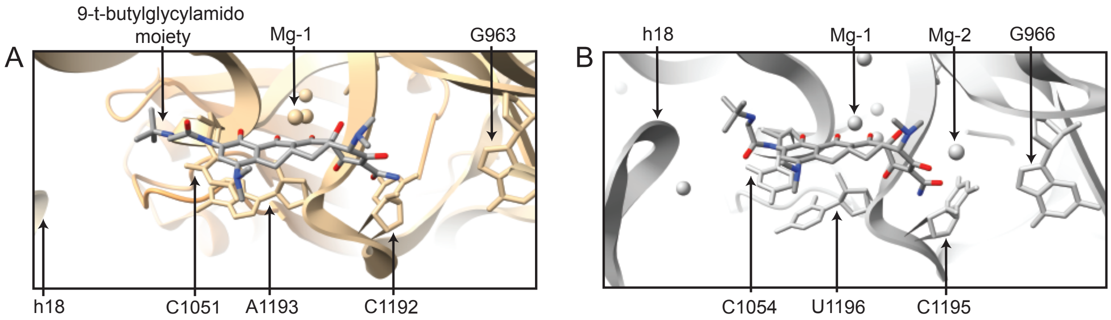

A. baumannii 70S (this study)

T. thermophilus 70S (PDB 4V9B)

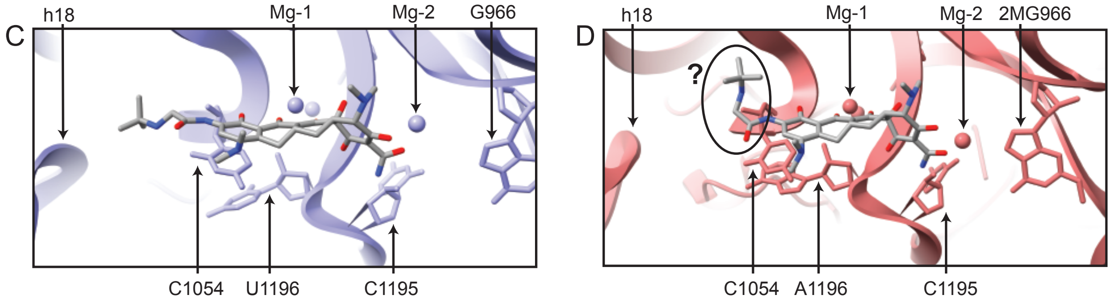

T. thermophilus 30S (PDB 4YHH)

E. coli 70S (PDB 5J91)

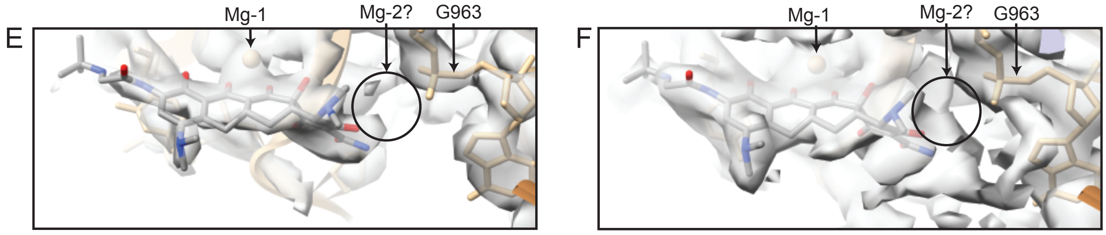

A. baumannii 30S head (high contour)

A. baumannii 30S head (low contour)

Figure 26 The primary tigecycline binding site in ribosomes and ribosomal subunits of various bacteria. (A–D) Atomic models of the primary tigecycline binding site in ribosomes and ribosomal subunits of different bacteria. The nature of tigecycline binding is broadly similar across the structures, but with differences including the stacking interaction of tigecycline with C1051 (1054) of 16S rRNA, variations in the conformation of the 9-t-butylglycylamido moiety, and differences in coordination of a second magnesium ion. A) Atomic model of tigecycline (grey) bound to the 70S of the *A. baumannii* ribosome (brown). The 30S head model and h18 from the 30S body model are shown. The consensus cryo-EM reconstruction was used to confirm the relative proximity of these features. B) Atomic model of tigecycline (grey) bound to the 70S *T. thermophilus* ribosome (grey, PDB 4V9B). C) Atomic model of tigecycline (grey) bound to the 30S *T. thermophilus* ribosomal subunit (blue, PDB 4YHH). D) Atomic model of tigecycline (grey) bound to the 70S *E. coli* ribosome (red, PDB 5J91). The density is not strong enough to support either an extended or a bent conformation of the 9-t-butylglycylamido moiety, as indicated by the question mark. E) Sharpened cryo-EM reconstruction of the 30S head of the *A. baumannii* ribosome-tigecycline complex at the primary tigecycline site, high-contour level. F) Sharpened cryo-EM reconstruction of the 30S head of the *A. baumannii* ribosome-tigecycline complex at the primary tigecycline site, low-contour level. It is impossible to discern possible magnesium ion density (Mg-2) from noise.

Additional density into which models for tigecycline could be built was seen in the 50S at the central protuberance of the *A. baumannii* ribosome-tigecycline structure. Here, three tigecycline molecules appear to bind in a cavity between the 23S rRNA, 5S rRNA, and protein bL27. This is accommodated by a significant conformational change of the surrounding rRNA, with a particularly large movement of residue U2308 (G2319) of the 23S rRNA, which flips out to interact with the 9-t-butylglycylamido moiety of one of the molecules (Figure 25D).

The three molecules interact with one another through stacking interactions and through bridging magnesium ions, as well as with the backbone and bases of the surrounding rRNA and protein bL27 (Figure 27A, the three molecules labelled 1, 2, and 3). Interactions between these ligands and the surrounding ribosome were calculated using Arpeggio [179] and represented in two dimensions in Figure 28A-C. From the 5S rRNA, the base of A12 (G13) forms a carbon-π interaction with a methyl group of the amine of ring D of tigecycline 1, and the 2′-OH of G15 (16) forms a donor-π interaction with ring D of tigecycline 1. From the 23S rRNA, a carbonyl and a sugar ring oxygen of U2308 (G2319) form polar contacts with the 9-t-butylglycylamido moiety of tigecycline 1, the base of A2309 (U2320) forms a π-π stacking interaction with ring D of tigecycline 3, and the base of A2322 (2333) forms a carbon-π interaction with a methyl group of the amine of ring D of tigecycline 3. Finally, the main-chain carbonyl and Cγ of Gln74 of bL27 form van der Waals contacts with the amide of ring A and ring B of tigecycline 2. Additional interactions between the tigecycline molecules and the surrounding phosphate rRNA backbone are facilitated by coordination of magnesium ions, most clearly seen by the ion that bridges the phosphate of 23S A2309 (U2320) with oxygen atoms of ring A of tigecycline 2 and rings B and C of tigecycline 3. Overall, the presence of these tigecycline molecules promotes a series of interactions bridging the 23S and 5S rRNAs, with contributions from bL27.

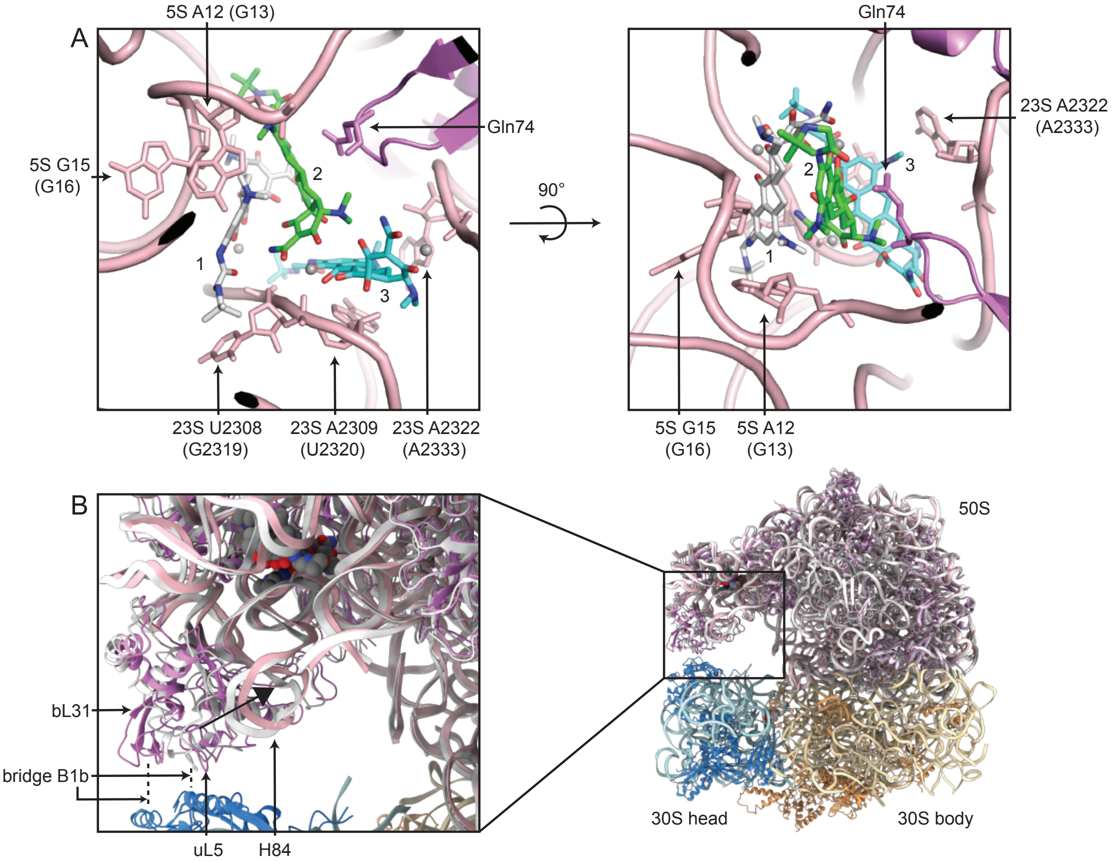

Figure 27 A secondary tigecycline binding site at the 50S central protuberance. A) Two views of the secondary binding site in the *A. baumannii* ribosome-tigecycline structure. The three tigecycline molecules are labelled 1 (white), 2 (green), and 3 (cyan). The 23S rRNA nucleotides U2308 (G2319), A2309 (U2320), and A2322 (2333); the 5S rRNA nucleotides A12 (G13) and G15 (16); and the bL27 residue Gln74, which all interact with the drug molecules, are labelled. Magnesium ions are shown as grey spheres. B) Changes in the conformation of the central protuberance and intersubunit bridge B1b upon tigecycline binding at this secondary site. The atomic model of the tigecycline-bound ribosome (50S pink, 30S body brown, 30S head blue) is overlaid with the atomic model of the amikacin-bound 50S, which has no tigecycline bound (white) after alignment of the 23S rRNA chains. H84 and uL5 undergo a shift upon tigecycline binding, and bL31 becomes partially resolved in the density. *E. coli* numbering is shown in parentheses.

To investigate the possibility of tigecycline binding to this secondary site in other bacteria, the structure of this site in the *A. baumannii* ribosome-amikacin model was compared with the same region in structures of ribosomes from *E. coli*, *S. aureus*, and *T. thermophilus*, so that the site is compared in its empty state (Figure 28D-E). The sites in *A. baumannii* and *E. coli* are very similar (Figure 28D), with the most noticeable differences found in U2308 (G2319) of the 23S rRNA, which takes up slightly different conformations in the two structures. However, given that this base dramatically changes conformation on tigecycline binding anyway, it is difficult to conclude whether this difference would have an impact on binding. Another obvious difference is the identity of residue 74 of bL27, which is glutamine in *A. baumannii* but proline in *E. coli*. However, as discussed, in *A. baumannii* this residue appears only to form van der Waals contacts with tigecycline through its main chain and Cγ, and these contacts could likely still be made with a proline residue.

The secondary tigecycline site differs much more greatly in *S. aureus* and *T. thermophilus* (Figure 28E). In these structures, the surrounding rRNA and the loop in bL27 take up different folds compared with their equivalents in *A. baumannii*. Overall, this crude analysis suggests that tigecycline might be able to bind to this site in *E. coli*, but is less likely to bind in *S. aureus* and *T. thermophilus*. However, it should be noted that tigecycline was not seen in this site in the previously solved tigecycline : *E. coli* ribosome structure (PDB 5J91 [259]).

These interactions appear to have a long-range effect beyond the binding pocket, with H84 of the 23S rRNA pulled toward the binding site, along with uL5, which is pulled away from its interaction with the 30S where it normally forms part of bridge B1b (Figure 27B). Protein bL31, which also forms part of bridge B1b, is partly resolved in this tigecycline-bound structure but much less well resolved in the amikacin-bound structure, so it appears that these conformational shifts make bL31 more rigid.

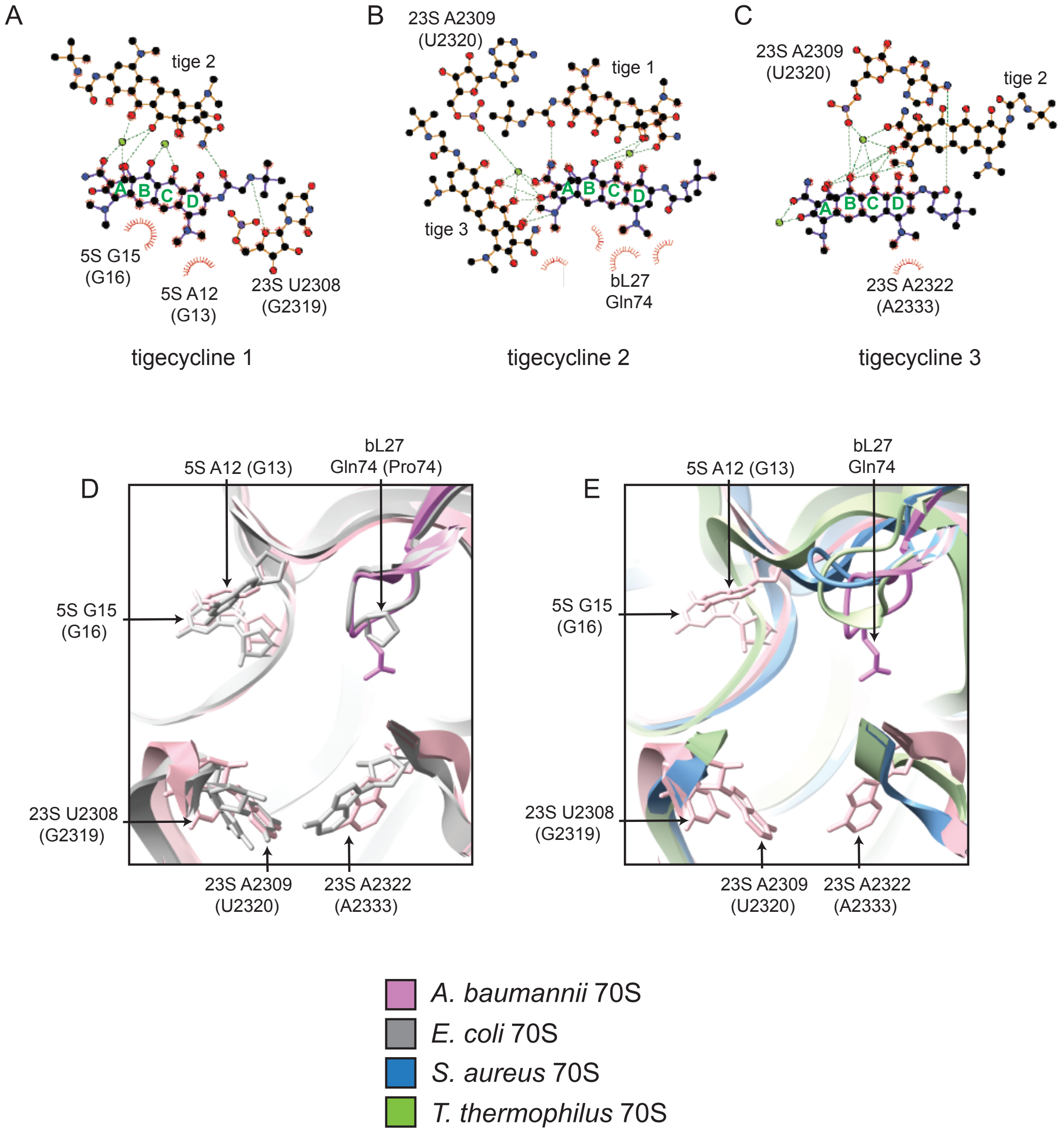

Figure 28 Detailed interactions at the secondary tigecycline bindings site and species comparison. A-C) Two dimensional diagrams representing the interactions that the three tigecycline molecules make with each other and the surrounding ribosome. Red spikes represent hydrophobic interactions and green dashes represent polar or ionic interactions. LigPlot+ [180] was used to generate the diagrams, which were then adapted to highlight the major interactions calculated by Arpeggio [179]. D) Atomic model of the *A. baumannii* ribosome-amikacin complex showing the secondary tigecycline binding site (with no drug bound), with residues that interact with tigecycline shown (pink), and atomic model of the *E. coli* ribosome with the equivalent *E. coli* residues shown (grey, PDB 5MDZ). Many of the residues proposed to be involved in tigecycline binding take similar conformations in the two structures. E) Atomic models of the secondary tigecycline binding site in the *A. baumannii* ribosome-amikacin complex (pink), *S. aureus* ribosome (blue, PDB 5LI0) and *T. thermophilus* ribosome (green, PDB 5E81). The rRNA surrounding the binding site and the loop in bL27, proposed to be involved in tigecycline binding, take up quite different folds in these structures. *E. coli* numbering is shown in parentheses.

3.3 Discussion

To summarise, high-resolution cryo-EM structures of the ribosome from ESKAPE pathogen *A. baumannii* were solved, a bacterium with a concerning tendency to resist the action of antibacterial drugs. The structures of the amikacin-ribosome and tigecycline-ribosome complexes were solved to 2.8 Å and 2.6 Å, respectively, and atomic models built after multibody refinement was employed to improve the 30S density. Structural features unique to this ribosome were identified, many of which clustered around the solvent-facing exit of the NPET and around the edge of the 50S-30S interface. The recent structure of the ribosome from *A. baumannii* strain AB0057 allowed for a comparison with the structure solved here of the ribosome from *A. baumannii* ATCC 19606, showing that even ribosomes from different strains of the same species can vary. Finally, the interactions of amikacin and tigecycline with the *A. baumannii* ribosome were studied, with a focus on an unexpected secondary tigecycline binding site at the 50S central protuberance.

In this discussion, the significance of the unique structural features of the *A. baumannii* ribosome is evaluated, before comparing the binding of amikacin and tigecycline to that seen in other ribosome-drug structures. In particular, the biological relevance of the secondary tigecycline binding site will be assessed.

3.3.1 Unique structural features of the *A. baumannii* ribosome

The overall structure of the *A. baumannii* ribosomes was highly similar to ribosomes from other bacteria, especially *E. coli*, as implied by sequence similarities, with differences mainly localised to solvent-facing portions of the ribosome subunits. Importantly, functional regions of the ribosome, such as the PTC, NPET entrance and the DC were largely conserved. These regions are those which the majority of ribosome-targeting antibiotics bind to, suggesting that there are limitations to the extent to which the activity of these antibiotic classes could be directed towards specific bacterial species.

However, there are some unique structural features of this ribosome which could be functionally important, most notably those on the 50S subunit surface around the exit of the NPET. This region is the site where a number of ribosome-associated factors dock to facilitate downstream processing of the newly formed protein, such as trigger factor, a molecular chaperone that aids protein folding [252], and the signal recognition particle and Sec translocon, both involved in protein targeting to the cell membrane [31]. Structural features unique to the *A. baumannii* ribosome also cluster around the subunit interface, a key functional site important for 70S stability and translocation [253]. For example, thermorubin and some aminoglycosides such as neomycin bind to H69 to perturb intersubunit bridge B2, thereby inhibiting tRNA delivery or subunit rotation to impede translation [57,62].

Although these sites are not as directly involved in protein synthesis as the PTC, NPET or DC, they do have functional importance and could be a target in the development of classes of antibiotics different to those currently in use as a strategy to mitigate rising antibiotic resistance. Since these sites tend to vary between bacterial species, they might also be targets for the development of drugs specific to, or at least especially effective against, certain pathogenic bacteria.

3.3.2 Interactions of amikacin and tigecycline with the *A. baumannii* ribosome

Amikacin binds to the *A. baumannii* ribosome at the expected aminoglycoside site. Specifically, it binds within an internal loop of h44 of the 16S rRNA at the A-site, causing nucleotides A1489 (*E. coli* numbering 1492) and A1490 (1493) to flip out into the DC (Figure 25C).

No structures of ribosome-amikacin complexes have previously been solved, so it is not possible to compare the binding of this drug to the *A. baumannii* ribosome with binding to ribosomes of other bacterial species. Nevertheless, a number of structures of ribosomes in complex with other aminoglycoside antibiotics have been solved, and these all show a similar mode of binding to that seen here. For example the 4,5-disubstituted deoxystreptamine aminoglycoside paromomycin (PDB 1IBK) [19] and the 4,6-disubstituted deoxystreptamine aminoglycoside gentamicin (PDB 4V53) [61] both bind to the *T. thermophilus* (PDB 1IBK) [19] and *E. coli* ribosomes (PDB 4V53) [61] in a similar manner as amikacin (also a 4,6-disubstituted deoxystreptamine) does to the *A. baumannii* ribosome (Figure 29). In all three cases, the drug binds inside h44 of 16S rRNA to flip out A1489 (1492) and A1490 (1493) into the DC. The conformation of the 16S rRNA around the binding site differs somewhat, although this may due to the different drugs rather than genuine species-specific differences of the site.

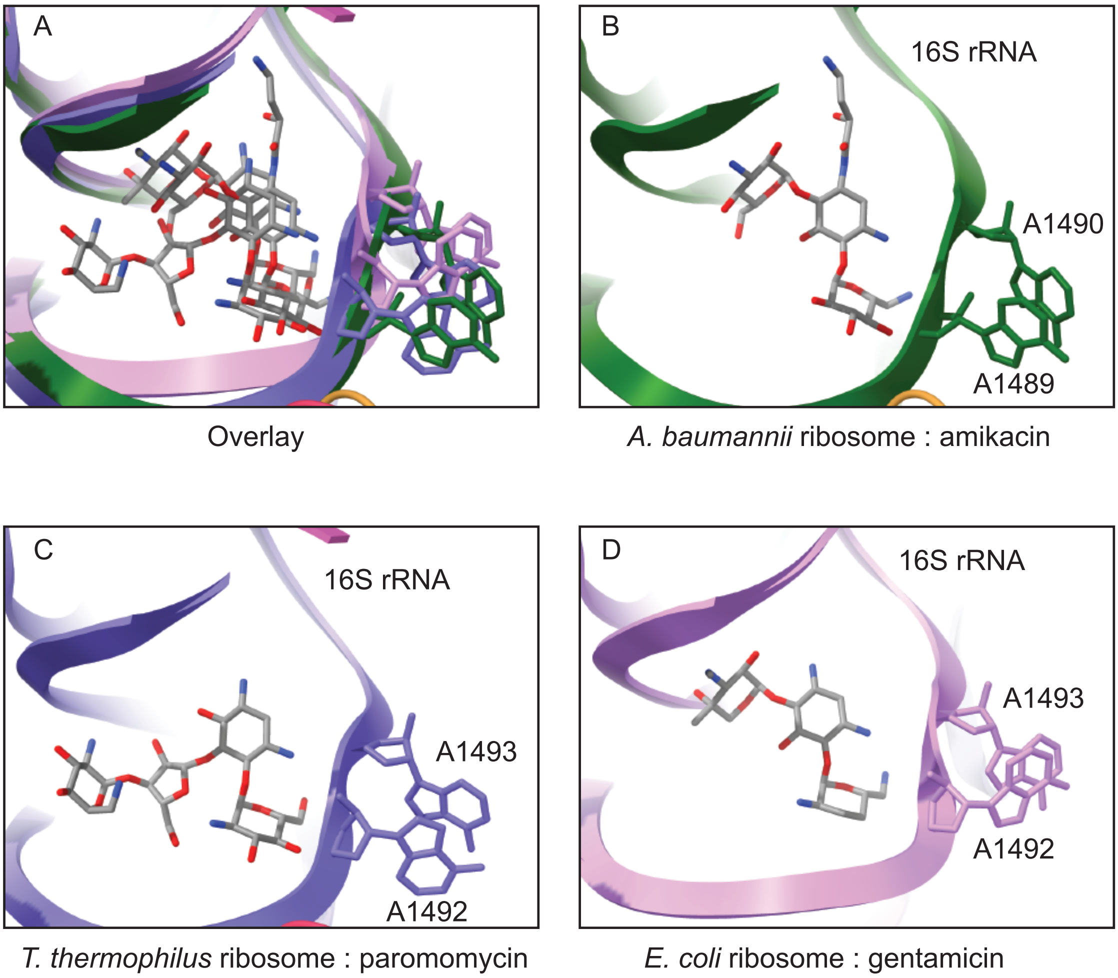

Overlay

A. baumannii ribosome : amikacin

T. thermophilus ribosome : paromomycin

E. coli ribosome : gentamicin

Figure 29 Comparison of aminoglycoside-ribosome interactions. A) Overlay of aminoglycoside binding sites shown in (B-D). B) Structure of amikacin (grey) bound to the *A. baumannii* ribosome (green). C) Structure of paromomycin (grey) bound to the *T. thermophilus* ribosome (purple, PDB 1IBK). D) Structure of gentamicin bound to the *E. coli* ribosome (pink, PDB 4V53)

Tigecycline binds at the expected site at the A-site of the 30S subunit head of *A. baumannii* to interfere with delivery of A-site tRNA (Figure 25E). As described in section 3.2.7 above, this binding mode is largely conserved in *E. coli* and *T. thermophilus* (Figure 26), with a few minor differences including the part of tigecycline that interacts with 16S rRNA C1051 (1054), the conformation of the 9-t-butylglycylamido moiety and the presence or absence of a magnesium ion coordinating the drug with G963 (2N-methyl-G966). It should be noted that these structures comprise a number of different ribosome conformations, with the relative positioning of 30S head and 30S body potentially playing a role in the exact mode of tigecycline binding due to the location of the tigecycline site at the interface of the independently moving 30S body and 30S head. This certainly seems to be the case for the conformation of the 9-t-butylglycylamido moiety, which generally adopts a more extended conformation as h18 of the 30S body moves away from tigecycline site (Figure 26). Therefore, it is difficult to determine whether the different modes of tigecycline binding in these structures are due to differences in the binding site between different bacterial species or merely caused by different ribosome conformations.

Overall, the primary binding sites of amikacin and tigecycline in the *A. baumannii* ribosome are similar to that observed in ribosomes of other bacterial species, with only small differences that cannot be confidently attributed to species-specific variation. Therefore, although there is potential for rational redesign of aminoglycosides or tigecycline to increase their binding affinity for these sites in *A. baumannii*, it's likely that such an approach would also improve their binding affinity to ribosomes of other bacterial species.

More interestingly, tigecycline binds at a secondary site in the 50S central protuberance, which involves simultaneous binding of three tigecycline molecules to bridge the 23S rRNA, 5S rRNA and bL27 (Figure 25D, Figure 27). Tigecycline was not seen in this site in the two previously solved tigecycline-70S ribosome structures comprising ribosomes from *E. coli* and *T. thermophilus* [55,259], and this binding site is considerably different in *S. aureus* and *T. thermophilus* compared with *A. baumannii* (Figure 28E) and slightly different in *E. coli* (Figure 28D). Therefore, it is possible that tigecycline does indeed bind here specifically to *A. baumannii*. This binding event pulls H84 and uL5 away from intersubunit bridge B1b, and might increase the rigidity of subunit bridging protein bL31 (Figure 27B). Such a rearrangement of bridge B1b could plausibly affect the stability of the ribosome or the dynamics of translation.

However, it is possible that the secondary tigecycline binding site is an artefact from incubation of the ribosome with excess drug. Indeed, the stacking of three separate drug molecules is unusual, and the fact that no density for tigecycline in this site was seen in the other tigecycline-70S ribosome structures [55,259] could be indicative of an artefactual binding event, rather than an indication of genuine species-specific binding.

Nevertheless, it should be noted that none of the previously reported secondary binding sites for tetracycline within the 30S subunit were occupied in the cryo-EM density of our structure [49,53]. In our density, the site at the central protuberance was the only place where density for tigecycline was seen, other than the reported primary site, suggesting that tigecycline binds at least moderately tightly to this secondary site.

Based on this structural snapshot, it is not possible to know whether tigecycline binding at this site contributes a biological secondary mode of action for the drug beyond inhibition of A-site tRNA delivery. The first step in exploring this further would be to assess the binding of tigecycline to isolated *A. baumannii* 50S subunits and 50S subunits of other bacterial species when using lower concentrations of the drug. This could be done by measuring the amount of tigecycline bound to the ribosome subunit after pelleting the sample through a sucrose cushion, e.g. by using a radiolabel [125] or by heat treatment followed by mass spectrometry [260].

3.3.3 Further work

As in this study, previously determined structures of drug-ribosome complexes tend to involve empty ribosomes [259], or ribosomes with tRNA and mRNA bound *in vitro* [55]. These structures provide an important starting point to understand the action of ribosome-targeting antibiotics in different bacteria and may be used to aid the design of new drugs. They also pave the way for structural studies on more complex systems in which ribosomes are stalled or inhibited mid-translation by the drug in question to gain snapshots of antibiotics "in action," trapping the ribosome in particular conformational states. Some previous structures have already been determined using this approach, such as the erythromycin-bound ErmBL- and ErmCL-stalled bacterial ribosomes [261,262], and the human ribosome stalled by PF846, a drug-like molecule that binds to the NPET [263]. Building a repertoire of structures of drug-bound ribosomes isolated from a variety of bacterial species and strains that are empty, filled with tRNA and mRNA, or stalled in particular conformational states may provide a platform for the rational design of new drugs with improved activity against specific species or strains of bacteria and which inhibit different stages of translation. Only by accelerating development of new antibiotics will we be able to successfully treat increasingly drug-resistant infections in the future, including those caused by *A. baumannii*.

Chapter 4 The structural basis of resistance to ribosome-targeting antibiotics mediated by Sal-type ABC-F proteins

4.1 Introduction

Bacterial resistance to ribosome-targeting antibiotics is mediated in a variety of ways, one of which involves the binding of ABC-F proteins to the ribosome resulting in the displacement of antibiotics by type I or type II target protection (see Chapter 1). In this chapter, the high resolution structure of the complex between the ABC-F protein Sal(B) and the *S. aureus* ribosome is presented. The effect on antibiotic resistance of mutations in a residue of Sal that interacts with the drug binding site is analysed, and the protein sequence of the surrounding region is compared among Sal variants conferring different resistance phenotypes. These results are used to evaluate possible mechanisms by which Sal-type ABC-F proteins protect the ribosome from PTC-targeting antibiotics. These findings are considered alongside previous studies on other antibiotic resistance (ARE) ABC-F proteins to explore the possibility of a common mechanism of ABC-F protein mediated ribosome-protection.

To introduce this chapter, the ABC-F protein family as a whole will be outlined, with a focus on ARE ABC-F proteins. Structures of previously solved ABC-F protein : ribosome complexes will be described, and the mechanisms by which ARE ABC-F proteins might displace antibiotics will be reviewed. Finally, the clinical relevance and phylogeny of Sal-type ABC-F proteins will be examined.

4.1.1 The ABC-F protein family

The ABC protein superfamily is found in all domains of life, and its members are often involved in coupling ATP hydrolysis and transport of physiological substrates across cell membranes [264]. However, ABC-F proteins are soluble and lack transmembrane domains. They are composed of a single polypeptide comprising two nucleotide binding domains (NBDs), separated by an interdomain linker of about 80 amino acids [126,265]. The NBDs comprise Walker A and B motifs that are involved in ATP hydrolysis, and a five-residue signature sequence, frequently LSGGQ. The signature sequence motif in one NBD forms an ATP binding site with the Walker A/B motifs of the second, giving rise to two pseudo-symmetric ATP binding sites per protein [266]. Some ABC-F proteins also contain a C-terminal extension, which generally forms a two-stranded α-helical coiled-coil [267]. A schematic of the ABC-F protein domain structure is shown in Figure 30. Members of the ABC-F protein family have been shown to be involved in DNA repair [268], translational control [269-271], and resistance to antibiotics that target bacterial protein synthesis [126].

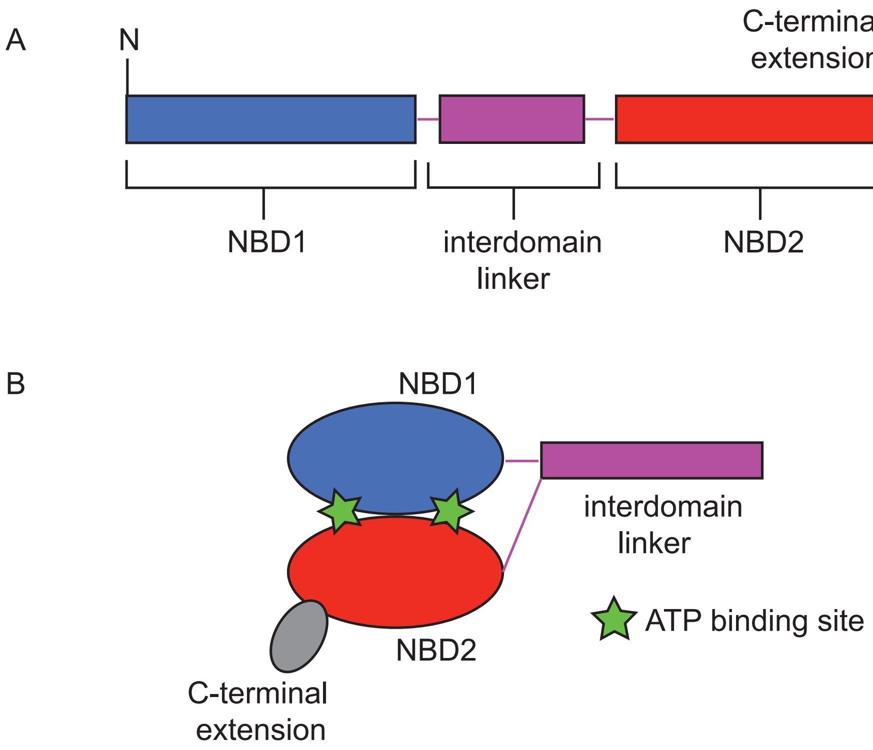

Figure 30 Schematic of the ABC-F protein domain structure. A) The sequence arrangement of the nucleotide bindings domains (blue = NBD1, red = NBD2), the interdomain linker (purple), and C-terminal extension (grey). B) The structural arrangement of these domains, with the pseudo-symmetric ATP binding sites shown (green stars).

Phylogenetic analysis has distinguished 45 groups of ABC-F proteins, seven of which contain ARE ABC-F proteins, termed ARE1-7. There is no clear sequence signature that distinguishes ARE ABC-F proteins from non-ARE proteins, suggesting that antibiotic resistance has arisen multiple times independently within the ABC-F family [272]. It is plausible that the antibiotic resistance function of ARE ABC-F proteins found in pathogenic bacteria might be coincidental to a housekeeping role of translation modulation [126].

4.1.2 Antibiotic resistance (ARE) ABC-F proteins

ARE ABC-F proteins mediate resistance to antibiotics that target the PTC or NPET in the 50S subunit of the bacterial ribosome, and can be categorized into three groups, with each group conferring resistance to chemically distinct antibiotics that target the same site of the ribosome [127,266,273-275]. Firstly, *vga*-, *lsa*-, *vmlr*- and *sal*-type genes confer resistance to lincosamides, streptogramin As and pleuromutilins (LS_AP), which target the PTC [276-278]. Secondly, *msr*-type genes confer resistance to macrolides and streptogramin Bs (MS_B), which target the NPET [279]. The third group includes *optrA* and *poxtA* genes, which confer resistance to phenicols and oxazolidinones (PhO), drugs that target the PTC [280,281].

Antibiotic-producing bacteria, such as streptomycetes, often employ ARE ABC-F proteins for self-protection [282], but these proteins are also found in clinically-relevant Gram positive pathogens such as enterococci [280], staphylococci [277] and streptococci species [283], and some have been reported in Gram-negative species [284]. Some genes that code for ARE ABC-F proteins are part of the core genome of certain bacterial species, such as *lsaA* in *E. faecalis* and *vmlR* in *B. subtilis*. Neither *lsaA* or *vmlR* are known to have transferred to any other species. On the other hand, *vga, optrA, poxtA* and *msr* genes are carried by mobile genetic elements found in multiple bacterial species [266].

Since members of the wider ABC protein superfamily are implicated in membrane transport, ARE ABC-F proteins were initially assumed to mediate resistance through antibiotic efflux [279,285]. However, LsaA and VgaA were found to rescue translation from an antibiotic-inhibited *in vitro* transcription/translation assay, and LsaA was found to displace radiolabelled lincomycin from purified staphylococcal ribosomes [125]. Likewise, MsrE rescues macrolide-inhibited translation *in vitro* [260]. These findings provide evidence that ABC-F proteins mediate resistance by ribosome protection, not efflux. Even before structures of ARE ABC-F proteins bound to the ribosome were solved, these proteins were predicted to bind to the ribosome in a manner analogous to non-ARE ABC-F protein EttA, a bacterial protein that modulates translation activity in response to cellular energy levels [270]. EttA binds to the ribosome at the E-site between the L1 stalk and P-site tRNA, with its interdomain linker inserted towards the PTC to make contacts with the acceptor stem of P-site tRNA and modulate the conformation of the PTC [286]. Most ARE ABC-F proteins have an interdomain linker around 30 amino acids longer than that of EttA, and so were predicted to probe further towards the PTC, likely displacing both the P-site tRNA acceptor stem and antibiotic from the PTC. The findings that mutagenesis of the interdomain linker of VgaA altered its resistance profile and that deletion of the linker in $VgaA_{LC}$ abolished resistance supported this model [287,288]. Structural studies confirmed that ARE ABC-F proteins bind ribosomes in an analogous manner to EttA (see section 4.1.3). A schematic showing how ARE ABC-F proteins bind the ribosome is shown in Figure 31.

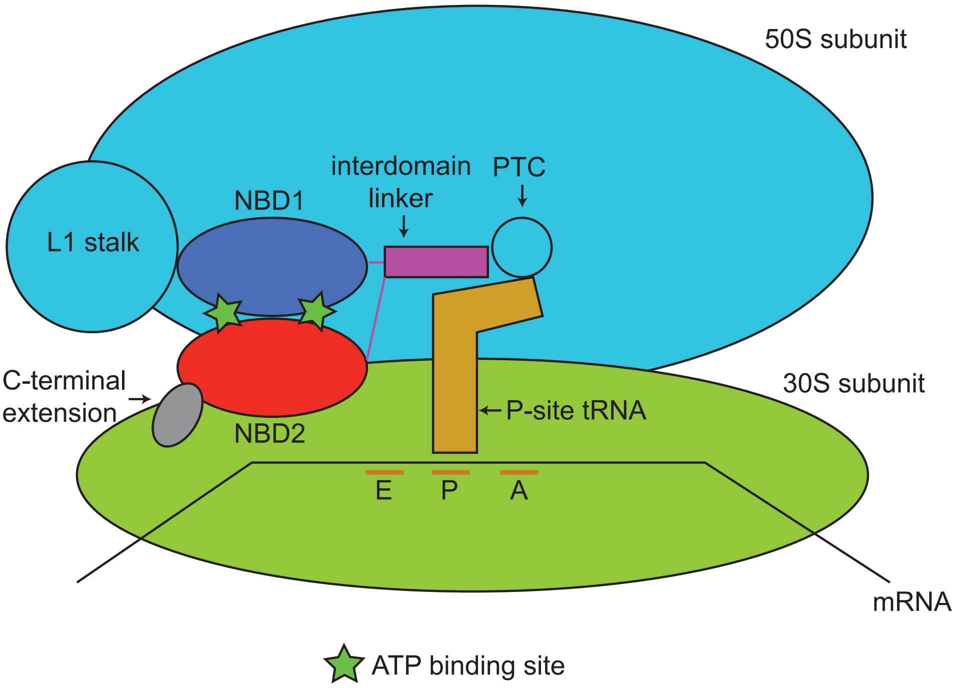

Figure 31 Schematic of an ARE ABC-F protein : ribosome complex. ARE ABC-F proteins bind to the ribosome in a similar fashion as EttA. The NBDs bind to the E-site of the ribosome between the L1 stalk and P-site tRNA, with the interdomain linker protruding towards the PTC to distort P-site tRNA and displace bound antibiotic.

ATP- (or, more generally, NTP-) binding and hydrolysis is likely required for antibiotic protection by ABC-F proteins [288]. Indeed, the EQ_2 mutant of VgaA, which has two glutamate to glutamine mutations in the NBD Walker motifs that prevent ATP hydrolysis, does not confer resistance [289]. Furthermore, antibiotic inhibition of peptidyl transferase in a reconstituted translation system is relieved by wild type $VgaA_{LC}$ or Lsa, but not their EQ_2 mutants [288]. Considering that EQ_2 mutants of MsrE can displace drugs as efficiently as wild type, ATP hydrolysis is likely involved in ABC-F protein recycling rather than antibiotic displacement [260]. Specifically, ATP hydrolysis likely drives separation of the two NBDs into a conformation no longer compatible with ribosome binding, which drives protein release [286,290]. It should be noted that mutation of a lysine crucial for ATP binding in the Walker A motif of ARE ABC-F protein LmrC has no impact on tylosin resistance [291], so the role of ATP hydrolysis may not be universal.

Further elucidation of the mechanisms by which ARE ABC-F proteins protect the ribosome required structural information. To this end, cryo-EM structures of such proteins bound to the ribosome were solved by Su et al. [260] and Crowe-McAuliffe et al. [187,267], and the interactions that these proteins make with the LS_AP binding site were analysed, focusing on the binding sites of virginiamycin M1 (a type A streptogramin), lincomycin (a lincosamide) and tiamulin (a pleuromutilin).

4.1.3 Structures of ARE ABC-F protein : ribosome complexes

The cryo-EM structure of the ARE ABC-F protein MsrE from *P. aeruginosa* bound to the ribosome from *T. thermophilus* was solved after *in vitro* complex formation [260]. MsrE, pre-incubated with the non-hydrolysable ATP analogue AMP-PNP, was mixed with ribosomes pre-incubated with $tRNA^{fMet}$ and mRNA. As ATP hydrolysis is required for protein release, AMP-PNP locks the protein to the ribosome.

Similarly to EttA [286], MsrE binds to the E-site of the ribosome with its interdomain linker protruding towards the PTC. This linker comprises two long, crossed helices, which interact with 23S rRNA H68, H74, H80 and H93, and the acceptor stem of P-site tRNA, which shifts by 30 Å towards the A-site. The linker helices are joined by an extended loop, which interacts with the PTC/NPET. The sidechains of residues Arg241, Leu242 and His244 of this loop approach the macrolide binding site (Figure 32A). In particular, Arg241 appears to deform 23S rRNA residues A2503, U2503 and U2506 from their azithromycin-binding positioning, and His244 blocks movement of A2062, and by doing so, likely blocks the relay of the macrolide stalling signal to the PTC [292]. U2585 is also displaced from the PTC to stack with A2602.

Another cryo-EM structure solved was of the complex between VmlR and the ribosome, both from *B. subtilis* [267]. This complex was generated by incubation of the ErmDL/telithromycin-stalled ribosome complex with the EQ_2 mutant of VmlR and ATP. As above, VmlR binds to the E-site of the ribosome with its interdomain linker protruding towards the PTC. Its NBDs contact the L1 stalk, 23S rRNA H68, 16S rRNA h41-42, ribosomal proteins uL5 and bL33, and the elbow of P-site tRNA. The interdomain linker contacts 23S rRNA H74-75 as well as the acceptor arm of P-site tRNA, which, as in the MsrE-ribosome complex, is distorted towards the A-site. 23S rRNA A2602, which normally interacts with the CCA-terminus of P-site tRNA, flips to stack with VmlR Trp223, clearing the way for distortion of the tRNA away from the PTC. Unlike MsrE, VmlR has a C-terminal extension that extends from NBD2 through a cleft between ribosomal proteins uS7 and uS11, towards the SD-anti-SD cavity.

The interdomain linker of VmlR is slightly shorter than that of MsrE, which coincides with the respective resistance phenotypes these proteins confer: VmlR confers resistance to PTC-binding LS_AP antibiotics, whereas MsrE confers resistance to MS_B antibiotics, which bind deeper in the ribosome at the entrance to the NPET. The linker loop of VmlR extends towards the A- and P-site pockets, where the LS_AP antibiotics bind (Figure 32B). In particular, Phe237 directly overlaps with the drug binding site. 23S rRNA regions that shift on VmlR binding include A2062, U2506 and U2585, the latter of which stacks with Tyr240 of VmlR, preventing it from adopting a drug-binding conformation.

The most recent cryo-EM structures solved were of complexes between *E. faecalis* LsaA, *S. haemolyticus* $VgaA_{LC}$ and *L. monocytogenes* VgaL and ribosomes from *E. faecalis*, *S. aureus* and *L. monocytogenes* respectively [187]. These proteins mediate resistance to LS_AP antibiotics. Ribosomes locked with FLAG-tagged EQ_2 mutant protein were isolated from bacterial cells by affinity purification. These complexes were found to contain initiator $tRNA^{fMet}$ in the P-site, identifying the ribosomes as 70S initiation complexes. Only $VgaA_{LC}$ and VgaL contain C-terminal extensions, which do not contact the SD-anti-SD helix in these complexes, suggesting they are not involved in substrate recognition.

As in the other structures, all three proteins bind to the E-site of the ribosome with their interdomain linkers protruding towards the PTC, the location where LS_AP drugs bind (Figure 32C), distorting the acceptor stem of P-site tRNA in the process. The residues of the interdomain linker loops reaching closest to the drug site were Phe257 in LsaA, Val219 in $VgaA_{LC}$ and Ala216 in VgaL. LsaA Phe257 and $VgaA_{LC}$ Val219 both overlap with the drug binding site, although there is no pattern between steric overlap and resistance phenotype. Other residues of note include Tyr223 of $VgaA_{LC}$, which stacks with 23S rRNA U2585 to flip it away from the drug binding site in a similar way to Tyr240 of VmlR, and Trp236 of LsaA, which stacks with 23S rRNA A2602 in a similar way to VmlR Trp223, to prevent the base from interacting with the CCA-terminus of P-site tRNA. $VgaA_{LC}$ residues Phe224 and Lys227 also interact with C2601-A2602, to elicit a similar effect.

The 23S rRNA region A2503-U2506, termed PL3, is distorted by the binding of all three ABC-F proteins. None of these proteins contact PL3 directly, but they do displace the loop around A2451, termed PL2, which may in turn distort PL3. Both PL2 and PL3 are involved in drug interactions (Figure 32C). In general, no single set of 23S rRNA rearrangements were seen among the LsaA-, $VgaA_{LC}$- and VgaL-ribosome complexes, although all involved displacement of PL3.

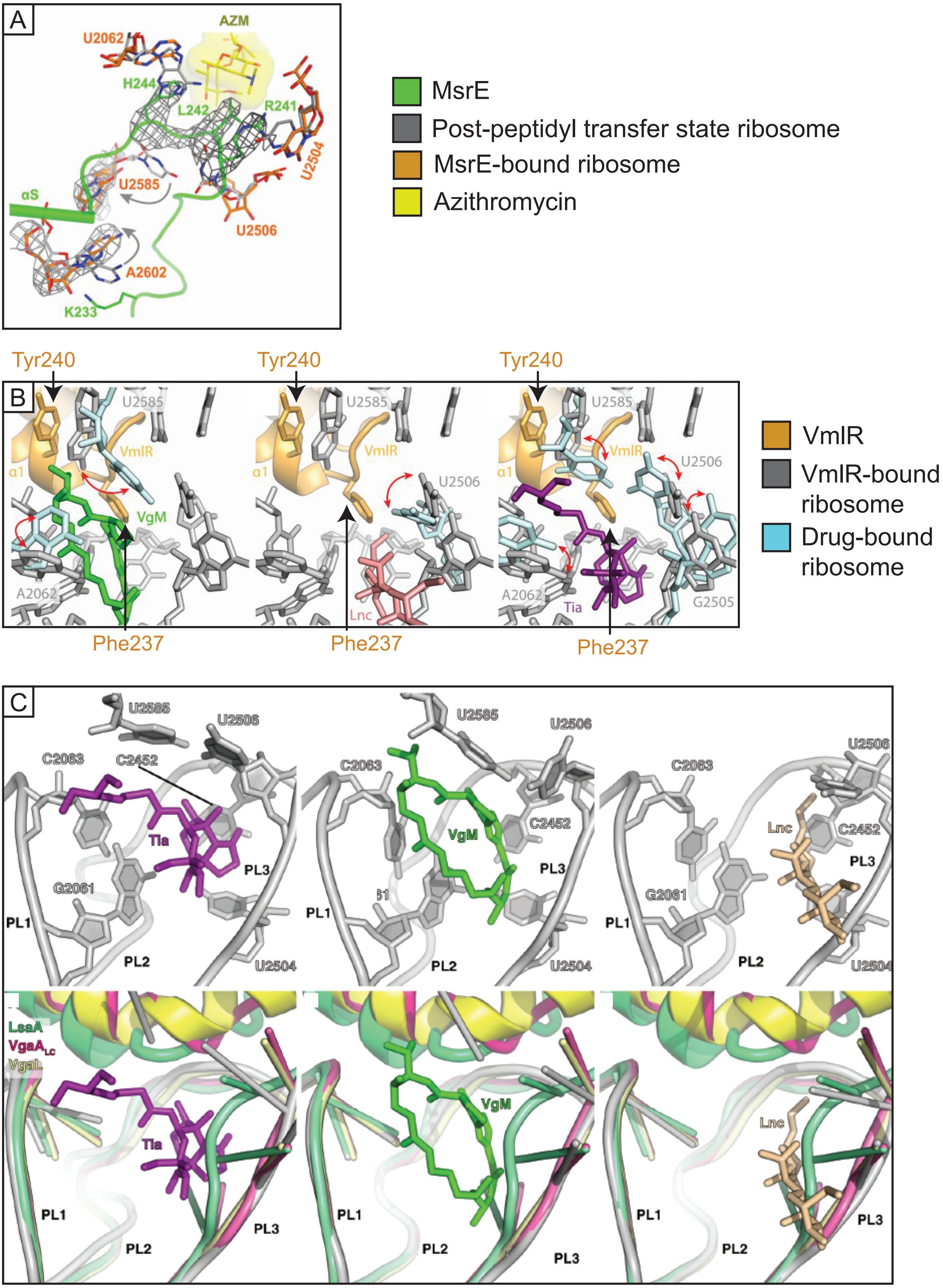
A
AZM
U2062
H244
L242
R241
U2504
U2585
αS
U2506
A2602
K233
🟩 MsrE
⬛ Post-peptidyl transfer state ribosome
🟧 MsrE-bound ribosome
🟨 Azithromycin
B
Tyr240
U2585
VmlR
α1
VgM
A2062
Phe237
U2506
Lnc
Tia
G2505
🟧 VmlR
⬛ VmlR-bound ribosome
🟦 Drug-bound ribosome
C
U2585
U2506
C2063
C2452
Tia
G2061
PL1
PL2
PL3
U2504
VgM
Lnc
LsaA
$VgaA_{LC}$
VgaL

Figure 32 Interactions between the interdomain linkers of ABC-F proteins and the PTC/NPET. A) Interaction between the interdomain linker loop of MsrE (green) with selected 23S rRNA residues. Residues in the PTC and macrolide binding site in the MsrE-ribosome complex (orange, PDB 5ZLU) are shown compared with the same residues in a ribosome in the post-peptidyl transfer state (grey, PDB 4V5C). Conformational changes shown by arrows. EM density shown for key MsrE and 23S rRNA residues (grey mesh). Position of azithromycin shown for reference (yellow, PDB 4V7Y). B) Interaction between the interdomain linker of VmlR (orange) with the PTC. Residues in the PTC in the VmlR-bound ribosome (grey, PDB 6HA8) are shown compared with residues in drug-bound ribosomes (light blue; left = ribosome in complex with virginiamycin M1 (VgM, green), PDB 1YIT; centre = lincomycin (Lnc, pink) : ribosome complex, PDB 5HKV; right = tiamulin (Tia, purple) : ribosome complex, PDB 1XBP). C) Changes in the PTC upon ABC-F protein binding to the ribosome. 23S rRNA residues in the drug-ribosome complexes (grey; left = tiamulin (Tia, purple) : ribosome complex, PDB 1XBP; centre = virginiamycin M1 (VgM, green) : ribosome complex, PDB 1YIT; right = lincomycin (Lnc, brown) : ribosome complex, PDB 5HKV) are shown compared with the same residues in the LsaA-ribosome complex (green), the VgaA$_{LC}$-ribosome complex (pink) and the VgaL-ribosome complex (yellow). Figure adapted from [187,260,267].

Alongside structure determination, mutagenesis studies were undertaken on these ABC-F proteins to determine the residues involved in drug displacement.

Mutations to alanine of Arg241, Leu242 or His244 of MsrE, residues on the interdomain linker loop which protrude towards, and overlap with, the macrolide binding site do not significantly affect MsrE-ribosome binding, but diminish the ability of the protein to mediate azithromycin resistance *in vivo* or to rescue azithromycin-affected translation *in vitro*. This suggests that the interdomain linker loop of MsrE mediates drug displacement through steric overlap (type I target protection), or possibly a combination of allosteric displacement (type II target protection) and steric overlap [260].

Interdomain linker residue Phe237 of VmlR overlaps with the LS$_A$P drug site. Mutation of Phe237 to valine, which has a side chain too short for such an overlap, has no effect on the resistance activity of VmlR, suggesting that VmlR does not displace drug through steric overlap. Even mutation of this residue to alanine merely altered the resistance specificity, maintaining resistance to lincomycin and tiamulin but not to virginiamycin M1. Similarly, no change in resistance was observed when LsaA Phe257 and VgaA$_{LC}$ Val219 were mutated to alanine. However, mutation to alanine of residues that interact with 23S rRNA around the binding site e.g. VgaA$_{LC}$ Tyr223, or residues that may be involved in positioning of the interdomain linker loop in the PTC, e.g. VgaA$_{LC}$ residues Phe224 and Lys227, diminished antibiotic resistance. These findings suggest that VmlR, LsaA, VgaA$_{LC}$ and VgaL remove antibiotic from the ribosome by allosteric displacement (type II target protection), with little or no contribution from steric overlap [187,267].

4.1.4 Mechanism of ribosome protection

These structural and mutagenesis studies involving ARE ABC-F proteins allow for mechanistic models of ribosome protection to be proposed [187,260,267].

ATP-bound NBDs of the ABC-F protein binds to a ribosome with an empty E-site, either a stalled ribosome in the case of proteins like MsrE that confer resistance to translation elongation inhibitors, or an initiation complex for those proteins like VgaA_{LC}, VgaL, Lsa and VmlR that mediate resistance to antibiotics inhibiting the first peptidyl transfer event [84,293]. In some cases, as in VmlR, a C-terminal extension may facilitate specificity by interacting with the 30S subunit at the mRNA exit channel [267]. The interdomain linker of the ABC-F protein protrudes towards the PTC/NPET region of the 50S subunit, distorting the acceptor stem of P-site tRNA in the process. Ribosome-bound drug is likely removed through steric overlap, allosteric displacement or a combination of the two. ATP hydrolysis then triggers the removal of ABC-F protein. The PTC is ‘reset’ [288], with P-site tRNA returned to the P/P-position, which allows for the first peptidyl transfer reaction to happen. The nascent chain likely blocks drug rebinding, which would mean that only one round of ABC-F binding and ATP hydrolysis per translation cycle is necessary for resistance. Other possible models are discussed in section 4.3.2.

4.1.5 Sal-type ABC-F proteins

Sal-type ABC-F proteins mediate resistance to $\text{LS}_{\text{A}}\text{P}$ antibiotics, i.e. lincosamides, streptogramin As and pleuromutilins, which target the ribosome at the PTC [277,294]. Since 2007, the pleuromutilin retapamulin has been approved for topical use to treat infections caused by *S. aureus* and other Gram-positive pathogens in humans [82], and in 2019 lefamulin was approved for systemic use [295]. Thankfully, pleuromutilin resistance amongst these pathogens is uncommon [84]. However, the prevalence of *vga*-, *lsa*- and *sal*-type genes among staphylococcal species is a cause for concern; for example, *sal(A)*-type genes have previously been detected in *S. scuiri*, *S. epidermis*, *S. haemolyticus* and *S. xylosus* [277,296].

More recently, pleuromutilin resistance genes were discovered in a collection of non-aureus staphylococcal species from human and animal sources, the majority of which were *sal*-type genes (*unpublished work: Merianne Mohamad, Chayan Kumar Saha, Gemma Atkinson and Alex J. O’Neill*). Genes coding for Sal(B), with 68% predicted protein sequence to Sal(A), were found in *S. lentus*, and genes coding for Sal(C), with 71% and

68% protein identity to Sal(A) and Sal(B) respectively, were found in *S. fleurettii*. Regulated expression of Sal(A), Sal(B) and Sal(C) in *S. aureus* RN4220 all conferred reductions in LS_AP susceptibilities (Table 6).

Further Sal variants were found by Basic Local Alignment Search Tool (BLAST) searching genome sequence data from non-aureus staphylococci. These included *sal(D)* from *S. gallinarum,* predicted to code for a protein with 45% identity to Sal(A), and *sal(E)* from *S. nepalensis*, predicted to code for a protein with 43% identity to Sal(A). Expression of these variants in *S. aureus* RN4220 shows that Sal(D) is less effective in reducing susceptibility to lincosamides compared with Sal(A), Sal(B) and Sal(C), while Sal(E) has no apparent effect on susceptibility to lincosamides or streptogramin As, and reduces susceptibility to pleuromutilins to a lesser degree than the other variants (Table 6). *In silico* analysis of genome data also detected gene variants in *S. xylosus* (41% protein identity to Sal(A)), *S. equorum* (42% protein identity to Sal(A)) and *S. saprophyticus* (40% protein identity to Sal(A)). None of these three variants caused any change in susceptibility to the antibiotics tested compared with a vector-only control (data not shown).

Construct carrying	MIC (µg/ml)				
	Pleuromutilins		Lincosamides		Streptogramins (group_A)
	Retapamulin	Tiamulin	Lincomycin	Clindamycin	Virginiamycin M1
Vector only control	0.03	0.5	0.125	0.06	1
sal(A)	4	8	8	2	4
sal(B)	8	4	4	2	2
sal(C)	16	4	4	1	4
sal(D)	4	8	1	0.06	2
sal(E)	2	2	0.125	0.06	1

Table 6 Antibiotic resistance profile of *sal*-type genes expressed in *S. aureus* RN4220. Minimum inhibitory concentrations (MICs) of antibiotics needed to inhibit the visible growth of cells after overnight incubation. Data from unpublished work: Merianne Mohamad, Chayan Kumar Saha, Gemma Atkinson and Alex J. O'Neill.

Phylogenetic analysis of ARE6, the ABC-F subfamily in which Sal(A) resides, confirms that all eight Sal variants identified above belong to this subfamily, and that it comprises a bipartite structure, with Sal(D) and Sal(E) in a clade distinct from Sal(A), Sal(B) and Sal(C). All *sal* genes share a well-conserved genomic context that is present even in species lacking *sal*, suggesting that *sal* genes are not being horizontally transferred among staphylococci; rather, *sal* is ancestral to the genus *Staphylococcus*, and gene loss accounts for species with no *sal*-type genes. This finding, along with the fact that three of the *sal* genes isolated did not appear to mediate resistance to antibiotics, strongly suggests that antibiotic resistance is not the original, evolved function of Sal-type proteins, but they rather have a housekeeping role, likely in modulating translation in similar ways to non-ARE ABC-F translation factors like EttA [270,286].

S. aureus is a species that has lost *sal*, but it could plausibly recapture it in the future, especially under increasing selection pressure as pleuromutilins are used in human and animal healthcare. Understanding the mechanism by which Sal proteins confer resistance will provide a head-start in improving and designing new pleuromutilin drugs to circumvent this mechanism, if such an event arises.

4.1.6 Aims of project

A better understanding of ribosome protection by ARE ABC-F proteins could help with the design of new antibiotics able to circumvent or inhibit such mechanisms. Biochemical and structural studies up to this point have revealed the interactions that some of these proteins make with the ribosome, and provided mechanistic insights into how PTC-binding antibiotics are removed. However, some questions remain unanswered. All the structures solved so far, i.e. those of complexes between the ribosome and MsrE, VmlR, LsaA, VgaA_{LC} and VgaL, show the importance of the interdomain linker in mediating drug removal, but how it does so appears to differ among the different proteins. Increasing the repertoire of ARE ABC-F protein : ribosome complexes will build on these findings, and possibly shed light on universal mechanisms by which ABC-F proteins displace antibiotics from the ribosome.

The discovery that *sal* variant genes from staphylococcal species confer different resistance phenotypes is also of interest (Table 6). A comparison of structures of such Sal variants in complex with the ribosome might reveal how sequence differences in these variants leads to differences in resistance phenotype. Shedding light on such a link between protein sequence and resistance phenotype would help in understanding the mechanisms by which ABC-F proteins mediate resistance more generally.

To that end, the aims of this project were to solve the cryo-EM structures of physiological Sal-ribosome complexes, compare the structures of Sal variants, and perform mutagenesis experiments to probe the drug-displacement mechanism. This work was carried out to answer the following questions:

1. How do ARE Sal-type ABC-F proteins protect the ribosome from $\text{LS}_{\text{A}}\text{P}$ antibiotics?
2. What are the reasons for the differences in antibiotic resistance profiles among the Sal variants?
3. Is there a common mechanism by which the ABC-F proteins MsrE, VmlR, LsaA, VgaA_{LC}, VgaL and Sal mediate resistance?

4.2 Results

4.2.1 Interdomain linker sequence comparison of the Sal variants

When ABC-F resistance proteins bind to the ribosome, the interdomain linker of the protein protrudes towards the PTC of the 50S subunit, where it displaces antibiotics bound to the PTC or NPET. Therefore, differences in the interdomain linker protein sequence between the Sal variants may explain the different resistance profiles among the variants (Table 6).

To identify the region of the Sal protein that corresponds to the interdomain linker, the Sal(A) protein sequence was aligned with the protein sequence of VmlR, an ARE ABC-F that similarly confers resistance to LS_AP antibiotics and has a known ribosome-bound structure (PDB 6HA8) [267]. Residues 213-256 of Sal(A) align with VmlR residues 192-235, which form the first, longer α-helix of the interdomain linker, residues 267-290 of Sal(A) align with VmlR residues 249-272 which form the second, shorter α-helix, and residues 257-266 of Sal(A) align with residues 236-245 of VmlR, which forms part of the interhelical loop. Overall, the interdomain linker of Sal(A) is predicted to comprise residues 213-290 (Figure 33).

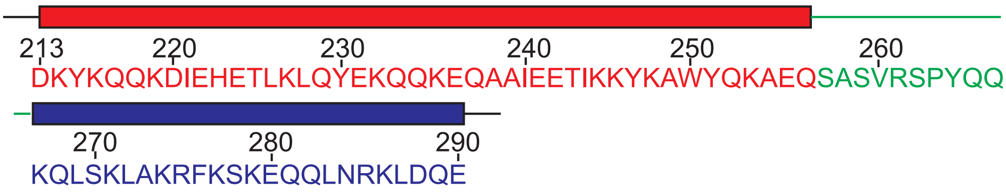

Figure 33 Predicted protein sequence of the interdomain linker of Sal(A). Sequence alignment with VmlR predicts that Sal(A) residues 213-290 form the interdomain linker. Residues 213-256 form the first α-helix (red), residues 257-266 form the interhelical loop (green), and residues 267-290 form the second α-helix (blue). Alignment of Sal(A) with the VmlR template was carried out using SWISS-MODEL [163].

The corresponding sequences of the eight Sal variants described in section 4.1.5 were aligned and their protein sequence identities calculated (Table 7). The variants that were analysed included five variants (Sal(A-E)) that confer resistance, and the Sal proteins from *S. xylosus*, *S. equorum* and *S. saprophyticus*, none of which confer resistance.

	Sal(A)	Sal(B)	Sal(C)	Sal(D)	Sal(E)	*S. xyl*	*S. equ*	*S. sap*
Sal(A)	**100**							
Sal(B)	**78**	**100**						
Sal(C)	**78**	**73**	**100**					
Sal(D)	*51*	*51*	*51*	**100**				
Sal(E)	*51*	*53*	*51*	60	**100**			
S. xyl	49	46	49	*57*	*58*	**100**		
S. equ	49	*50*	*50*	63	64	**76**	**100**	
S. sap	45	47	46	*53*	*54*	66	65	**100**

Table 7 Protein sequence identities (%) of Sal variant interdomain linkers. Interdomain linker percentage protein sequence identities between the five ARE Sal variants (Sal(A)-E) and the non-resistance Sal variants from *S. xylosus* (*S. xyl*), *S. equorum* (*S. equ*) and *S. saprophyticus* (*S. sap*). Bold = protein sequence identities >69%, underlined = 60-69%, italics = 50-59%, no formatting = <50%. Analysis was carried out using the Clustal Omega Multiple Sequence Alignment tool [297].

The interdomain linker protein sequences are highly similar for Sal(A-C) (73-78% identity). This correlates with the similar resistance profiles of these three variants. The interdomain linkers of the non-resistance Sal variants are perhaps unsurprisingly, more divergent (45-50% sequence identity). Following this pattern, Sal(D) and Sal(E), which exhibit weak resistance phenotypes, have quite similar interdomain linkers to Sal(A-C) (51-53% sequence identity).

Although they are not quite as similar as in Sal(A-C), the interdomain linkers of the three non-resistance Sal variants also form a group of high sequence identity (65-76%), and the linkers of Sal(D) and Sal(E) are also moderately similar to each other (60% sequence identity). Finally, the linkers of Sal(D) and Sal(E) are moderately similar to the linkers of the three non-resistance variants (53-64% identity).

Overall, groupings based on interdomain linker protein sequence appear to roughly correspond with groupings based on resistance profiles, with Sal(A-C) forming one group, Sal(D-E) another, and the non-ARE Sal variants a third. However, this overall sequence comparison is of limited use without corresponding structural information to identify which residues of the interdomain linker are likely to be important in ribosome binding and antibiotic displacement.

4.2.2 Isolation of physiological Sal-ribosome complexes

To acquire purified Sal-ribosome complexes for cryo-EM structure determination, *in vivo* FLAG-tag affinity purification was performed to pull the complexes directly out of *S. aureus* cells after overexpression of the Sal variants. This approach was performed to yield physiological complexes more likely to be representative of a true biological complex compared with complexes reconstituted *in vitro*. Furthermore, *in vitro* reconstitution might prove challenging as it would require initial purification of the Sal protein, which might be unstable in its non-ribosome-bound state, followed by incubation with a number of components, namely tRNA, mRNA and purified ribosome [260].

Firstly, genes coding for C-terminally $FLAG_3$-tagged ‘EQ_2 mutants’ of the Sal variants (Sal(A-E)) were synthesised (sequences can be found in Appendix). EQ_2 mutants were used to lock the proteins to the ribosome to ensure a homogenous sample suitable for cryo-EM structure determination [267,286]. The C-terminal $FLAG_3$-tag was included for affinity purification of the complexes.

These genes were expressed from the pRMC2 expression vector in *S. aureus* SH1000, allowing formation of locked Sal-ribosome complexes *in vivo*, which were isolated by FLAG-tag affinity purification. To assess whether Sal-ribosome complexes were eluted at the expected stage, samples were taken throughout the purification of the Sal(B)-ribosome complex and run on an SDS-PAGE gel, which was then silver stained to reveal bands corresponding to protein and RNA. These samples were compared with those taken from the same procedure carried out on an empty vector negative control containing no $FLAG_3$-tagged Sal (Figure 34).

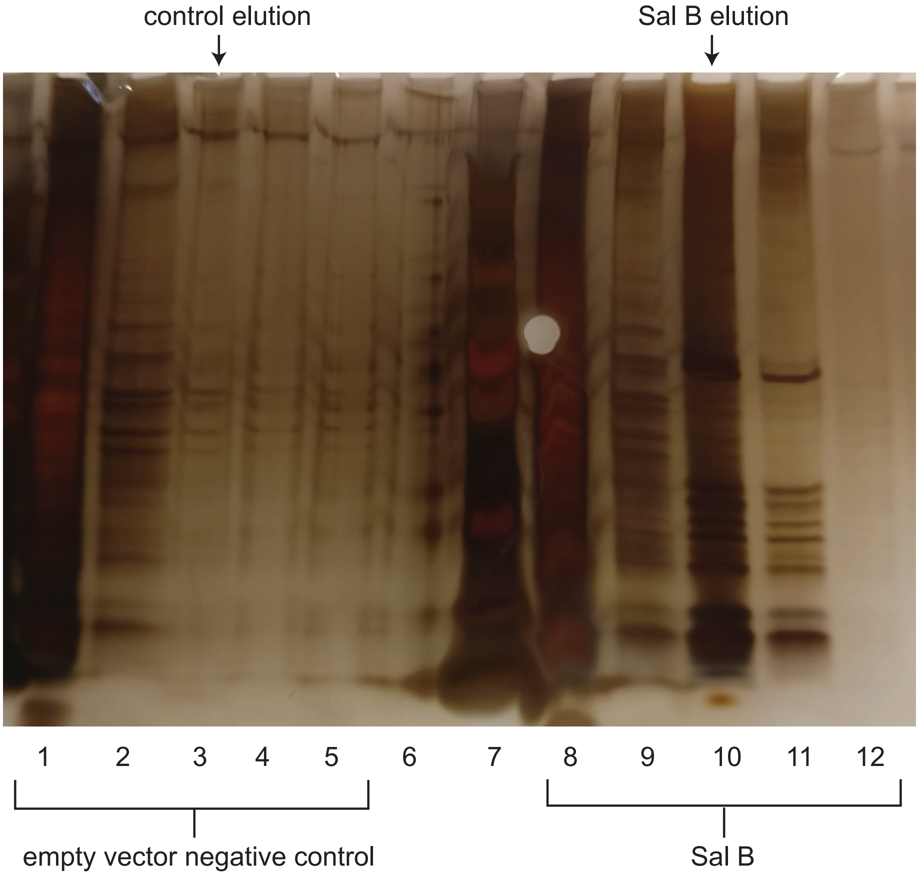

Figure 34 Silver-stained SDS-PAGE gel of the Sal(B)-ribosome complex purification. Samples were taken at stages throughout the FLAG-tag affinity purification of the Sal(B)-ribosome complex (lanes 8-12), as well as throughout the same procedure performed on an empty vector negative control (lanes 1-5). Lane 1 control flow-through, lane 2 control final wash, lane 3 control elution, lane 4 control post-elution wash, lane 5 control glycine-HCl bead strip, lane 6 empty, lane 7 protein ladder, lane 8 Sal(B) flow-through, lane 9 Sal(B) final wash, lane 10 Sal(B) elution, lane 11 Sal(B) post-elusion wash, lane 12 Sal(B) glycine-HCl bead strip

The elution fraction from the purification of the Sal(B)-ribosome complex gave many strong bands when run on a gel (Figure 34, lane 10), presumably corresponding to ribosomal proteins, rRNA and Sal(B). In comparison, only very weak bands were seen for the elution fraction from the empty vector control experiment (Figure 34, lane 3). This suggests that although some non-specific binding to the anti-FLAG beads occurs, the Sal(B)-ribosome complex is by far the dominant product in the Sal(B)-ribosome elution. Bands were also found in the samples taken from the pre-elution and post-elution wash steps (Figure 34, lane 9 & 11), although these were much weaker than the bands of the elution fraction, suggesting much of the complex was eluted in the expected fraction.

To confirm that the elution fraction protein bands in the SDS-PAGE gel truly do correspond to a ribosome complex, and to assess purity, a sample from the elution fraction was imaged by negative stain TEM. The micrograph showed highly pure ribosome particles at high concentration (Figure 35C). The ribosome yield was clearly larger in this sample compared with that in the elution fraction from the negative control (Figure 35A). The small number of ‘background’ ribosome particles seen in the negative control (Figure 35A), shows that some *S. aureus* ribosomes with no $FLAG_3$-tagged Sal protein bound attached non-specifically to the anti-FLAG beads.

Overall, the SDS-PAGE gel and the negative-stain TEM micrographs show that overexpression of $FLAG_3$-tagged Sal(B) in *S. aureus* followed by FLAG-tag affinity purification gave large, pure yields of Sal(B)-ribosome complex. Therefore, the same procedure was carried out for the other Sal variants.

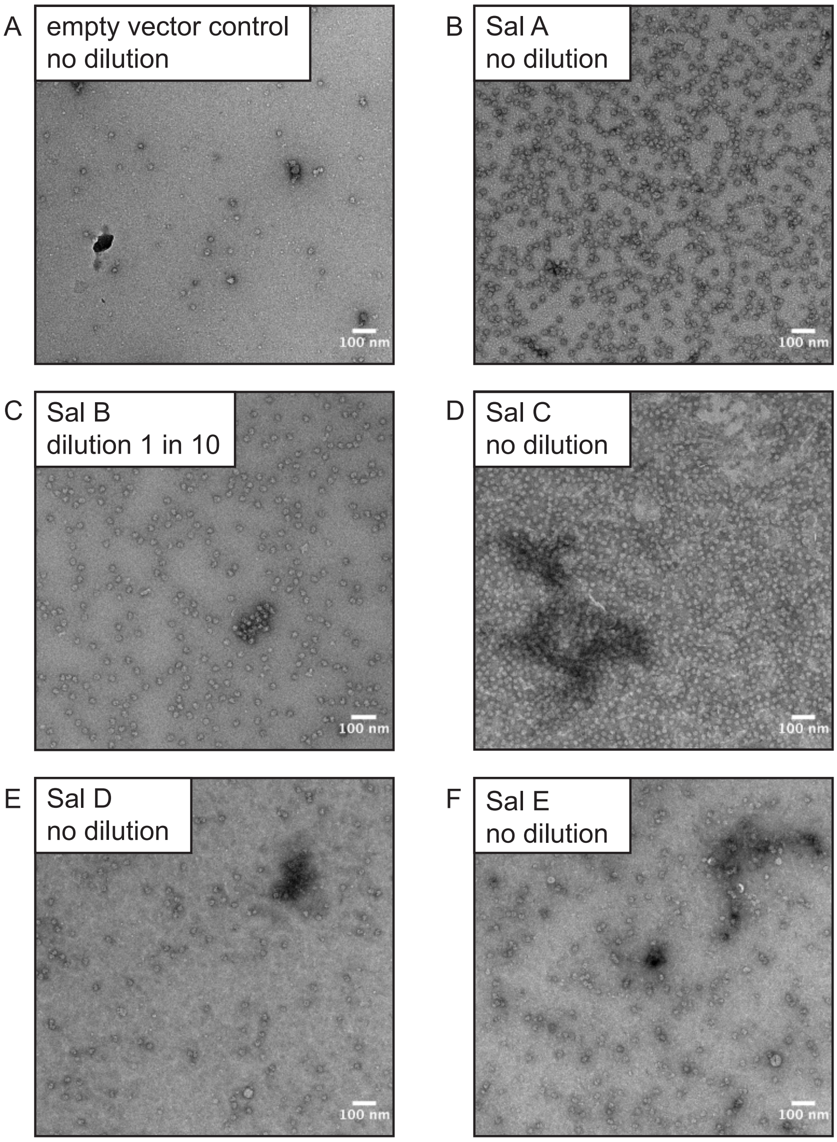

Figure 35 Representative negative stain TEM micrographs of elution fractions from FLAG-tag affinity purification of Sal-ribosome complexes. A) Empty vector negative control, undiluted. B) Elution fraction from Sal(A)-ribosome complex purification, undiluted. C) Elution fraction from Sal(B)-ribosome complex purification, diluted 1 in 10. D) Elution fraction from Sal(C)-ribosome complex purification, undiluted. E) Elution fraction from Sal(D)-ribosome complex purification, undiluted. F) Elution fraction from Sal(E)-ribosome complex purification, undiluted. Scale bar 100 nm.

The same procedure was carried out for the FLAG$_3$-tagged EQ$_2$ mutants of Sal(A) and Sal(C), and samples from the elution fractions were visualised by negative stain TEM (Figure 35B&D). Similarly to Sal(B), high yields of ribosomes, presumably in complex with Sal, were found in both cases.

However, the procedure was less successful for Sal(D) and Sal(E). Samples taken from the elution fractions were run on an SDS-PAGE gel, which was then silver stained (Figure

36, lanes 3&4). These samples gave bands of similar strength to sample taken from the negative control (Figure 36, lane 2).

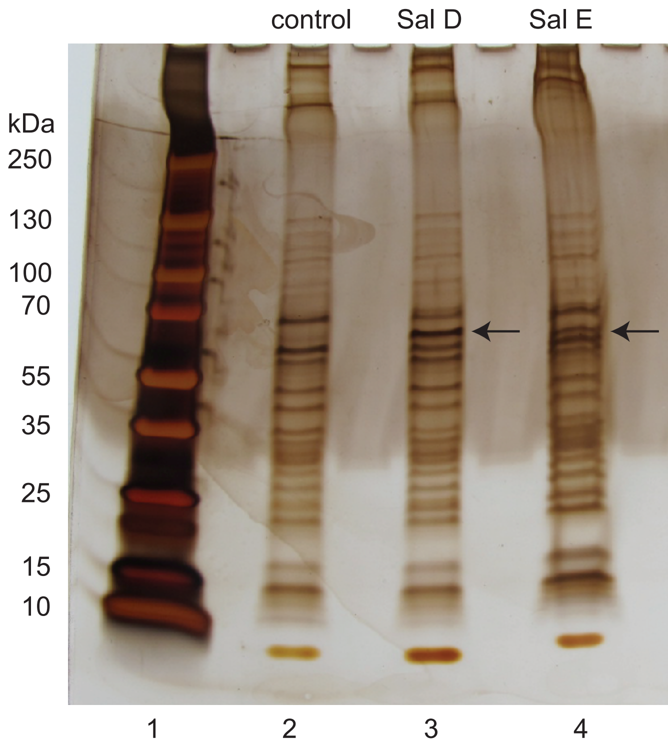

Figure 36 Silver-stained SDS-PAGE gel of elution fractions from the Sal(D)-ribosome and Sal(E)-ribosome complex purifications. Lane 1 protein ladder, lane 2 empty vector control elution, lane 3 Sal(D) elution , lane 4 Sal(E) elution. Arrows point to band that may correspond to the Sal protein. N.B. This elution was carried out using smaller volumes of buffer and higher concentration of 3X FLAG peptide compared to that used for the elution of the Sal(A)-, Sal(B)- and Sal(C)-ribosome complexes in an attempt to yield a more concentrated product.

Furthermore, imaging the Sal(D) and Sal(E) elution samples by negative-stain TEM showed that these samples contained only marginally more ribosomes than the negative control, and also contained greater numbers of non-ribosome impurities (Figure 35A,E&F). These results suggest that few, if any, Sal-ribosome complexes were found in the elution fractions of the Sal(D) and Sal(E) purifications. Such low yields presumably allowed for more non-specific binding to the anti-FLAG beads, leading to relatively impure samples compared with the Sal(A)-, Sal(B)-, and Sal(C)-ribosome complexes.

Possible reasons for the lower yields of Sal(D)- and Sal(E)-ribosome complexes compared with Sal(A)-, Sal(B)- and Sal(C)-ribosome complexes are discussed in section 4.2.3 below. Despite the low yields and purities of the Sal(D) and Sal(E) samples, cryo-EM structure determination was attempted for all five Sal-ribosome complexes, with the intention of separating out heterogeneity computationally [153].

4.2.3 Cryo-EM structure determination of the Sal-ribosome complexes

The Sal(B)-ribosome complex was the first to be analysed by cryo-EM. The structure determination workflow of this complex will be described in detail in section 4.2.3.1, and then significant differences in the workflow for the other four complexes will be outlined in section 4.2.3.2.

4.2.3.1 Sal(B)-ribosome complex

Sample from the elution fraction was applied to a cryo-grid and frozen in liquid ethane. Highly concentrated ribosome particles were found to be evenly spread across the grid holes where imaging occurs, giving large numbers of particles per micrograph (Figure 37).

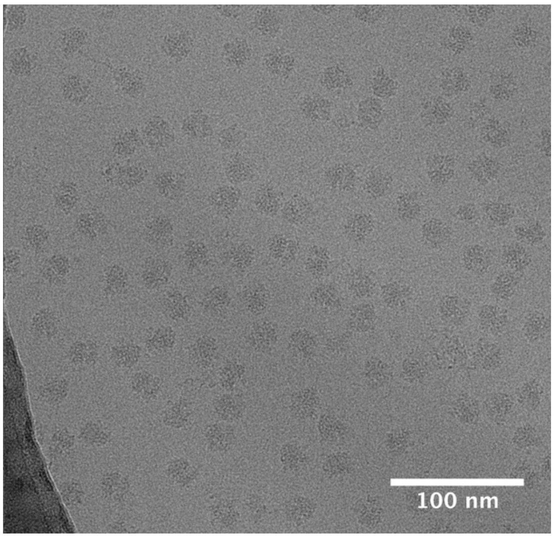

Figure 37 Representative cryo-EM micrograph of the Sal(B)-ribosome complex. Particles were distributed evenly across the grid holes, allowing for large number of particles per micrograph.

847 micrographs were collected, from which particles were extracted, aligned and classified in 2D (Figure 38A). Particles assigned to lowly populated classes showing no high-resolution features were discarded as junk. Removal of junk particles was similarly performed by 3D classification, leaving 67,139 particles. These were aligned and refined in 3D, and Bayesian particle polishing and CTF refinement was performed. 3D classification

without particle alignment removed further poorly-aligned particles, leaving 64,101 particles. These yielded a 2.9 Å resolution map after alignment and refinement in 3D.

In order to improve the resolution and estimate the occupancy of the Sal protein, focussed classification was performed with a mask around density in the E- and P-sites of the ribosome (Figure 38B), since the globular NBDs of ABC-F proteins are known to bind to the E-site of the ribosome, and P-site tRNA is consistently present in known ABC-F protein : ribosome complex structures [187,260,267]. The majority of the particles (59,889, 93%) were assigned to classes that contained E-site and P-site density, which together yielded a final 3D reconstruction of 2.9 Å (Figure 38C-D).

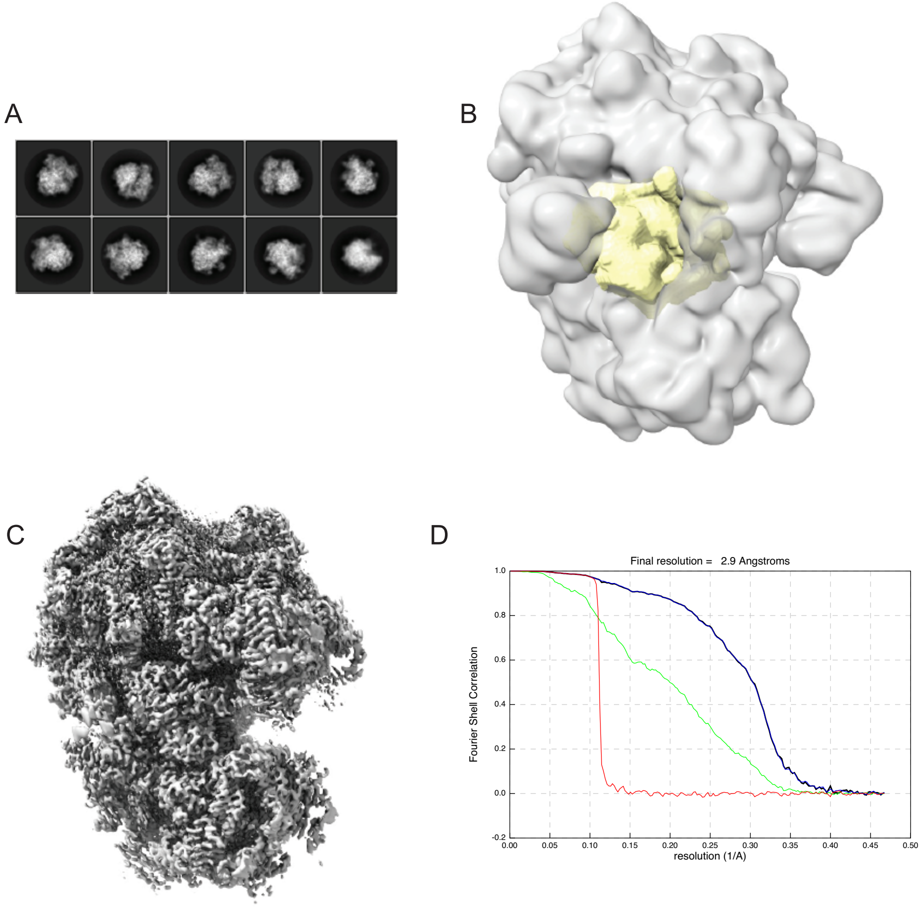

Figure 38 Image processing workflow for structure determination of the Sal(B)-ribosome complex. A) Representative 2D classes after alignment of the extracted particle projection images. B) Mask around the P- and E-sites that was used in the focussed classification procedure (yellow). Shown around a 3D reconstruction of the complex low-passed filtered to 15 Å (transparent grey). C) Final 3D reconstruction of the Sal(B)-ribosome complex. The map was sharpened and filtered by estimated local resolution. D) FSC curves as a function of resolution for the final reconstruction. The resolution that corresponds to an FSC coefficient of 0.143 is 2.9 Å. FSC curves are shown for phase-randomised maps (red), unmasked maps (green), masked maps (blue), and masked maps after correction for mask convolution effects (black).

The local resolution of the final reconstruction was estimated to range from 2.5 Å in the core of the 50S subunit to 4.5 Å in the periphery of the subunits, with generally worse resolution in the 30S subunit than the 50S subunit (Figure 39A). This is likely because image alignment is dominated by the larger 50S subunit and there is some inter-subunit rotation despite the bridging Sal(B) and P-site tRNA. Multibody refinement was carried out, using masks around the 50S subunit, the 30S body and the 30S head (Figure 39B). This had only a minor effect on the density of the already well-aligned 50S subunit, but offered improved resolution and quality of density for the 30S subunit (Figure 39C). The resolutions of the 50S, 30S body and 30S head following multibody refinement were 2.8, 3.0 and 3.0 Å respectively (Figure 39D-F).

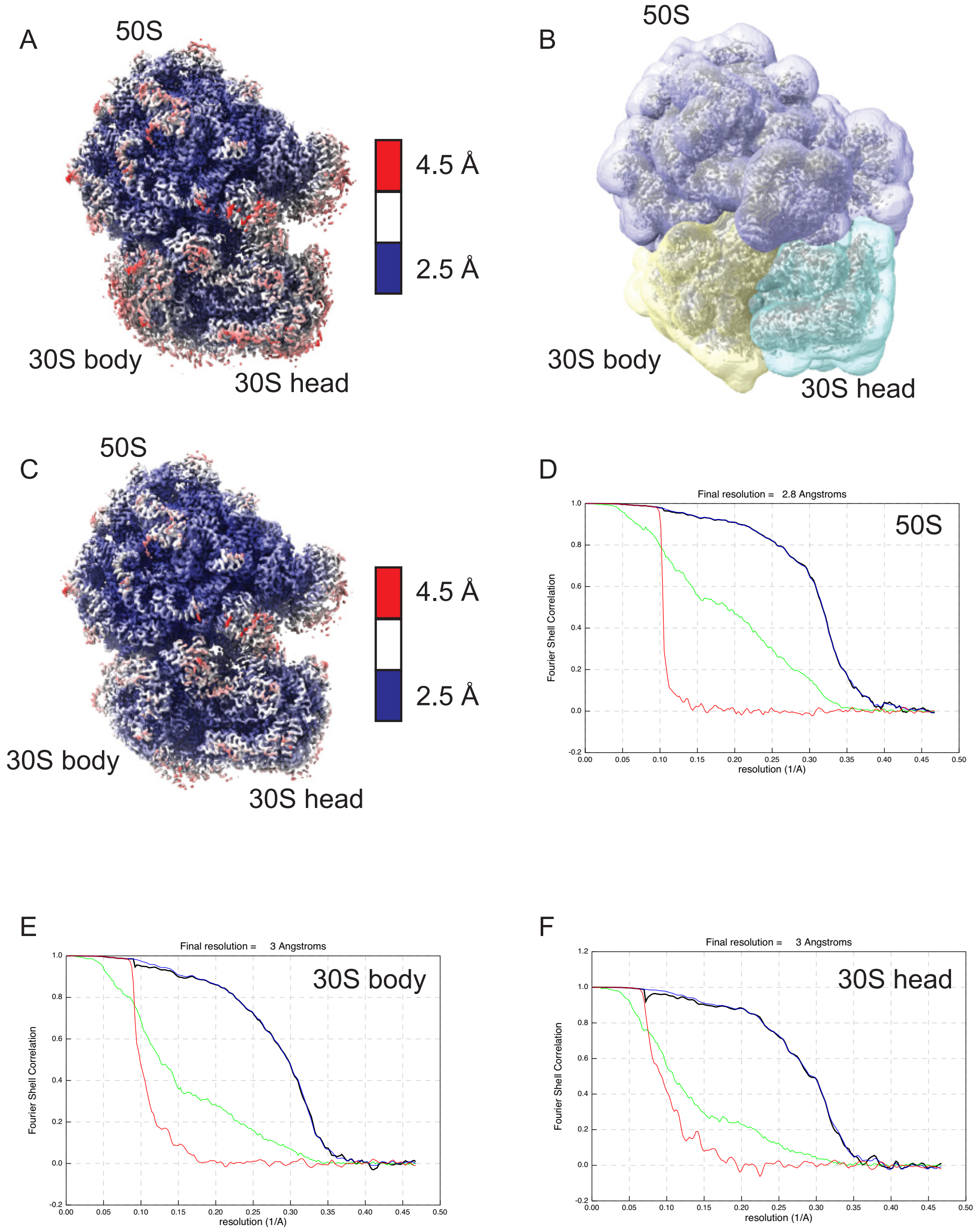

Figure 39 Local resolution estimation and multibody refinement of the Sal(B)-ribosome complex. A) Consensus map of the Sal(B)-ribosome complex filtered and coloured by estimated local resolution. B) 50S mask (purple), 30S body mask (yellow) and 30S head mask (blue) used for multibody refinement shown around the consensus map (grey). C) Superposed maps of the 50S, 30S body and 30S head following multibody refinement, filtered and coloured by estimated local resolution. D) FSC curves as a function of resolution for the 50S reconstruction. The resolution that corresponds to an FSC coefficient of 0.143 is 2.8 Å. E) FSC curves as a function of resolution for the 30S body reconstruction. The resolution that corresponds to an FSC coefficient of 0.143 is 3.0 Å. F) FSC curves as a function of resolution for the 30S head reconstruction. The resolution that corresponds to an FSC coefficient of 0.143 is 3.0 Å. FSC curves are shown for phase-randomised maps (red), unmasked maps (green), masked maps (blue), and masked maps after correction for mask convolution effects (black).

The local resolution of the E-site density corresponding to Sal(B) ranges from 2.6 Å in the interdomain linker to 4.6 Å at the interface of NBD1 with the L1 stalk (Figure 40). The high resolution of the interdomain linker is likely a result of its rigidity due to the large number of contacts it makes with the ribosome and P-site tRNA. The P-site tRNA contacts the 30S subunit at its anticodon stem loop, the 50S subunit at its acceptor stem, and Sal(B) at its acceptor stem, TΨC loop and D loop (see section 4.2.4.4). Therefore, the P-site tRNA is expected to be fairly rigid, which explains a consistent resolution with only a small variation from 2.8 Å at the anticodon stem loop and acceptor stem to 3.4 Å at the interface with NBD2 of Sal(B).

The high resolution of these regions allowed atomic models for Sal(B) and P-site tRNA to be built with high confidence, with the exception of residues 80-109 of Sal(B) that interact with the L1 stalk, which were left unbuilt. The interdomain linker was especially high resolution and built with particularly high confidence.

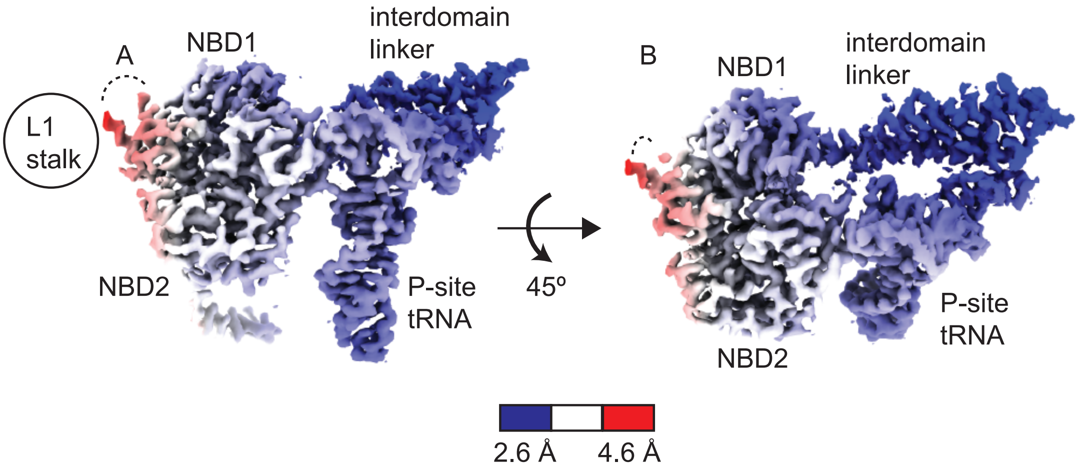

Figure 40 Local resolution of the density for Sal(B) and the distorted P-site tRNA. The resolution of the Sal(B) density ranges from 2.6 Å in the interdomain linker to 4.6 Å where NBD1 interacts with the L1 stalk. The resolution of the P-site tRNA density remains fairly consistent, with a small variation from 2.8 Å to 3.4 Å. Left = front view, right = top view. Dashed line represents unbuilt residues 80-109. The relative positioning of the L1 stalk is shown by a black circle.

4.2.3.2 Other Sal-ribosome complexes

A similar approach to that outlined above was used to solve the structures of the Sal(A)-ribosome and Sal(C)-ribosome complexes to 3.3 Å and 3.0 Å respectively. Similarly to the Sal(B)-ribosome complex, globular density in the E-site was present, presumably corresponding to the NBDs of Sal (Figure 41). These maps were less well resolved than the map of the Sal(B)-ribosome complex, despite the fact they were derived from similar numbers of particles (Sal(A): 49,621 particles, Sal(B): 59,889, Sal(C): 66,665). This may be due to poorer distributions of particle views in the micrographs; indeed, the reconstructions appear slightly elongated, which is a symptom of non-uniform projection distributions [137]. Therefore the Sal(B)-ribosome complex was taken forward as the representative of these three complexes which contain Sal variants highly similar in protein sequence (Table 7) and resistance phenotype (Table 6).

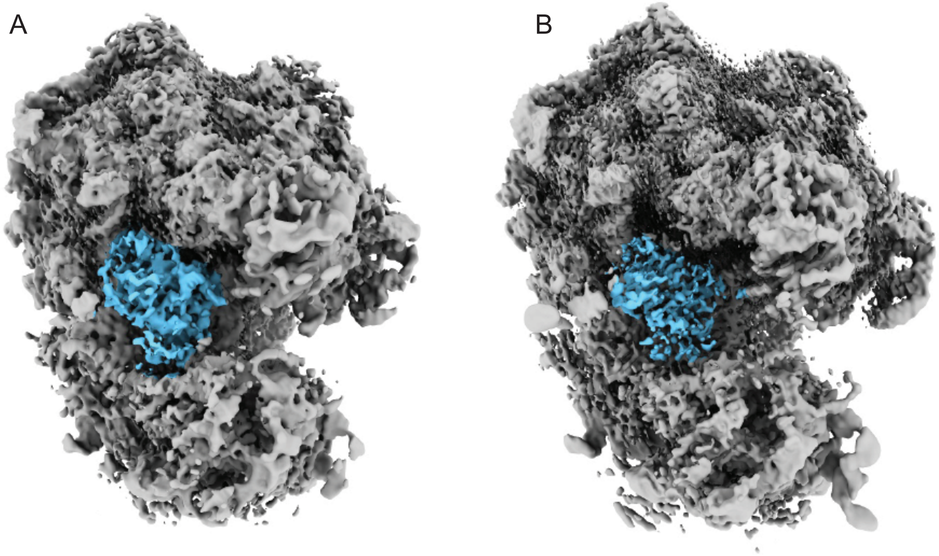

Figure 41 3D reconstructions of the Sal(A)-ribosome and Sal(C)-ribosome complexes. A) Sharpened map of the Sal(A)-ribosome complex filtered by estimated local resolution. Globular E-site density, presumably corresponding to the NBDs of Sal(A), is shown in blue. B) Sharpened map of the Sal(C)-ribosome complex filtered by estimated local resolution. Globular E-site density, presumably corresponding to the NBDs of Sal(C), is shown in blue.

The same approach was used to attempt to solve the structures of the Sal(D)-ribosome and Sal(E)-ribosome complexes. However, the resulting 3D reconstructions contained comparatively little density in the E-site, suggesting that fewer of the particles, if any, contained Sal protein. As above, focussed classification using a mask around the P- and E-sites was carried out in an attempt to classify out a subset of particles with Sal present. 41,537 particles of the supposed ‘Sal(D)-ribosome complex’ sample contributed to classes with E-site density out of a total dataset of 150,506 particles that contributed to the initial ribosome reconstruction (28%). 3D reconstruction of these particles revealed a map with E-site density comparable in strength with the density of the rest of the ribosome (Figure 42A). This density does not appear globular, as expected for the NBDs of Sal, but rather RNA-like. Indeed, the model for E-site tRNA from PDB 5AFI [175] fits well into this density

(Figure 42C). This suggests that most, if not all, of the particles contributing to classes containing E-site density were in fact ribosomes with E-site tRNA bound.

99,958 particles of the supposed ‘Sal(E)-ribosome complex’ sample out of a total dataset of 213,820 particles (47%) contributed to classes containing E-site density. However, after 3D reconstruction of these particles, this E-site density was weak compared with the density of the rest of the ribosome, and only visible at low contour levels (Figure 42B). This suggests that the focussed classification procedure was relatively unsuccessful at separating out particles based on E-site density. Even if this density corresponds to Sal protein, the weakness of the density suggests that most particles contributing to this dataset contained empty E-sites, and so high-resolution structure determination of a Sal(E)-ribosome complex was not possible.

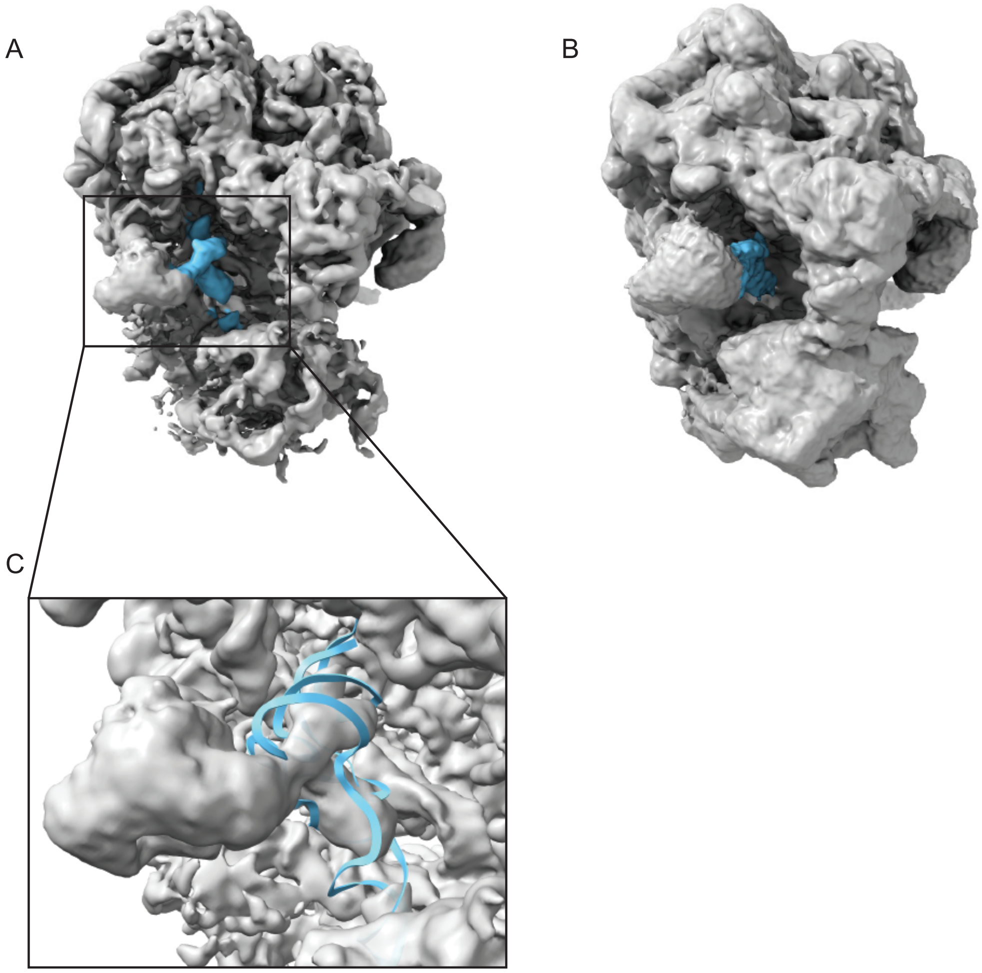

Figure 42 E-site density in supposed ‘Sal(D)-ribosome’ and ‘Sal(E)-ribosome’ complexes. A) Unsharpened 3D reconstruction of the supposed ‘Sal(D)-ribosome complex’ after focussed classification, viewed at $\sigma = 4.7$. The E-site density (blue) appears RNA-like. B) Unsharpened 3D reconstruction of the supposed ‘Sal(E)-ribosome complex’ after focused classification, viewed at $\sigma = 1.6$. The E-site density (blue) is very weak. C) Zoomed-in view of the E-site density of the supposed ‘Sal(D)-ribosome complex’ reconstruction (grey). The model of the E-site tRNA from PDB 5AFI was rigid body fitted to this density (blue).

These results suggest that no Sal-ribosome complexes were isolated during the FLAG-tag affinity purification procedure in these two cases, or that such low numbers were isolated compared to a background of empty or E-tRNA containing ribosomes that focussed classification image processing techniques could not separate them from the total dataset.

This is consistent with the SDS-PAGE (Figure 36) and negative stain TEM results (Figure 35E&F), which also suggested that far fewer Sal-ribosome complexes were purified after overexpression of the Sal(D) and Sal(E) variants compared with the Sal(A-C) variants. There are a number of possible reasons for this. Firstly, the FLAG$_3$-tagged EQ$_2$ Sal(D) and Sal(E) variants may not have been overexpressed correctly in the cells. However, in both cases, the SDS-PAGE gel appeared to show a band at around 63 kDa, the mass expected for full-length Sal protein (Figure 36, arrow), which implies the protein was expressed to some degree. A western blot could be performed using an anti-FLAG antibody to determine whether this band does indeed correspond to Sal protein. This band is quite weak, so it may be that not enough $FLAG_3$-tagged Sal protein was expressed to generate Sal-ribosome complexes at a concentration suitable for cryo-EM structure determination. Another possibility is that the Sal variants did not fold correctly after expression, preventing them from binding to the ribosome. Or it may be the case that these variants may bind to the ribosome less strongly than Sal variants A-C, despite the EQ_2 mutation. If this is the case, it may contribute to their reduced effect on antibiotic susceptibilities in *S. aureus* compared to the other three variants (Table 6).

Although it was disappointing that high resolution reconstructions were not solved for all five Sal-ribosome complexes, the 3D reconstruction of the Sal(B)-ribosome complex was taken forward for atomic model building and structural analysis. Despite not having structural information for the other complexes, the alignments described in section 4.2.1 above were used to map the variant sequences onto the Sal(B) structure (section 4.2.7) to help explain how sequence differences among the Sal variants might lead to differences in how the proteins bind to the ribosome, which may in turn explain the differences in antibiotic resistance phenotypes.

4.2.4 Structure of the Sal(B)-ribosome complex

4.2.4.1 Atomic model building and overview of complex structure

An atomic model was built and refined into the cryo-EM reconstructions of the Sal(B)-ribosome complex using a model of the *S. aureus* 70S ribosome as a starting model (PDB 6S0X [188]). The 23S rRNA, 5S rRNA, distorted P-site tRNA, 50S ribosomal proteins and Sal protein were built into the 2.9 Å sharpened consensus map after it was low-pass filtered by local resolution. The 16S rRNA, mRNA codon and 30S ribosomal proteins were built into the 30S body or 30S head multibody maps, both of which were resolved to 3.0 Å and were sharpened and filtered by local resolution. Most of the rRNA residues were modelled, with the exception of some poorly resolved regions in the periphery of the ribosome such as the 50S L1 stalk. The resolution was suitable for all ribosomal proteins of the starting model to be fully built, with the exception of uL5, residues 2-60 of uL6, residues 45-56 uL24, and bL31B, which were less well resolved and so were built with truncated sidechains.

Furthermore, residues 60-69 of subunit-bridging bL31B were completely unresolved and so were left unmodeled. Model validation statistics are found in Table 8.

Model composition		**R.m.s. deviations**[a]	
Non-hydrogen atoms[a]	138824	Bond lengths (Å)	0.020
Protein residues[b]	5925	Bond angles (°)	1.47
Nucleic acid residues[b]	4329	**Protein geometry validation**[a]	
Metal ions[a]	3 Zn, 2 Mg	Rotamer outliers (%)	0.58
Ligand[a]	2 ATP	Ramachandran outliers (%)	0.38
General validation[a]		Ramachandran favoured (%)	86.11
CC (model to map fit)[c]	0.77	**RNA geometry validation**[b]	
Clashscore	12.33	Sugar pucker outliers (%)	1.18
MolProbity score	2.24	Backbone conformation outliers (%)	29.96

Table 8 Model validation statistics. [a]Obtained from Phenix refine log and phenix molprobity. [b]Obtained from MolProbity web server. [c]CC = correlation coefficient, measure of fit into consensus map.

Similar to structures of other ABC-F protein : ribosome complexes [187,260,267], the globular NBDs of Sal(B) bind to the E-site of the ribosome, sandwiched between the L1 stalk and P-site tRNA (Figure 43). The NBDs also contact 16S rRNA h42 of the 30S subunit and uL5, bL33 and 23S rRNA H68 of the 50S subunit. The interdomain linker reaches towards the PTC in the 50S subunit, contacting 23S rRNA helices H68, H74, H80 and H93 down its length (Figure 44). Most of these are interactions with the phosphate backbone of 23S rRNA, the most notable exception being a stacking interaction with A2629 (2602), which would normally interact with the 3’-end of P-site tRNA. This interaction is likely important in allowing the interdomain linker to distort the acceptor stem of the P-site tRNA away from the PTC (see section 4.2.4.4 below). Finally, the C-terminal extension of Sal(B) contacts uS7 and uS11 as it wraps around the 30S subunit and reaches towards the mRNA exit channel (Figure 43, Figure 44) (see section 4.2.4.3 below).

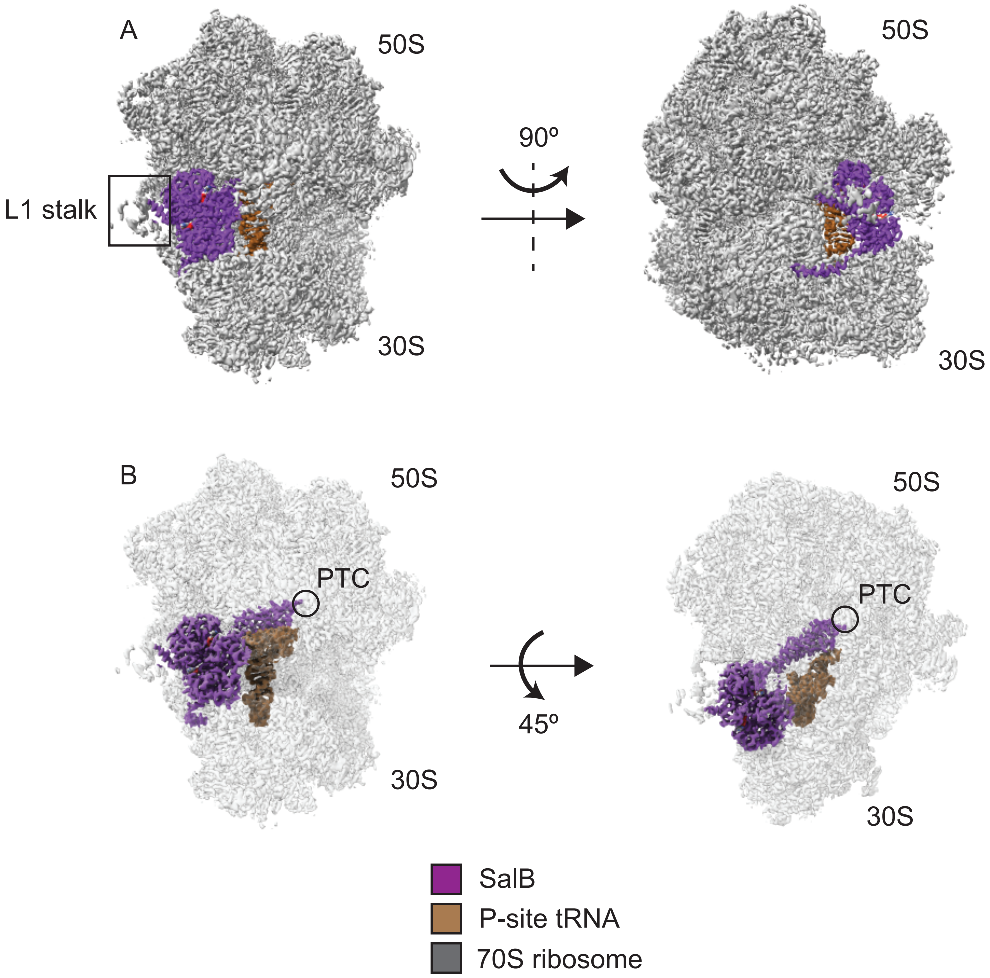

Figure 43 Structure of the Sal(B)-ribosome complex. Map of the Sal(B)-ribosome complex coloured according to atomic models of the *S. aureus* ribosome, distorted P-site tRNA, and Sal(B) after model building and refinement. Sal(B) (purple) binds to the E-site of the ribosome (grey). The interdomain linker of Sal(B) contacts and distorts P-site tRNA (brown). ATP molecules coloured by atom (red/blue/grey/white). A) Left = front view showing the NBDs of Sal(B) bound to the E-site. A box is drawn around the L1 stalk. Right = side view showing the C-terminal tail of Sal wrapping around the 30S subunit. B) Left = front view with transparent ribosome density to show the interdomain linker of Sal(B) reaching towards the centre of the 50S ribosomal subunit. Right = top view showing the interaction of the interdomain linker of Sal(B) with P-site tRNA. Location of the PTC labelled with a black circle.

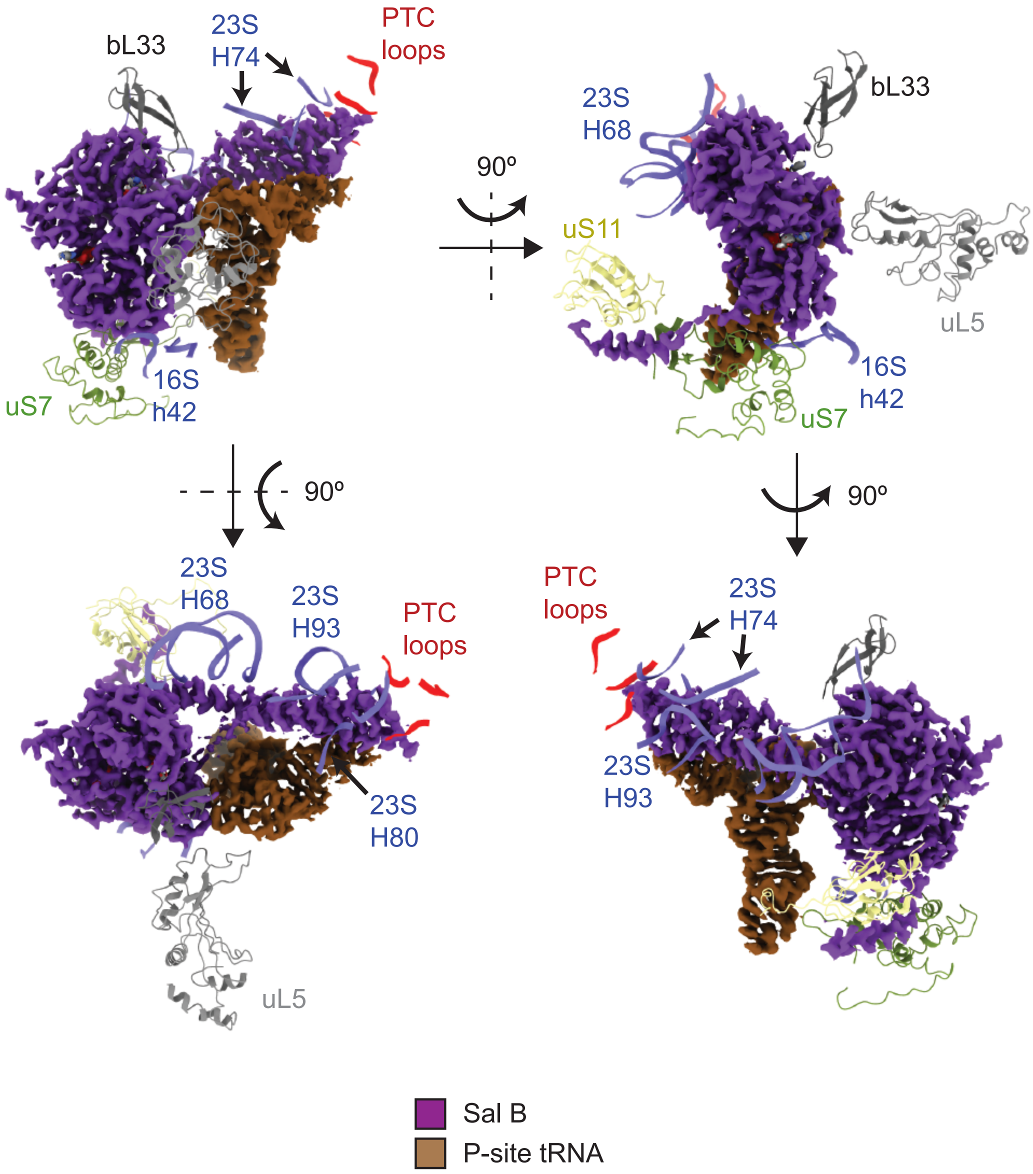

Figure 44 Interactions of Sal(B) with the ribosome. Regions of the *S. aureus* ribosome that contact Sal(B) in the Sal(B)-ribosome complex. Sal(B) and P-site tRNA are shown as purple and brown EM density respectively, whereas ribosome proteins and rRNA that contact Sal(B) are shown as atomic models in cartoon format. Views from the front, side, back and top are shown, as indicated by the arrows. The three PTC loops discussed in section 4.2.5 that are distorted on Sal(B) binding are shown in red.

4.2.4.2 Structural analysis of Sal(B)

Similarly to other ABC-F proteins, Sal(B) comprises an N-terminal NBD1 and a C-terminal NBD2, which together bind to the E-site of the ribosome. An interdomain linker, formed of two alpha helices joined by an interhelix loop, is situated between these domains based on sequence order. As discussed, this interdomain link protrudes towards to the catalytic centre of the 50S ribosomal subunit. The protein also contains a C-terminal extension at the end of NBD2 (Figure 45A).

Two ATP molecules are sandwiched between NBD1 and NBD2 of Sal(B), one proximal to the interdomain linker and ribosome, and one distal. The adenine ring of the proximal ATP molecule is sandwiched between Ile12 of NBD1 and Gln430 of NBD2, and a magnesium ion coordinates the β- and γ-phosphates of ATP with sidechains of Ser42 and Gln61 of NBD1 (Figure 45B). The adenine ring of the distal ATP is sandwiched between Thr130 of NBD1 and Tyr324 of NBD2, and a magnesium ion coordinates its β- and γ-phosphates with the sidechains of Ser354 and Gln384 of NBD2 (Figure 45C). The density is well resolved for both ATP molecules, their coordinated magnesium ions and the surrounding protein residues.

The loop joining the two helices of the interdomain linker reaches towards the PTC, the site targeted by LS_AP antibiotics. Therefore, this loop plausibly plays a role in Sal(B)-mediated resistance, and will be studied in detail in section 4.2.5 below. The local resolution of the density for this region is high (Figure 40), with side chains resolved (Figure 45D).

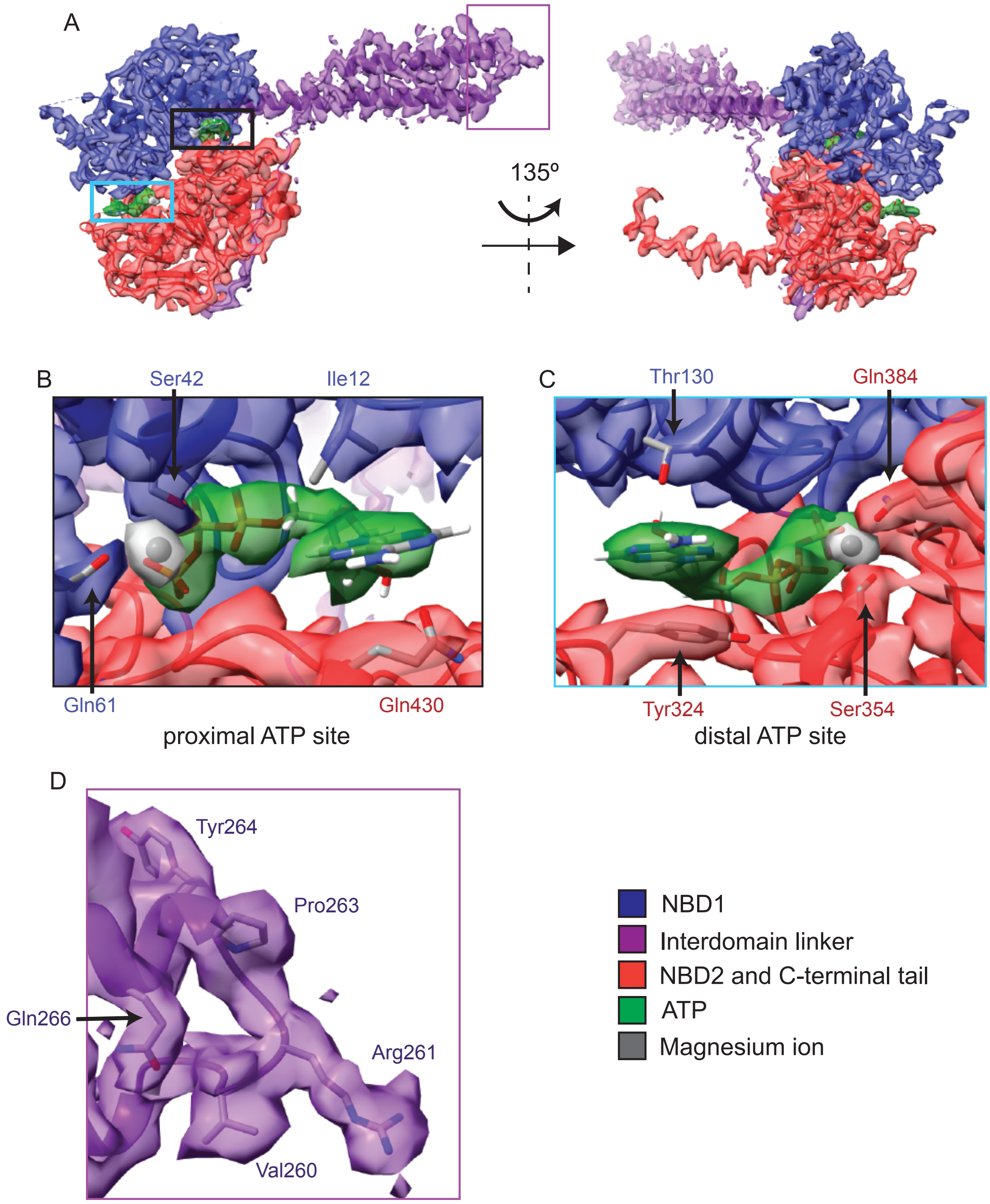

Figure 45 Structure of Sal(B), focussing on ATP binding sites and interdomain linker loop. A) Atomic model and cryo-EM density of Sal(B), showing NBD1 (blue), the interdomain linker (purple), NBD2 and the C-terminal tail (red), two sandwiched ATP molecules (green) and magnesium ions that coordinate the β- and γ-phosphates of ATP (grey). Left = front view. Right = back view. B) Proximal ATP binding site showing atomic models of the ATP molecule, magnesium ion and selected Sal protein side chains involved in ATP binding. C) Distal ATP binding site showing atomic models of the ATP molecule, magnesium ion and selected Sal protein side chains involved in ATP binding. D) The loop between the two helices of the interdomain linker. The density of this region is well resolved, allowing for unambiguous visualisation of side chains.

4.2.4.3 The C-terminal extension of Sal(B)

Some ABC-F proteins contain a C-terminal extension, which generally forms a two-stranded α-helical coiled-coil. This extension contributes to the DNA-binding ability of the *E. coli* ABC-F protein Uup [298], and therefore could feasibly be involved in RNA recognition in the mRNA exit channel. Deletion of the C-terminal extension abolishes or reduces antibiotic resistance in the ABC-F proteins VmlR and VgaA respectively [267,289]. The C-terminal extension of VmlR protrudes towards the mRNA exit channel, where it may be involved in substrate recognition through probing of the mRNA : 16S rRNA duplex [267].

Similarly to the C-terminal extension of VmlR in the VmlR-ribosome complex [267], the C-terminal extension of Sal(B) wraps around the 30S ribosome subunit, making contacts with 30S proteins uS7 and uS11, and reaches towards the mRNA exit channel (Figure 46A). However, the C-terminal extension of Sal(B) is shorter than in VmlR. Sal(B) residues Asp533, Asn536 and Lys537 are closest to the duplex between the mRNA and 16S rRNA in this channel (Figure 46B). However, these residues are still >7 Å away, making an interaction unlikely, suggesting that the C-terminal extension of Sal is not involved in substrate recognition. It should be noted that there is no biochemical evidence showing that the C-terminal extension of Sal(B) plays a role in its antibiotic resistance phenotype, so it may play a different role in Sal(B) compared with VmlR, where it is strongly associated with antibiotic resistance [267].

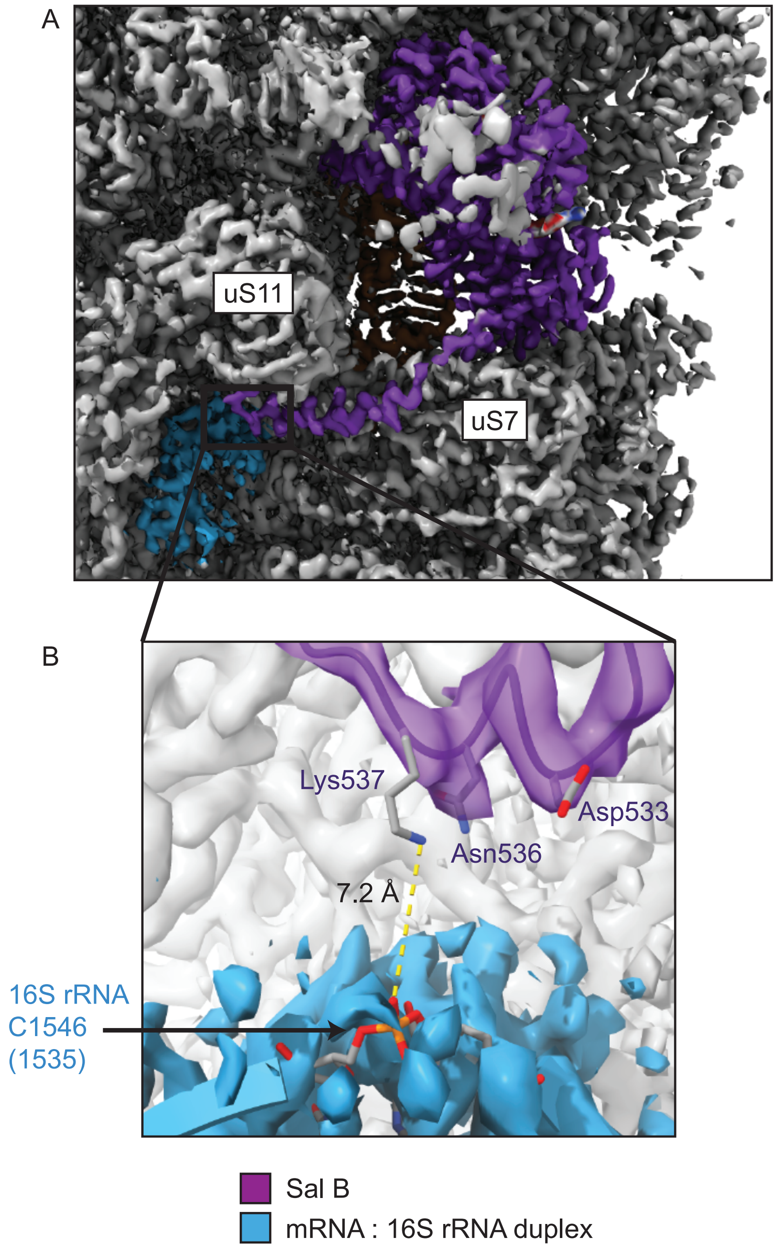

Figure 46 The C-terminal extension of Sal(B). A) Density of Sal(B) (purple) situated in the E-site of the ribosome, with C-terminal extension wrapping around the 30S ribosome subunit, making contacts with 30S subunit proteins uS7 and uS11, and reaching towards the mRNA : 16S rRNA duplex in the mRNA exit channel (blue). B) Proximity of the C-terminal extension to the mRNA : 16S rRNA duplex. 16S rRNA residue labelled according to *S. aureus* numbering followed by *E. coli* numbering in parentheses.

4.2.4.4 Identification and distortion of the P-site tRNA

A model of the P-site tRNA was built from a starting model of *E. coli* P-site tRNA^{fMet} (PDB 5MDZ, chain 5 [171]), which was rigid body fitted into the cryo-EM density of the Sal(B)-ribosome complex. Residues were then mutated to match those for *S. aureus* fMet-tRNA and the model real-space refined into the density. The tRNA bases of this mutated model were found to fit very well into the P-site tRNA density, strongly suggesting that the P-site tRNA of the Sal(B)-ribosome complex was indeed *S. aureus* tRNA^{fMet} (Figure 47A). This identification was confirmed by a good fit of a unique run of G-C base pairs in the anticodon stem unique to tRNA^{fMet} (Figure 47B), and a good fit of the appropriate CAU anticodon base-paired to the AUG mRNA start codon (Figure 47C). Identification of P-site tRNA^{fMet} and an mRNA start codon in the Sal(B)-ribosome complex implies that Sal(B) is predominantly bound to 70S initiation complexes.

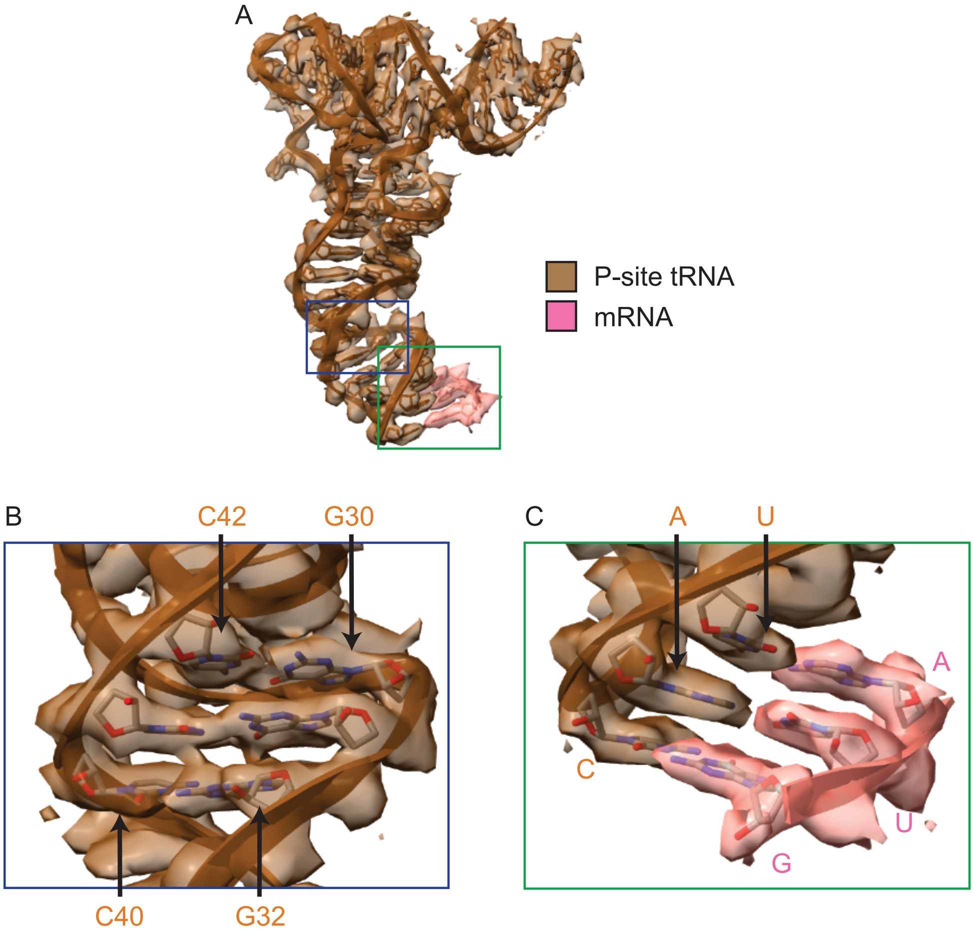

Figure 47 Identification of P-site tRNA^{fMet}. A) A model of *S. aureus* tRNA^{fMet} fit well to the P-site tRNA density of the Sal(B)-ribosome complex (brown) and a model of an AUG mRNA start codon fit well into the mRNA density (pink). B) A run of G-C base pairs in the anticodon stem confirms the identification of tRNA^{fMet}. C) The base-pairing of an AUG mRNA start codon with a CAU anticodon also confirms the identification of tRNA^{fMet}.

The interdomain linker of Sal(B) overlaps with the position of the acceptor stem of P-site tRNA in an elongation-competent ribosome. When Sal(B) binds the ribosome, it distorts the acceptor stem away from the PTC, moving the 3’-CCA by 22 Å, to allow for the interdomain linker loop to interact with the PTC (Figure 48A). In shifting away from the PTC, the tRNA loses a number of favourable binding interactions with the ribosome, which might be compensated by additional interactions between the tRNA and Sal(B). For example, the end of the first helix of the interdomain loop, i.e. residues Gln252, Arg253, Gln256 and Lys257 interacts with the acceptor stem of distorted P-site tRNA (Figure 48B).

Furthermore, this movement of the acceptor stem is accompanied by a swing of the TΨC and D loops of the tRNA towards NBD2 of Sal(B) (Figure 48A). This allows the formation of additional contacts, which again may help to stabilise the distorted tRNA conformation. These include the stacking of U21 of the D loop of P-site tRNA with aromatic residue Tyr445 of Sal(B), and G20 of the D loop and C57 of the TΨC loop of P-site tRNA with an α-helix of Sal(B) NBD2 comprising residues Thr408, Arg411 and Thr412 (Figure 48C).

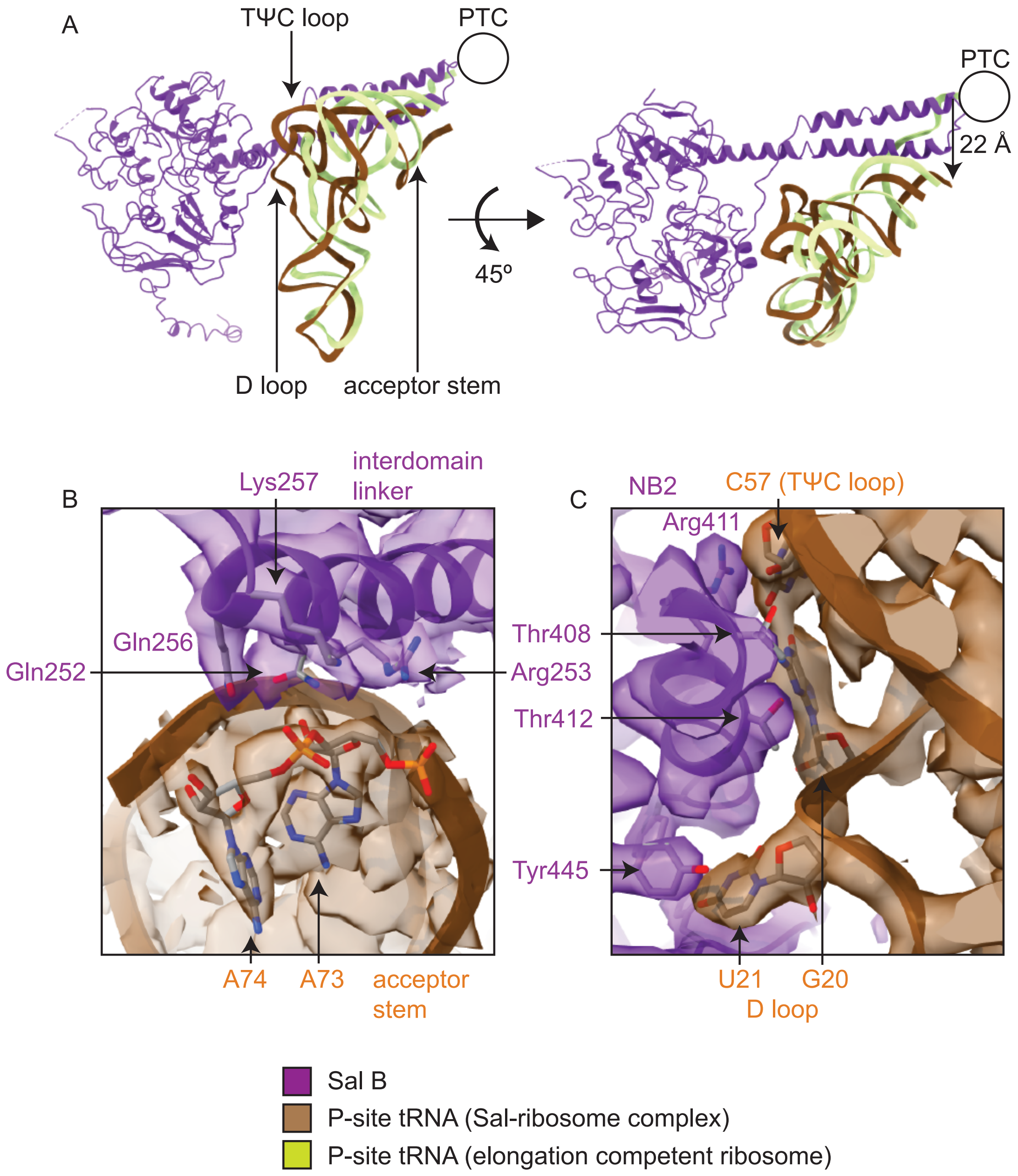

Figure 48 Distortion of P-site tRNA on Sal(B) binding. Superposition of P-site tRNA from an elongation-competent ribosome (green; PDB 6O9J) onto the distorted P-site tRNA of the Sal(B)-ribosome complex (brown). The acceptor stem of the elongation-competent P-site tRNA would overlap with the position of the interdomain linker of Sal(B). Therefore, on Sal(B) binding, the acceptor stem of the P-site tRNA is distorted away from the PTC, with the 3'-CCA moving by 22 Å, as shown. To allow for this movement, the TΨC and D loops of P-site tRNA swing towards NBD2 of Sal(B). The location of the PTC is represented by a black circle. B) Contacts between the interdomain linker of Sal(B) and the acceptor step of P-site tRNA in the Sal(B)-ribosome complex. C) Contacts between NBD2 of Sal(B) and the TΨC and D loops of P-site tRNA in the Sal(B)-ribosome complex.

In summary, the structure of the Sal(B)-ribosome complex shows that Sal(B) binds to the E-site of a 70S initiation complex, where its interdomain linker protrudes towards the PTC, making multiple contacts with the ribosome and distorting the acceptor stem of P-site tRNA^{fMet} away from the PTC. This distortion might be stabilised through contacts between the interdomain linker and NBD2 of Sal(B) with the P-site tRNA. To understand the structural basis of Sal(B)-mediated antibiotic resistance and the differences in resistance phenotype among the Sal variants, the structure of the interdomain linker tip and its interaction with the PTC, where LS$_A$P antibiotics bind, is analysed in the rest of this section.

4.2.5 Interaction of the Sal(B) interdomain linker loop with the PTC

The interdomain linker of Sal(B) contains two alpha helices joined by a loop (Figure 45D), which protrudes towards the P-site pocket of the PTC (Figure 49A). Several 23S rRNA loops comprise the PTC, and two of these interact directly with the interdomain linker loop of Sal(B). Firstly, the backbone of the rRNA loop containing residues A2477, A2478, and C2479 (2450-2452 *E. coli* numbering) interacts with the backbone of Sal(B) residues Arg261 and Ser262, and the ring of Pro263. Secondly, the base of U2612 (2585) stacks with the aromatic ring of Tyr264 of Sal(B) (Figure 49B).

The closest contacts are made by the ring of Pro263 and the carbonyl oxygen of the backbone of Arg261, which are situated 3.2 Å and 3.5 Å from the sugar backbone of A2478 (2451) respectively (Figure 49C). Meanwhile, the aromatic rings of U2612 (2585) and Tyr264 are situated about 3.4-3.8 Å apart, facilitating a π-π stacking interaction. Also, the sugar oxygen of U2612 (2585) is 3.8 Å from the hydroxy group of Tyr264, which may allow for weak hydrogen bonding (Figure 49D).

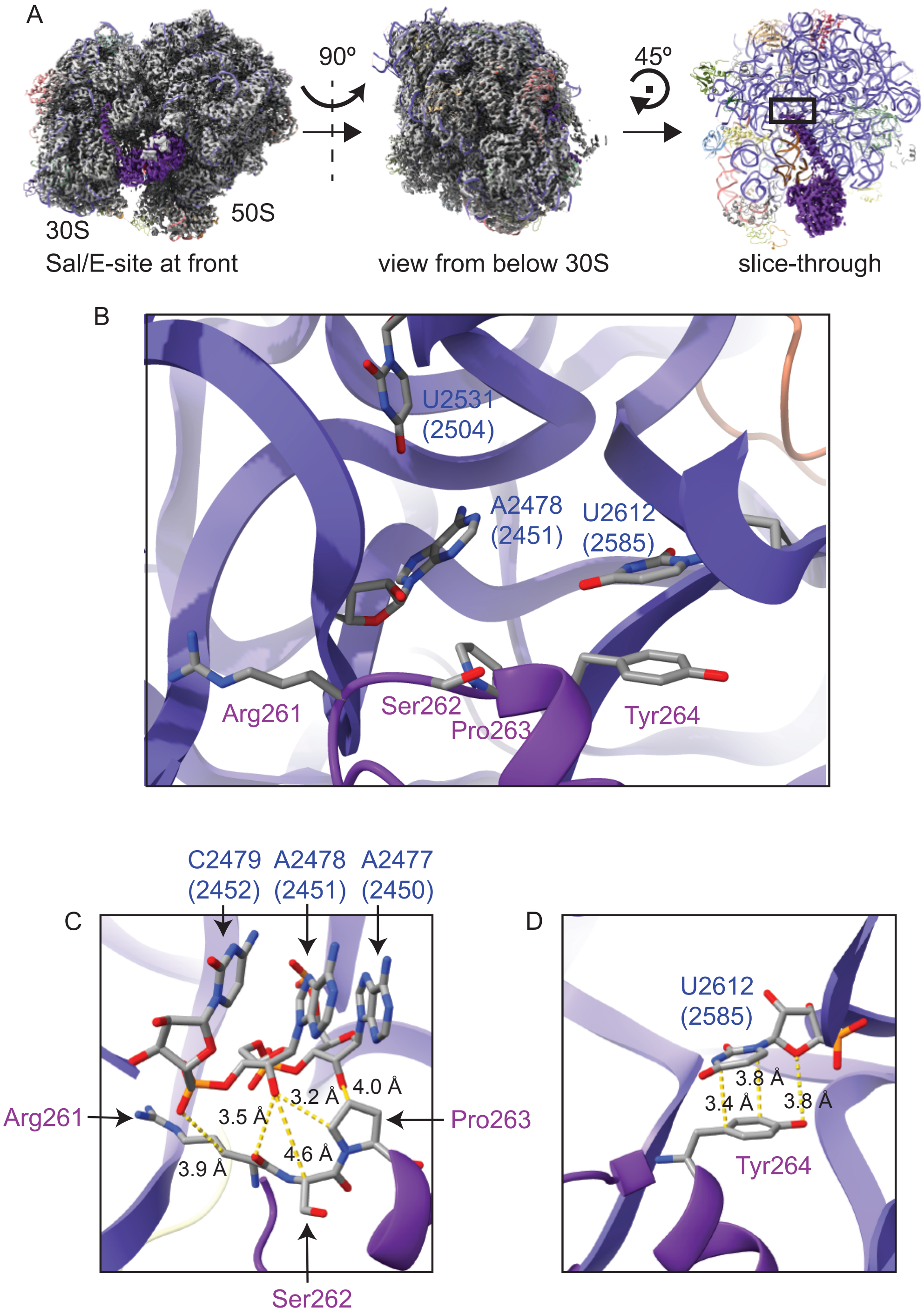

Figure 49 Interaction of the Sal(B) interdomain linker with the ribosome PTC. A) Sal(B)-ribosome complex with Sal(B) protein cryo-EM density coloured purple and the ribosome density coloured grey, fitted around the atomic model in cartoon form. Left to right: view from E-site, with L1 stalk and Sal(B) at the front; view from below the 30S subunit; in plane rotation and slice through with ribosome density removed to show interaction of the Sal(B) interdomain linker with the ribosome. Zoomed-in view of boxed region shown in part (B). B) Atomic model of the interdomain linker loop of Sal(B) (dark purple) with key sidechains shown, and atomic model of 23S rRNA (light purple) with key residues shown. C) Atomic model of 23S rRNA residues A2477-C2479 (2450-2452) and Sal(B) residues Arg261-Pro263, with inter-chain distances shown. D) Atomic model of 23S rRNA residue U2612 (2585) and Sal(B) residue Tyr264, with inter-chain distances shown. For 23S rRNA residues, *E. coli* numbering is shown in parentheses.

Importantly, no region of the Sal interdomain linker reaches closely enough to the drug-binding site to allow for direct displacement of a bound antibiotic. For example, the distance between Pro263, the closest residue to the antibiotic site, and tiamulin (superimposed from PDB 1XBP [299]) is about 8 Å, which is too large to allow for any interaction, let alone steric displacement (cf. the Van der Waals radius of carbon is 1.7 Å [300]) (Figure 50A).

However, displacement of drug by an allosteric mechanism might be possible. In other words, binding of Sal(B) may induce conformational changes in ribosome 23S rRNA residues, which in turn causes displacement of antibiotic. This discussion will focus on three regions of the 23S rRNA affected by Sal(B) binding: residues A2477-C2479 (2450-2452), which interact with Sal(B) residues Arg261-Pro263 as discussed (Figure 50B); residues A2530-G2532 (2503-2505), which may interact indirectly with Sal(B) residues Arg261-Pro263 through 23S rRNA residues A2477-C2479 (2450-2452) (Figure 50E); and residue U2612 (U2585), which stacks with Tyr264, as discussed (Figure 50H). Differences in these regions between the apo *S. aureus* ribosome and the Sal(B)-ribosome complex will be examined. To explore how these changes might affect the binding of PTC-targeting antibiotics, the tiamulin-ribosome structure will be referenced.

Firstly, there is a small shift in the backbone of residues A2477-C2479 (2450-2452) on Sal(B) binding (Figure 50C), which presumably occurs due to the proximity of the backbone of residues Arg261-Ser262 and the ring of Pro263 (Figure 49C). This shifts these 23S rRNA residues slightly away from the tricyclic core of tiamulin, which may weaken ribosome-tiamulin binding (Figure 50D).

Secondly, there is a modest shift in residues A2530-G2532 (2503-2505) on Sal(B) binding, most obviously in the backbone of U2531 (2504) and G2532 (2505) (Figure 50F). This brings the rRNA backbone closer to the tricyclic core of tiamulin, so that the backbone is only about 3-3.5 Å from the drug site compared with 4-4.5 Å with no Sal(B) bound (Figure 50G). It is possible that this positioning of the backbone is too close to the drug site, making binding less favourable.

It should be noted that 23S rRNA residues A2530-G2532 (2503-2505) do not directly interact with Sal(B). However, residues C2479 (2452) and A2480 (2453) are slightly shifted due to direct interaction with Sal(B) Arg261 (see Figure 49C). This shift may perturb hydrogen bonding interactions between C2479 (2452) and U2531 (2504), and between A2480 (2453) and U2527 (2500), which in turn may cause the shift in the backbone around A2530-G2532 (2503-2505) (Figure 51).

Finally, U2612 (2585) is brought close to Tyr264 of Sal(B) so that the aromatic rings of the two residues can interact by π-π stacking. The density for U2612 (2585) is very weak in the apo ribosome map, suggesting that this residue is conformationally flexible when no Sal protein is bound (Figure 50I). On tiamulin binding, this residue moves towards the C-14 glycolic acid chain of tiamulin. Such an interaction with the drug may not be possible when it stacks with Tyr264, potentially leading to weaker drug binding (Figure 50J).

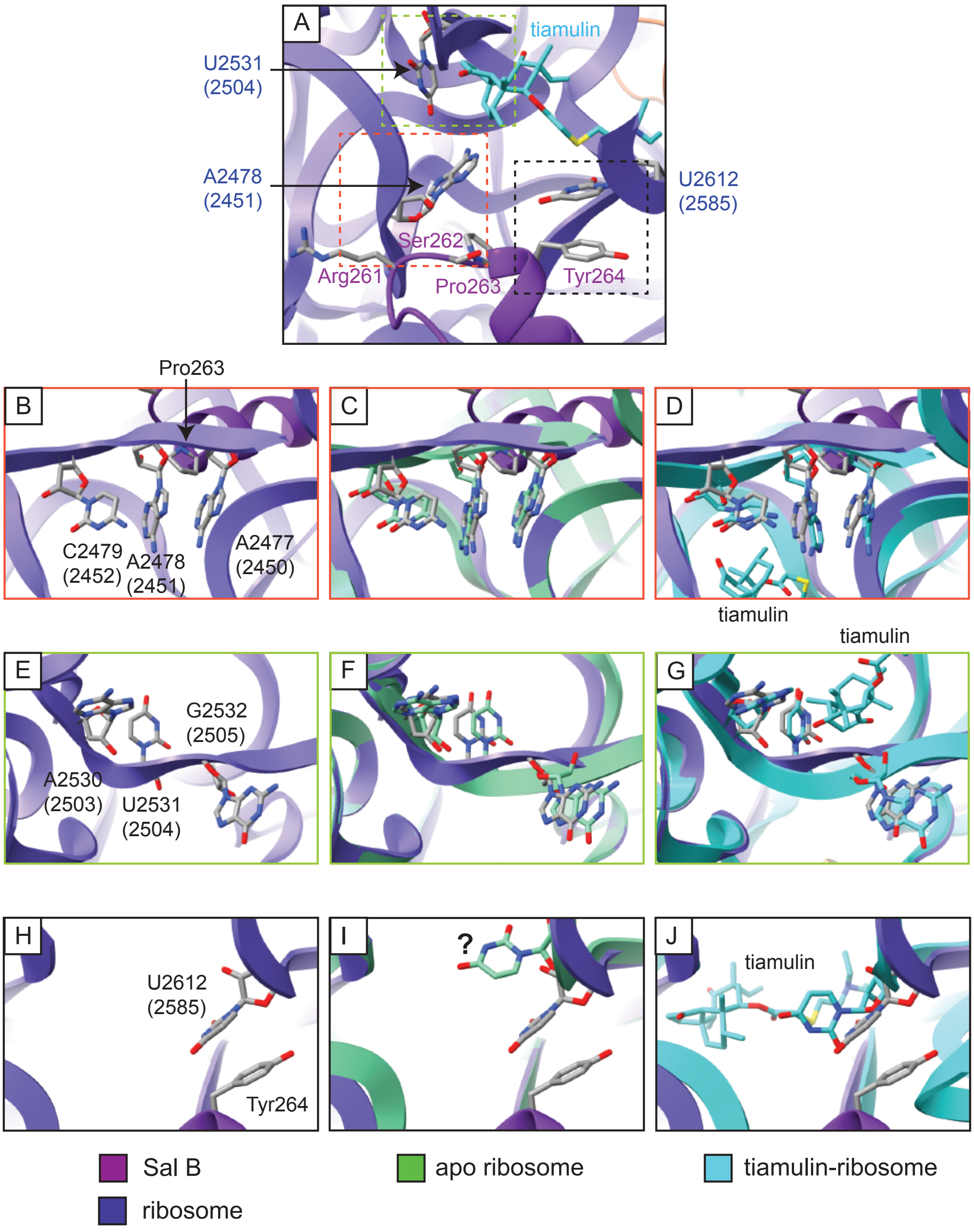

Figure 50 Changes in PTC conformation on binding of Sal(B) or tiamulin to the ribosome. A) Atomic model of the Sal(B)-ribosome complex, zoomed-in on the interdomain linker loop of Sal(B) and ribosome PTC. Sal(B) is shown in dark purple and 23S rRNA in light purple, with selected residues shown as atomic models. The atomic model of tiamulin from PDB 1XBP is superimposed (light blue) after alignment of the 23S rRNA chains of PDB 1XBP and the Sal(B)-ribosome model. Dashed coloured boxes outline the regions shown in detail in (B)-(J). B, E, H) Selected regions of the 23S rRNA from the Sal(B)-ribosome model. C, F, I) The same regions with a model of the apo *S. aureus* ribosome superimposed. The apo *S. aureus* model was made by refining the relevant 23S rRNA regions from the Sal(B)-ribosome model into map EMD-10076. The question mark in part (I) highlights that residue U2612 (2585) of the apo ribosome has poor density and so is likely conformationally flexible. D, G, J) The same regions with a model of the ribosome from *D. radiodurans* in complex with tiamulin superimposed, PDB 1XBP.

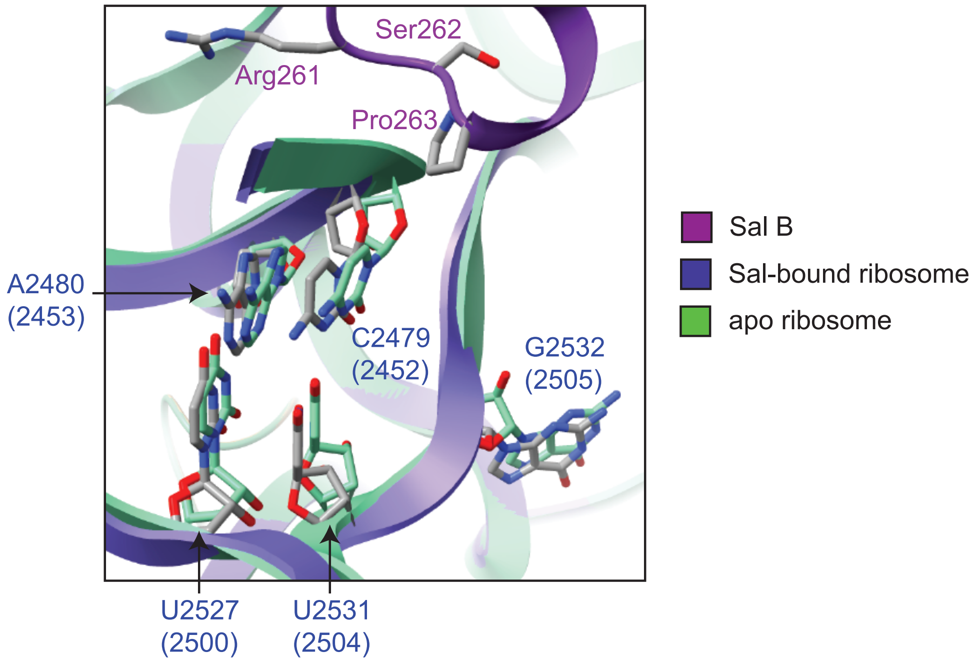

Figure 51 Indirect interaction of 23S rRNA residues U2527 (2500), U2531 (2504) and G2532 (2505) with Sal(B). Atomic model of apo *S. aureus* ribosome (green) superimposed on atomic model of the Sal(B)-ribosome complex (Sal(B) dark purple, ribosome light purple). Sal(B) directly interacts with 23S rRNA residues C2479 (2452) and A2480 (2453), which in turn may cause a shift in 23S rRNA residues U2527 (2500), U2531 (2504) and G2532 (2505).

4.2.6 Structural analysis of the Sal(B) resistance phenotype

Sal(B) mediates resistance to LS$_A$P antibiotics. Section 4.2.5 explored the possible impact that Sal(B)-mediated conformational changes in 23S rRNA might have on tiamulin binding. This section will briefly describe the spatial arrangement between the binding sites of other LS$_A$P drugs and the 23S rRNA bases that are shifted by binding of Sal(B) (Figure 52A-G). This analysis is used to examine whether the overall resistance profile of Sal(B) (Figure 52H) could correspond to an allosteric displacement mechanism mediated through these regions of 23S rRNA.

Sal(B) expression in *S. aureus* RN4220 decreases retapamulin susceptibility by 267 times and tiamulin susceptibility by 8 times. This decrease in susceptibility could be explained by reduced binding affinity due to shifts in the regions around A2478 (2451) and U2531 (2504) (Figure 50C,F), which interact with the tricyclic core of pleuromutilin, and movement of U2612 (2585) to stack with Tyr264 instead of the C-14 glycolic acid tail of the drug (Figure 52A,B). It is difficult to explain the differences in the susceptibility changes between the two pleuromutilin drugs, but binding of the bulkier tail of retapamulin might plausibly be more influenced by the stacking of nearby U2612 (2585) than that of tiamulin.

Sal(B) expression in *S. aureus* decreases lincomycin susceptibility by 32 times and clindamycin susceptibility by 33 times. Unlike the pleuromutilin drugs, these are probably too far from U2612 (2585) to be affected by changes there, but they could be affected by changes in A2478 (2451) and U2531 (2504), which interact with the pyrrolidine ring of the lincosamides (Figure 52C,D).

Sal(B) expression decreases virginiamycin M1 susceptibility by just 2 times. Like pleuromutilin drugs, virginiamycin M1 bridges across the PTC to potentially interact with all three highlighted 23S rRNA regions (Figure 52E). It may be the case that virginiamycin M1 is less affected by conformational changes in these 23S rRNA regions than the pleuromutilin and lincosamide drugs are.

Finally, the susceptibilities of both erythromycin and pristinamycin IA are unaffected by Sal(B) expression. This fits with an allosteric displacement model because these molecules bind in the NPET, too far from the three discussed 23S rRNA PTC loops to plausibly be directly affected by Sal(B) binding (Figure 52F,G).

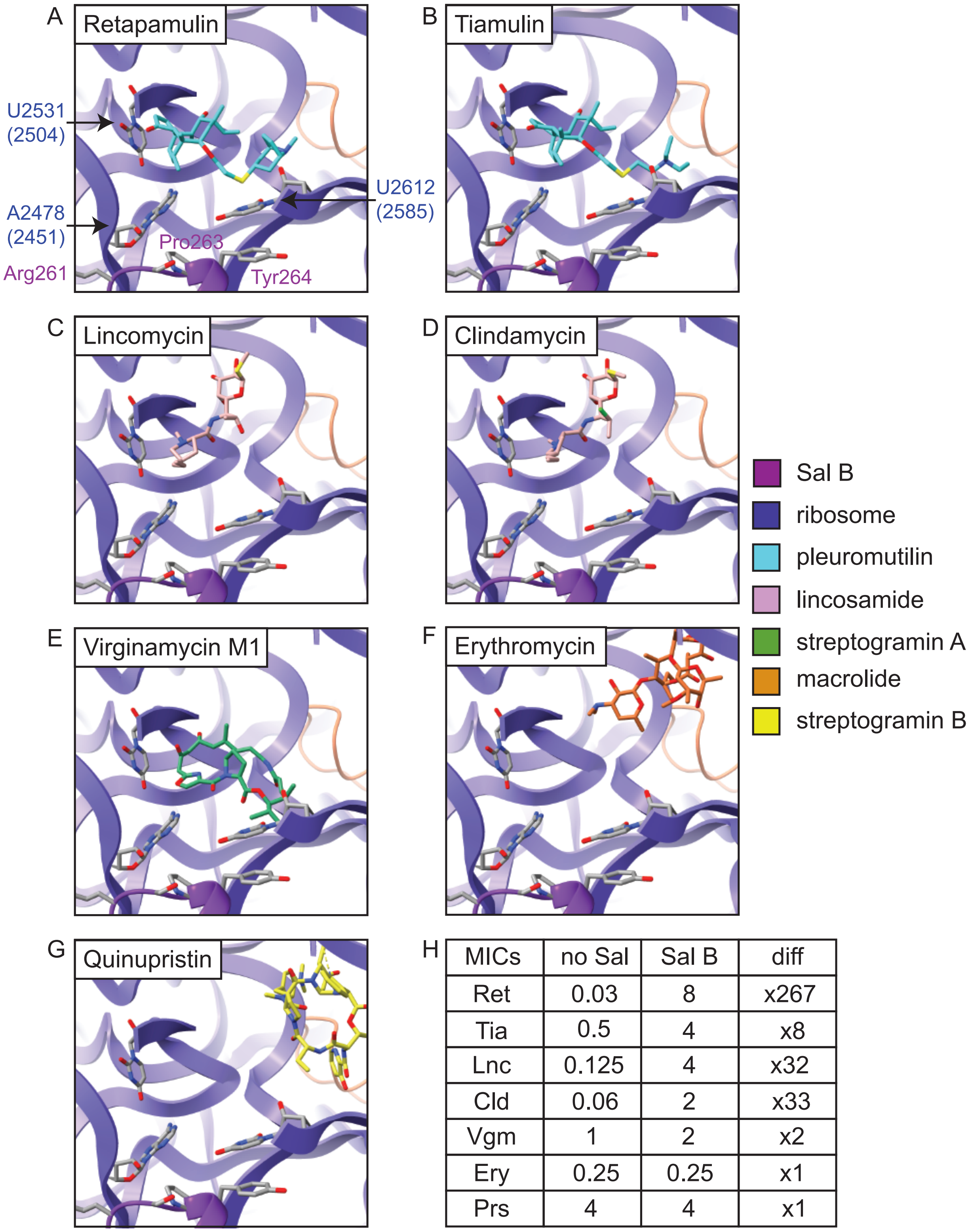

MICs	no Sal	Sal B	diff
Ret	0.03	8	x267
Tia	0.5	4	x8
Lnc	0.125	4	x32
Cld	0.06	2	x33
Vgm	1	2	x2
Ery	0.25	0.25	x1
Prs	4	4	x1

Figure 52 Relative positions of Sal(B) and ribosome-targeting antibiotics. A-G) Superposition of the atomic models of antibiotics and the Sal(B)-ribosome complex, after alignment of antibiotic-ribosome and Sal-ribosome complexes by their 23S rRNA chains. A) Retapamulin from PDB 2OGO. B) Tiamulin from 1XBP. C) Lincomycin from 5HKV. D) Clindamycin from 4V7V. E) Virginiamycin M1 from 1YIT. F) Erythromycin from 6S0X. G) Quinupristin from 4U1U. Quinupristin is derived from pristinamycin IA, and so presumably binds the ribosome in a similar manner. H) MICs (µg/ml) of ribosome-targeting antibiotics in *S. aureus* RN4220 with no expression of Sal or with expression of Sal(B), showing fold differences (diff). Ret = retapamulin. Tia = tiamulin. Lnc = lincomycin. Cld = clindamycin. Vgm = virginiamycin M1. Ery = erythromycin. Prs = pristinamycin IA. *MIC data from unpublished work: Merianne Mohamad, Chayan Kumar Saha, Gemma Atkinson and Alex J. O'Neill.*

4.2.7 Structural analysis of the resistance phenotypes exhibited by eight Sal variants

If residues 261-264 of the interdomain linker loop of Sal(B) mediate allosteric displacement of PTC-binding drugs, differences in the identities of these residues between the Sal variants may explain differences in resistance phenotype.

As a reminder, Sal(A-C) all give substantial resistance to pleuromutilins, lincosamides and group A streptogramins, Sal(D) gives comparable resistance to pleuromutilins and group A streptogramins but is less effective in reducing susceptibility to lincosamides, and Sal(E) gives modest resistance to pleuromutilins but gives no apparent resistance to lincosamides or group A streptogramins (Table 6). Sal variants from *S. xylosus*, *S. equorum*, and *S. saprophyticus* do not provide resistance to any of these antibiotics.

The sequences corresponding to the five ARE Sal variants (Sal(A-E)) and the three non-ARE Sal variants (Sal proteins from *S. xylosus*, *S. equorum*, and *S. saprophyticus*), were mapped onto the structure of the Sal(B) interdomain linker loop (Figure 53).

Arg261 and Pro263 are conserved in all cases. Position 262 does vary among the variants: it is a polar serine in Sal(A) and Sal(B), a slightly larger polar asparagine in Sal(C), Sal(D) and Sal(E), and a negatively charged aspartate in the Sal variants with no resistance phenotype (Figure 53). However, it should be noted that the sidechain of residue 262 is not close enough to interact with 23S rRNA in the Sal(B)-ribosome complex. Only the backbone is close enough, but even that is further than the backbone of Arg261 and the ring of Pro263, and so likely plays a minimal role (Figure 49C). Nevertheless, it is possible that a change in residue 262 might change the overall conformation of the interdomain linker loop, which could affect the interaction of Sal with the 23S rRNA. Although there is no correlation between the identity of residue 262 and the resistance phenotype conferred by the five ARE Sal variants A-E, the more obvious phenotypic difference between the ARE and non-ARE Sal variants does correlate with a different chemistry of this residue.

The identity of residue 264 also differs across the variants. It is an aromatic tyrosine residue in Sal variants A, B and C (Figure 53A&B), which allows it to π-stack with 23S rRNA residue U2612 (2585), pulling it away from the drug binding pocket (Figure 49D). This π-π stacking interaction is not possible in any of the other Sal variants, which might explain why Sal(A-C) generally give the largest increases in LS_AP resistance. In Sal(D), this residue is leucine, and in Sal(E) and the non-ARE Sal variant from *S. xylosus*, it is isoleucine (Figure 53C-E). These residues are not aromatic, so only weaker hydrophobic interactions with U2612 (2585) would be possible. In the other two non-ARE Sal variants, this position is hydrophilic (S or N), which would abolish any hydrophobic interactions (Figure 53F&G). Although hydrogen bonding interactions between this residue and U2612 (2585) might be possible, it would require precise sidechain positioning.

It should be noted that even if changes in Sal residue 264 do modify the interaction with 23S rRNA U2612 (2585), this rRNA residue only directly interacts with pleuromutilins and streptogramin As, not with lincosamides (Figure 52). Therefore, it is difficult to see from this structural snapshot how changes in Tyr264 would affect lincosamide resistance.

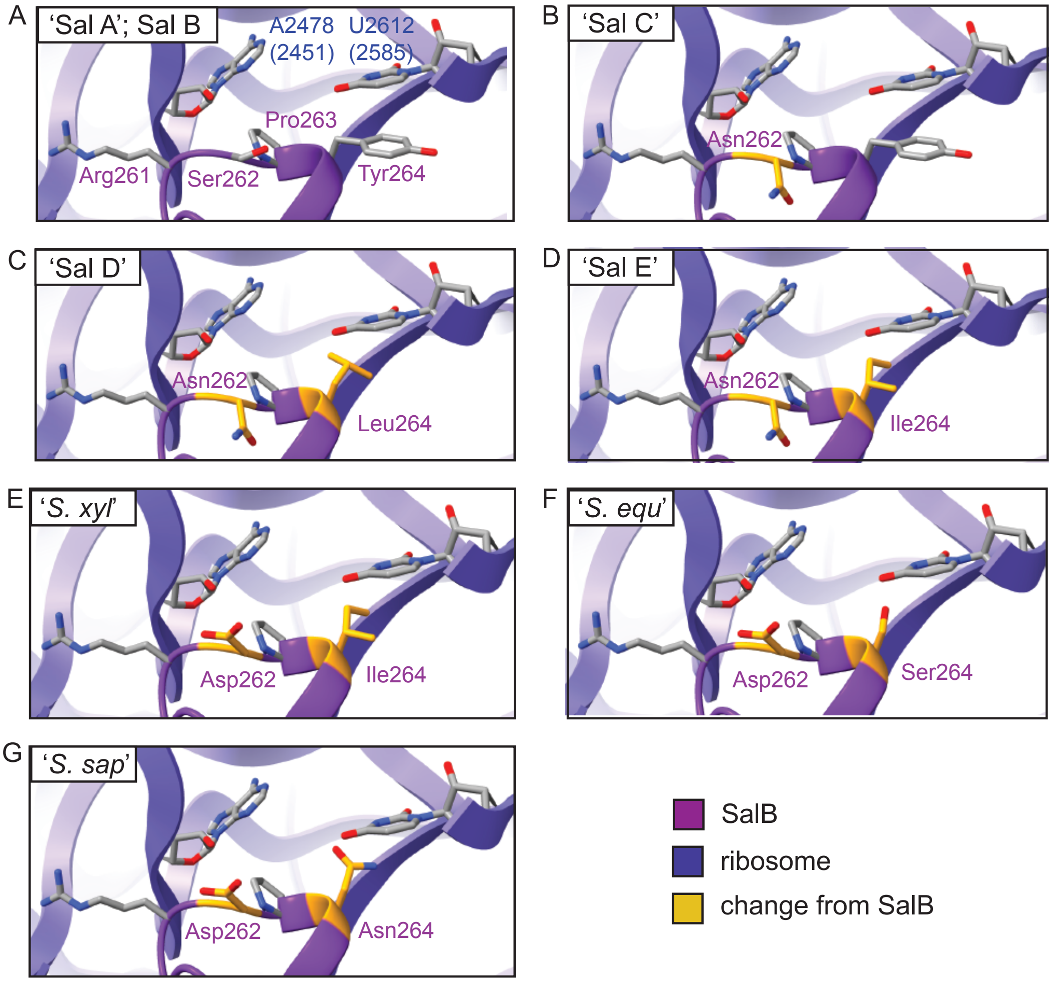

Figure 53 Sequences of the Sal variants mapped onto the structure of the Sal(B) interdomain linker. A) Structure of the Sal(B) interdomain linker loop in the Sal(B)-ribosome complex, with residues Arg261-Tyr264 shown. These residues are identical in Sal(A) and Sal(B). B) The same structure as in (A) but with Ser262 virtually mutated to Asn to give a representative 'Sal(C)' structure, assuming no change in the overall structure of the linker loop. C) The same structure but with virtual mutations Ser262Asn and Tyr264Leu to represent 'Sal(D)'. D) The same structure but with virtual mutations Ser262Asn and Tyr264Ile to represent 'Sal(E)'. E) The same structure but with virtual mutations Ser262Asp and Tyr264Ile to represent 'Sal from *S. xylosus*'. F) The same structure but with virtual mutations Ser262Asp and Tyr264Ser to represent 'Sal from *S. equorum*'. G) The same structure but with virtual mutations Ser262Asp and Tyr264Asn to represent 'Sal from *S. saprophyticus*'. Residues that differ from Sal(B) are highlighted in gold.

4.2.8 Investigating the link between Sal residue 264 and antibiotic resistance with mutagenesis experiments

The analysis in section 4.2.7 above identified the potential involvement of Sal residue 264 in mediating resistance. To probe this further, mutagenesis experiments were performed (mutant gene sequences can be found in the Appendix).

Firstly, a gain of function experiment was carried out, where position 264 (Sal(B) numbering) of the non-ARE Sal variant from *S. saprophyticus* was mutated from asparagine to tyrosine (Figure 54). It was hypothesized that if Tyr264 plays a major role in the resistance profile of Sal variants A-C, then this mutation should introduce resistance.

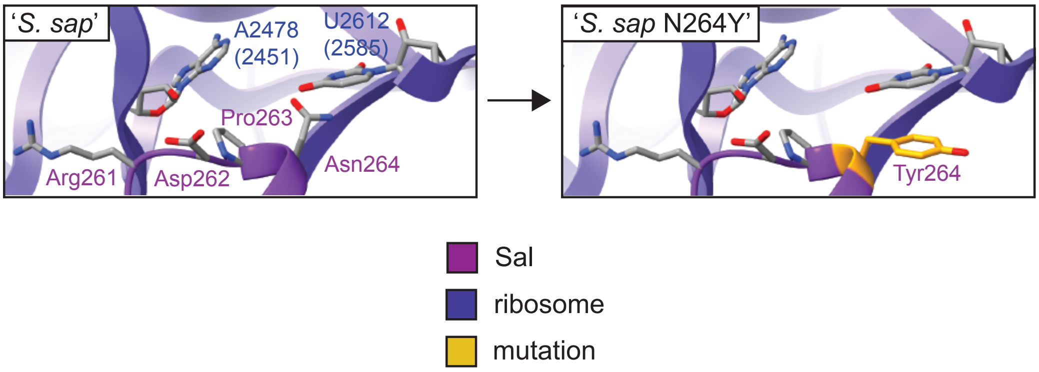

Figure 54 Representation of gain-of-function mutagenesis experiment. Left = sequence of Sal from *S. saprophyticus* mapped onto the structure of the Sal(B) interdomain linker loop in the Sal(B)-ribosome complex. Right = as left, but with Asn264 virtually mutated to Tyr264 (gold), as found in Sal(B).

The *S. saprophyticus* Sal N264Y mutant was introduced and expressed in *S. aureus* RN4220 by Merianne Mohamad, and minimum inhibitory concentration (MIC) experiments were performed by Merianne to measure the antibiotic resistance profile (Table 9). The resistance profile remained largely unchanged, with the exception of a modest (4-fold) but reproducible reduction in susceptibility to tiamulin. That any change is seen shows that Tyr264 plays a role in resistance conferred by Sal(A-C), at least to tiamulin. However, the fact that resistance to other drugs is unaffected suggests that the interaction mediated by Tyr264 is only one factor involved in resistance.

	MIC (µg/ml)			
Isolate	retapamulin	tiamulin	lincomycin	clindamycin
pRMC2 (empty vector control)	0.06	0.25	0.25	0.06
Sal(B) WT	8	16	8	1
Sal(B) Y264L	4 (1/2)	16 (1)	4 (1/2)	0.5 (1/2)
Sal(B) Y264I	4 (1/2)	16 (1)	4 (1/2)	0.5 (1/2)
Sal(B) Y264S	2 (1/4)	16 (1)	4 (1/2)	0.25 (1/4)
Sal(B) Y264N	2 (1/4)	16 (1)	8 (1)	1 (1)
Sal from *S. saprophyticus* WT	0.06	0.25	0.25	0.06
Sal from *S. saprophyticus* N264Y	0.06 (1)	1 (4)	0.25 (1)	0.06 (1)

Table 9 Antibiotic resistance profile of Sal(B), Sal from *S. saprophyticus* and related mutants. Fold differences shown in brackets, comparing Sal(B) mutants with Sal(B) WT and comparing Sal from *S. saprophyticus* N264Y mutant with Sal from *S. saprophyticus* WT.

Loss-of-function experiments were also performed. Here, Tyr264 of Sal(B) was mutated to leucine, isoleucine, serine and asparagine with the expectation of bringing the resistance profile more in line with that of Sal(D) (leucine), Sal(E) and Sal from *S. xylosus* (isoleucine), Sal from *S. equorum* (serine) and Sal from *S. saprophyticus* (asparagine) (Figure 55).

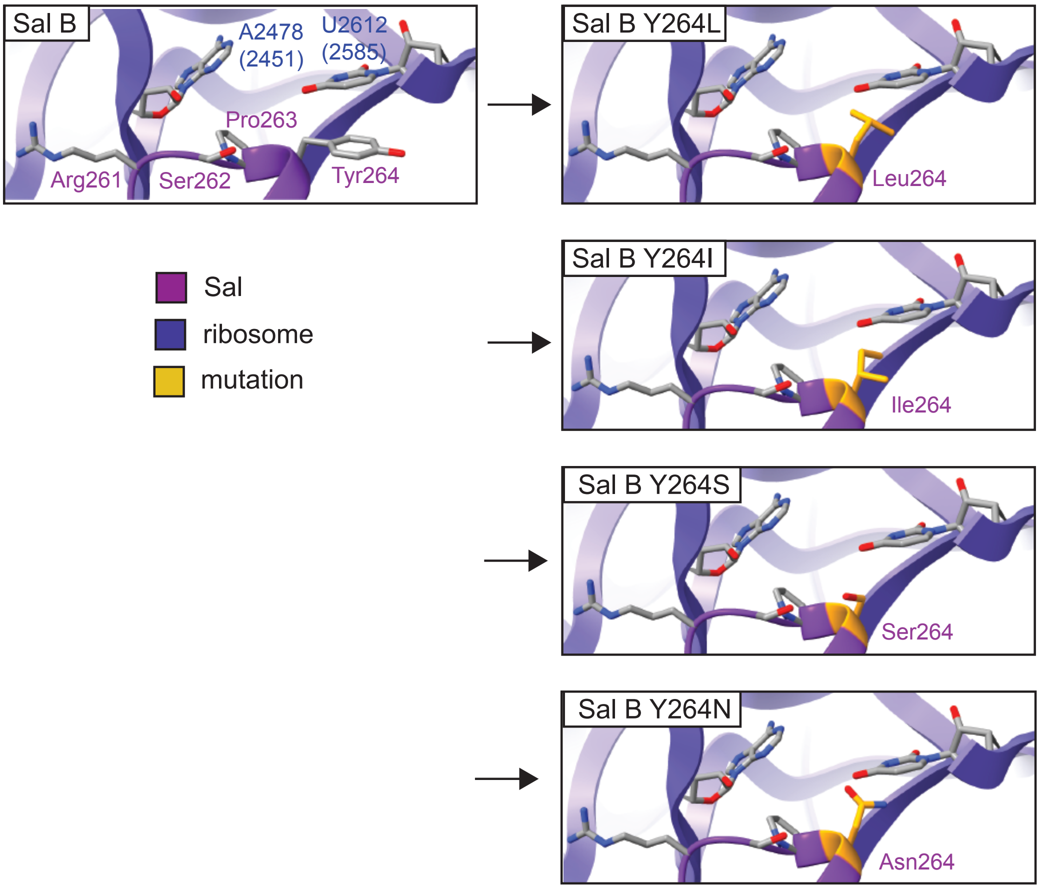

Figure 55 Representation of the loss-of-function mutagenesis experiments. Left = model of the structure of the Sal(B) interdomain linker loop in the Sal(B)-ribosome complex. Right = as left, but with Tyr264 virtually mutated (gold) to Leu264 as found in Sal(D), Ile264 as found in Sal(E) and Sal from *S. xylosus*, Ser264 as found in Sal from *S. equorum*, and Asn264 as found in Sal from *S. saprophyticus*.

The Sal(B) Y264L/I/S/N mutants were introduced and expressed in *S. aureus* RN4220 by Merianne Mohamad, and MIC experiments were performed by Merianne to measure the antibiotic resistance profiles (Table 9).

The retapamulin susceptibility of all mutants increased compared with wild type Sal(B), though not to empty vector control levels. Susceptibilities to the lincosamides lincomycin and clindamycin also increased compared to wild type for all mutants except Sal(B) Y264N, again not to empty vector control levels. This was unexpected, as it is not obvious from the Sal(B)-ribosome structure how changes in position 264 could affect lincosamide resistance since these drugs do not interact with U2612 (2585). Also unexpectedly, these loss-of-function mutations had no effect on tiamulin resistance, unlike the gain-of-function experiment described above. Presumably, differences between Sal(B) and the Sal from *S. saprophyticus* at other residues lead to these seemingly contradictory findings.

Regardless, these findings suggest that Tyr264 plays some role in strengthening pleuromutilin and lincosamide resistance in Sal(A-C), along with a number of other contributing factors. Clearly, more in-depth mutagenesis experiments throughout the entire interdomain linker loop are needed to identify other residues contributing to the differences in conferred resistance phenotype among the Sal variants.

4.3 Discussion

The possibility of Sal-type ABC-F protein mediated pleuromutilin resistance occurring in *S. aureus* is concerning, which prompted cryo-EM structure determination of the Sal(B)-ribosome complex and mutagenesis experiments to help understand the mechanisms by which these proteins protect the ribosome from LS_AP antibiotics.

Section 4.3.1 overviews the structure of the Sal(B)-ribosome complex and proposes a model that describes how Sal(B) protects the ribosome. Section 4.3.2 explores possible alternative mechanisms of drug displacement, and experiments needed to probe these further. Both of these sections also explore the differences in antibiotic resistance profiles among the Sal variants. Finally, section 4.3.3 views the Sal(B)-ribosome complex in the context of other ARE ABC-F protein : ribosome complexes. The structures and potential ribosome-protection mechanisms are compared, and the likelihood of a general ARE ABC-F protein mediated drug displacement mechanism is assessed.

4.3.1 Summary of structure and proposed model

The cryo-EM structure of a physiological complex between the *S. aureus* 70S initiation complex and the EQ_2 mutant of Sal(B) was solved to 2.9 Å resolution (Figure 38). The two globular NBDs of Sal(B) adopt a closed conformation, with two ATP molecules sandwiched between them, and bind to the E-site of the ribosome between the L1 stalk and P-site tRNA (Figure 43, Figure 45). These ATP molecules are not hydrolysed due to the EQ_2 mutation, which fixes the NBDs in their closed state and locks Sal(B) to the ribosome. The interdomain linker loop protrudes towards the PTC in the 50S subunit, the site where LS_AP antibiotics bind. In doing so, the interdomain linker distorts the acceptor stem of the P-site $tRNA^{fMet}$ away from the PTC by 22 Å, which may be energetically compensated for by newly formed interactions between the distorted P-site tRNA and the interdomain linker and NBD2 regions of Sal(B) (Figure 48). The interdomain linker loop induces conformational changes in three 23S rRNA loops comprising the PTC. Specifically, the backbone of Arg261 and Ser262 and the ring of Pro263 of the loop distort the PTC loops containing residues A2477-C2479 (2450-2452) and A2530-G2532 (2503-2505), whereas Tyr264 π-stacks with U2612 (U2585), moving this base away from the drug binding site (Figure 50). Finally, a C-terminal extension of Sal(B) wraps around the 30S subunit of the ribosome but does not reach the mRNA : 16S rRNA duplex in the exit channel, so is unlikely to contribute to substrate recognition (Figure 46).

A proposed mechanism of Sal(B) mediated resistance based on these findings follows. Sal(B) binds to the E-site of predominantly 70S initiation complexes. Since the C-terminal extension of Sal(B) does not reach into the mRNA exit channel, there is no obvious way that Sal(B) would recognise initiation complexes over elongating ribosomes. Instead, Sal(B) likely initially targets any ribosome with an empty E-site that allows its NBDs to bind, i.e. initiation complexes or ribosomes stalled during elongation. In initiation complexes, the interdomain linker of Sal(B) distorts the acceptor stem fMet-tRNA^{fMet} away from the PTC, which may be compensated for by interactions between Sal(B) and the tRNA molecule. In elongation complexes, the P-site tRNA carries a nascent polypeptide chain which would be partially pulled out of the peptide exit tunnel as the acceptor stem is distorted. It might be the case that the energetic cost of such a process would be too large to be compensated by the additional interactions formed between Sal(B) and the P-site tRNA, which is what leads to the binding specificity of Sal(B) for initiation complexes. Such exclusive targeting of Sal(B) to initiation complexes is likely sufficient for mediation of resistance to LS$_A$P antibiotics, as these are thought to disrupt translation primarily at the start codon [84,293]. In contrast, Sal(B) does not mediate resistance to phenicols and oxazolidinones, which bind the PTC during translation elongation [75].

The distortion of P-site tRNA allows the interdomain linker of Sal(B) to reach the PTC. This process leads to the reduction in binding affinity of PTC-targeting antibiotics, giving rise to Sal-mediated antibiotic resistance in *S. aureus*. Such displacement certainly does not happen due to direct displacement from steric overlap with the drug, as the closest distance between the interdomain linker loop and the drug site is about 8 Å. Instead, the loop may displace the drug through an allosteric mechanism, by distorting the 23S rRNA loops comprising the PTC (i.e. type II target protection). However, the residues of the loop that form the closest contacts with 23S rRNA A2477-C2479 (2450-2452), i.e. Arg261 and Pro263, remain conserved across all Sal variants, so it is unclear how allosteric displacement of drug would happen in ARE Sal variants A-E, but not in the non-ARE Sal variants based on these residues (Figure 53). On the other hand, residue 264, which interacts with U2612 (U2585), does differ among the Sal variants, therefore differences in an allosteric displacement interaction through residue 264 could theoretically explain differences in resistance (Figure 53). However, this is complicated by the fact that lincosamides do not directly interact with U2612 (U2585) (Figure 52), and that mutagenesis at this position only has modest effects on resistance (Table 9). Therefore, allosteric displacement of antibiotics through the interaction of Tyr264 with U2612 (2585), can only be one of multiple factors that leads to LS$_A$P drug displacement.

However Sal(B) achieves the displacement of LS_AP antibiotics, the distortion of P-site tRNA and occupancy of the PTC by the interdomain linker loop of Sal(B) both prevent peptidyl transfer, and so translation cannot occur until Sal(B) dissociates from the ribosome. This presumably occurs through the hydrolysis of one or both of the bound ATP molecules to drive the NBDs apart [290], forcing Sal(B) to dissociate and allowing P-site tRNA to return to the P/P-site, although the trigger for such a mechanism remains unknown. A tRNA can then be delivered and accommodated at the A-site, and the first peptidyl transfer reaction can occur, resulting in a short nascent chain that likely precludes PTC-targeting antibiotics from rebinding. In this model, only one round of Sal(B) binding and ATP hydrolysis per translation cycle is necessary to give rise to drug resistance.

4.3.2 Other possible mechanisms of drug displacement

The discussion above proposes an allosteric mechanism of drug displacement by Sal(B), but recognises there is conflicting evidence. This section will explore other possible mechanisms.

Although the Sal(B)-ribosome structure is ‘physiologically relevant’, meaning that it was solved from complete Sal-ribosome complexes isolated from *S. aureus* cells, it should be noted that it only shows a snapshot. The complex involves the EQ_2 mutant of Sal(B), which locks the protein onto the ribosome. Conformational changes in the Sal-ribosome complex before or after this state might be involved in dislodging bound antibiotics, in which case, visualisation of these changes would be necessary to fully understand the resistance mechanism. These two possible scenarios, i.e. changes before or after this structural snapshot being the cause of drug displacement, will be discussed in turn.

Firstly, the structure solved here might show a pre-antibiotic-dissociation state, with Sal(B) still to undergo a conformational change to displace the drug. Considering there is no steric overlap between the interdomain linker loop of Sal(B) with the drug site, it is feasible that an antibiotic could stay bound to the EQ_2 Sal(B)-ribosome complex. In this scenario, ATP hydrolysis might be involved in both Sal(B) release and drug displacement; in fact, the two ATP sites might undergo ATP hydrolysis independently. One possibility is that ATP hydrolysis at one site provides the energy for a conformational change in Sal(B) that causes drug displacement, whilst hydrolysis at the other site drives Sal(B) dissociation. Indeed, there is evidence that the eukaryotic protein ABCE1 delivers energy for ribosome splitting by asymmetric, allosterically-coupled ATP binding and hydrolysis events at its two

ATP sites [301]. Such a mechanism could be investigated by solving the cryo-EM structure of the EQ_2 Sal(B)-ribosome complex after incubation with PTC antibiotics, in which concurrent binding of non-hydrolysable EQ_2 Sal(B) and PTC drugs would support some form of ATP-hydrolysis-mediated mechanism of drug displacement. Biochemical and structural studies using single ‘EQ’ mutants could also be performed to explore possible asymmetric function of the ATP sites.

On the other hand, although antibiotic could feasibly stay bound to the EQ_2 Sal(B)-ribosome complex, there is some indirect evidence to oppose this. For one, the EQ_2 mutant of MsrE displaces azithromycin from the ribosome, and secondly, the interdomain linker loop of EQ_2 VmlR directly overlaps with the drug binding site in the PTC [267]. One might expect a similar mutual exclusivity in ribosome binding of Sal(B) and PTC-targeting antibiotics, in which case the structure solved in this study would show a post-antibiotic-dissociation state. Such a scenario would allow two possibilities for the mechanism of drug displacement.

Firstly, the interdomain linker loop of Sal(B) may displace drugs through an allosteric mechanism (type II target protection), as discussed in section 4.3.1 above. The Sal(B) residues that directly interact with 23S rRNA cannot fully explain such a mechanism, but residues further from the PTC might affect allosteric displacement by changing the shape of the linker loop more generally. This could be investigated by performing a thorough series of mutagenesis experiments throughout the interdomain linker loop and the surrounding region.

Alternatively, rather than the distortion of P-site tRNA being a means to allow the interdomain linker loop to reach the PTC, it is possible that this distortion itself is what drives antibiotic displacement. The 3’-terminus of P-tRNA, situated in the P-site of the PTC in an initiation complex, undergoes a large shift on Sal(B) binding, which could potentially disrupt the 23S rRNA of the PTC in the process to allosterically displace PTC-bound antibiotic.

No matter the mechanism of drug displacement, distortion of P-site tRNA is required for Sal(B) binding. All Sal variants, including those that do not mediate resistance, contain an interdomain linker of equal length, and so all would be expected to distort P-site tRNA on binding to the ribosome. However, it is possible that some variants are not able to energetically compensate for this as efficiently as others, in which case the binding of these variants to the ribosome would be less favourable and they would be less effective at displacing PTC-bound drug. Indeed, this might explain why Sal(D)- or Sal(E)-ribosome complexes could not be isolated by the *in vivo* $FLAG_3$-tag affinity approach: these variants may be less able to compensate for P-site tRNA distortion compared with Sal(A-C), and thereby bind the ribosome with lower affinities to give lower levels of drug resistance. Following this pattern, the Sal variants that do not mediate resistance might bind so weakly as to cause no significant drug displacement, but presumably still strongly enough to perform their housekeeping role.

Pelleting assays, where binding of a protein to the ribosome is measured after pelleting through a sucrose cushion, could be carried out for the EQ_2 mutants of all Sal variants following the *in vivo* $FLAG_3$-tag affinity procedure to ascertain whether the amount of ribosome binding correlates with the level of resistance to PTC-binding antibiotics. Furthermore, mutagenesis experiments of the residues in the interdomain linker and NBD2 of Sal(B) that are likely involved in compensatory interactions with distorted P-tRNA (Figure 48B) might uncover a link between Sal variant sequence and resistance profile.

4.3.3 ABC-F mediated resistance: a general mechanism, or protein-specific?

The structure of the Sal(B)-ribosome complex shows that, like MsrE, VmlR, LsaA, $VgaA_{LC}$ and VgaL, Sal(B) binds to the E-site of the ribosome, and its interdomain linker reaches towards the PTC, distorting P-site tRNA in the process [187,260,267]. In general, the interactions that the NBDs and interdomain linker make with the ribosomal proteins and rRNA helices are similar. However, the details of the interaction between the interdomain linker loop and the PTC, and the likely mechanisms by which this loop displaces antibiotics, seem to differ slightly among the ARE ABC-F proteins.

In all cases, 23S rRNA residues A2503-U2506 are distorted on ABC-F protein binding. This is achieved by direct interaction by MsrE residue Arg241, and indirect interactions by the other proteins. U2585 is also displaced in most cases, either by stacking with 23S rRNA A2602 in the MsrE complex, VmlR Tyr240, $VgaA_{LC}$ Tyr223 or Sal(B) Tyr264. However, U2585 is poorly ordered in the LsaA and VgaL complexes. For all these ARE ABC-F proteins, these allosteric interactions with the 23S rRNA likely cause displacement of bound antibiotic, or at least play a role in this process. At least in the case of Sal(B), ABC-F protein residues that do not contact the 23S rRNA may contribute to such a mechanism, perhaps by changing the shape of the interdomain linker loop.

On the other hand, there are differences in the extent to which steric overlap could play a role in drug displacement. Residues Leu242 of MsrE, Phe237 of VmlR, Phe257 of LsaA and Val219 of $VgaA_{LC}$ all overlap with the drug binding site, however mutations in the latter three have limited impact on antibiotic resistance, suggesting that steric overlap plays a minimal role in drug displacement by these three proteins. No residue of VgaL or Sal(B) overlaps with the drug site, so steric overlap certainly plays no role in these two cases.

It should be noted that OptrA has a much shorter interdomain linker than the other ARE ABC-F proteins discussed here, and is instead similar in length to the linker of EttA [272]. Since the linker of OptrA likely cannot reach the PTC to sterically or allosterically displace drugs, it presumably mediates resistance to PTC-binding phenicols and oxazolidinones through a different mechanism. Other ARE ABC-F proteins might also implement such a mechanism in addition to PTC interaction, and could explain why mutations in the 23S rRNA-contacting Sal(B) residues only have a minor effect on resistance.

Differences in target protection mechanisms among the ARE ABC-F proteins is consistent with phylogenetic analyses, which suggest that these proteins have likely evolved independently, and so may have functionally converged on drug resistance through different mechanisms [127,272].

4.3.4 Future work

More structural work should be carried out to build on the single snapshot solved so far. For example, solving the structure of a Sal-ribosome complex after incubation of drug, or better yet, a Sal-drug-ribosome complex isolated directly from cells, would provide additional mechanistic details if such a ternary complex is possible, and confirm the EQ_2 Sal(B)-ribosome complex is in a pre-antibiotic-dissociation state. Furthermore, solving structures of Sal-ribosome complexes containing single EQ Sal mutants might help to visualise mechanistic conformational changes in Sal if asymmetric, allosteric coupling of ATP binding and hydrolysis occurs.

Experiments to supplement such structural work to further elucidate the mechanism of Sal(B)-mediated drug displacement should be performed, including additional mutagenesis experiments throughout the interdomain linker loop and regions of the protein that interact with P-site tRNA; biochemical studies involving single EQ mutants; and pelleting assays of *in vivo* FLAG-tag purified complexes between the ribosome and the different Sal variants. Molecular dynamics simulations could also be carried out to predict how the mobility or flexibility of the Sal(B) linker loop, and hence its interaction with the PTC, is affected by changes in sequence.

Looking beyond Sal, elucidating more structures of physiological ABC-F protein : ribosome complexes containing ARE ABC-F proteins from a variety of phenotypic groups might confirm whether mechanisms of drug displacement are protein-specific. In particular, the structure of the complex between the ribosome and OptrA might reveal how an ABC-F protein whose interdomain linker is too short to reach the PTC can displace PTC-bound antibiotics, and the structure of a physiological complex between the ribosome and a protein that displaces drugs during elongation like MsrE [260], might reveal how a P-site tRNA carrying a nascent polypeptide chain is distorted in such complexes.

Such experiments might provide a better understanding of ribosome protection by Sal and other ARE ABC-F proteins, which could help with the improvement of current antibiotics or the development of new ones, a topic which will be further discussed in Chapter 5.

Chapter 5 Concluding remarks

5.1 Summary

This thesis describes high resolution structures of ribosomes from clinically important pathogenic bacteria, complexed with either an antibiotic or an ARE ABC-F protein. These studies provide new insights into structural features of these ribosomes, and help to explain how small molecule drugs and target protection proteins interact with ribosomes to inhibit or rescue translation, respectively.

Chapter 3 describes structures of the ribosome from the pathogen *A. baumannii* in complex with amikacin and tigecycline, two drugs commonly used to treat *A. baumannii* infections in the clinic. Analysis of these structures revealed unique features of the *A. baumannii* ribosome compared with the *E. coli* ribosome. The major, known antibiotic binding sites on the ribosome, such as the PTC, NPET entrance and the DC, are largely conserved, however, there are some species-specific differences in functional sites which are less directly involved in protein synthesis, such as the solvent-facing exit of the NPET and the periphery of the interface between the large and small ribosomal subunits. Further analysis of the ribosome structures revealed that amikacin binds within an internal loop of 16S rRNA h44 and tigecycline binds to 16S rRNA h34, as seen in other structures involving ribosomes from different bacterial species. In contrast, tigecycline was also found to bind to the 50S central protuberance at a site not seen in other tigecycline-ribosome structures. Binding at this site could feasibly affect translation by rearrangement of the subunit interface. However, as discussed in Chapter 3, orthogonal validation of this finding via other experiments is needed to assess the binding of lower concentrations of tigecycline to *A. baumannii* 50S subunits. This could be via measuring the amount of tigecycline bound to the subunit after pelleting the sample through a sucrose cushion, e.g. by using a radiolabel or by heat treatment followed by mass spectrometry.

Chapter 4 describes the structure of the ribosome from the pathogen *S. aureus* in complex with the ARE ABC-F protein, Sal(B). Structural analysis revealed that Sal(B) binds the E site of the ribosome with its interdomain linker protruding towards the PTC. Sal(B)'s interdomain linker loop does not sterically overlap with the antibiotic binding site, and likely mediates drug displacement by allosteric displacement. Comparison of the interdomain linker loop sequences from known Sal variants that confer different resistance phenotypes identified that Tyr264 plays an important role in this allosteric interaction. However, mutational analysis shows that other residues must also contribute. As discussed, Sal(B) interacts with the ribosome in a broadly similar manner to that observed previously for other ARE ABC-F proteins, but the exact mechanism by which the interdomain linker displaces antibiotic appears to vary. Further structural and mutational experiments involving a variety of ABC-F proteins should help to build a broader picture of how this protein family operates.

5.2 Implications for antibiotic design

The work outlined in this thesis contributes to our molecular understanding of the mechanisms by which antibiotics inhibit the growth of pathogenic bacteria, and the mechanisms by which such bacteria resist the action of antibiotics. Not only is this knowledge of fundamental biological interest, but it may also play a role in the design of new antibiotics needed to combat the rising threat of drug resistance.

Most current classes of ribosome-binding antibiotics target the PTC, NPET entrance and DC. These regions are highly conserved in the *A. baumannii* ribosome compared with ribosomes from other bacteria, so there appears to be limited scope to improve the effectiveness of such antibiotics in a species-selective manner. However, there are some unique features at functional sites less directly involved in protein synthesis, such as the solvent-facing exit of the NPET and the periphery of the subunit interface that might provide new therapeutic opportunities. The NPET exit is the site where a number of ribosome-associated factors dock, and the subunit interface is important for 70S stability and translocation. Therefore, these sites are potential targets for the development of new types of antibiotics that could theoretically have particular effectiveness against *A. baumannii*, either alone or as part of combination therapies. Such specificity might be useful in avoiding side effects arising from disturbance of the gut microbiota [247]. In addition, if binding of tigecycline to the secondary site in the central protuberance does indeed inhibit ribosome function, then this site could be the focus of structure-based design of new scaffolds that disrupt translation by a novel mechanism. Furthermore, solving structures of the *A. baumannii* ribosome in different conformational states or stalled mid-translation by an antibiotic of interest might provide even more insight for the rational design of new drugs.

A more complete understanding of Sal-mediated target protection is needed before a concrete strategy to design antibiotics that circumvent or inhibit this resistance mechanism can be established. As discussed, this will require mutational analysis throughout the interdomain linker loop and surrounding areas of Sal(B) to pinpoint which residues contribute to resistance. Structures of ribosomes in complex with Sal variants that confer a different resistance profile to Sal(B), or no resistance at all, would also provide insight into the features that drive resistance by some Sal proteins but not others. In addition, structural determination of a Sal(B)-antibiotic-ribosome ternary complex would also provide more detail on the interactions between these three components, if formation of such a complex is possible. Biochemical and structural experimentation with single EQ mutants would also help to visualize mechanistic-important conformational changes in Sal if ATP hydrolysis in one site dislodges bound drugs, while hydrolysis in the other drives Sal dissociation. Finally, molecular dynamics simulations might complement such structural snapshots to provide clues on how the dynamics of Sal(B) contribute to displacement of bound drug. The calculations required for simulating the dynamics of such a large complex would be computationally expensive, and so modelling would likely need to be focused on the Sal(B)-PTC interaction.

Although the precise mechanism by which LS$_{A}$P antibiotics are displaced by ARE Sal proteins remains to be elucidated, we can start to consider how antibiotics can be developed that overcome this resistance mechanism. Possible strategies include the modification of the LS$_{A}$P drug in a manner that mitigates resistance, as seen for tetracycline-derivatives such as tigecycline, or the pairing of the LS$_{A}$P drug with a small molecule inhibitor of the resistance mechanism in a combination therapy, similar to the use of β-lactamase inhibitors to protect β-lactams from hydrolysis. However, using a drug to inhibit a resistance mechanism would likely only be useful if it was known to be the major or sole cause of resistance to a specific antibiotic [120].

Modification of an LS$_{A}$P drug to overcome Sal-mediated allosteric displacement would be challenging, as it would involve fundamentally changing how the LS$_{A}$P drug interacts with the PTC. It might be possible to modify LS$_{A}$P drugs so that they avoid the 23S rRNA regions distorted by Sal, whilst still maintaining contacts with the rest of the PTC. This would leave them unaffected by Sal binding but still able to perform their inhibitory function. However, this would likely prove difficult in practice as there is significant overlap between the regions of the 23S rRNA that interact with Sal(B) and those that make up the drug binding site. A more blunt method would be to design drugs with increased binding affinity to the PTC. For example, tedizolid, an oxazolidinone derived from linezolid, has increased potency compared with its parent compound, likely due to additional 23S rRNA interactions [302]. This increased potency is maintained in strains containing the ARE ABC-F protein OptrA [280], implying that drugs that bind strongly enough to the PTC might overcome allosteric target protection [120]. OptrA was also the target for fragment-based screening, which identified an inhibitor that suppressed its ATP hydrolysis activity *in vitro* [303]. This suggests that inhibition of ARE ABC-F proteins may also be a potential strategy to mitigate resistance.

Combatting antibiotic resistance is one of the most urgent challenges facing society, requiring concerted global action by governments, the pharmaceutical and agricultural industries, healthcare providers, academics and members of the public. The UN's Interagency Coordination Group on Antimicrobial Resistance has proposed that the three ways to do this are to reduce the need for, and unintentional exposure to, antimicrobials, optimise the use of antimicrobials, and improve innovation, supply and access [304]. This final strategy requires the pharmaceutical industry to make novel antibiotics, which is particularly challenging as antibiotic development is highly unprofitable [130]. Fundamental scientific research, including structural biology, could help the industry to innovate in this area by revealing how current antibiotics work and how resistance can occur, improving our understanding of potential drug targets, and discovering new drug scaffolds. Such collaboration between academia and industry is an important step towards a world where the development of new antibiotics outpaces the emergence of resistance.

Bibliography

1. Kohanski, M.A., Dwyer, D.J., Hayete, B., Lawrence, C.A. & Collins, J.J. A common mechanism of cellular death induced by bactericidal antibiotics. *Cell* **130**, 797-810 (2007).
2. Wilson, D.N. The A-Z of bacterial translation inhibitors. *Crit Rev Biochem Mol Biol* **44**, 393-433 (2009).
3. Lin, J., Zhou, D., Steitz, T.A., Polikanov, Y.S. & Gagnon, M.G. Ribosome-Targeting Antibiotics: Modes of Action, Mechanisms of Resistance, and Implications for Drug Design. *Annu Rev Biochem* **87**, 451-478 (2018).
4. Schmeing, T.M. & Ramakrishnan, V. What recent ribosome structures have revealed about the mechanism of translation. *Nature* **461**, 1234-42 (2009).
5. Ratje, A.H. et al. Head swivel on the ribosome facilitates translocation by means of intra-subunit tRNA hybrid sites. *Nature* **468**, 713-6 (2010).
6. Cornish, P.V. et al. Following movement of the L1 stalk between three functional states in single ribosomes. *Proc Natl Acad Sci U S A* **106**, 2571-6 (2009).
7. Diaconu, M. et al. Structural basis for the function of the ribosomal L7/12 stalk in factor binding and GTPase activation. *Cell* **121**, 991-1004 (2005).
8. Ramakrishnan, V. Ribosome structure and the mechanism of translation. *Cell* **108**, 557-72 (2002).
9. Rodnina, M.V. Translation in Prokaryotes. *Cold Spring Harb Perspect Biol* **10**, a032664 (2018).
10. Cech, T.R. Structural biology. The ribosome is a ribozyme. *Science* **289**, 878-9 (2000).
11. Nikolay, R., van den Bruck, D., Achenbach, J. & Nierhaus, K.H. Ribosomal Proteins: Role in Ribosomal Functions. *eLS, John Wiley & Sons, Ltd (Ed.)* (2015).
12. Voorhees, R.M., Weixlbaumer, A., Loakes, D., Kelley, A.C. & Ramakrishnan, V. Insights into substrate stabilization from snapshots of the peptidyl transferase center of the intact 70S ribosome. *Nat Struct Mol Biol* **16**, 528-33 (2009).
13. Peske, F., Rodnina, M.V. & Wintermeyer, W. Sequence of steps in ribosome recycling as defined by kinetic analysis. *Mol Cell* **18**, 403-12 (2005).
14. Antoun, A., Pavlov, M.Y., Lovmar, M. & Ehrenberg, M. How initiation factors maximize the accuracy of tRNA selection in initiation of bacterial protein synthesis. *Mol Cell* **23**, 183-93 (2006).
15. Milon, P., Konevega, A.L., Gualerzi, C.O. & Rodnina, M.V. Kinetic checkpoint at a late step in translation initiation. *Mol Cell* **30**, 712-20 (2008).
16. Grigoriadou, C., Marzi, S., Kirillov, S., Gualerzi, C.O. & Cooperman, B.S. A quantitative kinetic scheme for 70 S translation initiation complex formation. *J Mol Biol* **373**, 562-72 (2007).
17. Rodnina, M.V. Translation in Prokaryotes. *Cold Spring Harb Perspect Biol* **10**(2018).
18. Yamamoto, H. et al. 70S-scanning initiation is a novel and frequent initiation mode of ribosomal translation in bacteria. *Proc Natl Acad Sci U S A* **113**, E1180-9 (2016).
19. Ogle, J.M. et al. Recognition of cognate transfer RNA by the 30S ribosomal subunit. *Science* **292**, 897-902 (2001).
20. Loveland, A.B., Demo, G., Grigorieff, N. & Korostelev, A.A. Ensemble cryo-EM elucidates the mechanism of translation fidelity. *Nature* **546**, 113-117 (2017).
21. Demeshkina, N., Jenner, L., Westhof, E., Yusupov, M. & Yusupova, G. A new understanding of the decoding principle on the ribosome. *Nature* **484**, 256-9 (2012).
22. Pape, T., Wintermeyer, W. & Rodnina, M. Induced fit in initial selection and proofreading of aminoacyl-tRNA on the ribosome. *EMBO J* **18**, 3800-7 (1999).

23. Sievers, A., Beringer, M., Rodnina, M.V. & Wolfenden, R. The ribosome as an entropy trap. *Proc Natl Acad Sci U S A* **101**, 7897-901 (2004).
24. Wallin, G. & Aqvist, J. The transition state for peptide bond formation reveals the ribosome as a water trap. *Proc Natl Acad Sci U S A* **107**, 1888-93 (2010).
25. Kuhlenkoetter, S., Wintermeyer, W. & Rodnina, M.V. Different substrate-dependent transition states in the active site of the ribosome. *Nature* **476**, 351-4 (2011).
26. Polikanov, Y.S., Steitz, T.A. & Innis, C.A. A proton wire to couple aminoacyl-tRNA accommodation and peptide-bond formation on the ribosome. *Nat Struct Mol Biol* **21**, 787-93 (2014).
27. Agirrezabala, X. et al. Visualization of the hybrid state of tRNA binding promoted by spontaneous ratcheting of the ribosome. *Mol Cell* **32**, 190-7 (2008).
28. Julian, P. et al. Structure of ratcheted ribosomes with tRNAs in hybrid states. *Proc Natl Acad Sci U S A* **105**, 16924-7 (2008).
29. Belardinelli, R., Sharma, H., Peske, F., Wintermeyer, W. & Rodnina, M.V. Translocation as continuous movement through the ribosome. *RNA Biol* **13**, 1197-1203 (2016).
30. Waudby, C.A., Dobson, C.M. & Christodoulou, J. Nature and Regulation of Protein Folding on the Ribosome. *Trends Biochem Sci* **44**, 914-926 (2019).
31. Jomaa, A., Boehringer, D., Leibundgut, M. & Ban, N. Structures of the E. coli translating ribosome with SRP and its receptor and with the translocon. *Nat Commun* **7**, 10471 (2016).
32. Klaholz, B.P. et al. Structure of the Escherichia coli ribosomal termination complex with release factor 2. *Nature* **421**, 90-4 (2003).
33. Rawat, U.B. et al. A cryo-electron microscopic study of ribosome-bound termination factor RF2. *Nature* **421**, 87-90 (2003).
34. Weixlbaumer, A. et al. Insights into translational termination from the structure of RF2 bound to the ribosome. *Science* **322**, 953-6 (2008).
35. Loh, P.G. & Song, H. Structural and mechanistic insights into translation termination. *Curr Opin Struct Biol* **20**, 98-103 (2010).
36. Laurberg, M. et al. Structural basis for translation termination on the 70S ribosome. *Nature* **454**, 852-7 (2008).
37. Rodnina, M.V. The ribosome as a versatile catalyst: reactions at the peptidyl transferase center. *Curr Opin Struct Biol* **23**, 595-602 (2013).
38. Gao, H. et al. RF3 induces ribosomal conformational changes responsible for dissociation of class I release factors. *Cell* **129**, 929-41 (2007).
39. Gao, N. et al. Mechanism for the disassembly of the posttermination complex inferred from cryo-EM studies. *Mol Cell* **18**, 663-74 (2005).
40. Chen, Y., Kaji, A., Kaji, H. & Cooperman, B.S. The kinetic mechanism of bacterial ribosome recycling. *Nucleic Acids Res* **45**, 10168-10177 (2017).
41. Huter, P. et al. Structural Basis for Polyproline-Mediated Ribosome Stalling and Rescue by the Translation Elongation Factor EF-P. *Mol Cell* **68**, 515-527 e6 (2017).
42. Wilson, D.N., Arenz, S. & Beckmann, R. Translation regulation via nascent polypeptide-mediated ribosome stalling. *Curr Opin Struct Biol* **37**, 123-33 (2016).
43. Huter, P., Muller, C., Arenz, S., Beckert, B. & Wilson, D.N. Structural Basis for Ribosome Rescue in Bacteria. *Trends Biochem Sci* **42**, 669-680 (2017).
44. Chan, K.H. et al. Mechanism of ribosome rescue by alternative ribosome-rescue factor B. *Nat Commun* **11**, 4106 (2020).
45. Wilson, D.N. Ribosome-targeting antibiotics and mechanisms of bacterial resistance. *Nat Rev Microbiol* **12**, 35-48 (2014).
46. Poehlsgaard, J. & Douthwaite, S. The bacterial ribosome as a target for antibiotics. *Nat Rev Microbiol* **3**, 870-81 (2005).

47. Zhang, L. et al. Ribosome-targeting antibacterial agents: Advances, challenges, and opportunities. *Med Res Rev* (2021).
48. Kohanski, M.A., Dwyer, D.J., Wierzbowski, J., Cottarel, G. & Collins, J.J. Mistranslation of membrane proteins and two-component system activation trigger antibiotic-mediated cell death. *Cell* **135**, 679-90 (2008).
49. Pioletti, M. et al. Crystal structures of complexes of the small ribosomal subunit with tetracycline, edeine and IF3. *EMBO J* **20**, 1829-39 (2001).
50. Dinos, G. et al. Dissecting the ribosomal inhibition mechanisms of edeine and pactamycin: the universally conserved residues G693 and C795 regulate P-site RNA binding. *Mol Cell* **13**, 113-24 (2004).
51. Schuwirth, B.S. et al. Structural analysis of kasugamycin inhibition of translation. *Nat Struct Mol Biol* **13**, 879-86 (2006).
52. Schluenzen, F. et al. The antibiotic kasugamycin mimics mRNA nucleotides to destabilize tRNA binding and inhibit canonical translation initiation. *Nat Struct Mol Biol* **13**, 871-8 (2006).
53. Brodersen, D.E. et al. The structural basis for the action of the antibiotics tetracycline, pactamycin, and hygromycin B on the 30S ribosomal subunit. *Cell* **103**, 1143-54 (2000).
54. Grossman, T.H. Tetracycline Antibiotics and Resistance. *Cold Spring Harb Perspect Med* **6**, a025387 (2016).
55. Jenner, L. et al. Structural basis for potent inhibitory activity of the antibiotic tigecycline during protein synthesis. *Proc Natl Acad Sci U S A* **110**, 3812-6 (2013).
56. Schedlbauer, A. et al. Structural characterization of an alternative mode of tigecycline binding to the bacterial ribosome. *Antimicrob Agents Chemother* **59**, 2849-54 (2015).
57. Bulkley, D., Johnson, F. & Steitz, T.A. The antibiotic thermorubin inhibits protein synthesis by binding to inter-subunit bridge B2a of the ribosome. *J Mol Biol* **416**, 571-8 (2012).
58. Carter, A.P. et al. Functional insights from the structure of the 30S ribosomal subunit and its interactions with antibiotics. *Nature* **407**, 340-8 (2000).
59. Ogle, J.M., Murphy, F.V., Tarry, M.J. & Ramakrishnan, V. Selection of tRNA by the ribosome requires a transition from an open to a closed form. *Cell* **111**, 721-32 (2002).
60. Borovinskaya, M.A., Shoji, S., Fredrick, K. & Cate, J.H. Structural basis for hygromycin B inhibition of protein biosynthesis. *RNA* **14**, 1590-9 (2008).
61. Borovinskaya, M.A. et al. Structural basis for aminoglycoside inhibition of bacterial ribosome recycling. *Nat Struct Mol Biol* **14**, 727-32 (2007).
62. Wang, L. et al. Allosteric control of the ribosome by small-molecule antibiotics. *Nat Struct Mol Biol* **19**, 957-63 (2012).
63. Feldman, M.B., Terry, D.S., Altman, R.B. & Blanchard, S.C. Aminoglycoside activity observed on single pre-translocation ribosome complexes. *Nat Chem Biol* **6**, 54-62 (2010).
64. Stanley, R.E., Blaha, G., Grodzicki, R.L., Strickler, M.D. & Steitz, T.A. The structures of the anti-tuberculosis antibiotics viomycin and capreomycin bound to the 70S ribosome. *Nat Struct Mol Biol* **17**, 289-93 (2010).
65. Ermolenko, D.N. et al. The antibiotic viomycin traps the ribosome in an intermediate state of translocation. *Nat Struct Mol Biol* **14**, 493-7 (2007).
66. Marrero, P., Cabanas, M.J. & Modolell, J. Induction of translational errors (misreading) by tuberactinomycins and capreomycins. *Biochem Biophys Res Commun* **97**, 1047-42 (1980).

67. Holm, M., Mandava, C.S., Ehrenberg, M. & Sanyal, S. The mechanism of error induction by the antibiotic viomycin provides insight into the fidelity mechanism of translation. *Elife* **8**(2019).
68. Mohan, S., Donohue, J.P. & Noller, H.F. Molecular mechanics of 30S subunit head rotation. *Proc Natl Acad Sci U S A* **111**, 13325-30 (2014).
69. Boslego, J.W. et al. Effect of spectinomycin use on the prevalence of spectinomycin-resistant and of penicillinase-producing Neisseria gonorrhoeae. *N Engl J Med* **317**, 272-8 (1987).
70. Polacek, N. & Mankin, A.S. The ribosomal peptidyl transferase center: structure, function, evolution, inhibition. *Crit Rev Biochem Mol Biol* **40**, 285-311 (2005).
71. Simonovic, M. & Steitz, T.A. A structural view on the mechanism of the ribosome-catalyzed peptide bond formation. *Biochim Biophys Acta* **1789**, 612-23 (2009).
72. Tu, D., Blaha, G., Moore, P.B. & Steitz, T.A. Structures of MLSBK antibiotics bound to mutated large ribosomal subunits provide a structural explanation for resistance. *Cell* **121**, 257-70 (2005).
73. Dunkle, J.A., Xiong, L., Mankin, A.S. & Cate, J.H. Structures of the Escherichia coli ribosome with antibiotics bound near the peptidyl transferase center explain spectra of drug action. *Proc Natl Acad Sci U S A* **107**, 17152-7 (2010).
74. Bulkley, D., Innis, C.A., Blaha, G. & Steitz, T.A. Revisiting the structures of several antibiotics bound to the bacterial ribosome. *Proc Natl Acad Sci U S A* **107**, 17158-63 (2010).
75. Marks, J. et al. Context-specific inhibition of translation by ribosomal antibiotics targeting the peptidyl transferase center. *Proc Natl Acad Sci U S A* **113**, 12150-12155 (2016).
76. Hansen, J.L., Moore, P.B. & Steitz, T.A. Structures of five antibiotics bound at the peptidyl transferase center of the large ribosomal subunit. *J Mol Biol* **330**, 1061-75 (2003).
77. Fredrick, K. & Noller, H.F. Catalysis of ribosomal translocation by sparsomycin. *Science* **300**, 1159-62 (2003).
78. Ippolito, J.A. et al. Crystal structure of the oxazolidinone antibiotic linezolid bound to the 50S ribosomal subunit. *J Med Chem* **51**, 3353-6 (2008).
79. Wilson, D.N. et al. The oxazolidinone antibiotics perturb the ribosomal peptidyl-transferase center and effect tRNA positioning. *Proc Natl Acad Sci U S A* **105**, 13339-44 (2008).
80. Svidritskiy, E., Ling, C., Ermolenko, D.N. & Korostelev, A.A. Blasticidin S inhibits translation by trapping deformed tRNA on the ribosome. *Proc Natl Acad Sci U S A* **110**, 12283-8 (2013).
81. Eyal, Z. et al. A novel pleuromutilin antibacterial compound, its binding mode and selectivity mechanism. *Sci Rep* **6**, 39004 (2016).
82. Novak, R. Are pleuromutilin antibiotics finally fit for human use? *Ann N Y Acad Sci* **1241**, 71-81 (2011).
83. Poulsen, S.M., Karlsson, M., Johansson, L.B. & Vester, B. The pleuromutilin drugs tiamulin and valnemulin bind to the RNA at the peptidyl transferase centre on the ribosome. *Mol Microbiol* **41**, 1091-9 (2001).
84. Paukner, S. & Riedl, R. Pleuromutilins: Potent Drugs for Resistant Bugs-Mode of Action and Resistance. *Cold Spring Harb Perspect Med* **7**(2017).
85. Vazquez-Laslop, N. & Mankin, A.S. How Macrolide Antibiotics Work. *Trends Biochem Sci* (2018).
86. Kannan, K. et al. The general mode of translation inhibition by macrolide antibiotics. *Proc Natl Acad Sci U S A* **111**, 15958-63 (2014).
87. Kannan, K., Vazquez-Laslop, N. & Mankin, A.S. Selective protein synthesis by ribosomes with a drug-obstructed exit tunnel. *Cell* **151**, 508-20 (2012).

88. Hansen, J.L. et al. The structures of four macrolide antibiotics bound to the large ribosomal subunit. *Mol Cell* **10**, 117-28 (2002).
89. Lonks, J.R. & Goldmann, D.A. Telithromycin: a ketolide antibiotic for treatment of respiratory tract infections. *Clin Infect Dis* **40**, 1657-64 (2005).
90. Llano-Sotelo, B. et al. Binding and action of CEM-101, a new fluoroketolide antibiotic that inhibits protein synthesis. *Antimicrob Agents Chemother* **54**, 4961-70 (2010).
91. Harms, J.M., Schlunzen, F., Fucini, P., Bartels, H. & Yonath, A. Alterations at the peptidyl transferase centre of the ribosome induced by the synergistic action of the streptogramins dalfopristin and quinupristin. *BMC Biol* **2**, 4 (2004).
92. Noeske, J. et al. Synergy of streptogramin antibiotics occurs independently of their effects on translation. *Antimicrob Agents Chemother* **58**, 5269-79 (2014).
93. Mikolajka, A. et al. Differential effects of thiopeptide and orthosomycin antibiotics on translational GTPases. *Chem Biol* **18**, 589-600 (2011).
94. Belova, L., Tenson, T., Xiong, L., McNicholas, P.M. & Mankin, A.S. A novel site of antibiotic action in the ribosome: interaction of evernimicin with the large ribosomal subunit. *Proc Natl Acad Sci U S A* **98**, 3726-31 (2001).
95. Harms, J.M. et al. Translational regulation via L11: molecular switches on the ribosome turned on and off by thiostrepton and micrococcin. *Mol Cell* **30**, 26-38 (2008).
96. D'Costa, V.M. et al. Antibiotic resistance is ancient. *Nature* **477**, 457-61 (2011).
97. Jiang, X. et al. Dissemination of antibiotic resistance genes from antibiotic producers to pathogens. *Nat Commun* **8**, 15784 (2017).
98. Forsberg, K.J. et al. The shared antibiotic resistome of soil bacteria and human pathogens. *Science* **337**, 1107-11 (2012).
99. Davies, J. & Davies, D. Origins and evolution of antibiotic resistance. *Microbiol Mol Biol Rev* **74**, 417-33 (2010).
100. Blair, J.M., Webber, M.A., Baylay, A.J., Ogbolu, D.O. & Piddock, L.J. Molecular mechanisms of antibiotic resistance. *Nat Rev Microbiol* **13**, 42-51 (2015).
101. Kojima, S. & Nikaido, H. Permeation rates of penicillins indicate that Escherichia coli porins function principally as nonspecific channels. *Proc Natl Acad Sci U S A* **110**, E2629-34 (2013).
102. Davin-Regli, A. et al. Membrane permeability and regulation of drug "influx and efflux" in enterobacterial pathogens. *Curr Drug Targets* **9**, 750-9 (2008).
103. Piddock, L.J. Multidrug-resistance efflux pumps - not just for resistance. *Nat Rev Microbiol* **4**, 629-36 (2006).
104. Fitzpatrick, A.W.P. et al. Structure of the MacAB-TolC ABC-type tripartite multidrug efflux pump. *Nat Microbiol* **2**, 17070 (2017).
105. Garneau-Tsodikova, S. & Labby, K.J. Mechanisms of Resistance to Aminoglycoside Antibiotics: Overview and Perspectives. *Medchemcomm* **7**, 11-27 (2016).
106. Norris, A.L. & Serpersu, E.H. Ligand promiscuity through the eyes of the aminoglycoside N3 acetyltransferase IIa. *Protein Sci* **22**, 916-28 (2013).
107. Yang, W. et al. TetX is a flavin-dependent monooxygenase conferring resistance to tetracycline antibiotics. *J Biol Chem* **279**, 52346-52 (2004).
108. Gasparrini, A.J. et al. Tetracycline-inactivating enzymes from environmental, human commensal, and pathogenic bacteria cause broad-spectrum tetracycline resistance. *Commun Biol* **3**, 241 (2020).
109. Forsberg, K.J., Patel, S., Wencewicz, T.A. & Dantas, G. The Tetracycline Destructases: A Novel Family of Tetracycline-Inactivating Enzymes. *Chem Biol* **22**, 888-97 (2015).
110. Wright, G.D. Bacterial resistance to antibiotics: enzymatic degradation and modification. *Adv Drug Deliv Rev* **57**, 1451-70 (2005).

111. Billal, D.S., Feng, J., Leprohon, P., Legare, D. & Ouellette, M. Whole genome analysis of linezolid resistance in Streptococcus pneumoniae reveals resistance and compensatory mutations. *BMC Genomics* **12**, 512 (2011).
112. Fyfe, C., Grossman, T.H., Kerstein, K. & Sutcliffe, J. Resistance to Macrolide Antibiotics in Public Health Pathogens. *Cold Spring Harb Perspect Med* **6**(2016).
113. Bosling, J., Poulsen, S.M., Vester, B. & Long, K.S. Resistance to the peptidyl transferase inhibitor tiamulin caused by mutation of ribosomal protein l3. *Antimicrob Agents Chemother* **47**, 2892-6 (2003).
114. Chittum, H.S. & Champney, W.S. Ribosomal protein gene sequence changes in erythromycin-resistant mutants of Escherichia coli. *J Bacteriol* **176**, 6192-8 (1994).
115. Beauclerk, A.A. & Cundliffe, E. Sites of action of two ribosomal RNA methylases responsible for resistance to aminoglycosides. *J Mol Biol* **193**, 661-71 (1987).
116. Cundliffe, E. & Demain, A.L. Avoidance of suicide in antibiotic-producing microbes. *J Ind Microbiol Biotechnol* **37**, 643-72 (2010).
117. Weisblum, B. Erythromycin resistance by ribosome modification. *Antimicrob Agents Chemother* **39**, 577-85 (1995).
118. Svetlov, M.S. et al. Structure of Erm-modified 70S ribosome reveals the mechanism of macrolide resistance. *Nat Chem Biol* **17**, 412-420 (2021).
119. Long, K.S., Poehlsgaard, J., Kehrenberg, C., Schwarz, S. & Vester, B. The Cfr rRNA methyltransferase confers resistance to Phenicols, Lincosamides, Oxazolidinones, Pleuromutilins, and Streptogramin A antibiotics. *Antimicrob Agents Chemother* **50**, 2500-5 (2006).
120. Wilson, D.N., Hauryliuk, V., Atkinson, G.C. & O'Neill, A.J. Target protection as a key antibiotic resistance mechanism. *Nat Rev Microbiol* **18**, 637-648 (2020).
121. Manavathu, E.K., Fernandez, C.L., Cooperman, B.S. & Taylor, D.E. Molecular studies on the mechanism of tetracycline resistance mediated by Tet(O). *Antimicrob Agents Chemother* **34**, 71-7 (1990).
122. Burdett, V. Purification and characterization of Tet(M), a protein that renders ribosomes resistant to tetracycline. *J Biol Chem* **266**, 2872-7 (1991).
123. Arenz, S., Nguyen, F., Beckmann, R. & Wilson, D.N. Cryo-EM structure of the tetracycline resistance protein TetM in complex with a translating ribosome at 3.9-A resolution. *Proc Natl Acad Sci U S A* **112**, 5401-6 (2015).
124. Connell, S.R., Tracz, D.M., Nierhaus, K.H. & Taylor, D.E. Ribosomal protection proteins and their mechanism of tetracycline resistance. *Antimicrob Agents Chemother* **47**, 3675-81 (2003).
125. Sharkey, L.K., Edwards, T.A. & O'Neill, A.J. ABC-F Proteins Mediate Antibiotic Resistance through Ribosomal Protection. *MBio* **7**, e01975 (2016).
126. Sharkey, L.K.R. & O'Neill, A.J. Antibiotic Resistance ABC-F Proteins: Bringing Target Protection into the Limelight. *ACS Infect Dis* **4**, 239-246 (2018).
127. Wilson, D.N., Hauryliuk, V., Atkinson, G.C. & O'Neill, A.J. Target protection as a key antibiotic resistance mechanism. *Nat Rev Microbiol* (2020).
128. Gao, Y.G. et al. The structure of the ribosome with elongation factor G trapped in the posttranslocational state. *Science* **326**, 694-9 (2009).
129. Tomlinson, J.H., Thompson, G.S., Kalverda, A.P., Zhuravleva, A. & O'Neill, A.J. A target-protection mechanism of antibiotic resistance at atomic resolution: insights into FusB-type fusidic acid resistance. *Sci Rep* **6**, 19524 (2016).
130. O’Neill, J. The Review on Antimicrobial Resistance. (2016).
131. Hede, K. Antibiotic resistance: An infectious arms race. *Nature* **509**, S2-3 (2014).
132. Cheng, Y., Grigorieff, N., Penczek, P.A. & Walz, T. A primer to single-particle cryo-electron microscopy. *Cell* **161**, 438-449 (2015).
133. Egelman, E.H. Three-dimensional reconstruction of helical polymers. *Arch Biochem Biophys* **581**, 54-8 (2015).

134. Orlova, E.V. & Saibil, H.R. Structural analysis of macromolecular assemblies by electron microscopy. *Chem Rev* **111**, 7710-48 (2011).
135. Passmore, L.A. & Russo, C.J. Specimen Preparation for High-Resolution Cryo-EM. *Methods Enzymol* **579**, 51-86 (2016).
136. Milne, J.L. et al. Cryo-electron microscopy--a primer for the non-microscopist. *FEBS J* **280**, 28-45 (2013).
137. Lyumkis, D. Challenges and opportunities in cryo-EM single-particle analysis. *J Biol Chem* **294**, 5181-5197 (2019).
138. Noble, A.J. et al. Routine single particle CryoEM sample and grid characterization by tomography. *Elife* **7**(2018).
139. Drulyte, I. et al. Approaches to altering particle distributions in cryo-electron microscopy sample preparation. *Acta Crystallogr D Struct Biol* **74**, 560-571 (2018).
140. Chen, J., Noble, A.J., Kang, J.Y. & Darst, S.A. Eliminating effects of particle adsorption to the air/water interface in single-particle cryo-electron microscopy: Bacterial RNA polymerase and CHAPSO. *J Struct Biol X* **1**(2019).
141. Feng, X. et al. A Fast and Effective Microfluidic Spraying-Plunging Method for High-Resolution Single-Particle Cryo-EM. *Structure* **25**, 663-670 e3 (2017).
142. Noble, A.J. et al. Reducing effects of particle adsorption to the air-water interface in cryo-EM. *Nat Methods* **15**, 793-795 (2018).
143. Klebl, D.P. et al. Need for Speed: Examining Protein Behavior during CryoEM Grid Preparation at Different Timescales. *Structure* **28**, 1238-1248 e4 (2020).
144. Thompson, R.F., Walker, M., Siebert, C.A., Muench, S.P. & Ranson, N.A. An introduction to sample preparation and imaging by cryo-electron microscopy for structural biology. *Methods* **100**, 3-15 (2016).
145. Sigworth, F.J. Principles of cryo-EM single-particle image processing. *Microscopy (Oxf)* **65**, 57-67 (2016).
146. Cheng, Y. Single-Particle Cryo-EM at Crystallographic Resolution. *Cell* **161**, 450-457 (2015).
147. McMullan, G., Clark, A.T., Turchetta, R. & Faruqi, A.R. Enhanced imaging in low dose electron microscopy using electron counting. *Ultramicroscopy* **109**, 1411-6 (2009).
148. McMullan, G., Faruqi, A.R. & Henderson, R. Direct Electron Detectors. *Methods Enzymol* **579**, 1-17 (2016).
149. Scheres, S.H. Beam-induced motion correction for sub-megadalton cryo-EM particles. *Elife* **3**, e03665 (2014).
150. Nogales, E. & Scheres, S.H. Cryo-EM: A Unique Tool for the Visualization of Macromolecular Complexity. *Mol Cell* **58**, 677-89 (2015).
151. Scheres, S.H. RELION: implementation of a Bayesian approach to cryo-EM structure determination. *J Struct Biol* **180**, 519-30 (2012).
152. Zheng, S.Q. et al. MotionCor2: anisotropic correction of beam-induced motion for improved cryo-electron microscopy. *Nat Methods* **14**, 331-332 (2017).
153. Scheres, S.H. Processing of Structurally Heterogeneous Cryo-EM Data in RELION. *Methods Enzymol* **579**, 125-57 (2016).
154. Rohou, A. & Grigorieff, N. CTFFIND4: Fast and accurate defocus estimation from electron micrographs. *J Struct Biol* **192**, 216-21 (2015).
155. Zhang, K. Gctf: Real-time CTF determination and correction. *J Struct Biol* **193**, 1-12 (2016).
156. Zivanov, J. et al. New tools for automated high-resolution cryo-EM structure determination in RELION-3. *Elife* **7**(2018).
157. Wagner, T. et al. SPHIRE-crYOLO is a fast and accurate fully automated particle picker for cryo-EM. *Commun Biol* **2**, 218 (2019).

158. Scheres, S.H. & Chen, S. Prevention of overfitting in cryo-EM structure determination. *Nat Methods* **9**, 853-4 (2012).
159. Cardone, G., Heymann, J.B. & Steven, A.C. One number does not fit all: mapping local variations in resolution in cryo-EM reconstructions. *J Struct Biol* **184**, 226-36 (2013).
160. Jakobi, A.J., Wilmanns, M. & Sachse, C. Model-based local density sharpening of cryo-EM maps. *Elife* **6**(2017).
161. Sanchez-Garcia, R. et al. DeepEMhancer: a deep learning solution for cryo-EM volume post-processing. *bioRxiv*, 2020.06.12.148296 (2020).
162. Nakane, T., Kimanius, D., Lindahl, E. & Scheres, S.H. Characterisation of molecular motions in cryo-EM single-particle data by multi-body refinement in RELION. *Elife* **7**(2018).
163. Waterhouse, A. et al. SWISS-MODEL: homology modelling of protein structures and complexes. *Nucleic Acids Res* **46**, W296-W303 (2018).
164. Adams, P.D. et al. PHENIX: a comprehensive Python-based system for macromolecular structure solution. *Acta Crystallogr D Biol Crystallogr* **66**, 213-21 (2010).
165. Murshudov, G.N. et al. REFMAC5 for the refinement of macromolecular crystal structures. *Acta Crystallogr D Biol Crystallogr* **67**, 355-67 (2011).
166. Williams, C.J. et al. MolProbity: More and better reference data for improved all-atom structure validation. *Protein Sci* **27**, 293-315 (2018).
167. Topf, M. et al. Protein structure fitting and refinement guided by cryo-EM density. *Structure* **16**, 295-307 (2008).
168. Khusainov, I. et al. Structure of the 70S ribosome from human pathogen Staphylococcus aureus. *Nucleic Acids Res* **44**, 10491-10504 (2016).
169. Mehta, P., Woo, P., Venkataraman, K. & Karzai, A.W. Ribosome purification approaches for studying interactions of regulatory proteins and RNAs with the ribosome. *Methods Mol Biol* **905**, 273-89 (2012).
170. Thompson, R.F., Iadanza, M.G., Hesketh, E.L., Rawson, S. & Ranson, N.A. Collection, pre-processing and on-the-fly analysis of data for high-resolution, single-particle cryo-electron microscopy. *Nat Protoc* (2018).
171. James, N.R., Brown, A., Gordiyenko, Y. & Ramakrishnan, V. Translational termination without a stop codon. *Science* **354**, 1437-1440 (2016).
172. Schwede, T., Kopp, J., Guex, N. & Peitsch, M.C. SWISS-MODEL: An automated protein homology-modeling server. *Nucleic Acids Res* **31**, 3381-5 (2003).
173. Pettersen, E.F. et al. UCSF Chimera--a visualization system for exploratory research and analysis. *J Comput Chem* **25**, 1605-12 (2004).
174. Emsley, P. & Cowtan, K. Coot: model-building tools for molecular graphics. *Acta Crystallogr D Biol Crystallogr* **60**, 2126-32 (2004).
175. Fischer, N. et al. Structure of the E. coli ribosome-EF-Tu complex at <3 A resolution by Cs-corrected cryo-EM. *Nature* **520**, 567-70 (2015).
176. Berman, H., Henrick, K. & Nakamura, H. Announcing the worldwide Protein Data Bank. *Nat Struct Biol* **10**, 980 (2003).
177. Schneider, C.A., Rasband, W.S. & Eliceiri, K.W. NIH Image to ImageJ: 25 years of image analysis. *Nat Methods* **9**, 671-5 (2012).
178. Goddard, T.D. et al. UCSF ChimeraX: Meeting modern challenges in visualization and analysis. *Protein Sci* **27**, 14-25 (2018).
179. Jubb, H.C. et al. Arpeggio: A Web Server for Calculating and Visualising Interatomic Interactions in Protein Structures. *J Mol Biol* **429**, 365-371 (2017).
180. Laskowski, R.A. & Swindells, M.B. LigPlot+: multiple ligand-protein interaction diagrams for drug discovery. *J Chem Inf Model* **51**, 2778-86 (2011).

181. Fairweather, N., Kennedy, S., Foster, T.J., Kehoe, M. & Dougan, G. Expression of a cloned Staphylococcus aureus alpha-hemolysin determinant in Bacillus subtilis and Staphylococcus aureus. *Infect Immun* **41**, 1112-7 (1983).
182. Horsburgh, M.J. et al. sigmaB modulates virulence determinant expression and stress resistance: characterization of a functional rsbU strain derived from Staphylococcus aureus 8325-4. *J Bacteriol* **184**, 5457-67 (2002).
183. Corrigan, R.M. & Foster, T.J. An improved tetracycline-inducible expression vector for Staphylococcus aureus. *Plasmid* **61**, 126-9 (2009).
184. Sambrook, J. & Russell, D.W. Preparation and Transformation of Competent E. coli Using Calcium Chloride. *CSH Protoc* **2006**(2006).
185. Schenk, S. & Laddaga, R.A. Improved method for electroporation of Staphylococcus aureus. *FEMS Microbiol Lett* **73**, 133-8 (1992).
186. Monk, I.R., Shah, I.M., Xu, M., Tan, M.W. & Foster, T.J. Transforming the untransformable: application of direct transformation to manipulate genetically Staphylococcus aureus and Staphylococcus epidermidis. *mBio* **3**(2012).
187. Crowe-McAuliffe, C. et al. Structural basis of ABCF-mediated resistance to pleuromutilin, lincosamide, and streptogramin A antibiotics in Gram-positive pathogens. *Nat Commun* **12**, 3577 (2021).
188. Halfon, Y. et al. Exit tunnel modulation as resistance mechanism of S. aureus erythromycin resistant mutant. *Sci Rep* **9**, 11460 (2019).
189. Shapovalov, M.V. & Dunbrack, R.L., Jr. A smoothed backbone-dependent rotamer library for proteins derived from adaptive kernel density estimates and regressions. *Structure* **19**, 844-58 (2011).
190. CLSI. Methods for Dilution Antimicrobial Susceptibility Tests for Bacteria that Grow Aerobically. *CLSI standard M07* (2018).
191. Dijkshoorn, L., Nemec, A. & Seifert, H. An increasing threat in hospitals: multidrug-resistant Acinetobacter baumannii. *Nat Rev Microbiol* **5**, 939-51 (2007).
192. Howard, A., O'Donoghue, M., Feeney, A. & Sleator, R.D. Acinetobacter baumannii: an emerging opportunistic pathogen. *Virulence* **3**, 243-50 (2012).
193. Montefour, K. et al. Acinetobacter baumannii: an emerging multidrug-resistant pathogen in critical care. *Crit Care Nurse* **28**, 15-25; quiz 26 (2008).
194. Peleg, A.Y., Seifert, H. & Paterson, D.L. Acinetobacter baumannii: emergence of a successful pathogen. *Clin Microbiol Rev* **21**, 538-82 (2008).
195. Centers for Disease, C. & Prevention. Acinetobacter baumannii infections among patients at military medical facilities treating injured U.S. service members, 2002-2004. *MMWR Morb Mortal Wkly Rep* **53**, 1063-6 (2004).
196. Turton, J.F. et al. Comparison of Acinetobacter baumannii isolates from the United Kingdom and the United States that were associated with repatriated casualties of the Iraq conflict. *J Clin Microbiol* **44**, 2630-4 (2006).
197. Sharma, D., Misba, L. & Khan, A.U. Antibiotics versus biofilm: an emerging battleground in microbial communities. *Antimicrob Resist Infect Control* **8**, 76 (2019).
198. Lorente, C., Del Castillo, Y. & Rello, J. Prevention of infection in the intensive care unit: current advances and opportunities for the future. *Curr Opin Crit Care* **8**, 461-4 (2002).
199. Choi, C.H. et al. Outer membrane protein 38 of Acinetobacter baumannii localizes to the mitochondria and induces apoptosis of epithelial cells. *Cell Microbiol* **7**, 1127-38 (2005).
200. Camarena, L., Bruno, V., Euskirchen, G., Poggio, S. & Snyder, M. Molecular mechanisms of ethanol-induced pathogenesis revealed by RNA-sequencing. *PLoS Pathog* **6**, e1000834 (2010).

201. Jacobs, A.C. et al. Inactivation of phospholipase D diminishes Acinetobacter baumannii pathogenesis. *Infect Immun* **78**, 1952-62 (2010).
202. Gaddy, J.A. & Actis, L.A. Regulation of Acinetobacter baumannii biofilm formation. *Future Microbiol* **4**, 273-8 (2009).
203. Fishbain, J. & Peleg, A.Y. Treatment of Acinetobacter infections. *Clin Infect Dis* **51**, 79-84 (2010).
204. Asif, M., Alvi, I.A. & Rehman, S.U. Insight into Acinetobacter baumannii: pathogenesis, global resistance, mechanisms of resistance, treatment options, and alternative modalities. *Infect Drug Resist* **11**, 1249-1260 (2018).
205. Baron, S., Hadjadj, L., Rolain, J.M. & Olaitan, A.O. Molecular mechanisms of polymyxin resistance: knowns and unknowns. *Int J Antimicrob Agents* **48**, 583-591 (2016).
206. Perez, F. et al. Global challenge of multidrug-resistant Acinetobacter baumannii. *Antimicrob Agents Chemother* **51**, 3471-84 (2007).
207. Poirel, L. & Nordmann, P. Carbapenem resistance in Acinetobacter baumannii: mechanisms and epidemiology. *Clin Microbiol Infect* **12**, 826-36 (2006).
208. Wright, H., Bonomo, R.A. & Paterson, D.L. New agents for the treatment of infections with Gram-negative bacteria: restoring the miracle or false dawn? *Clin Microbiol Infect* **23**, 704-712 (2017).
209. Zilberberg, M.D., Kollef, M.H. & Shorr, A.F. Secular trends in Acinetobacter baumannii resistance in respiratory and blood stream specimens in the United States, 2003 to 2012: A survey study. *J Hosp Med* **11**, 21-6 (2016).
210. Tsioutis, C. et al. Clinical epidemiology, treatment and prognostic factors of extensively drug-resistant Acinetobacter baumannii ventilator-associated pneumonia in critically ill patients. *Int J Antimicrob Agents* **48**, 492-497 (2016).
211. Falagas, M.E. & Bliziotis, I.A. Pandrug-resistant Gram-negative bacteria: the dawn of the post-antibiotic era? *Int J Antimicrob Agents* **29**, 630-6 (2007).
212. Fournier, P.E. et al. Comparative genomics of multidrug resistance in Acinetobacter baumannii. *PLoS Genet* **2**, e7 (2006).
213. Perez, F., Endimiani, A. & Bonomo, R.A. Why are we afraid of Acinetobacter baumannii? *Expert Rev Anti Infect Ther* **6**, 269-71 (2008).
214. Potron, A., Poirel, L. & Nordmann, P. Emerging broad-spectrum resistance in Pseudomonas aeruginosa and Acinetobacter baumannii: Mechanisms and epidemiology. *Int J Antimicrob Agents* **45**, 568-85 (2015).
215. Tahbaz, S.V., Azimi, L. & Lari, A.R. Characterization of aminoglycoside resistance mechanisms in Acinetobacter Baumannii isolates from burn wound colonization. *Ann Burns Fire Disasters* **32**, 115-121 (2019).
216. Shrestha, S. et al. Emergence of Aminoglycoside Resistance Due to armA methylase in Multi-drug Resistant Acinetobacter Baumannii Isolates in a University Hospital in Nepal. *J Nepal Health Res Counc* **14**, 72-76 (2016).
217. Chiang, M.H. et al. Confronting Tigecycline-Resistant Acinetobacter baumannii via Immunization Against Conserved Resistance Determinants. *Front Microbiol* **11**, 536 (2020).
218. Deng, M. et al. Molecular epidemiology and mechanisms of tigecycline resistance in clinical isolates of Acinetobacter baumannii from a Chinese university hospital. *Antimicrob Agents Chemother* **58**, 297-303 (2014).
219. Moffatt, J.H. et al. Colistin resistance in Acinetobacter baumannii is mediated by complete loss of lipopolysaccharide production. *Antimicrob Agents Chemother* **54**, 4971-7 (2010).
220. Boucher, H.W. et al. Bad bugs, no drugs: no ESKAPE! An update from the Infectious Diseases Society of America. *Clin Infect Dis* **48**, 1-12 (2009).

221. Tacconelli, E. et al. Discovery, research, and development of new antibiotics: the WHO priority list of antibiotic-resistant bacteria and tuberculosis. *Lancet Infect Dis* **18**, 318-327 (2018).
222. Ban, N., Nissen, P., Hansen, J., Moore, P.B. & Steitz, T.A. The complete atomic structure of the large ribosomal subunit at 2.4 A resolution. *Science* **289**, 905-20 (2000).
223. Schluenzen, F. et al. Structure of functionally activated small ribosomal subunit at 3.3 angstroms resolution. *Cell* **102**, 615-23 (2000).
224. Wimberly, B.T. et al. Structure of the 30S ribosomal subunit. *Nature* **407**, 327-39 (2000).
225. Yusupov, M.M. et al. Crystal structure of the ribosome at 5.5 A resolution. *Science* **292**, 883-96 (2001).
226. Schlunzen, F. et al. Structural basis for the interaction of antibiotics with the peptidyl transferase centre in eubacteria. *Nature* **413**, 814-21 (2001).
227. Brown, A. & Shao, S. Ribosomes and cryo-EM: a duet. *Curr Opin Struct Biol* **52**, 1-7 (2018).
228. Davis, J.H. et al. Modular Assembly of the Bacterial Large Ribosomal Subunit. *Cell* **167**, 1610-1622 e15 (2016).
229. Kaledhonkar, S. et al. Late steps in bacterial translation initiation visualized using time-resolved cryo-EM. *Nature* (2019).
230. Sohmen, D. et al. Structure of the Bacillus subtilis 70S ribosome reveals the basis for species-specific stalling. *Nat Commun* **6**, 6941 (2015).
231. Kohler, R., Mooney, R.A., Mills, D.J., Landick, R. & Cramer, P. Architecture of a transcribing-translating expressome. *Science* **356**, 194-197 (2017).
232. Noeske, J. et al. High-resolution structure of the Escherichia coli ribosome. *Nat Struct Mol Biol* **22**, 336-41 (2015).
233. Watson, Z.L. et al. Structure of the bacterial ribosome at 2 A resolution. *Elife* **9**(2020).
234. Golubev, A. et al. Cryo-EM structure of the ribosome functional complex of the human pathogen Staphylococcus aureus at 3.2 A resolution. *FEBS Lett* (2020).
235. Yang, K. et al. Structural insights into species-specific features of the ribosome from the human pathogen Mycobacterium tuberculosis. *Nucleic Acids Res* **45**, 10884-10894 (2017).
236. Halfon, Y. et al. Structure of Pseudomonas aeruginosa ribosomes from an aminoglycoside-resistant clinical isolate. *Proc Natl Acad Sci U S A* (2019).
237. Morgan, C.E. et al. Cryo-electron Microscopy Structure of the Acinetobacter baumannii 70S Ribosome and Implications for New Antibiotic Development. *mBio* **11**(2020).
238. Murphy, E.L. et al. Cryo-electron microscopy structure of the 70S ribosome from Enterococcus faecalis. *Sci Rep* **10**, 16301 (2020).
239. Eyal, Z. et al. Structural insights into species-specific features of the ribosome from the pathogen Staphylococcus aureus. *Proc Natl Acad Sci U S A* **112**, E5805-14 (2015).
240. Hentschel, J. et al. The Complete Structure of the Mycobacterium smegmatis 70S Ribosome. *Cell Rep* **20**, 149-160 (2017).
241. Byrgazov, K., Vesper, O. & Moll, I. Ribosome heterogeneity: another level of complexity in bacterial translation regulation. *Curr Opin Microbiol* **16**, 133-9 (2013).
242. Polikanov, Y.S., Melnikov, S.V., Soll, D. & Steitz, T.A. Structural insights into the role of rRNA modifications in protein synthesis and ribosome assembly. *Nat Struct Mol Biol* **22**, 342-344 (2015).

243. Maguire, B.A., Beniaminov, A.D., Ramu, H., Mankin, A.S. & Zimmermann, R.A. A protein component at the heart of an RNA machine: the importance of protein l27 for the function of the bacterial ribosome. *Mol Cell* **20**, 427-35 (2005).
244. Wall, E.A. et al. Specific N-terminal cleavage of ribosomal protein L27 in Staphylococcus aureus and related bacteria. *Mol Microbiol* **95**, 258-69 (2015).
245. Wilson, D.N. On the specificity of antibiotics targeting the large ribosomal subunit. *Ann N Y Acad Sci* **1241**, 1-16 (2011).
246. Berisio, R. et al. Structural insight into the role of the ribosomal tunnel in cellular regulation. *Nat Struct Biol* **10**, 366-70 (2003).
247. Dethlefsen, L., Huse, S., Sogin, M.L. & Relman, D.A. The pervasive effects of an antibiotic on the human gut microbiota, as revealed by deep 16S rRNA sequencing. *PLoS Biol* **6**, e280 (2008).
248. Rivera, M.C., Maguire, B. & Lake, J.A. Isolation of ribosomes and polysomes. *Cold Spring Harb Protoc* **2015**, 293-9 (2015).
249. Nierhaus, K.H. Mg2+, K+, and the ribosome. *J Bacteriol* **196**, 3817-9 (2014).
250. Cornish, P.V., Ermolenko, D.N., Noller, H.F. & Ha, T. Spontaneous intersubunit rotation in single ribosomes. *Mol Cell* **30**, 578-88 (2008).
251. Rozov, A. et al. Novel base-pairing interactions at the tRNA wobble position crucial for accurate reading of the genetic code. *Nat Commun* **7**, 10457 (2016).
252. Deuerling, E., Gamerdinger, M. & Kreft, S.G. Chaperone Interactions at the Ribosome. *Cold Spring Harb Perspect Biol* **11**(2019).
253. Liu, Q. & Fredrick, K. Intersubunit Bridges of the Bacterial Ribosome. *J Mol Biol* **428**, 2146-64 (2016).
254. Hujer, K.M. et al. Analysis of antibiotic resistance genes in multidrug-resistant Acinetobacter sp. isolates from military and civilian patients treated at the Walter Reed Army Medical Center. *Antimicrob Agents Chemother* **50**, 4114-23 (2006).
255. Valentine, S.C. et al. Phenotypic and molecular characterization of Acinetobacter baumannii clinical isolates from nosocomial outbreaks in Los Angeles County, California. *J Clin Microbiol* **46**, 2499-507 (2008).
256. Tsai, A. et al. The impact of aminoglycosides on the dynamics of translation elongation. *Cell Rep* **3**, 497-508 (2013).
257. Davies, J., Gorini, L. & Davis, B.D. Misreading of RNA codewords induced by aminoglycoside antibiotics. *Mol Pharmacol* **1**, 93-106 (1965).
258. Magnet, S. & Blanchard, J.S. Molecular insights into aminoglycoside action and resistance. *Chem Rev* **105**, 477-98 (2005).
259. Cocozaki, A.I. et al. Resistance mutations generate divergent antibiotic susceptibility profiles against translation inhibitors. *Proc Natl Acad Sci U S A* **113**, 8188-93 (2016).
260. Su, W. et al. Ribosome protection by antibiotic resistance ATP-binding cassette protein. *Proc Natl Acad Sci U S A* (2018).
261. Arenz, S. et al. Drug sensing by the ribosome induces translational arrest via active site perturbation. *Mol Cell* **56**, 446-52 (2014).
262. Arenz, S. et al. Molecular basis for erythromycin-dependent ribosome stalling during translation of the ErmBL leader peptide. *Nat Commun* **5**, 3501 (2014).
263. Li, W. et al. Structural basis for selective stalling of human ribosome nascent chain complexes by a drug-like molecule. *Nat Struct Mol Biol* **26**, 501-509 (2019).
264. Davidson, A.L., Dassa, E., Orelle, C. & Chen, J. Structure, function, and evolution of bacterial ATP-binding cassette systems. *Microbiol Mol Biol Rev* **72**, 317-64, table of contents (2008).
265. Kerr, I.D. Sequence analysis of twin ATP binding cassette proteins involved in translational control, antibiotic resistance, and ribonuclease L inhibition. *Biochem Biophys Res Commun* **315**, 166-73 (2004).

266. Ousalem, F., Singh, S., Chesneau, O., Hunt, J.F. & Boel, G. ABC-F proteins in mRNA translation and antibiotic resistance. *Res Microbiol* (2019).
267. Crowe-McAuliffe, C. et al. Structural basis for antibiotic resistance mediated by the Bacillus subtilis ABCF ATPase VmlR. *Proc Natl Acad Sci U S A* (2018).
268. Romero, Z.J. et al. Frequent template switching in postreplication gaps: suppression of deleterious consequences by the Escherichia coli Uup and RadD proteins. *Nucleic Acids Res* **48**, 212-230 (2020).
269. Andersen, C.B. et al. Structure of eEF3 and the mechanism of transfer RNA release from the E-site. *Nature* **443**, 663-8 (2006).
270. Boel, G. et al. The ABC-F protein EttA gates ribosome entry into the translation elongation cycle. *Nat Struct Mol Biol* **21**, 143-51 (2014).
271. Marton, M.J., Vazquez de Aldana, C.R., Qiu, H., Chakraburtty, K. & Hinnebusch, A.G. Evidence that GCN1 and GCN20, translational regulators of GCN4, function on elongating ribosomes in activation of eIF2alpha kinase GCN2. *Mol Cell Biol* **17**, 4474-89 (1997).
272. Murina, V. et al. ABCF ATPases Involved in Protein Synthesis, Ribosome Assembly and Antibiotic Resistance: Structural and Functional Diversification across the Tree of Life. *J Mol Biol* (2018).
273. Ero, R., Kumar, V., Su, W. & Gao, Y.G. Ribosome protection by ABC-F proteins - molecular mechanism and potential drug design. *Protein Sci* (2019).
274. Fostier, C.R. et al. ABC-F translation factors: from antibiotic resistance to immune response. *FEBS Lett* (2020).
275. Wilson, D.N. The ABC of Ribosome-Related Antibiotic Resistance. *MBio* **7**(2016).
276. Singh, K.V., Weinstock, G.M. & Murray, B.E. An Enterococcus faecalis ABC homologue (Lsa) is required for the resistance of this species to clindamycin and quinupristin-dalfopristin. *Antimicrob Agents Chemother* **46**, 1845-50 (2002).
277. Hot, C., Berthet, N. & Chesneau, O. Characterization of sal(A), a novel gene responsible for lincosamide and streptogramin A resistance in Staphylococcus sciuri. *Antimicrob Agents Chemother* **58**, 3335-41 (2014).
278. Allignet, J., Loncle, V. & el Sohl, N. Sequence of a staphylococcal plasmid gene, vga, encoding a putative ATP-binding protein involved in resistance to virginiamycin A-like antibiotics. *Gene* **117**, 45-51 (1992).
279. Ross, J.I. et al. Inducible erythromycin resistance in staphylococci is encoded by a member of the ATP-binding transport super-gene family. *Mol Microbiol* **4**, 1207-14 (1990).
280. Wang, Y. et al. A novel gene, optrA, that confers transferable resistance to oxazolidinones and phenicols and its presence in Enterococcus faecalis and Enterococcus faecium of human and animal origin. *J Antimicrob Chemother* **70**, 2182-90 (2015).
281. Antonelli, A. et al. Characterization of poxtA, a novel phenicol-oxazolidinone-tetracycline resistance gene from an MRSA of clinical origin. *J Antimicrob Chemother* **73**, 1763-1769 (2018).
282. Schoner, B. et al. Sequence similarity between macrolide-resistance determinants and ATP-binding transport proteins. *Gene* **115**, 93-6 (1992).
283. Schroeder, M.R. & Stephens, D.S. Macrolide Resistance in Streptococcus pneumoniae. *Front Cell Infect Microbiol* **6**, 98 (2016).
284. Kadlec, K. et al. Molecular basis of macrolide, triamilide, and lincosamide resistance in Pasteurella multocida from bovine respiratory disease. *Antimicrob Agents Chemother* **55**, 2475-7 (2011).
285. Novotna, G. & Janata, J. A new evolutionary variant of the streptogramin A resistance protein, Vga(A)LC, from Staphylococcus haemolyticus with shifted

substrate specificity towards lincosamides. *Antimicrob Agents Chemother* **50**, 4070-6 (2006).

286. Chen, B. et al. EttA regulates translation by binding the ribosomal E site and restricting ribosome-tRNA dynamics. *Nat Struct Mol Biol* **21**, 152-9 (2014).
287. Lenart, J., Vimberg, V., Vesela, L., Janata, J. & Balikova Novotna, G. Detailed mutational analysis of Vga(A) interdomain linker: implication for antibiotic resistance specificity and mechanism. *Antimicrob Agents Chemother* **59**, 1360-4 (2015).
288. Murina, V., Kasari, M., Hauryliuk, V. & Atkinson, G.C. Antibiotic resistance ABCF proteins reset the peptidyl transferase centre of the ribosome to counter translational arrest. *Nucleic Acids Res* (2018).
289. Jacquet, E. et al. ATP hydrolysis and pristinamycin IIA inhibition of the Staphylococcus aureus Vga(A), a dual ABC protein involved in streptogramin A resistance. *J Biol Chem* **283**, 25332-25339 (2008).
290. Smith, P.C. et al. ATP binding to the motor domain from an ABC transporter drives formation of a nucleotide sandwich dimer. *Mol Cell* **10**, 139-49 (2002).
291. Dorrian, J.M., Briggs, D.A., Ridley, M.L., Layfield, R. & Kerr, I.D. Induction of a stress response in Lactococcus lactis is associated with a resistance to ribosomally active antibiotics. *FEBS J* **278**, 4015-24 (2011).
292. Vazquez-Laslop, N., Ramu, H., Klepacki, D., Kannan, K. & Mankin, A.S. The key function of a conserved and modified rRNA residue in the ribosomal response to the nascent peptide. *EMBO J* **29**, 3108-17 (2010).
293. Orelle, C. et al. Tools for characterizing bacterial protein synthesis inhibitors. *Antimicrob Agents Chemother* **57**, 5994-6004 (2013).
294. Wendlandt, S., Kadlec, K., Fessler, A.T. & Schwarz, S. Identification of ABC transporter genes conferring combined pleuromutilin-lincosamide-streptogramin A resistance in bovine methicillin-resistant Staphylococcus aureus and coagulase-negative staphylococci. *Vet Microbiol* **177**, 353-8 (2015).
295. Lee, Y.R. & Jacobs, K.L. Leave it to Lefamulin: A Pleuromutilin Treatment Option in Community-Acquired Bacterial Pneumonia. *Drugs* **79**, 1867-1876 (2019).
296. Deng, F. et al. Detection and Genetic Environment of Pleuromutilin-Lincosamide-Streptogramin A Resistance Genes in Staphylococci Isolated from Pets. *Front Microbiol* **8**, 234 (2017).
297. Madeira, F. et al. The EMBL-EBI search and sequence analysis tools APIs in 2019. *Nucleic Acids Res* **47**, W636-W641 (2019).
298. Burgos Zepeda, M.Y., Alessandri, K., Murat, D., El Amri, C. & Dassa, E. C-terminal domain of the Uup ATP-binding cassette ATPase is an essential folding domain that binds to DNA. *Biochim Biophys Acta* **1804**, 755-61 (2010).
299. Schlunzen, F., Pyetan, E., Fucini, P., Yonath, A. & Harms, J.M. Inhibition of peptide bond formation by pleuromutilins: the structure of the 50S ribosomal subunit from Deinococcus radiodurans in complex with tiamulin. *Mol Microbiol* **54**, 1287-94 (2004).
300. Bondi, A. Van Der Waals Volumes + Radii. *J Phys Chem* **68**, 441 (1964).
301. Nurenberg-Goloub, E., Heinemann, H., Gerovac, M. & Tampe, R. Ribosome recycling is coordinated by processive events in two asymmetric ATP sites of ABCE1. *Life Sci Alliance* **1**(2018).
302. Shaw, K.J. et al. In vitro activity of TR-700, the antibacterial moiety of the prodrug TR-701, against linezolid-resistant strains. *Antimicrob Agents Chemother* **52**, 4442-7 (2008).
303. Zhong, X. et al. A novel inhibitor of the new antibiotic resistance protein OptrA. *Chem Biol Drug Des* **92**, 1458-1467 (2018).
304. Interagency Coordination Group on Antimicrobial Resistance. AMR framework for action supported by the IACG. (2017).

Appendix

Below are the DNA sequences of the Sal genes analysed throughout this study. Mutations of wild type gene are highlighted in bold.

Sal(A) EQ$_2$ mutant (i.e. E156Q E456Q)

ATGCTATTTTTATTTGAAGAAAAAGCATTAGAAGTTGAACATAAAGTATTAATACCCGAGTTGACTTTTTCAATAGAGGACCAT
GAACATTTAGCAATCGTTGGTGTTAATGGTGTTGGAAAATCAACATTATTAAAAGTCATTCATCAAGATCAATCAGTTGATTCA
GCGATGATGGAACAAGATTTAACACCTTATTATGATTGGACTGTTATGGATTATATAATTGAATCATATCCTGAAATCGCAAAG
ATTAGATTGCAACTTAATCATACAGATATGATTAATAAATATATTGAATTAGATGGATACATTATAGAAGGTGAAATCGTAACA
GAAGCAAAAAAGCTCGGAATAAAAGAGGAACAACTAGAACAGAAAATTTCTACTTTAAGTGGTGGAGAACAAACAAAAGTATCA
TTTTTAAAAGTGAAAATGTCTAAAGCATCATTACTATTAATCGAT**CAA**CCAACAAACCACATGGATTTAGAAATGAAGGAATGG
TTGACGAAAGCTTTTAAACAAGAACAACGTGCTATATTATTTGTATCTCATGACCGAACATTTTTAAATGAAACGCCAGATGCT
ATATTAGAATTGAGTCTTGATGGGGCTAAGAAGTATATCGGTAAATACGATAAATACAAACAACAAAAAGATATAGAGCATGAA
ACATTAAAGCTACAGTATGAAAAACAACAAAAAGAACAAGCGGCCATTGAAGAAACGATTAAAAAATATAAAGCATGGTATCAA
AAAGCAGAACAAAGTGCTTCTGTGAGAAGCCCATATCAACAAAAACAATTAAGTAAGTTAGCGAAACGGTTTAAATCAAAAGAA
CAACAATTAAATCGTAAACTTGATCAAGAGCATATCCCAAATCCACATAAAAAAGAGAAAACTTTCTCAATACAACATCATAAT
TTTAAATCACATTATTTAGTTCAATTTAATCATGTTTCGTTTGCTTATGATAACCGGAAAATATTCGATGATGTATCATTCTAT
ATTAAGCGAAATCAAAATGTTATTGTTGAAGGCAGAAATGGTACAGGTAAATCAACTTTAATCAAATTGATACTCGGTGAACTC
GAGCCAACTAAAGGTGATATAACTGTTCATCCAGAATTAGAAATTGGATATTTCTCTCAAGATTTTGAGAATTTAAATATGCAT
CATACTGTCTTAGATGAAATATTAGAAATTCCTGAAATGAAAGAAGCAGATGCAAGAACCATATTAGCAAGCTTTTATTTTGAT
AAAGATAGGATAAATGATGTTGTTGAAACACTATCGATGGGTGAAAAATGTAGGTTACAATTTGTAAAATTATATTTTTCAAAT
CCTCATATTATGATATTAGAT**CAG**CCAACAAACTATTTCGATATTGGCATGCAAGAAAATATCATTCAATTAATACAATCATTT
CAAGGTTCGGTCCTTATTGTATCTCATGATAATTATTTTAAATCACAAATTAAAGATCAGACTTGGACTATAAAAAATCATCAA
ATGACGCATGAAAATGTTCAAGTCAAAGATCCTATTAATACAGAATCTATGAAACATCATTTAAAAGAATTAGAACAATATACA
GATGAAAGAAATCGTGAAACAGAGTTCGGCGGTGACTACAAAGACCATGACGGTGATTATAAAGATCATGACATCGATTACAAG
GATGACGATGACAAATAG

Sal(B) EQ$_2$ mutant (i.e. E156Q E456Q)

ATGCTATTTTTATTTGAAGAAAAACCATTAGAAATTGAGAATAAACAGCTTATAAAACGTTTGTCATTTCATATCGAAGACCAT
GAGCATTTAGCCCTTATCGGTGTTAATGGTATTGGTAAATCTACGCTATTACATCATATTCATAAAAATGAATTGATTGATACA
GCTATGATGGAACAAGATTTAAGTAAACATGATGATATTGATGTTATGGATTATGTCATGTCTGCATATCCAAAGTTAGTTGAA
TTGAGAAAAGATTTATCTGACATTGATTCTTTAAATAGTTATATAGAATTAGACGGATATAACGTTGAAAATAACATTATTATT
GAAGGAAATAAATTAGGATTATCATCAACACATTTTGAGCAAAAGATAGGCACTTTAAGTGGTGGTGAGCAAACTAAAGTCTCA
TTTTTAAAAGTTATTTTATCAGATGCACCATTATTATTAATAGAC**CAA**CCAACTAACCATATGGATAAAGAGATGAAAGTGTGG
TTAATAAAAGCTTTTAAATCAGAACAAAGAGCTATTCTATTCGTATCGCATGATAGAGAGTTTTTAAATGAAACACCAGATGCT
ATTTTAGAACTCACAAAAGATGGTGCAACTCGATATTCAGGTCATTATGATGATTATAAAAATCAAAAAGATATTGAAATTGAA
ACAGAAAAATTAAAATATGAAAAAGAACAGAAAGAACAAAAAGCAATAGAAGAAAGTATTAAGAAATACAAAGAATGGTATCAA
AGGGCTGCTCAGAAAGCTTCTGTTCGTAGTCCATATGCTCAAAAACAATTAAGTAAATTAGCTAAAAGATTTAAATCAAAAGAA
CATCAGTTAAATCGTAAATTAGAAGAATCAAAATCTGATAATCCGTTAGAAGAAAATAAATCCTTTTCTATAGAAAATAATGAA
TTTAAATCACATTATTTAGTAAGATTCGAAAATGTTTCATTTTCATATAAGAGTCGTGAAATTTTTAAAGACACTTATTTTGAA
ATAAAGAGAAATCAAACTGTAATTATAGAAGGTAAAAATGGGTCCGGTAAATCTACATTGATACAATTAATTTTAGGTAACTTA
TTACCAATGAGTGGAGCTGTCAAAAAGCACCCAGACTTAGACATAGGATACTTCTCGCAAGATTTTCAAAATTTAAACCCAAAC

AACTCGGTATTAGAAGAAGTTATGGATATTGAGAATATGATGATAACAGACGCGAGGACTATTTTAGCGAGTTTTTATTTTGAT
AAGAGCAGGATGAATGATAAAGTTCGTCAGTTATCAATGGGAGAAAAGTGCAGGTTACAATTTGTAAAATTATATTTTTCTAAC
CCACACATCTTAATTTTAGAT**CAA**CCAACTAATTATTTTGATATTAGTATGCAAGAGAAAATCATACAATTAATCCAAAGTTTT
AATGGTGCAGTAATTATTGTGTCGCATGATGAAATTTTTAAAGATGAAATAAGAGACCAAGTTTGGAAGATTGAAAACTGTAAG
CTCATTCATGAAAATGTATCTATTAATACACCTATTGATGCTGAATCGATGAAGGATGAGTTAAAAATATTAGAGCAATATACA
GATGAAAGAAATAAAGAAACAGACTTCGGCGGTGACTACAAAGACCATGACGGTGATTATAAAGATCATGACATCGATTACAAG
GATGACGATGACAAATAG

Sal(C) EQ$_2$ mutant (i.e. E156Q E456Q)

ATGCTATTTTTATTTGAAAAAAAGTCTTTAGAGATTGACAATAAACTGCTCATACCTTCACTAACATTTATTATTGAAGAAAAT
GAACATTTGGCAATAGTCGGCATAAATGGTATCGGAAAATCTACACTTTTAAATAAAATCCATCATAAAGAAAATATTGAAACA
GCAATGATGGAACAAGATTTAACTAAATATGGAACTTTAAATGTCATGGAGTATATTATGTTAACTTATCCACAATTATCATCG
TTAAGAGAAAATCTAAGTGATTTGGATAATATAAATAGATATATTGAATTAGACGGTTACGAAATTGAGCAAAACATTATAATT
GAAGGAAAAAAGTTAGGATTAACAGAAAGGCACTTTGATCAATTAATTTCTACTTTAAGTGGTGGTGAGCAAACAAAAGTTTCG
TTTTTGAAAGTTAAATTAGATAAAGCACGATTATTATTAATTGAT**CAA**CCAACTAACCATATGGATGAAGAAATGAAAGTATGG
TTAACTAATGCATTTAAACAAGAAAAACGTGCAATATTATTTGTTTCTCACGATAAGACTTTTTTAAATGAAACACCAGACGCA
ATTTTGGAACTGAGTAGTAGTGGTGCAACAAAATACTCAGGTCAGTATGACAATTACAAGCAACAAAAAGATTTAGAATATAAA
ACGATTAAGCTACAATACGAAAAACAAGAAAAAGAGCAACGAGCAATTGAAGAAACAATTAAAAAATATAAAGAATGGTATCAA
AAAGCTTCACAAAAAGCTTCAGTAAGAAATCCTTATCAACAAAAACAACTTAGCAAGCTTGCGAAAAAGTTTAAATCGAAAGAA
TATCAAATGAATAAAAAACTTGAACAAACCAATTTATCAGATCCTGAAGAGGAAGGAAAAACATTTTCAATGCAACATCACGCC
TTCAAATCTCATTATTTAGTTAAATTTAAAAATGTGACATTTTCATATAATGAAAAGCCTATTTTTAATGATGTCTCTTTTCAT
ATTAAGCGAAATCAAAATGTTATCATTGAAGGTCAAAATGGCTCAGGTAAATCTACTTTGATCAAGTTGATACTAGGTCAACTG
ACACCTGATGAGGGAGAAGTAATCGTACATCCTGAATTAGAAATAGGTTATTTTTCACAAGATTTTAATAACTTAAATATGAAA
AATACTGTGTTAGAAGAAATAATGTCTATTCAAGAAATGAAAGAAGCGGAAGCAAGAACAATTTTAGCGAATTATTATTTTAAT
GAAAATAGAATTAATGATGTTGTTGCCAATTTATCTATGGGTGAAAAATGTAGAATACAGTTTGTTAAATTGTATTTTTCAAAT
CCACATATACTCATATTAGAT**CAG**CCAACTAACTATTTTGATATTGAAATGCAAGAAAAAATCATACAATTAATTCAATCTTTT
CAAGGATCAACACTTATCATTTCACATGATAAATATTTTAAAGAAAAGCTTAAAGATCAAATTTGGACAATAAAGAATCTAGAT
TTGGTACATGAAAATCTTAAAATTGAGAATCCATTAAATGCTGATTCTATTAAAAATCAATTAAATGAATTAGAGCAATATACC
GACGAAAGAAATAGAGAAACAGAGTTCGGCGGTGACTACAAAGACCATGACGGTGATTATAAAGATCATGACATCGATTACAAG
GATGACGATGACAAATAG

Sal(D) EQ$_2$ mutant (i.e. E157Q E458Q)

ATGTCTTTTTATTTTACAGAAAAGCCATTTGAAAGGTTCGGCAAGACATTAATAGAAGAGGTTAATTTAAGTGTTGAACCAGGT
GAACATATAGCAATTGTTGGTGATAACGGGGTAGGTAAATCAACATTACTCAATGCAATTTACAATAAATATAATGATTCAACG
TATTTGATGGATCAAGAATTATCGAAGTATAAAAATGAAACGGCAATAAATTATATTATGTCGTGGTATCCAGAATTATTAGAT
ATTAAACTTGCTATGCAAACTGATTATGAAAAAATTGGTGACTATATAGAACTTAATGGATATGAAATAGAAGAACAAATCATT
TTACAAGCAAAGCAATTAAATTTAGAAGAGTCAGATTTAGATAAACAAATGGGGCAGTTAAGCGGCGGACAACAAACCAAAGTA
GCATTAGTTCGAGCAATGATTTCAGAAAAAAATTTAATCTTGTTGGAT**CAA**CCAACAAATCACTTAGATAAACAAATGATTCAT
ATTGTCGTGGATTATATAAAGCAAGCAAAGCAAAGTATATTATACGTGTCACATCATAGAGGATTTATCGACGAAACTGCAACG
CACATTATTGAAATTACACCACAAGCTACAAGAAAATTTACTGGTAATTATAGTCAATATAAATCCATTATAGATGTTGAAAGA
GAAACTCAAAAAAAGGTATACGAGAAAAAGCAAAAAGAAATAAAAGCTTTGGAAGCAACCGTAGATAGAGTTAAAAATTGGCAT
AAAACTGCGAATCAATCTGCAAGTGTTCGTAATCCGTTAGAGCAAAAGCGTTTGAGTAAATTAGCTCAAAAGGCAAAGGTTAAA

GAATCACAAATAAATCAAAAACTTGAAAAGATTAAAGTCCAACAGCCTAAGTCGGATGATCGTCACTTCCATTTTGAGAATCAA
GATGCGCTAAATAAAAAATATTTAATGCAATTATATGATTTTAGCATCACTATTGATGGTAAGAATATTTATCAAAATGCAAAT
TTCGAAATTAAAGATAATGAAAACATTATACTTACTGGCCCGAATGGTAGTGGCAAATCATTATTAATCTCAATTATCAAGCAG
TCAATAATACCAGATGAGGGTGATATTTATATAACGCCTTCTCTAAAAATAGCTTATTTTGACCAAAAAAATGACAATTTAAAT
TATGACAGCACAGCATTAACAATGTTATTAAACATGGAGGGTATGGAACGTAGTCAAGCACAAACGATATTAGCGTCATTTGGA
TTTGATAACCAAAAAATAAACCTTCCAATTTCTCAATTATCTATGGGAGAGAAAAGTAGATTACAGTTTGTATTATTATATTTC
TCAAATCCACATTTATTAATTCTCGAC**CAA**CCAACCAATTACTTCGATATTGCTACGCAAGATTTAATATTACAGATGCTAAAG
CAATTTGCAGGACAAGTAATGATTGTGACGCATGATGAATACTTGAAATCTCAAATTACAGCGACACATTGGACAATTAAAGAT
AAAAAGTTAATGAATTTAACATTATCAGAGAAGCATTCACCCAATATGGTGGATGATACATTAAAATTATTAGATGATTATAAG
TCGATAGATGAATTCGGACATTTTGAAACAGACAACGGCGGTGACTACAAAGACCATGACGGTGATTATAAAGATCATGACATC
GATTACAAGGATGACGATGACAAATAG

Sal(E) EQ$_2$ mutant (i.e. E157Q E458Q)

ATGTCTTTTTATTTTGCCCAAAAACCTTTTGAAATGTTTGGAAAAACACTGATTCAGTCAGTGGATTTACAATTTGAAAAGGGT
GAACATATTGCTGTGATTGGTAATAATGGCGTTGGGAAAACGACTTTATTAAAAGCATTAAATAATAAGTATAAAGAAGATACT
TATTTGATGGACCAAAACATGACTACCTTTGGAAACATGACGGGGATAGACTATGTAATAAGCTTAAACACAGAATTGTTTCAT
TTAAAACAAGCGTTAATGGATAACTATGAAAAAGTTTCAGATTATATCGCTTTAAATGGCTATGAATTTGAACAAACCATTATA
ACTAAAGCGAAGCAAATGGCTCTAACGGAAGCAGATCTTGACAAACCAATTAAAGTATTAAGCGGCGGCCAACAAACTAGGCTT
GCTTTATTGAGAGCATTTATTTCAAACAAACCATTGATATTGCTGGAC**CAA**CCAACCAATCATTTAGACCAAGAAATGATAGAC
CAATTGATTAACCATATACAACAATCAAAACGCACAATCATATATGTGTCGCATCATAGAGGATTTATAGATCAGACCGCGAGT
CATGTTATAGAAATAACACCCGAAAGTACAAGAAAATTTAATGGCAATTATAAGCAATACAAAGAGATAAAAGATTTAGAAAGT
CAAACAGAACAACGTATATATAATAAACAACAAAAAGAAATACAAGACCTCGAACGTACGATCAAACGCGTACAAACATGGCAT
CATTCTGCTCAGCAAAAAGCAAGTGTACGTAATCCGATTGAACAGAAAAAGTTGAGCAAATTAGCGCAAAGGGCAAAGGTGAAG
GAAAAACAATTAAACCAAAAATTACAAGAAAAACATATTCAAGAACCGAGTAAAGAAACAAAGTCATATTACTTTAGTCATCAG
ACTAGCCTTCCTAAACGTTTCTTAATTCGTTTTGAAGATGTTAGCGTTAATATTGATGGACAAGATATATATAAACACGCTCAT
TTTGAAATGAAACAAAATGAAAATATATTACTTACTGGTCCAAATGGAAGTGGTAAATCGCTTTTCATCGCTTTGATTAGACAG
CATTTATCACCAGACGAAGGTATTATAGAGATTACGCCATCGTTAAAGATAGGTTACTTTGATCAGACAAATAACAATCTAAAT
GAAGCAGAATCTCCATTATCAATGTTGTTAGTAAGAACTAACATAACGCGTAGCCAAGCGCAGACATTACTTGCTTCATTTAAT
TTTGATAAGGATCAAATCAAAAAACCAATTCGCTATTTGTCTATGGGGGAAAAAAGTCGTTTACAATTTGTATTATTATATTTT
TCAGGTGCTAATTTATTAGTATTGGAT**CAG**CCTACGAACTATTTTGATATTGTAACTCAAGATTTAATTTTAAGTATGATTCAA
AGTTTTACCGGTCAAGTATTGATTGTTACACATGATTCATATTTACAATCTCAATTTAAAGCTGTACATTGGGAAATAAAAAAT
CAACAACTTTATAATGTATCCTTAACTCATACGCGTGAATCAAACTTAGATGAAACCCTTAAGTTACTAGGTGAATATAAATTT
ATAGATGAAAATGGTCATTTTGAAACAGACAACTAG

Sal from *S. xylosus*

ATGTCTTTTTATTATGAACAAAAACCATTTGAACAGTATGGACGAATACTGATTGACAAAGTGCTAATTGATATAGAAGAAGGA
GAGCATGTTGCATTTTTAGGAGATAATGGTGTTGGAAAATCAACACTTTTATATGCACTTAAGAATGCTTATAAAGAAAGTGCA
TATCTAATGGAACAAGATATGACTGATTATTACGAAATGACAGCAATGGATTTTCTCCTGTTTTTAAAACCACAATTAGCTCAA
TTAAAAAAAGAGATGCTAAATAATTATGAAAAAATAAGCGACTACGTAGCGTTGGAAGGCTATGAATTTGAACAAGAAATCATT
ACGCAAGCGAAATTATTTGATTTAACGGAAATTGACTTAGATAAAAAGATTAAGTTTCTTAGTGGAGGACAGCAAACACGTGTA
GCGATATTAAGAGCTTTCTTATCGAAAAAATCGTTAATATTACTTGATGAACCTACTAATCATCTTGATATGACAATGCTAGAT
AATTTAATAATTAATATTAATAAATCTAAACAGACTATTGTTTTTGTGTCACATCATAGAGGATTCATCAATCAAACGGCATCA
CACATTTATCAAATAACACGTAATGGAACGAGAAAATTCCAAGGGGATTATGACCATTATAAACATGTAGTAGATTTGGCCCAT
CAATCACAAGTCAATGCTTATGAAAAACAACAAAAAGAAGTCAAAGCACTTGAAGTAACTATTAAACGTGTGAACGAATGGCAT

TCAGCCTCGCAAAGAACGACTAGTGTGCGAGACCCGATACAACAAAAAAGGTTAAGCAAATTAGCACAAAAAGCTAAAGTTAAG
GAATCACAACTAAAACAAAAGATAAATGAAAAGCAAATTGAAGCACCCGAAAATGATAATAGAGAATTTCATTTTAATGAACAA
ACACATTTCCGAAAACGTAGCTTGATTAGATTTGAAAATGTTAGTATAACTATAAATCAACAAGAAATTTATAGAAATGCTAAC
TTTGAAATGAAAAATAAAGAAAATATACTTTTAACAGGCCCAAATGGTAGTGGGAAATCATTATTTATCGCGATGATAAAACAA
AGCATAAAACCAAATAAAGGTGATATATATATTACGCCATCTCTTAATATTGCTTCTTTTGACCAACAAAGTAGCAATTTAAAA
TATAATAGCAGTCCATTAGACATGGTGATGGCATTAGAAAGTGTGACTCGTAGTGAAGCACAAACAATCTTAGCTACTTTTGAT
TTTAATAATGAAAAAATTAATCAGCATATCGCATTTTTATCCATGGGTGAGAAAAGTAGATTGCAGTTTGTATTATTATATTTC
TCTAATCCACATCTTCTTATTTTAGATGAACCAACCAATTATTTTGATATCGCTACACAAGATTTAATATTAAAAATGATTGAT
AGTTTTCAAGGTCAAGTGCTTATCGTTACACATGATCATTATTTACAATCAAGAATCAACGCTACACACTGGCATATTAATGAT
AAAAAATTGCAAAATATGACTTTGAATAGTAAACAAGCAGCAGACATAAAAAATACTATGAAATTATTAGAGGAATTTAAAGAT
ATTGATGAAAATGGTCATTTTGAAACAGACAACTAG

Sal from *S. equorum*

ATGTCTTTTTATTATGTTCAAAAACCATTTGAAAAATATGGTAAAACGTTGATAAATCACGTGAATATAAGTGTTGAAATAGGA
GAACACATAGCGCTCGTGGGTGATAATGGTGTTGGTAAAACAACCTTACTGAATGAACTATACTTAAAGTATAGAGATAATGCA
TATCTTATGAAGCAAGATATGACGGATTATTATAATGAAACTGGAATGGAATTTGTTTTATCTTTATTTCCGGAAATATTAAAA
TTAAAAAAGGAAATAACTTATAATTATGAAAAAATAGCTGATTATATAGCATATAATGGTTATGAAGTAGAACAAAAAATTATT
ACACAAGCGAATTTATTTAATTTAACCGAAACTGATTTAGACAAACAAATGGGTCTTTTAAGTGGAGGCCAACAAACACGCGTC
GCATTATTACGTTCGATTATTTCAGAGAAAGATTTGATTTTATTAGATGAACCAACTAATCATCTTGATCAAACTATGCTTAAT
GATTTGATAACTCACATAAATAAATCAAAATGTACAATAATCTATGTATCTCATCACCGTGGCTTTATCAATGCAACTGCTAGT
CATATCATAGAGATAAATCGAACACAGACAAGGAAATTTACGGGTAATTATAACCAGTATAAAGAAATTATAGATTTAGAGTTT
CAAACACAAGTGAATGCTTATGAAAAACAGCAGAAAGAAGTTAAGAAACTTGAAGACACCATTAAAAGAGTTAAAGAATGGCAT
GCTGCTTCTAAGCAAACAACGAGTGTTCGCGATCCCTCTATGCAAAAACGATTGAGTAAATTAGCACAAAAATCAAAAGTAAAA
GAATCACAATTAAATCAAAAATTAAACGAAAAAAATATCGAAGAACCCGAAAAAGATAATAGAAAGTTTCGTTTCGAACATCAT
GAAAAAAAGCGTAAACGTTATTTATTGAGGTTAGAAGATTTCAGTATTTCAATAAATGATCTTTGTATTTATAATCAAGCGAAT
TTCGAAATTAAGAATAATGAAAACATTTTACTTACTGGACCTAATGGCAGTGGAAAATCACTATTAATCAACTTGATTAGACAA
AAAATAAAACCTGATCAAGGCTTTATCCATATTACACCTTCACTTAAAATAGGTTATTTCGATCAACAAAATAATAATTTAAAG
TATCGTGAGACACCTTTAAATACTTTGTTAGCTTTAGAAGGTATGACACGTAGCCAGGCCCAAACGATTTTAGCTGCATTTGGT
TTCGACCAAGATAAAATTATTGAACCCGTTGCTTATTTGTCAATGGGAGAGAAAAGTAGGTTGCAGTTTGTATTATTATTTTTC
TCAAATCCTAATTTATTGATATTAGACGAACCAACAAACTATTTTGATATCACAACACAAGACTTGATTATGGACATGATTCAT
AGTTTTAGTGGTCAAGTGCTCATTGTCACACATGACCAGTACTTACAATCACGATTCACAGCGACGCATTGGGAAGTATCCAAT
AAGCAACTTCATAATTTGACGCTCAATCAATATCGTAAGACAAATACCGTTGATACTTTGAAATTATTAGATGATTACAAAACA
ATTGATGAAAGTGGACATTTTGAAACAGAGAACTAG

Sal from *S. saprophyticus*

ATGTCTTTTTATTTTTCAGAAAAACCATTTGAACAGTTTGGTAAAATATTGATAGAAGACGTAAATATTGATATTGAACTAGGT
AAGCATGTTGCAATGATTGGTGATAATGGTGTCGGCAAGTCAACATTGTTAAATGCTTTAAATTTAAAATATGAAACGCAATCA
TATTTAATGAAGCAAGACTTGACGCAAGTATTTGATTTAACCGCGATGACCTTTATCATTTCAATATTTCCTGAGGTTGCAACT
TTGAAAACGCAAATTGTAACCGATTATGACAAGATAAGTGATTATATCGCTTTAAATGGTTATGAGATAGAACAAAAAATAATT
ACTACCGCAAAGCGGTTTAATATAAGTGAACAAGATTTAGATAAGCCAATACGATTATTAAGTGGCGGACAACAAACAAGCGTT
GCATTAATCAGAGCGTTTATATCTGAAAAACCGCTAATTATATTAGATGAACCTACAAATCATCTTGATCAAGCAATGCTAGAT
AATTTAATTTTAGAAATAAATAAGTCTAAGCAAACGATACTCTACGTTTCACATCACCGTGGTTTTATAAATCAGACTGCGAGT
CATGTTTATGAAATCACTAAAAAAACATCGAGAAAATTTCAAGGTGATTATAATCAATACCATTCAGTCAAACAATTAGAATTT

CAATCTCATAAAAATGCATATGATAAGCAACAAAAAGAAATCAAAGCGCTGGAAGAATCAATTGCACGCGTGAATGAATGGCAT
TCAACTGCCAAAGCTACGACAAGTGTGCGTGATCCTAACCAACAAAAGCGTCTTAGCAAACTAGCTAAAAAAGCAAAAGTAAAA
AATGCTCAGTTAACACATAAATTAAATGAAAAGCAGTTAGAGTCTCCGGATAAACAGGATAGAAAGTTTCATTTTAATGATGAA
CAATCAGTGCATAATCGAGAATTAGTGAAATTAGAAGATATATGTATAGGTATTGGACAAAAAATAATTTATAACAAAGCAAAT
TTTGAAATTAAAAAAGATGAACATATTTTATTAACTGGTCCGAATGGTAGTGGTAAATCATTACTAATTGCGCTTATAAGACAA
CAAGTGAAACCGGATAAAGGTACAGTTTATGTAACGCCTTCAGTAAAAATTGCGTATTTTGATCAACAAAATAATAATTTGAAT
TACAGACAAACACCATTAGATATGGTCATGTCAATAGATCATATGACACGTAGTTATGCTCAAACAATCTTGGCTTCGTTCGGT
TTTGATAAAGATAAAATACAACAAACGATTCGTTCTTTATCTATGGGTGAAAAAAGTAGATTGCAATTTGTACTATTGTTTTTT
TCAAATGCTAATTTACTCATTTTAGATGAACCAACGAATTACTTTGATATTACAACGCAAGACTTAATTTTAAATATGATCAAA
CAGTTCAAAGGACAAGTTTTGATTGTTACACATGATTTATATTTACAAAAACATTTTGATGCGACACATTGGGTTGTAAAAAAC
AAACAATTACTTAATGTTACAATGAATAGTGAACAAAAAATTAATACGCAAAATACGTTGAATTTATTAAATGATTTCAGAGAT
ATAGATGAAAATGGCCATTTTGAAACAGACGACTAG

Sal from *S. saprophyticus* N265Y

ATGTCTTTTTATTTTTCAGAAAAACCATTTGAACAGTTTGGTAAAATATTGATAGAAGACGTAAATATTGATATTGAACTAGGT
AAGCATGTTGCAATGATTGGTGATAATGGTGTCGGCAAGTCAACATTGTTAAATGCTTTAAATTTAAAATATGAAACGCAATCA
TATTTAATGAAGCAAGACTTGACGCAAGTATTTGATTTAACCGCGATGACCTTTATCATTTCAATATTTCCTGAGGTTGCAACT
TTGAAAACGCAAATTGTAACCGATTATGACAAGATAAGTGATTATATCGCTTTAAATGGTTATGAGATAGAACAAAAAATAATT
ACTACCGCAAAGCGGTTTAATATAAGTGAACAAGATTTAGATAAGCCAATACGATTATTAAGTGGCGGACAACAAACAAGCGTT
GCATTAATCAGAGCGTTTATATCTGAAAAACCGCTAATTATATTAGATGAACCTACAAATCATCTTGATCAAGCAATGCTAGAT
AATTTAATTTTAGAAATAAATAAGTCTAAGCAAACGATACTCTACGTTTCACATCACCGTGGTTTTATAAATCAGACTGCGAGT
CATGTTTATGAAATCACTAAAAAAACATCGAGAAAATTTCAAGGTGATTATAATCAATACCATTCAGTCAAACAATTAGAATTT
CAATCTCATAAAAATGCATATGATAAGCAACAAAAAGAAATCAAAGCGCTGGAAGAATCAATTGCACGCGTGAATGAATGGCAT
TCAACTGCCAAAGCTACGACAAGTGTGCGTGATCCT**TAT**CAACAAAAGCGTCTTAGCAAACTAGCTAAAAAAGCAAAAGTAAAA
AATGCTCAGTTAACACATAAATTAAATGAAAAGCAGTTAGAGTCTCCGGATAAACAGGATAGAAAGTTTCATTTTAATGATGAA
CAATCAGTGCATAATCGAGAATTAGTGAAATTAGAAGATATATGTATAGGTATTGGACAAAAAATAATTTATAACAAAGCAAAT
TTTGAAATTAAAAAAGATGAACATATTTTATTAACTGGTCCGAATGGTAGTGGTAAATCATTACTAATTGCGCTTATAAGACAA
CAAGTGAAACCGGATAAAGGTACAGTTTATGTAACGCCTTCAGTAAAAATTGCGTATTTTGATCAACAAAATAATAATTTGAAT
TACAGACAAACACCATTAGATATGGTCATGTCAATAGATCATATGACACGTAGTTATGCTCAAACAATCTTGGCTTCGTTCGGT
TTTGATAAAGATAAAATACAACAAACGATTCGTTCTTTATCTATGGGTGAAAAAAGTAGATTGCAATTTGTACTATTGTTTTTT
TCAAATGCTAATTTACTCATTTTAGATGAACCAACGAATTACTTTGATATTACAACGCAAGACTTAATTTTAAATATGATCAAA
CAGTTCAAAGGACAAGTTTTGATTGTTACACATGATTTATATTTACAAAAACATTTTGATGCGACACATTGGGTTGTAAAAAAC
AAACAATTACTTAATGTTACAATGAATAGTGAACAAAAAATTAATACGCAAAATACGTTGAATTTATTAAATGATTTCAGAGAT
ATAGATGAAAATGGCCATTTTGAAACAGACGACTAG

Sal(B)

ATGCTATTTTTATTTGAAGAAAAACCATTAGAAATTGAGAATAAACAGCTTATAAAACGTTTGTCATTTCATATCGAAGACCAT
GAGCATTTAGCCCTTATCGGTGTTAATGGTATTGGTAAATCTACGCTATTACATCATATTCATAAAAATGAATTGATTGATACA
GCTATGATGGAACAAGATTTAAGTAAACATGATGATATTGATGTTATGGATTATGTCATGTCTGCATATCCAAAGTTAGTTGAA
TTGAGAAAAGATTTATCTGACATTGATTCTTTAAATAGTTATATAGAATTAGACGGATATAACGTTGAAAATAACATTATTATT
GAAGGAAATAAATTAGGATTATCATCAACACATTTTGAGCAAAAGATAGGCACTTTAAGTGGTGGTGAGCAAACTAAAGTCTCA
TTTTTAAAAGTTATTTTATCAGATGCACCATTATTATTAATAGACGAACCAACTAACCATATGGATAAAGAGATGAAAGTGTGG

TTAATAAAAGCTTTTAAATCAGAACAAAGAGCTATTCTATTCGTATCGCATGATAGAGAGTTTTTAAATGAAACACCAGATGCT
ATTTTAGAACTCACAAAAGATGGTGCAACTCGATATTCAGGTCATTATGATGATTATAAAAATCAAAAAGATATTGAAATTGAA
ACAGAAAAAATTAAAATATGAAAAAGAACAGAAAGAACAAAAAGCAATAGAAGAAAGTATTAAGAAATACAAAGAATGGTATCAA
AGGGCTGCTCAGAAAGCTTCTGTTCGTAGTCCATATGCTCAAAAACAATTAAGTAAATTAGCTAAAAGATTTAAATCAAAAGAA
CATCAGTTAAATCGTAAATTAGAAGAATCAAAATCTGATAATCCGTTAGAAGAAAATAAATCCTTTTCTATAGAAAATAATGAA
TTTAAATCACATTATTTAGTAAGATTCGAAAATGTTTCATTTTCATATAAGAGTCGTGAAATTTTTAAAGACACTTATTTTGAA
ATAAAGAGAAATCAAACTGTAATTATAGAAGGTAAAAATGGGTCCGGTAAATCTACATTGATACAATTAATTTTAGGTAACTTA
TTACCAATGAGTGGAGCTGTCAAAAAGCACCCAGACTTAGACATAGGATACTTCTCGCAAGATTTTCAAAATTTAAACCCAAAC
AACTCGGTATTAGAAGAAGTTATGGATATTGAGAATATGATGATAACAGACGCGAGGACTATTTTAGCGAGTTTTTATTTTGAT
AAGAGCAGGATGAATGATAAAGTTCGTCAGTTATCAATGGGAGAAAAGTGCAGGTTACAATTTGTAAAATTATATTTTTCTAAC
CCACACATCTTAATTTTAGATGAACCAACTAATTATTTTGATATTAGTATGCAAGAGAAAATCATACAATTAATCCAAAGTTTT
AATGGTGCAGTAATTATTGTGTCGCATGATGAAATTTTTAAAGATGAAATAAGAGACCAAGTTTGGAAGATTGAAAACTGTAAG
CTCATTCATGAAAATGTATCTATTAATACACCTATTGATGCTGAATCGATGAAGGATGAGTTAAAAATATTAGAGCAATATACA
GATGAAAGAAATAAAGAAACAGACTTCTAG

Sal(B) Y264L

ATGCTATTTTTATTTGAAGAAAAACCATTAGAAATTGAGAATAAACAGCTTATAAAACGTTTGTCATTTCATATCGAAGACCAT
GAGCATTTAGCCCTTATCGGTGTTAATGGTATTGGTAAATCTACGCTATTACATCATATTCATAAAAATGAATTGATTGATACA
GCTATGATGGAACAAGATTTAAGTAAACATGATGATATTGATGTTATGGATTATGTCATGTCTGCATATCCAAAGTTAGTTGAA
TTGAGAAAAAGATTTATCTGACATTGATTCTTTAAATAGTTATATAGAATTAGACGGATATAACGTTGAAAATAACATTATTATT
GAAGGAAATAAATTAGGATTATCATCAACACATTTTGAGCAAAAGATAGGCACTTTAAGTGGTGGTGAGCAAACTAAAGTCTCA
TTTTTAAAAGTTATTTTATCAGATGCACCATTATTATTAATAGACGAACCAACTAACCATATGGATAAAGAGATGAAAGTGTGG
TTAATAAAAGCTTTTAAATCAGAACAAAGAGCTATTCTATTCGTATCGCATGATAGAGAGTTTTTAAATGAAACACCAGATGCT
ATTTTAGAACTCACAAAAGATGGTGCAACTCGATATTCAGGTCATTATGATGATTATAAAAATCAAAAAGATATTGAAATTGAA
ACAGAAAAAATTAAAATATGAAAAAGAACAGAAAGAACAAAAAGCAATAGAAGAAAGTATTAAGAAATACAAAGAATGGTATCAA
AGGGCTGCTCAGAAAGCTTCTGTTCGTAGTCCA**TTA**GCTCAAAAACAATTAAGTAAATTAGCTAAAAGATTTAAATCAAAAGAA
CATCAGTTAAATCGTAAATTAGAAGAATCAAAATCTGATAATCCGTTAGAAGAAAATAAATCCTTTTCTATAGAAAATAATGAA
TTTAAATCACATTATTTAGTAAGATTCGAAAATGTTTCATTTTCATATAAGAGTCGTGAAATTTTTAAAGACACTTATTTTGAA
ATAAAGAGAAATCAAACTGTAATTATAGAAGGTAAAAATGGGTCCGGTAAATCTACATTGATACAATTAATTTTAGGTAACTTA
TTACCAATGAGTGGAGCTGTCAAAAAGCACCCAGACTTAGACATAGGATACTTCTCGCAAGATTTTCAAAATTTAAACCCAAAC
AACTCGGTATTAGAAGAAGTTATGGATATTGAGAATATGATGATAACAGACGCGAGGACTATTTTAGCGAGTTTTTATTTTGAT
AAGAGCAGGATGAATGATAAAGTTCGTCAGTTATCAATGGGAGAAAAGTGCAGGTTACAATTTGTAAAATTATATTTTTCTAAC
CCACACATCTTAATTTTAGATGAACCAACTAATTATTTTGATATTAGTATGCAAGAGAAAATCATACAATTAATCCAAAGTTTT
AATGGTGCAGTAATTATTGTGTCGCATGATGAAATTTTTAAAGATGAAATAAGAGACCAAGTTTGGAAGATTGAAAACTGTAAG
CTCATTCATGAAAATGTATCTATTAATACACCTATTGATGCTGAATCGATGAAGGATGAGTTAAAAATATTAGAGCAATATACA
GATGAAAGAAATAAAGAAACAGACTTCTAG

Sal(B) Y264I

ATGCTATTTTTATTTGAAGAAAAACCATTAGAAATTGAGAATAAACAGCTTATAAAACGTTTGTCATTTCATATCGAAGACCAT
GAGCATTTAGCCCTTATCGGTGTTAATGGTATTGGTAAATCTACGCTATTACATCATATTCATAAAAATGAATTGATTGATACA
GCTATGATGGAACAAGATTTAAGTAAACATGATGATATTGATGTTATGGATTATGTCATGTCTGCATATCCAAAGTTAGTTGAA
TTGAGAAAAAGATTTATCTGACATTGATTCTTTAAATAGTTATATAGAATTAGACGGATATAACGTTGAAAATAACATTATTATT

GAAGGAAATAAATTAGGATTATCATCAACACATTTTGAGCAAAAGATAGGCACTTTAAGTGGTGGTGAGCAAACTAAAGTCTCA
TTTTTAAAAGTTATTTTATCAGATGCACCATTATTATTAATAGACGAACCAACTAACCATATGGATAAAGAGATGAAAGTGTGG
TTAATAAAAGCTTTTAAATCAGAACAAAGAGCTATTCTATTCGTATCGCATGATAGAGAGTTTTTAAATGAAACACCAGATGCT
ATTTTAGAACTCACAAAAGATGGTGCAACTCGATATTCAGGTCATTATGATGATTATAAAAATCAAAAAGATATTGAAATTGAA
ACAGAAAAATTAAAATATGAAAAAGAACAGAAAGAACAAAAAGCAATAGAAGAAAGTATTAAGAAATACAAAGAATGGTATCAA
AGGGCTGCTCAGAAAGCTTCTGTTCGTAGTCCA**ATT**GCTCAAAAACAATTAAGTAAATTAGCTAAAAGATTTAAATCAAAAGAA
CATCAGTTAAATCGTAAATTAGAAGAATCAAAATCTGATAATCCGTTAGAAGAAAATAAATCCTTTTCTATAGAAAATAATGAA
TTTAAATCACATTATTTAGTAAGATTCGAAAATGTTTCATTTTCATATAAGAGTCGTGAAATTTTTAAAGACACTTATTTTGAA
ATAAAGAGAAATCAAACTGTAATTATAGAAGGTAAAAATGGGTCCGGTAAATCTACATTGATACAATTAATTTTAGGTAACTTA
TTACCAATGAGTGGAGCTGTCAAAAAGCACCCAGACTTAGACATAGGATACTTCTCGCAAGATTTTCAAAATTTAAACCCAAAC
AACTCGGTATTAGAAGAAGTTATGGATATTGAGAATATGATGATAACAGACGCGAGGACTATTTTAGCGAGTTTTTATTTTGAT
AAGAGCAGGATGAATGATAAAGTTCGTCAGTTATCAATGGGAGAAAAGTGCAGGTTACAATTTGTAAAATTATATTTTTCTAAC
CCACACATCTTAATTTTAGATGAACCAACTAATTATTTTGATATTAGTATGCAAGAGAAAATCATACAATTAATCCAAAGTTTT
AATGGTGCAGTAATTATTGTGTCGCATGATGAAATTTTTAAAGATGAAATAAGAGACCAAGTTTGGAAGATTGAAAACTGTAAG
CTCATTCATGAAAATGTATCTATTAATACACCTATTGATGCTGAATCGATGAAGGATGAGTTAAAAATATTAGAGCAATATACA
GATGAAAGAAATAAAGAAACAGACTTCTAG

Sal(B) Y264S

ATGCTATTTTTATTTGAAGAAAAACCATTAGAAATTGAGAATAAACAGCTTATAAAACGTTTGTCATTTCATATCGAAGACCAT
GAGCATTTAGCCCTTATCGGTGTTAATGGTATTGGTAAATCTACGCTATTACATCATATTCATAAAAATGAATTGATTGATACA
GCTATGATGGAACAAGATTTAAGTAAACATGATGATATTGATGTTATGGATTATGTCATGTCTGCATATCCAAAGTTAGTTGAA
TTGAGAAAAGATTTATCTGACATTGATTCTTTAAATAGTTATATAGAATTAGACGGATATAACGTTGAAAATAACATTATTATT
GAAGGAAATAAATTAGGATTATCATCAACACATTTTGAGCAAAAGATAGGCACTTTAAGTGGTGGTGAGCAAACTAAAGTCTCA
TTTTTAAAAGTTATTTTATCAGATGCACCATTATTATTAATAGACGAACCAACTAACCATATGGATAAAGAGATGAAAGTGTGG
TTAATAAAAGCTTTTAAATCAGAACAAAGAGCTATTCTATTCGTATCGCATGATAGAGAGTTTTTAAATGAAACACCAGATGCT
ATTTTAGAACTCACAAAAGATGGTGCAACTCGATATTCAGGTCATTATGATGATTATAAAAATCAAAAAGATATTGAAATTGAA
ACAGAAAAATTAAAATATGAAAAAGAACAGAAAGAACAAAAAGCAATAGAAGAAAGTATTAAGAAATACAAAGAATGGTATCAA
AGGGCTGCTCAGAAAGCTTCTGTTCGTAGTCCA**TCT**GCTCAAAAACAATTAAGTAAATTAGCTAAAAGATTTAAATCAAAAGAA
CATCAGTTAAATCGTAAATTAGAAGAATCAAAATCTGATAATCCGTTAGAAGAAAATAAATCCTTTTCTATAGAAAATAATGAA
TTTAAATCACATTATTTAGTAAGATTCGAAAATGTTTCATTTTCATATAAGAGTCGTGAAATTTTTAAAGACACTTATTTTGAA
ATAAAGAGAAATCAAACTGTAATTATAGAAGGTAAAAATGGGTCCGGTAAATCTACATTGATACAATTAATTTTAGGTAACTTA
TTACCAATGAGTGGAGCTGTCAAAAAGCACCCAGACTTAGACATAGGATACTTCTCGCAAGATTTTCAAAATTTAAACCCAAAC
AACTCGGTATTAGAAGAAGTTATGGATATTGAGAATATGATGATAACAGACGCGAGGACTATTTTAGCGAGTTTTTATTTTGAT
AAGAGCAGGATGAATGATAAAGTTCGTCAGTTATCAATGGGAGAAAAGTGCAGGTTACAATTTGTAAAATTATATTTTTCTAAC
CCACACATCTTAATTTTAGATGAACCAACTAATTATTTTGATATTAGTATGCAAGAGAAAATCATACAATTAATCCAAAGTTTT
AATGGTGCAGTAATTATTGTGTCGCATGATGAAATTTTTAAAGATGAAATAAGAGACCAAGTTTGGAAGATTGAAAACTGTAAG
CTCATTCATGAAAATGTATCTATTAATACACCTATTGATGCTGAATCGATGAAGGATGAGTTAAAAATATTAGAGCAATATACA
GATGAAAGAAATAAAGAAACAGACTTCTAG

Sal(B) Y264N

ATGCTATTTTTATTTGAAGAAAAACCATTAGAAATTGAGAATAAACAGCTTATAAAACGTTTGTCATTTCATATCGAAGACCAT
GAGCATTTAGCCCTTATCGGTGTTAATGGTATTGGTAAATCTACGCTATTACATCATATTCATAAAAATGAATTGATTGATACA

GCTATGATGGAACAAGATTTAAGTAAACATGATGATATTGATGTTATGGATTATGTCATGTCTGCATATCCAAAGTTAGTTGAA
TTGAGAAAAGATTTATCTGACATTGATTCTTTAAATAGTTATATAGAATTAGACGGATATAACGTTGAAAATAACATTATTATT
GAAGGAAATAAATTAGGATTATCATCAACACATTTTGAGCAAAAGATAGGCACTTTAAGTGGTGGTGAGCAAACTAAAGTCTCA
TTTTTAAAAGTTATTTTATCAGATGCACCATTATTATTAATAGACGAACCAACTAACCATATGGATAAAGAGATGAAAGTGTGG
TTAATAAAAGCTTTTAAATCAGAACAAAGAGCTATTCTATTCGTATCGCATGATAGAGAGTTTTTAAATGAAACACCAGATGCT
ATTTTAGAACTCACAAAAGATGGTGCAACTCGATATTCAGGTCATTATGATGATTATAAAAATCAAAAAGATATTGAAATTGAA
ACAGAAAAATTAAAATATGAAAAAGAACAGAAAGAACAAAAAGCAATAGAAGAAAGTATTAAGAAATACAAAGAATGGTATCAA
AGGGCTGCTCAGAAAGCTTCTGTTCGTAGTCCA**AAC**GCTCAAAAACAATTAAGTAAATTAGCTAAAAGATTTAAATCAAAAGAA
CATCAGTTAAATCGTAAATTAGAAGAATCAAAATCTGATAATCCGTTAGAAGAAAATAAATCCTTTTCTATAGAAAATAATGAA
TTTAAATCACATTATTTAGTAAGATTCGAAAATGTTTCATTTTCATATAAGAGTCGTGAAATTTTTAAAGACACTTATTTTGAA
ATAAAGAGAAATCAAACTGTAATTATAGAAGGTAAAAATGGGTCCGGTAAATCTACATTGATACAATTAATTTTAGGTAACTTA
TTACCAATGAGTGGAGCTGTCAAAAAGCACCCAGACTTAGACATAGGATACTTCTCGCAAGATTTTCAAAATTTAAACCCAAAC
AACTCGGTATTAGAAGAAGTTATGGATATTGAGAATATGATGATAACAGACGCGAGGACTATTTTAGCGAGTTTTTATTTTGAT
AAGAGCAGGATGAATGATAAAGTTCGTCAGTTATCAATGGGAGAAAAGTGCAGGTTACAATTTGTAAAATTATATTTTTCTAAC
CCACACATCTTAATTTTAGATGAACCAACTAATTATTTTGATATTAGTATGCAAGAGAAAATCATACAATTAATCCAAAGTTTT
AATGGTGCAGTAATTATTGTGTCGCATGATGAAATTTTTAAAGATGAAATAAGAGACCAAGTTTGGAAGATTGAAAACTGTAAG
CTCATTCATGAAAATGTATCTATTAATACACCTATTGATGCTGAATCGATGAAGGATGAGTTAAAAATATTAGAGCAATATACA
GATGAAAGAAATAAAGAAACAGACTTCTAG